New Design Methodologies for Printed Circuit Axial Field Brushless DC Motors

by

Daniele Marco Gambetta, MPhil, B.Sc (Hons)

Dissertation

Submitted in Fulfillment

of the Requirements

for the Degree of

Doctor of Philosophy

at the

The University of Southern Queensland

Faculty of Engineering & Surveying

December 2009

Abstract

A number of factors are contributing to the increased practical importance of printed circuit axial flux brushless direct current (BLDC) machines. The main ones are the availability of low cost power electronic devices and digital controllers as well as cost effective high strength permanent magnets. Advancement of multi-layer printed circuit technology is also an important factor.

Existing printed circuit board motors, found in applications such as computer disk drives and portable audio-visual equipment, are typically rated at a few watts per thousand revolutions per minute (krpm). The focus of this thesis project has been on printed circuit motors with ratings of a few tens of watts per krpm.

A significant part of this thesis project has been devoted to development of systematic design procedures for printed circuit stators. In particular those procedures include algorithms which allow performance comparisons of several stator coil shapes. A new coil shape, with improved torque capability, has been developed.

BLDC motors that operate in sensorless mode has advantages such as lower cost, better reliability and space saving. A new generalised version of the previously reported *equal inductance method* has been developed which allows sensorless commutation of printed circuit BLDC motors down to zero speed and start-up with practically no back rotation.

Computer efficient numerical models have been developed to predict phase inductances and stator eddy-current loss. Sufficiently accurate phase inductance predictions make possible theoretical assessment of performance of motors under sensorless commutation control that is based on the *equal inductance method*. The proposed method of calculation of eddy current loss allows designers to determine the track width beyond which eddy current loss becomes excessive.

The mathematical model on which the enhanced equal inductance method is based and those that have been used for performance assessment, inductance prediction and eddy-current loss evaluation have all been validated by specially designed laboratory tests carried out on prototype motors.

Certification of Thesis

I certify that the ideas, experimental work, results, analyses, software and conclusions reported in this dissertation are entirely my effort, except where otherwise acknowledged. I also certify that the work is original and has not been previously submitted for any other award, expect where otherwise acknowledged.

Signature of Candidate	Date

ENDORSEMENT

Signature of Supervisors	Date

Acknowledgments

I would sincerely like to thank and acknowledge the following people for their assistance, guidance and support throughout the duration of this thesis project.

First of all I would like to thank my supervisor Dr Tony Ahfock. Throughout the course of the research he maintained a constant interest and provided invaluable assistance and guidance in the development of this work. Much of the work developed and presented herein was discussed with and reviewed by Dr Tony Ahfock. I wish to acknowledge the significant contributions he made by in the preparation and production of this thesis.

I am also very grateful to Mr Aspesi, Mr Romano (CEO of the funding company, Metallux SA), Mr Sassone (President of the Eltek Group) and Mr Colombo for their continued support, interest in and assistance with the thesis project.

I wish to thank the Faculty of Engineering and Surveying and the Office of Research and Higher Degrees for their support and assistance. My thanks also extends to all those at the University who made this such a pleasant experience.

Finally, I wish to thank my beloved Federica, my mother, my father and my sister for their continued support.

Contents

List of Tables

List of Figures

List of Symbols

Chapter 2

t_i	iron axial thickness
t_m	permanent magnet axial thickness
t_{ag}	mechanical air-gap axial length
t_s	stator axial thickness
R_o	outer radius
R_i	inner radius
t_a	total axial length
t_c	stator/magnet clearance
P_l	max allowable stator power loss
B_r	remanence
B_s	rotor peak flux density
P	number of rotor poles

N	number of turns per coil
L	number of printed circuit layers per phase

Chapter 3

N	number of turns per coil
R_o	outer radius
R_i	inner radius
w	track minimum width
c	minimum clearance between tracks
N_s	number of spirals per layer
R_x	x point radius
n	number of turns counting from the inter-coil boundary line
E	EMF per spiral
ω_m	rotational speed
P	number of poles
B_{pk}	airgap peak flux density
B_r	remanence of permanent magnet.
t_m	permanent magnet axial thickness
g	airgap length measured axially between opposite magnet surfaces
S_c	combined length, spread and pitch factors of coil
B_s	maximum allowable flux density in the rotor iron
S_m	pitch factor magnet
t_i	iron axial thickness
t_s	stator axial thickness

t_a	total axial length
t_{ag}	mechanical air-gap axial length
dE	contribution to total EMF from each track segment
B*	estimated flux density at point C in figure 3.7
ω_m	rotational speed
H	magnetic field intensity
B	magnetic field density
P_l	max allowable stator power loss
R	phase resistance
R_{th} Prep-Preg	thermal resistance Pre-Preg
R_{th} FR4	thermal resistance FR4
$c_{pre\text{-}preg}$	pre-preg thermal conductivity
$c_{FR\text{-}4}$	FR-4 thermal conductivity
I_{phase}	phase current
R_{stator}	total three-phase stator resistance
α	typical heat transfer coefficient
k_f	copper fill factor
$R_{th\ S\text{-}A}$	thermal resistance surface to ambient
n_{used}	number of used layers
w_{new}	new optimized track width
k_{series}	series connection coefficient (of 2-layer elements)
EMF_{total}	total desired phase EMF
$EMF_{element}$	total EMF of 2-layer element

n_{max}	maximal number of layer
t_{layer}	layer thickness = Base cu thickness + Pre-Preg thickness
$n_{parallel}$	number of parallel layers
ρ_{Cu}	copper resistivity
l_{spiral}	length of the spiral
A_{spiral}	cross sectional area of the spiral

Chapter 4

L_{ii}	self inductance of phase i;
L_{ji}	mutual inductance between phase i and phase j
E_i	i-phase winding back EMF
v_{cy}	voltage measurements between phase c and rail y
v_{cy}^{+}	voltage measurements in states $a^{+}b^{-}$
v_{cy}^{-}	voltage measurements in states $b^{+}a^{-}$
v_{ay}	voltage measurements between phase a and rail y
v_{by}	voltage measurements between phase b and rail y
t_s^{+}	sampling instant during on pulse
t_s^{-}	sampling instant during “off” pulse
V_{dc}	dc bus voltage
V_t	switching device voltage drop
L_q	q-axis inductance

L_d	d-axis inductance
S	saliency ratio
θ_i	rotor initial position

Chapter 5

L_{ii}	self inductance of phase i;
L_{ji}	mutual inductance between phase i and phase j
E_i	i-phase winding back EMF
v_{cy}	voltage measurements between phase c and rail y
v_{cy}^{+}	voltage measurements in states $a^{+}b^{-}$
v_{cy}^{-}	voltage measurements in states $b^{+}a^{-}$
v_{by}	voltage measurements between phase b and rail y
v_{by}^{+}	voltage measurements in states $a^{+}c^{-}$
v_{by}^{-}	voltage measurements in states $c^{+}a^{-}$
v_{ay}	voltage measurements between phase a and rail y
v_{ay}^{+}	voltage measurements in states $b^{+}c^{-}$
v_{ay}^{-}	voltage measurements in states $c^{+}b^{-}$
t_s^{+}	sampling instant during on pulse
t_s^{-}	sampling instant during “off” pulse

v_{dc}	dc bus voltage
θ_i	rotor initial position
t_{ON}	on time of the PWM pulse
t_{OFF}	off time of the PWM pulse
R_{DSon}	dynamic resistance of power semiconductor

Chapter 6

H	magnetic flux intensity
J	current density
E	electric field induced within printed tracks
B	magnet flux density
J_i	imposed current density
J_e	induced current density
J_m	magnetisation current density
μ	magnetic permeability
σ	electric conductivity
M	magnetisation of permanent magnets
$B(r, \theta, z, t)$	flux density seen, at time t, by an observer fixed to the stator at location (r, θ, z)
ω	speed of the rotor
B_z	component of flux density normal to the conductor plane
v	relative speed between the magnetic field and the conductor
λ	angle between the conductor and the direction of relative motion
R_{ia}	resistance of internal branch along the track

R_{ea}	resistance of branch along the track on the grid edge
R_{ib}	resistance of internal branch across the track
R_{eb}	resistance of branch across the track on the edge of the grid
w_s	width of segment
w_f	width of filament
t_c	track thickness
σ	electrical conductivity of track
I_{loop}	array of loop currents
E_{loop}	array of loop EMFs
R_{loop}	loop resistance matrix
I_{branch}	array of branch currents
A	loop to branch incidence matrix
R	resistance of a track section
I	motor current
I_e	eddy current
P_e	eddy current loss
T_e	rotor driving torque
ω	the rotor speed
L_a	length of the torque arm
F_rL_a	bearing friction torque

Chapter 7

L_z	axial separation
A_z	area between conductor loops

μ	permeability of material
L_r	mean separation between inter-conductors mid-lines
A_r	(conductor perimeter) x (axial separation)
R	reluctance
σ	conductivity of the magnet
L_x	weighted average of all discrete distances between the last stator conductor that falls fully within the magnet profile and the edge of the magnet
A_{cell}	area of the cell
L_{ii}	self inductance of phase i ;
L_{ji}	mutual inductance between phase i and phase j
L_{da}	direct axis self-inductance of phase a
L_{db}	direct axis self-inductance of phase b
L_{qa}	quadrature axis self-inductance of phase a
L_{qb}	quadrature axis self-inductance of phase b
M_{bd}	mutual inductances ab when phase ‘a’ is aligned with the rotor d-axis
M_{cd}	mutual inductances ac when phase ‘a’ is aligned with the rotor d-axis
M_{bq}	mutual inductances ab when phase ‘a’ is aligned with the rotor q-axis
M_{cq}	mutual inductances ac when phase ‘a’ is aligned with the rotor q-axis

Publications

The following journal papers, that have been published or accepted for publication, are direct outcomes of this research project.

Ahfock A.**,** Gambetta D., '*Stator Eddy Current Losses in Printed Circuit Brushless DC Motors'*, Electric Power Applications, IET Proceedings, (accepted for publication)

Ahfock A.**,** Gambetta D., '*Sensorless Commutation of Printed Circuit Brushless DC Motors'*, Electric Power Applications, IET Proceedings, (accepted for publication)

Gambetta D., Ahfock A., '*Design of Printed Circuit Brushless Motors'*, Electric Power Applications, IET Proceedings, Vol 3, Issue 5, Sept 2009, Pages 482-490

Gambetta D., Ahfock A., *'A New Sensorless Commutation Technique for Brushless DC Motors'*, Electric Power Applications, IET Proceedings, Vol 3, Issue 1, Jan 2009, Pages 40-49

Chapter 1

Introduction

1.1 Focus of the Thesis Project

Printed circuit motors have some unique advantages such as high efficiency, zero cogging torque and reduced acoustic noise. They allow design flexibility and are relatively easy to manufacture. For example a change in dimensions of a printed circuit stator can be accommodated without any major alterations to production equipment and processes.

Printed circuit motors are relatively small axial field motors. They are used in applications such as computer hard disk drives and small fans. Printed spiral coils are particularly suited to motors of such low dimensions. There is variation in the spiral coil shape adopted by different

designers. To the author's knowledge, very little has been published on justification for the use of particular coil geometries.

Printed circuit motors may be operated as brushless synchronous motors or as brushless direct current (BLDC) motors. In both cases sensorless operation is highly desirable because elimination of physical position sensors improves cost and reliability and reduces space requirements. The control scheme of sensorless synchronous printed circuit motors is significantly more complex than that of sensorless BLDC motors. On the other hand, while sensorless synchronous motors typically provide superior performance, currently available sensorless BLDC motors meet the performance requirements of a large number of applications. The main drawback of the so-called back electromotive force (back EMF) method, which is the most widely used sensorless technique with BLDC motors, is its ineffectiveness near and at zero speed.

The focus of this thesis project is on the development of:

(a) systematic methods to optimise coil design for printed circuit BLDC motors and
(b) a cost-effective speed sensorless technique that would allow satisfactory operation of printed circuit BLDC motor performance at zero and near zero speeds.

1.2 Background Information on Brushless DC Motors

Brushless DC motors may be of radial field or of axial field design. Axial field design implies that the working or air-gap flux is parallel to the axis of rotation and that the active sections of the stator conductors are in the radial direction. Radial field design implies that working or air-gap flux is in the radial direction and that the active sections of the stator conductors are in the axial direction. The basic principles of axial field motors are identical to those of radial field machines. This section refers to the more common radial field machines.

Fundamentally the brushless DC (BLDC) motor is very similar to the classical separately excited DC motor. Excitation for the latter is provided by windings or permanent magnets mounted on the stator. In the BLDC motor excitation is provided by permanent magnets mounted on the rotor. Figures 1.1 and 1.2 show a number of methods used to mount the magnets on the rotor. There has been remarkable progress made in the development of high quality magnets in the last few decades. At present high performance NdFeB (neodymium-iron-boron) magnets are widely used in BLDC motors.

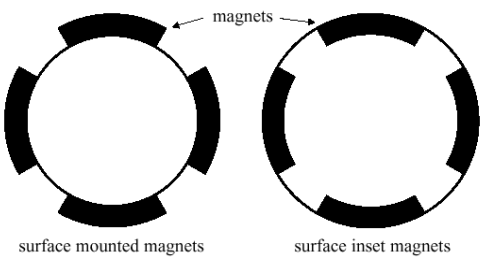

Figure 1.1 : BLDC Rotors with Surface Magnets (Source: reference [1])

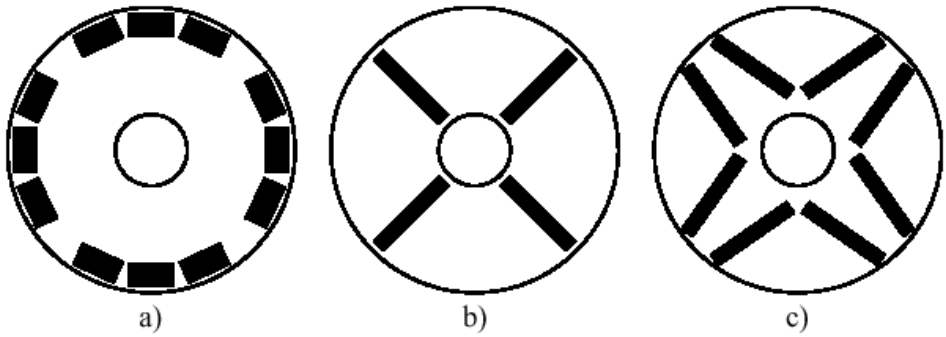

a) Surface buried,

b) radial, and c) v-arranged magnets (black areas are the magnets)

Figure 1.2 : BLDC Rotors with Internal Magnets (Source: reference [1])

Reversal of direction of coil currents at precise rotor positions is essential in both conventional DC motors and in BLDC motors. In conventional motors this is carried out by means of the shaft mounted mechanical commutator and the brushes. The commutator and brushes act both as a set of switches to carry out current reversal and as a position sensor which ensures that the reversals are initiated at the right instants. In the BLDC motor electrical energy is fed to coils residing on the stator and as mentioned before excitation is provided by rotor mounted permanent magnets. Therefore there is no requirement for brushes and this is the most important advantage of BLDC motors compared to classical DC motors. There is still a requirement for stator coil current reversals to be synchronized with appropriate rotor positions. As in the case of the classical DC motor, this involves switching and position sensing. In the BLDC motor, however, switching and position detection are done separately. Switching is performed by power semiconductors, typically in a three-phase inverter bridge configuration using MOSFETs or IGBTs (see figure

1.3). This implies that BLDC motors are normally three-phase wound with each motor line current controlled by one leg of the three-phase bridge. The inverter is operated in PWM mode with two out of the three-phase windings energized at any one time. Figure 1.4 displays idealized phase currents supplied by the inverter. Note that ideally there are six commutation states in one cycle of operation. These have been labelled CB, AB, AC, BC, BA and CA.

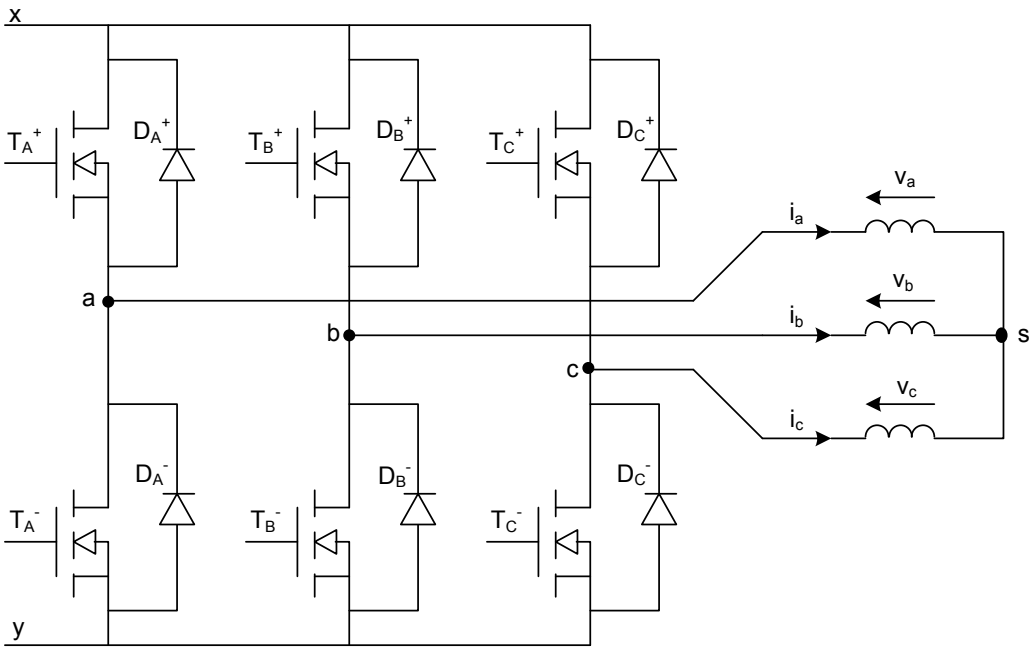

Note: 3-phase windings assumed star connected, some BLDC motors are delta connected.

Figure 1.3 : Inverter fed BLDC Stator Windings

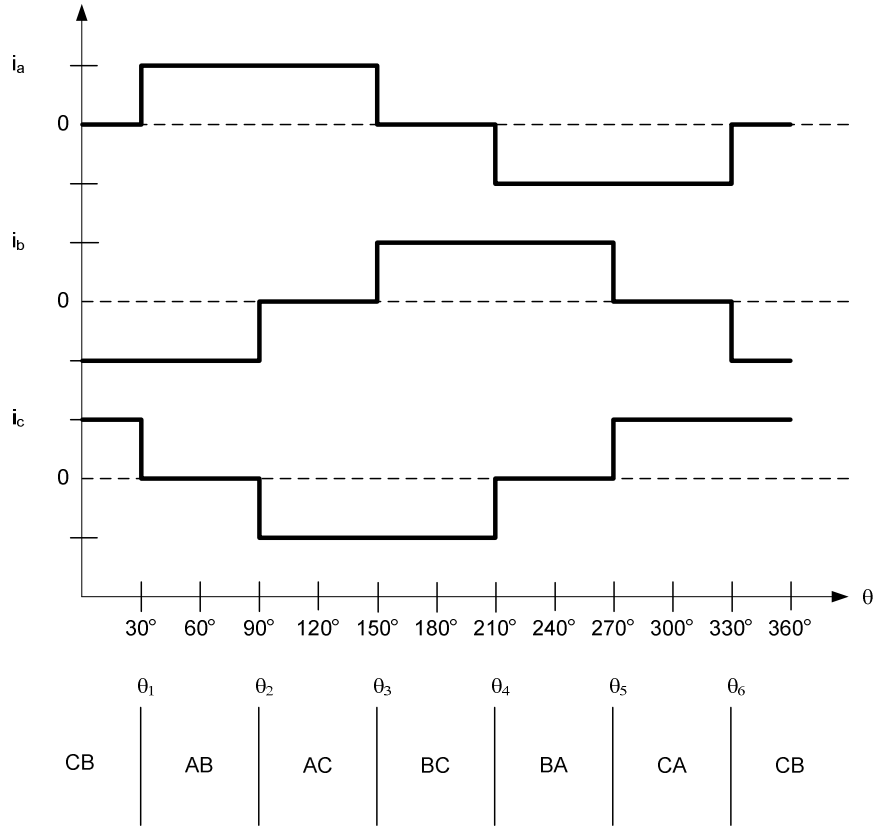

Figure 1.4 : Idealised Currents Supplied by Inverter

Phase current reversals have to be initiated at rotor angular positions θ_1, θ_2, θ_3, θ_4, θ_5, and θ_6. The rotor position detection technique has to be carefully selected for each application taking into consideration factors such as performance requirements, cost, available space envelope and the physical environment. Position detection based on physical position sensors such as Hall sensors are simple to implement, but sensorless techniques are preferable because they can reduce overall cost, space requirements and improve reliability. The most commonly used sensorless method is the so-called back EMF method. It is based on detection of the zero crossing of the

back EMF of the unenergised phase. The commutation controller relies on the fact that the ideal commutation position lags the back EMF zero crossing position by thirty electrical degrees [2,3]. As mentioned before the major problem with the back EMF method is its ineffectiveness at or near zero speed.

There is currently significant research work aimed at developing improved sensorless techniques for brushless motors. Many of the suggested methods are based on inductive saliency. The recently suggested equal inductance method [2, 3] has proven to be very effective and, when used together with the back EMF technique, meets performance requirements over very wide speed ranges down to zero speed.

1.3 Background Information on Printed Circuit BLDC Motors

Printed circuit motors made their first appearance more than forty years ago [4, 5]. They were originally conceived to be brushed DC motors. Advances in power electronics and the availability of relatively low cost permanent magnets have made possible brushless printed circuit motors. These motors may be operated in synchronous mode or they may be operated as brushless DC motors. While, in terms of speed accuracy and torque quality, superior performance is obtained by operating in the synchronous mode, operation in the brushless DC

mode is much simpler and cheaper and meets the performance requirements of most applications. The focus of this thesis project is on printed circuit BLDC motors.

There is a major difference between the coil configuration used in the original printed circuit motors and the coil configuration in modern printed circuit stators. In the original design, as shown in figure 1.5, every printed track is nominally identical to every other track except for a displacement by one track pitch (analogous to the slot pitch in conventional wire wound machines). The coil configuration illustrated in figure 1.5 is normally called a “wave winding”. In the modern design the printed coil is usually spirally shaped. This means that the length of the active sections of tracks become progressively smaller towards the centre of the spiral. An example is shown in figure 1.6. The advantage of using a spirally shaped coil is simplicity and also it is much easier to accommodate a spiral coil within a stator having small radial dimensions.

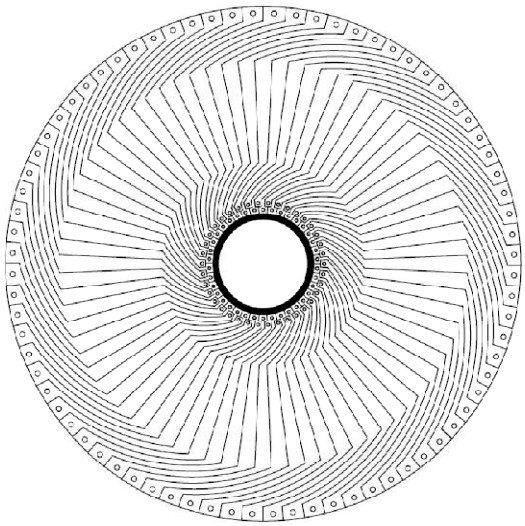

Figure 1.5 : Wave Winding (Source: reference [4])

Unfortunately there are only a few publications on printed circuit stators with spirally shaped coils. It appears that up to now researchers have not yet developed systematic methods for the design and production of printed circuit stators. Some qualitative statements have been made about the use of rhomboidal shaped turns to reduce copper loss, but the negative effect that this could have on torque capability has not been considered. Rhomboidal turns, as shown in figure 1.6, also leave significant unused areas on the substrate between neighbouring coils. Note that spirals exist in pairs on adjacent printed circuit layers. This allows the central terminal of one spiral to be series connected to the central terminal of another spiral located on the adjacent printed circuit layer. Thus the total number of layers is always even. There may well be better options than rhomboidal turns. A number of patented printed circuits make better use of the area of the substrate by using coils whose active sections follow lines that are parallel to the radial line separating neighbouring coils. Throughout this document these will be termed as “coils with parallel tracks”. An example is shown in figure 1.7. Potentially coils with parallel tracks can result in higher torque output than equivalent machines with rhomboidal coils. But this remains to be proven.

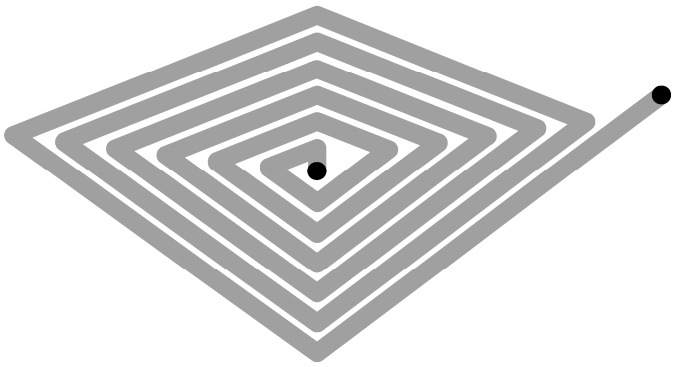

Figure 1.6 : Rhomboidal Winding (example of a spirally shaped coil)

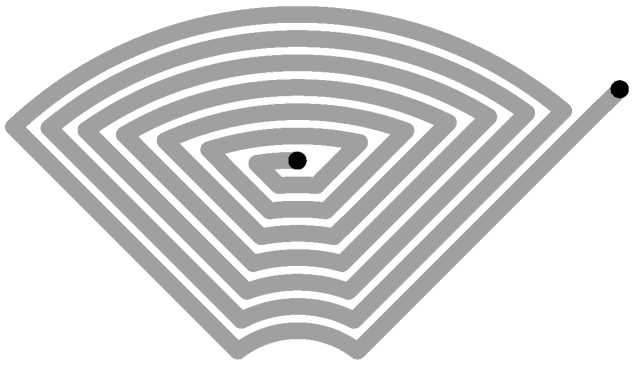

Figure 1.7 : Coils with Parallel Active Sections

Based on elementary electromagnetic theory, it could be argued that the maximum torque from a given length of track is obtained if that track runs along a radial line. This is the case because a printed circuit machine being considered is an axial flux machine. That is the working or air-gap flux is designed to be axial and motion of the rotor magnetic field relative to the stator tracks is purely circumferential. Consequently maximum torque is obtained from current on the stator if it flows in the radial direction, which is perpendicular to both the axial field and the direction of relative motion of the rotor field. However, as shown in figure 1.8, the number of radial tracks is heavily constrained by crowding near the inner radius of the substrate. Nevertheless, the radial track option was not completely eliminated because it could represent the optimum choice under special situations.

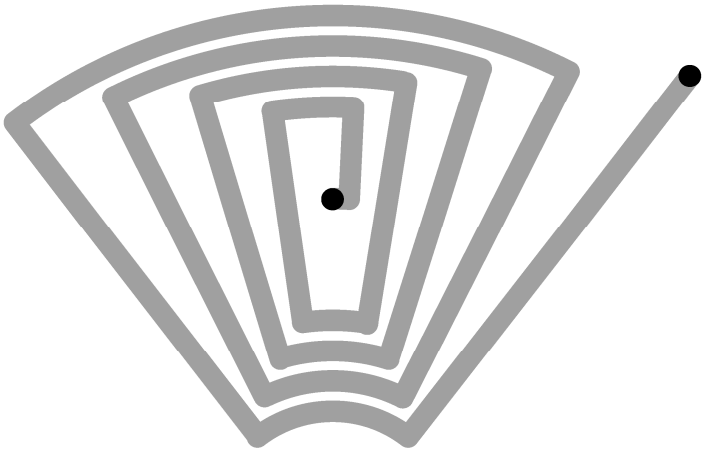

Figure 1.8 : Coils with Radial Active Sections

As mentioned in section 1.2, BLDC motors are normally three-phase machines. There are two basic ways of implementing a three phase printed circuit stator. In the conceptually simpler design, as exemplified in figure 1.9, a printed circuit layer belongs to one phase only. This means that the total number of layers is a multiple of six. The layers belonging to one phase would be identical to the layers belonging to the other two phases. However, as expected, the magnetic axes of the coils of one phase will be shifted from the magnetic axes of the coils of the other phases by 120 electrical degrees. The stator could be made up of a stack of three substrates, as shown in figure 1.10, or a single substrate could be used for all phases. A feature of this stator design is that the stator coil pitch is equal to the rotor pole pitch. This means that the number of coils per layer is equal to the number of poles.

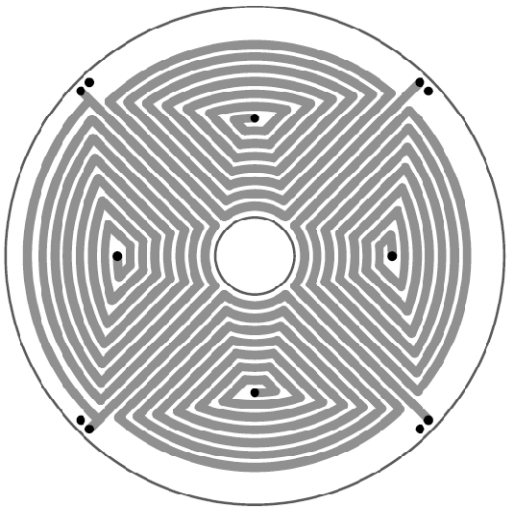

Figure 1.9 : Distribution of Coil on one Printed Circuit Layer (‘Four-Pole’ Flux Distribution)

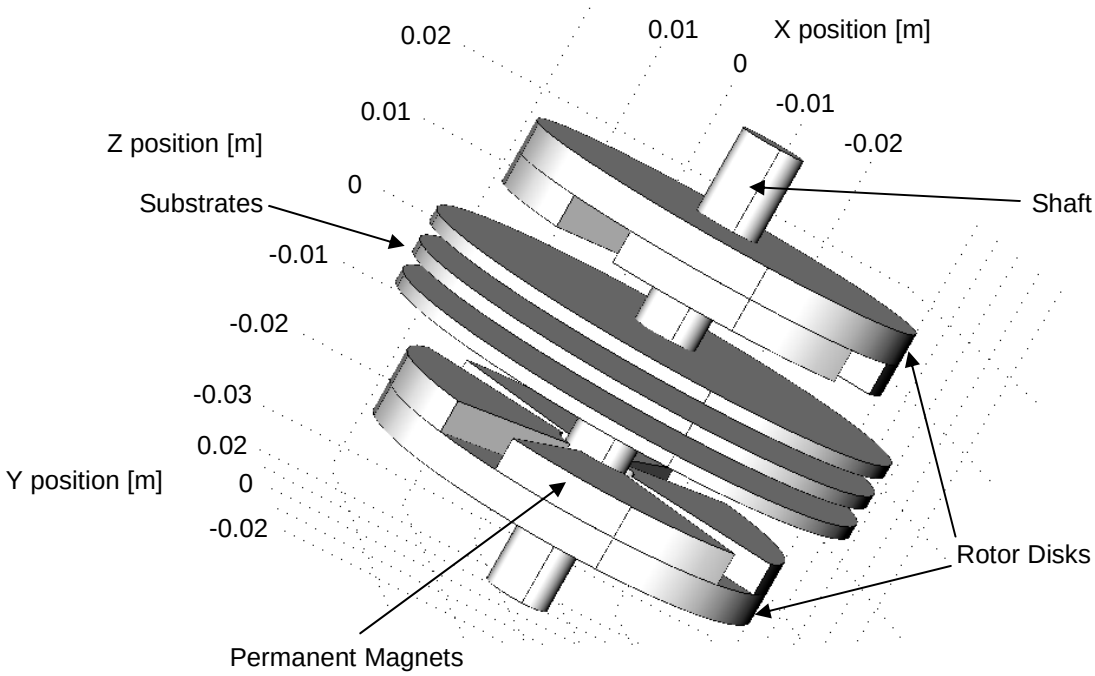

Figure 1.10 : Exploded View of a Printed Circuit Axial Field Brushless Motor

The other way of implementing a printed circuit stator would be to have all three phases sharing every printed layer. This means that the number of coils per layer must be a multiple of six. A feature of this stator design is that the stator coil pitch is generally different from the rotor pole pitch.

The following are some of the important variables that have to be considered in order to arrive at an optimum printed stator design for a given application.

(a) Number of rotor poles

(b) Stator coil shape (wave wound, rhomboidal, radial or parallel)

(c) Nature of printed layers (each equally shared between phases or single phase per layer)

(d) Number of layers

(e) Track thickness

(f) Track width

(g) Track clearance

(h) Insulation material and insulation thickness

(i) Substrate material and substrate thickness

(j) Number of substrates that make up the stator stack

The task of making the correct decision with regards to the design variables listed above would be greatly simplified if appropriate analytical and systematic design tools were available.

1.4 Sensorless Operation

Printed circuit brushless DC motors are relatively small motors and they are more likely to be cost competitive if they can operate without position sensors. The back EMF zero crossing method may be a good choice if good performance during starting and at low speeds are not critical requirements. As back EMF is proportional to speed, the method does not work at and near zero speed. Satisfactory sensorless operation at low speed and during start-up is possible only by implementation of special techniques. One way of addressing the commutation problem at start-up and at low speeds is to supplement the back EMF method with the "*equal inductance method*" [2]. The latter method relies on the variation of stator inductance with rotor position. This variation is characterised by the so-called saliency ratio of the machine. The method is called the "*equal inductance method*" because detected positions of equal inductance of the energised phase pair are used to determine the next commutation instant. While the equal inductance method has been found to work with wire-wound motors having saliency ratios of 1.1 or more, it is not clear whether the method would work with printed circuit motors. The significant differences between the characteristics of printed circuit machines and those of wire-wound machines suggest that modifications of the originally proposed equal inductance method would most likely be necessary for it to work with printed circuit motors.

Those, who at the motor design stage decide to use a sensorless method that is based on winding inductance, must be able to make theoretical prediction of such inductance. Printed circuit machine inductances are relatively easy to measure once the machine is built, but their

theoretical determination is not straightforward. The brute force approach to theoretical determination of inductance would require detailed three dimensional non-linear electromagnetic magnetic modelling under quasi static conditions. Typically such modelling would be carried out using the finite element method. However, this approach does not suit many designers because of lack of the necessary skills or computational resources. Also, due to the necessity for iterative analysis to arrive at optimal designs, computer processing time may also be too long. There is a need to develop sufficiently accurate but fast and computationally efficient techniques for determining printed circuit motor self and mutual inductances.

1.5 Thesis Project Objectives

It is very likely that printed circuit motors will be used in an increasing number of modern applications. However, there seems to be a lack of systematic design tools to assist printed circuit motor designers. Also, to the author's knowledge, there is no published work that specifically addresses the question of sensorless operation of printed circuit BLDC motors down to zero speed. The need to address those identified gaps has led to the following objectives for this thesis project:

(a) to develop guidelines and a theoretical basis for the optimum electromagnetic design of axial field printed circuit brushless DC motors;

(b) to experimentally validate the analytical techniques and design procedures that are developed as part of this thesis project;

(c) to develop a position sensorless commutation method for axial field printed circuit brushless DC motors that is effective down to zero speed;

(d) to experimentally validate the position sensorless commutation technique that is developed as part of this thesis project and

(e) to develop a computationally efficient modelling technique that would allow prediction of the self and mutual inductances of the phase windings of axial field printed circuit brushless DC motors;

1.6 Outline of Dissertation

A review of the published works that are of relevance to the thesis project objectives is presented in chapter 2. Details of the thesis project methodology and the reasoning behind it are given in the same chapter.

Chapter 3 is devoted to the development of tools to help with the optimum design of printed circuit board stators. These tools include computer algorithms for automatic stator track plotting and phase EMF waveform prediction. The mathematical basis for the algorithms and their experimental validation are also included.

Chapters 4 and 5 are about the enhancements made to and the generalisation of the originally proposed equal inductance method. The enhancements reported in chapter 4 include a commutation algorithm that incorporates a start-up technique which is also based on the equal

inductance method. Experimental results which validate the enhanced equal inductance method are presented. The modified method, unlike the originally proposed method, does not require a neutral connection.

The originally proposed equal inductance method assumes that the motor being controlled is nominally symmetrical. Chapter 5 presents the mathematical arguments which were used to arrive at a generalised equal inductance method applicable to the inherently asymmetric class of printed circuit BLDC motors that was the focus of this thesis project. Experimental results which confirm the validity of the generalised method are also presented.

Eddy currents induced within the stator tracks of printed circuit machines represent a parasitic load and cause increased stator heating. In chapter 6 a mathematical model is proposed to quantify stator eddy current loss. A specially designed laboratory test procedure is described which has allowed predictions made by the model to be verified.

Chapter 7 presents fast and computer resource efficient mathematical algorithms that allow stator winding inductances to be theoretically evaluated. Predictions made using the algorithms have been experimentally verified. The computer algorithms can be used by designers, before construction of physical prototypes, to check that sufficient inductive saliency is present for successful application of the equal inductance method.

Conclusions of the thesis project are presented in chapter 8.

1.7 Main Outcomes of the Thesis Project

This thesis project has resulted in a number of useful outcomes for printed circuit board machine designers. Analytical tools have been developed and validated to assist with optimisation of printed stators. Designers will be able to maximise output torque while satisfying requirements for maximum track width, minimum track width and inter-track clearance. In particular a technique has been developed for quantitative assessment of eddy current losses within copper tracks. Theoretical findings of the thesis project can be embedded into computer software for quick assessment of the effect of changes in important design parameters such as stator dimensions and pole numbers. It is also possible to use the developed design tools to explore ways of reducing stator losses and improve efficiency without compromising torque capability.

While printed circuit motors may be operated in synchronous mode to achieve high performance in terms of speed accuracy and torque quality, operating in brushless DC mode gives adequate performance for most applications. A main advantage of the brushless DC mode is the possibility of relatively simple sensorless implementation. Provided a brushless DC motor exhibits enough saliency, very satisfactory performance at start-up and near zero speed is possible if sensorless operation is based on the equal inductance method. The effectiveness of the equal inductance method relies on the existence of sufficient saliency. An important contribution from this thesis project is better understanding of the fundamental reasons behind the existence of saliency in brushless printed circuit motors. This improved understanding has

led to a simplified electromagnetic model that allows saliency ratio and winding inductances to be estimated by means of computationally efficient techniques.

An interesting point is that the equal inductance method was originally developed for nominally symmetrical three phase machines. This thesis project dealt with an important class of printed circuit machines which exhibits significant asymmetry. A significant outcome has been a generalised equal inductance method that takes into consideration phase asymmetry.

The following journal papers, that have been published or accepted for publication, are direct outcomes of this research project.

Ahfock A.**,** Gambetta D., '*Stator Eddy Current Losses in Printed Circuit Brushless DC Motors'*, Electric Power Applications, IET Proceedings, (accepted for publication)

Ahfock A.**,** Gambetta D., '*Sensorless Commutation of Printed Circuit Brushless DC Motors'*, Electric Power Applications, IET Proceedings, (accepted for publication)

Gambetta D., Ahfock A., '*Design of Printed Circuit Brushless Motors'*, Electric Power Applications, IET Proceedings, Vol 3, Issue 5, Sept 2009, Pages 482-490

Gambetta D., Ahfock A., *'A New Sensorless Commutation Technique for Brushless DC Motors'*, Electric Power Applications, IET Proceedings, Vol 3, Issue 1, Jan 2009, Pages 40-49

Chapter 2

Literature Review and Methodology

2.1 Literature Review

The purpose of the literature review was to find out about:

(a) any previously published work on design optimisation of printed circuit board motors;

(b) previously suggested techniques for low speed sensorless commutation control of brushless motors that could be useful with axial field printed circuit BLDC motors;

(c) computational electromagnetic methods that could help with prediction of performance of axial field printed circuit motors and

(d) computational electromagnetic methods that could help with the prediction of self and mutual inductances of axial field printed circuit motors.

2.1.1 Printed Circuit Motors

To date publications on printed circuit motors, such as references [6] to [10] have been limited to:

(a) motors, with output torque of the order of a few milli-newtonmetres or less than 1 watt per krpm, meant for applications such as computer drives and handheld video cameras;
(b) prediction of torque or back EMF for motors of predetermined coil configuration and dimensions such as magnet thickness, rotor back-iron thickness and rotor-to-stator axial length ratio.

In contrast, motors with power ratings up to tens of watts per krpm are being considered in this thesis project. It seems that the requirement to keep axial thickness to a minimum has led designers of axial field printed circuit to share printed circuit layers among all three phases. As part of this thesis project, investigations will be carried out to find out whether this approach is detrimental to electromagnetic torque production. There has been no rigorous analysis performed to support the idea that rhomboidal coils represent the optimum coil configuration for axial flux printed circuit motors. Systematic printed circuit board design algorithms will be developed as part of this thesis project. These will allow the best coil configuration to be chosen for given dimensional specifications of the motor space envelope.

Jang and Chang [6] use finite element analysis (FEA) to determine the axial force and torque for a printed coil BLDC motor of given dimensions. They state that coils shaped as a wave winding (figure 1.5) are not suited for stators with relatively small radii. They appear to use coils of

concentric shape with radial or near radial active sections and with circumferential end sections. No reasons are given for their choice of coil shape or their number of turns.

Tsai and Hsu [7] propose an analytical technique for prediction of air-gap flux density which is verified by experiment and by using FEA. Their analytical method does not take into consideration rotor back iron saturation and they do not specify if their three-dimensional FEA does. They point out the better suitability of the rhomboidal printed coil for stators of low radii. They also claim that the rhomboidal shape results in lower I^2R loss. However, no quantitative analysis is presented to support that claim. In particular there is no mention of whether the benefit of lower I^2R loss is gained at the expense of lower output torque capability.

Jang and Chang [8] present a relatively simple permeance model to predict the average airgap flux density in axial field printed motors. The model is based on three permeance branches, one for the axial path along the mechanical air-gap and printed coil, one for the axial path through the magnet and one representing leakage paths. The calculated average air-gap flux density is used to predict values for output torque for given coil currents. These compare well with measured values. Details of any methodology used for designing the stator are not mentioned.

Low, Jabbar and Tan [9] describe a radial field printed circuit motor. Their focus is on the elimination of cogging torque. They use a flexible PCB with concentric coils. The flexible PCB is wrapped around a slotless laminated magnetic core to form an inner stator. Permanent magnets are mounted on the inner surface of the outer hub. The reported electromagnetic design procedure is essentially a one-dimensional representation which is based on assumed average

values of flux density in the mechanical air-gap, printed circuit layers and iron cores. The one-dimensional model is used to determine the required magnet thickness. There is no mention of a systematic procedure aiming at design optimisation.

To the author's knowledge there are no publications on a design procedure for axial flux printed circuit motors where the electromagnetic design of the stator and that of the rotor are simultaneously and systematically considered. In a typical application the space envelope for the motor is usually specified in terms of a maximum radius and a maximum axial length. The challenge for the designer is to produce a design that would meet torque output requirements and that would fit in the specified envelope. The given axial length has to be shared between the motor housing, the clearance between the motor housing and the rotor back-iron, the rotor back-iron axial thickness ($2t_i$), the permanent magnet axial thickness ($2t_m$), the mechanical air-gap axial length ($2t_{ag}$) and the stator axial thickness (t_s). All the listed axial lengths may be considered fixed except t_i, t_m, and t_s. Since the total axial length is usually specified, the sum of t_i, t_m, and t_s would have to be equal to or smaller than a given value. This means that they cannot be independently chosen. Takano, Ito, Mori, Sakuta and Hirasa [10] arrive at an optimum value of 2 for t_m/ t_s for wire-wound machines. The existence of an optimum ratio is easily explained. Torque is proportional to the product of the air-gap flux density set up by the permanent magnets and the stator current. A relatively large value of t_m would also require a relatively large value of t_i to avoid rotor back iron saturation. The choice of an excessively large value of t_m leaves very little room for a stator with reasonable current capacity and this leads to low torque rating. On the other hand choosing an excessively large value of t_s to boost current capacity leaves very little room for the permanent magnets and the rotor back-iron. This leads to a weak air-gap flux

density and low torque rating. There is clearly an optimal value of t_m/t_s . That optimum ratio may be a function of other motor parameters. As part of this thesis project, generalised algorithms will be developed to identify optimum t_m/t_s ratios for printed circuit axial field motors.

For a given voltage rating, as the power rating of printed circuit stators increase, their printed tracks would tend to be wider. For a fixed conductor thickness a wider track would not necessarily mean a proportionately higher current carrying capacity since the track would also suffer from increased circulating or eddy currents. The problem of eddy currents within stator conductors of wire-wound machines has been previously analysed [11, 12]. However, to the author's knowledge, there is no publication on eddy currents induced in the conducting tracks of a printed circuit stator.

Walker and Pullen [11] use a semi-empirical formula to determine eddy-current losses in a flat-wire stator winding. Their method allows quick first estimation of eddy-current losses, but the authors do not report experimental results nor do they comment on accuracy. Wang and Kamper [12] use a combined numerical and analytical technique to solve a similar problem. The method being proposed here is entirely numerical and avoids many of the simplifying assumptions made in references [11] and [12]. For example no a priori assumptions are made about eddy current paths and the entire winding is modelled, unlike reference [12] which does not consider the end-winding.

2.1.2 Sensorless Operation

It is advantageous to design printed circuit brushless motors so that they can be operated as sensorless brushless DC motors. Sensorless position detection methods that have been proposed to date for BLDC motors fall into two categories. There are those based on the use of back EMF signals and those based on exploitation of inductive saliency. Back EMF based methods are only applicable if speed is high enough. Nevertheless, there are many applications, for example drives for fans or pumps, that do not require position control or closed-loop operation at low speeds. For these, a back EMF based method is quite appropriate. Widely used, is the so called back EMF "zero crossing" method, where the zero crossing instants of the un-energised phase are used to estimate position [13]. It is important to mention that there is a 30° (electrical) offset between the back EMF zero-crossing and the required commutation instant, which must be compensated for to ensure correct operation of the motor [2,3].

BLDC motors which rely solely on back EMF signals for commutation suffer from relatively poor starting performance characterised by initial back rotation of up to one hundred and eighty electrical degrees and large fluctuations in electromagnetic torque resulting from non-ideal commutation instants. This may not be acceptable for certain applications and there have been attempts to develop sensorless techniques that give good performance right down to zero speed. Most of those attempts, while being saliency based, have been aimed at the brushless synchronous motor rather than the BLDC motor [14-20]. Saliency based sensorless techniques for brushless synchronous motors are relatively complex because all the three phases are excited one hundred percent of the time. They rely on measurement of current and voltage responses to specially injected signals and require significant real time data processing. Ueki [21] and Weis

[22] propose position detection techniques, based on saliency, specifically for BLDC motors and they reduce complexity by exploiting the availability of an unexcited phase. But they also rely on imposition of special signals onto the stator windings. Imposition of special signals requires additional electronics, can cause additional heating and deterioration of torque quality.

In this thesis project a sensorless method of detection of commutation instants is proposed which relies on inductive saliency. Unlike other proposed methods, no special signal injection is needed. The computational burden to deduce commutation instants is negligible. The technique is based on the detection of rotor positions where the two energised phases experience equal inductances. It has therefore been termed the *equal inductance method* [2]. Gambetta [3] required a neutral connection for practical implementation of the original version of the equal inductance method. An objective of this thesis project is to modify the equal inductance method so as to make the connection to the stator neutral unnecessary. The proposed refinement of the original equal inductance method also incorporates initial position detection and start-up algorithms. It is also envisaged that further adaptation of the equal inductance method will be necessary. The originally proposed technique [2, 3] relies on the assumption that the BLDC motor is symmetrical and that its phase winding electrical time constant, that is phase inductance to phase resistance ratio, is relatively long compared the inverter pulse width modulation (PWM) frequency. Both those assumptions are questionable in the case of axial field printed circuit motors of the type shown in figure 1.9. The three phase windings of a symmetrical motor are designed to have inductances that are equal except for a positional phase shift of 120 electrical degrees. In the case of the printed circuit motor being considered the phase in the middle of the

stator stack does not have the same inductance as the other two phases. Also the phase winding time constant is relatively low because the stator is iron-less.

2.1.3 Measurement of Inductances and Inductive Saliency

When the equal inductance method is used, commutation positions are determined with a resolution that is directly proportional the magnitude of the saliency ratio [2, 3]. Those planning to use the method on existing machines can obtain the saliency ratio by measurement. In addition to the saliency ratio, there may be a need for measurement of phase inductance to ensure that the winding time constant is long enough compared to the inverter PWM period. There exist numerous publications on measurement of saliency ratios and the inductances of electrical machines [23-29]. However most of those relate to steady state performance of synchronous or reluctance machines connected to the AC network. In those cases saliency ratios or inductances are sought typically to allow determination of steady state performance under AC conditions. The classical technique of measuring the saliency ratio of synchronous or reluctance machines is the so-called slip test whereas the 'synchronous' inductance of synchronous machines is measured by the short circuit test. All those previously published methods of saliency measurement or synchronous inductance measurement are not applicable because the inductances that are relevant to the equal inductance method are not "steady-state" inductances. They are "transient" inductances in the same sense as the "transient reactance" used in synchronous machine theory. Transient reactance (or inductance) is typically smaller than synchronous reactance because it represents flux linkage for a phase winding which is mutually coupled with other nearby shorted circuits. In the case of standard synchronous machines or

reluctance machines, the windings to which the stator phase winding would be magnetically linked are the field winding, damper windings and even eddy current loops within the solid steel of the rotor. Ideally at steady state during balanced operation this coupling has no effect on phase reactance because phase currents cause no induced currents in rotor circuits. This is the case since under conditions of balanced stator currents and steady-state operation the rotating magnetic field set up by the stator currents travel at the same speed as the rotor circuits. There are no induced rotor currents to produce flux opposing the stator flux. Thus stator flux linkage per ampere of stator current is highest. On the other hand rotor circuits play a role that could be significant if the speed of magnetic fields set up by stator current is not equal to the rotor speed. Such differences in speeds would occur as a result of unbalanced stator currents, harmonic components in the stator current and stator current transients. In those cases flux linkage (and therefore effective inductance) of a stator winding per ampere of stator current is reduced because of the counter flux produced by induced currents in rotor circuit. The equal inductance method involves sensing of voltage a relatively short time after switching events within the inverter. Those switching events are occurring at the inverter PWM frequency. The reactance experienced by stator currents resulting from those switching events would be influenced by eddy currents induced within the body of magnets and within the solid rotor. Therefore the relevant inductances are “transient” inductances. But the term “transient inductance” is a rather loose term. In reality the value of such an inductance will be a minimum immediately after a sudden change of stator voltage, when rotor opposing currents in rotor circuits are most effective, to a maximum value after all currents in the rotor circuits have decayed to zero. Reference [25] provides a clue to the question of which inductance value to use. It states that for accurate results inductances must be measured under conditions approximating as closely as

possible to those of normal operation. Based on this, it was assumed that inductances measured with the rotor stationary and using sinusoidal currents at the inverter PWM frequency will be those that are relevant to the equal inductance method. As part of this thesis project, laboratory tests have been carried out to confirm the validity of this assumption. These tests consisted of a comparison between absolute position determined by the equal inductance method which is itself based on inductance values and those that are measured by a position sensor.

2.1.4 Prediction of Inductances and Inductive Saliency

Section 2.1.3 has focussed on measurement of saliency ratio or inductances that are applicable to the equal inductance method. A related question is the prediction of those inductances at the design stage of a brushless DC motor. Such information would be useful to those who intend to use the equal inductance method but do not have access to the motor because it is yet to be constructed.

As pointed out before the relevant transient inductances seem to be inductances experienced by the stator sinusoidal phase current at relatively high frequency, typically a few tens of kilohertz. A brute force approach to prediction of those inductances would be to use 3-D quasi-static finite element analysis. However the computing and other resources to do this are not always available. Long computation time could also be a problem, especially when multiple runs are necessary to arrive at an optimal design. The difficulties in performing non-static three-dimensional FEA on electrical machines are well documented [30-38].

A computational electromagnetic method which is not as popular as FEA is the coupled network method [39-51]. In its standard form, the method consists of a set of magnetic nodes and a set of electric nodes. The nodes are located in 3-D space forming a regular pattern and are joined by branches. The electric and magnetic nodes do not normally coincide. The magnetic branches are reluctive and the electric branches are resistive. Loops formed by the magnetic branches link loops formed by electric branches and vice-versa. Note that currents flowing in the electric network may be induced or imposed. The branch reluctances and the branch resistances are assumed to be known. The two networks are simultaneously analysed by a sets of node and/or loop equations which are based on Maxwell's Laws. An advantage of the coupled network method is that it is amenable to physical interpretation [47, 48, 52]. Unfortunately, the coupled network method, with no assumptions made about flux and current paths, is more restrictive than the finite element method (FEM). The number of nodes required is generally more than the number needed with FEM. It is a method that can be applied to simple geometries only.

Another version of the coupled network method is one based on assumed flux and current paths. Again, in general two electromagnetically coupled networks are to be considered. But with this method nodes do not have to be associated with regular spaced positions. The number of nodes is normally greatly reduced compared to FEA or the coupled network method. The magnetostatic version of the method is sometimes referred to as the permeance analysis method or the magnetic flux tube method [36]. The main advantage of the assumed flux path method is computational efficiency. However, the accuracy of the solution depends on the degree of validity of the assumed flux and current paths.

The adopted computational technique for the determination of inductance will be based on a standard regular 2-D network of nodes and branches representing the magnetic field and a set of assumed 1-D current paths making up the electric network. The two-dimensional approximation of the magnetic field and the simplification of the current distribution to a set of one-dimensional paths greatly improve computing efficiency. The physical reasoning behind the approximation and simplification is presented. Tests have been carried out to validate the proposed technique of inductance evaluation.

2.2 Methodology

The choice of thesis project methodology was influenced by the requirement to design cost competitive BLDC motors with ratings in the range of tens of watts per krpm that:

(a) could be manufactured using standard modern printed circuit manufacturing processes;
(b) would fit in a space envelope defined by an axial length and a radius; and
(c) could be operated down to zero speed by means of a simple position sensorless commutation technique such as the equal inductance method.

2.2.1 Design options and procedure

A number of choices exist for substrate and conducting materials for printed circuit boards. Examples of substrate material are ceramic and FR4 (Flame Retardant 4). Examples of

conducting material for the conducting track are silver and copper. It was quickly ascertained during the early stages of the thesis project that FR4 substrates with copper tracks represented the most practical and most economic option. FR4 copper clad laminate are widely available commercially with a number of standard FR4 and copper thicknesses. Other relevant variables in the manufacture of printed circuit boards are the number of printed circuit layers per substrate, minimum track width, minimum clearance between tracks and track thickness. The cost of manufacture depends non-linearly on the number of circuit layers. The cost of multi-layer printed circuit boards escalates rapidly as the number of layers grows. It was found that beyond eight to twelve layers per substrate the manufacturing costs of circuit boards become too prohibitive for them to be used in motors. Consequently it was decided to keep the maximum number of printed layers per substrate to eight. It was also decided to use standard commercial track thicknesses to keep cost to a minimum. Minimum clearances used were those recommended by FR4 laminate manufacturers. Those minimum clearances are a function of copper track thickness. It should be noted that while decisions were made to use standard track thicknesses, the design algorithm that was developed will allow the option of exploring non-standard thicknesses.

Some investigations were carried out to help decide whether the printed coils on one layer should belong to a single phase or whether they should be shared equally among three phases. It was concluded that from the point of view of printed circuit board manufacturing it was much simpler and cheaper not to have coils on a printed layer shared between phases. Another advantage of having all coils of one layer belonging to just one phase is that, for a given total stator axial thickness, torque per ampere is higher. Phase inductance variation from its q-axis

value to its d-axis value is also closer to sinusoidal. Sinusoidal variation of inductance is an important requirement of the equal inductance method which is planned to be used.

It was also decided to have one substrate per phase, as shown in figure 1.9. This allowed designs with a larger number of layers per phase without exceeding the previously stated eight layers per substrate.

Table 2.1 shows a list of the main design variables that had to be considered. These variables have been divided into four groups. The first group, made up of the variables 1 to 5, are design specifications. The assumptions are that they are fixed and that the objective is to arrive at a design that achieves maximum output torque while respecting the constraints in Table 2.1.

The second set of variables, numbered 6 to 14, are essentially data that are associated with the materials that have been selected by or provided to the designer for the manufacture of the motor being designed. The design procedure is based on the assumption that those variables are fixed. However, the designer may wish to go through the design procedure a number of times, each time with one or more of those variables changed. For example, given the design specifications, the design procedure could be separately used to arrive at the best design with different FR-4 laminates. This would allow the FR-4 laminate that gives the best design to be selected.

The third set of variables, that is the number of poles and the coil shape, are considered to be outcomes of the design process. The planned design procedure will be such that, the number of poles P and the coil shape will actually be input data to the procedure. However, if the most suitable value of P was being sought, the procedure could be run a number of times to identify that value of P. A similar statement can be made about the coil shape.

The last group of variables, labelled 17 to 20 in Table 2.1, are outcomes of the planned design procedure. The procedure is illustrated in figure 2.1. There are several iterative loops. Two of those are shown explicitly. The determination of the minimum back iron thickness t_i is performed iteratively by changing t_i and conducting non-linear 3-D magnetostatic analysis for each value of t_i. The search is for the minimum value of t_i that results in the specified maximum allowable flux density in the rotor back-iron. Note that the term 'iteratively' is being used to also cover what is in essence a one-dimensional search for a value that satisfies a particular design specification. For example t_m is incremented from a minimum value and for each value the motor torque capability is calculated. In this case the one dimensional search is for the value of t_m that results in maximum motor torque capability.

Table 2.1 : Main Printed Circuit Motor Design Parameters

	Design Parameter	**Degree of Flexibility**
1	Outer Radius (R_o)	Fixed specified value, dependent on intended application and considered to be a design specification
2	Inner Radius (R_i)	Fixed specified value, dependent on intended application and considered to be a design specification
3	EMF (at 1000 rpm)	Fixed specified value together with tolerance, for example: 1V ± 10%. Considered to be a design specification that is dependent on the intended application
4	Total axial length (t_a)	Fixed specified value, dependent on intended application and considered to be a design specification
5	Stator/Magnet Clearance(t_c)	Fixed specified value, typically 0.3 mm
6	FR4 insulation layer thickness	Fixed specified value obtained from data sheet of chosen FR4 / Cu laminate
7	Track thickness	Fixed specified value obtained from data sheet of chosen FR4 / Cu laminate
8	Clearance between tracks	Fixed specified value obtained from data sheet of chosen FR4 / Cu laminate
9	Minimum track width	Fixed specified value obtained from data sheet of chosen FR4 / Cu laminate

10	Max allowable stator power loss (P_l)	Fixed specified value dependent on stator material thermal properties, stator dimensions and maximum allowable temperature rise. This value is obtained from the one-dimensional thermal model.
11	Minimum Magnet thickness	Fixed specified value from supplier, typically 1 mm
12	Incremental change between consecutive standard magnet thicknesses	Fixed specified value obtained from magnet supplier, typically 0.25 mm
13	Remanence (B_r)	Fixed specified value from data sheet of chosen magnet, typically about 1.2 T
14	Rotor peak flux density (B_s)	Fixed value dependent on chosen rotor steel. Typical value is around 1.4 T. Value obtained from steel supplier or by test on a sample.
15	Number of rotor poles (P)	To be an output of the design procedure. Expected to be between 4 and 12. Developed algorithm should be able to quickly assess the suitability of any value of P. Choice of P may be influenced by mechanical requirement, inverter switching frequency and how low t_a is.

16	Coil shape	To be an output of the design procedure. For dimensions of Ro and R_i normally under consideration, the best coil shape will most likely have parallel active sections or mixed parallel and radial sections.
17	Rotor Iron thickness (t_i)	To be an output of the design procedure, but should be greater than 1 mm to ensure adequate mechanical strength.
18	Magnet thickness (t_m)	To be an output of the design procedure. However only discrete values above a minimum is allowed. The discrete values and the minimum value depend on the chosen supplier.
19	Number of turns per coil (N)	To be an output of the design procedure
20	Number of printed circuit layers per phase (L)	To be an output of the design procedure

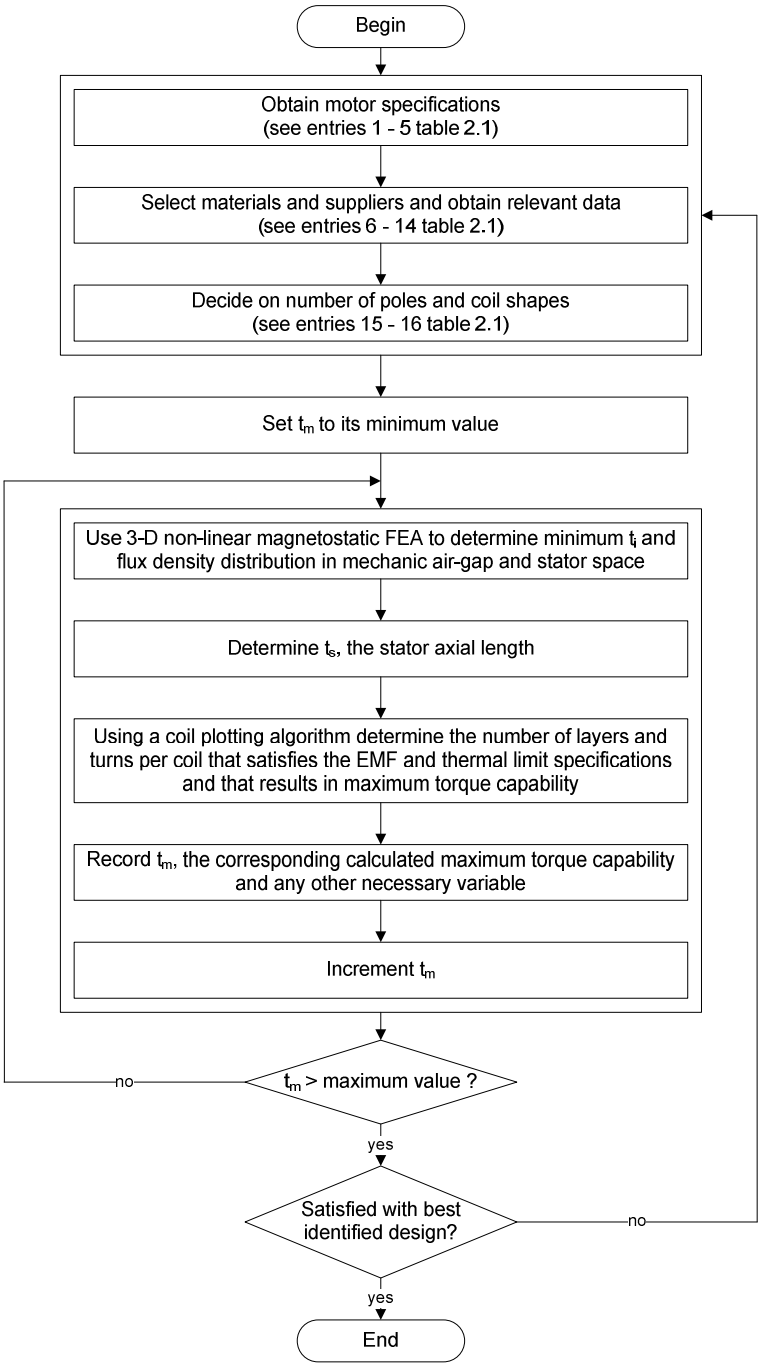

Figure 2.1 : Generalised Printed Circuit Motor Design Optimisation Flow-chart

Inspection of table 2.1 and figure 2.1 reveals that a number of tools are to be developed to implement the design optimisation procedure. These are:

(a) A 1-D thermal model to calculate, using material data, the maximum allowable stator power loss;
(b) A technique for the measurement of the magnetising curve of samples of the steel that is used for the rotor;
(c) Computer algorithms to automatically plot coil tracks;
(d) Computer algorithms to automatically determine phase EMF waveforms;
(e) A mathematical model to predict eddy current loss in stator copper tracks. There is a need to ensure that stator tracks are below the width that would cause excessive eddy currents.

Prototypes will be specially designed to validate theoretical predictions made in (d) and (e) above.

2.2.2 Modification and adaptation of the equal inductance method

Theoretical results and encouraging practical performance data reported in reference [2] were behind the decision to focus on the equal inductance method as the sensorless technique for the printed circuit motors being developed as part of this thesis project. As stated before the originally reported equal inductance method needed a connection to the neutral point of the star-connected stator. Also there were no reported starting performance data and the method had not

been tried with motors with low phase inductance. The plan was to further develop the equal inductance method so that it does not need a neutral connection and to adapt it so that it is compatible with the ironless printed circuit axial field machines. Since the equal inductance method cannot work successfully without a minimum level of saliency there is a need for a mathematical procedure to predict inductance and saliency at the design stage.

Considering the points presented in the preceding paragraph the following were planned:

(a) Theoretical analysis to confirm that the equal inductance method, if suitably modified, will work without a neutral connection;

(b) Confirmation, by laboratory tests performed on standard radial field wire-wound motors, that the modified equal inductance method performs well both at steady state and during starting;

(c) Measurement of the inductance and mutual inductance characteristics of printed circuit machines such as the one illustrated in figure 1.9 to ascertain the nature of further modifications that would be necessary to adapt the equal inductance method to suit those motors;

(d) Development of the necessary further modification of the equal inductance method to make it suitable to printed circuit motors. This would be based on theoretical analysis.

(e) Assessment of performance of the adapted equal inductance method by carrying out laboratory tests on printed circuit motors. The assessment is to cover both steady-state commutation performance and start-up performance.

(f) Development of an efficient computational method to determine d-axis and q-axis self and mutual inductance of the phase windings of printed circuit motors such as the one illustrated in figure 1.9. Analysis will be based on a coupled network made up of a 2-D permeance network coupled with assumed current paths in the form of discrete loops.

Chapter 3

Printed Circuit Stators for Brushless Permanent Magnet Motors

3.1 Introduction

While the first printed circuit armatures used brushes and mechanical commutation, developments in power electronic devices and control systems have led to printed circuit motors that are brushless. Modern cost effective neodymium magnets have allowed compact motor designs. Multi-layer circuit board production techniques have made the production of printed circuit coils cheaper and easier. However, in spite of the growing importance of printed circuit brushless motors, there is a lack of analytical tools to assist with their design. This chapter uses geometrical analysis to arrive at general mathematical expressions which allow the plotting of

printed circuit tracks to be carried out more systematically. Track plotting procedures have been developed for four different coil shapes.

These are spirals with purely radial active sections, spirals with active sections running parallel with each other, spirals with each active section having a radial part and a parallel part and rhomboidal shaped spirals. For each spiral shape, equations are derived for the maximum number of turns (N). The maximum number of turns is generally a function of the substrate inner radius (R_i), the substrate outer radius (R_o), the track minimum width (w) and the minimum clearance between tracks (c). To produce the printed stators, the tracks are plotted with the help of algorithms that maximizes the effectiveness of the coil. Appropriate measures of coil effectiveness are the EMF constant or the torque constant of the coil and the total resistance of the coil. Theoretical predictions of EMF constants and EMF waveforms are presented in section 3.3. The predictions are based on realistic flux distributions obtained from finite element analysis. Extensive tests on six prototype motors were carried out to validate the theory on which the proposed design techniques are based. A comparison between theoretical predictions and test results are presented in section 3.4. A general design algorithm based on the track plotting procedure and the EMF prediction technique is presented in section 3.5.

3.2 Analysis of Coil Geometries

Consider a section of the substrate as shown in figure 3.1. The simplest coil is made up of a spiral pair. The two spirals making up a pair are located on adjacent layers of the PCB or on opposite side of the substrate if there are only two layers. The spirals are joined by a via located at their common centre. In figure 3.1, the two spirals making up a pair are the “top layer spiral” and the “bottom layer spiral”. Current enters the coil from a terminal on the outer radius side of the substrate. It flows inwards, towards the coil center, through the tracks of one of the spirals, continues through the via at the centre of the spiral and then flows outwards, away from the coil center, through the tracks of the second spiral. The directions of current in the two spirals are such that the torque produced by one spiral is equal and adds to the torque produced by the second spiral. Similarly, the rotational EMF generated in one spiral is equal and adds to the EMF generated in the other spiral.

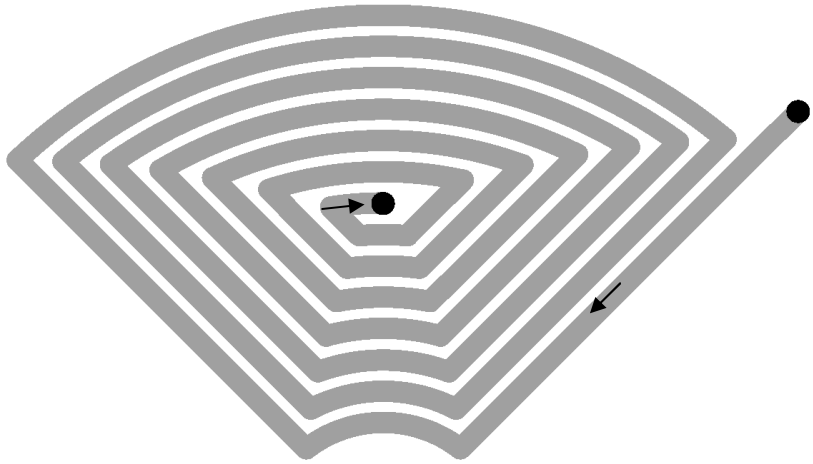

a)

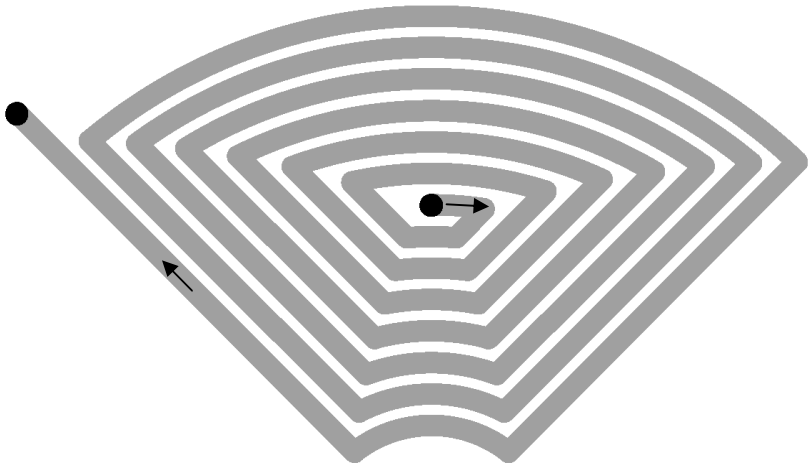

b)

Figure 3.1 : (a) Top Layer Spiral (b) Bottom Layer Spiral

In general each turn of a coil may be considered to be made up of four sections. Two of those are non-active arc-shaped end-sections, one on the outer radius side and one on the inner radius side. The other two sections are active. The length of some of the arc-shaped inner end-sections may degenerate to zero for low values of Ri/Ro. To maximize the effectiveness of a coil its number of turns, average active length per turn and overall pitch factor must be maximized. Assuming the air-gap flux is purely axial, the maximum EMF per unit length is obtained if the active conductor runs along a radial line. However, the number of turns can be adversely affected if R_i/R_o is small and the active sections are constrained to be radial. Parallel active sections are preferable although this leads to longer inactive sections. Coils with active sections which are partly parallel and partly radial are investigated because they offer the possibility of reduced total conductor length while maintaining performance in terms of EMF per unit speed or torque per unit current. Expressions are now derived for the maximum number of turns.

3.2.1 Purely Parallel Coils

In figure 3.2 (a) point X is at the centre of the coil and lies somewhere along the radial line which is the axis of symmetry of the coil. Proper placement of point X is required if a coil with maximum number of turns (N) is to be achieved. In general for given values of minimum track width (w) and minimum inter-track clearance (c), the number of turns is limited by (R_o-R_x) or XP or (R_x-R_i). If X is placed too far towards the outer edge of the substrate, N is reduced because it becomes restricted by the smaller value of (R_o-R_x). Similarly, if X is placed too far towards the inner edge of the substrate, N is again reduced because it becomes restricted either by the smaller value of XP or by the smaller value of (R_x-R_i).

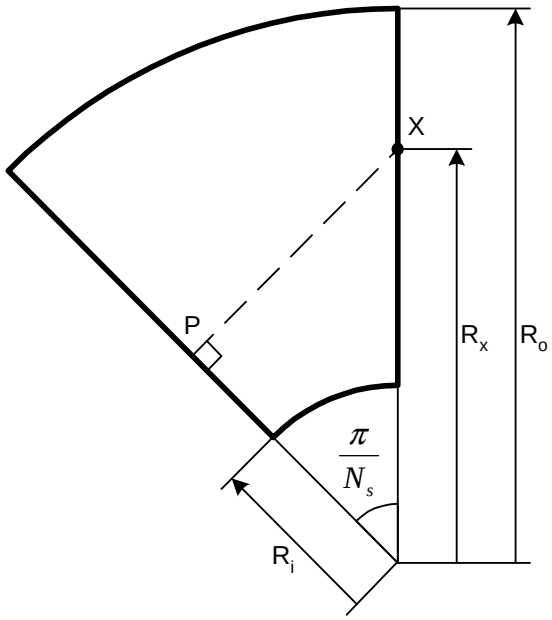

Figure 3.2(a) : Half Spiral Section of Substrate

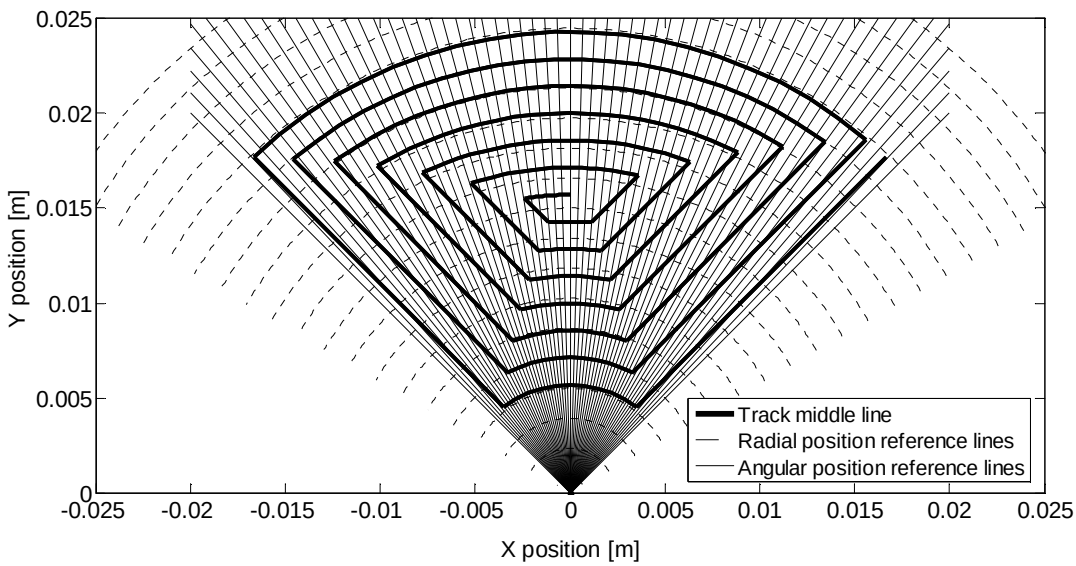

Figure 3.2(b) : Example of Printed Coil with Parallel Tracks

Based on the preceding arguments, it can be concluded that there is a position for X that results in the maximum number of turns. For small values of R_i/R_o, the number of turns is maximized if:

$$(R_o - R_x) = R_x \sin\left(\frac{\pi}{N_s}\right) \tag{3.1}$$

where N_s= number of spirals per layer

For larger values of R_i/R_o, the number of turns is maximized if:

$$(R_o - R_x) = (R_x - R_i) \tag{3.2}$$

That is the optimum value of R_x is $\frac{(R_o + R_i)}{2}$

From equation (3.1) it can be deduced that:

$$N = \frac{R_o \sin\left(\frac{\pi}{N_s}\right)}{(w+c)\left(1+\sin\left(\frac{\pi}{N_s}\right)\right)} \tag{3.3}$$

Equation (3.3) is applicable if:

$$\left(\frac{R_i}{R_o}\right) \leq \frac{\left(1-\sin\left(\frac{\pi}{N_s}\right)\right)}{\left(1+\sin\left(\frac{\pi}{N_s}\right)\right)} \tag{3.4}$$

From equation (3.2) it can be deduced that:

$$N = \frac{(R_o - R_i)}{2(w+c)} \tag{3.5}$$

Equation (3.5) if valid if:

$$\left(\frac{R_i}{R_o}\right) \geq \frac{\left(1-\sin\left(\frac{\pi}{N_s}\right)\right)}{\left(1+\sin\left(\frac{\pi}{N_s}\right)\right)} \tag{3.6}$$

Equation (3.3) and inequality (3.4) represent a circumferentially restricted coil whereas equation (3.5) and inequality (3.6) represent a radially restricted coil.

For a prescribed track width, equation (3.3) or (3.5) is to be used to determine N which has to be an integer. The equation can then be used again, with N fixed at its integer value, to readjust the track width to a higher value.

An example of a printed coil with parallel tracks is shown in figure 3.2(b).

3.2.2 Purely Radial Coils

Purely radial spirally wound coils are unlikely to be adopted by designers except possibly for cases where both R_i/R_o and N_s are high. Based upon arguments similar to those presented in section 3.2.1, it can be deduced that for large enough values of R_i/R_o:

$$N = \frac{(R_o - R_i)}{2(w+c)} \tag{3.7}$$

With the help of figure 3.3 (a), an expression can be derived for cases where values of R_i/R_o are low. In order for N to be a maximum equation (3.8) must be satisfied.

$$dn = \frac{rd\theta}{(w+c)}, \text{ for } 0 \leq \theta \leq \frac{\pi}{N_s} \tag{3.8}$$

where n= number of turns counting from the inter-coil boundary line

and $r = R_i + n(w+c)$

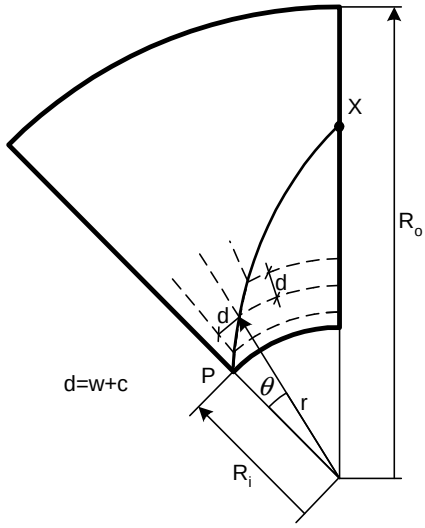

Figure 3.3(a) : Radial Tracks (d exaggerated for clarity)

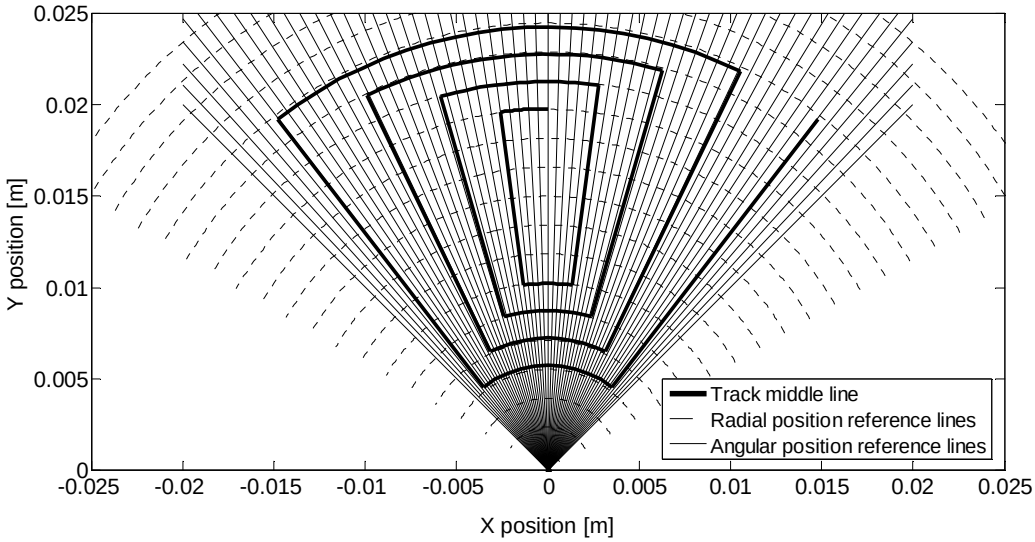

Figure 3.3(b) : Example of Printed Coil with Radial Tracks

Integration of both sides of equation (3.8) from $\theta = 0$ to $\theta = \frac{\pi}{N_s}$ leads to:

$$N = \frac{R_i\left(e^{\frac{\pi}{N_s}} - 1\right)}{(w+c)} \tag{3.9}$$

Equation (3.7) is applicable if:

$$\frac{R_i}{R_o} \geq \frac{1}{\left(2e^{\frac{\pi}{N_s}} - 1\right)} \tag{3.10}$$

Equation (3.9) is applicable for smaller values of R_i/R_o. Inequality (3.10) is arrived at by equating the right hand side of equations (3.9) and (3.7).

An example of a printed coil with purely radial tracks is shown in figure 3.3(b). The above equations were used to confirm that, with R_i/R_o ratios considered in this thesis project, purely radial coils represent significantly inferior designs compared with coils with parallel or mixed parallel and radial sections. Therefore purely radial coils are not given further consideration.

3.2.3 Mixed Parallel and Radial Track Sections

An example of a spiral coil with mixed track sections is shown in figure 3.4. Only the mid-track line is shown.

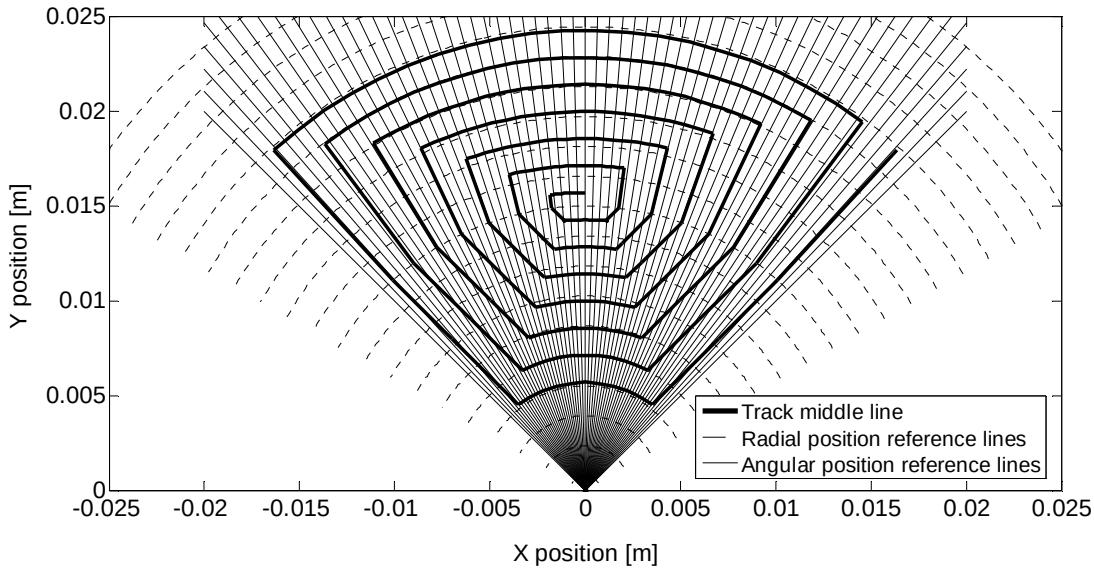

Figure 3.4 : Mixed Track (showing reference lines used for EMF evaluation)

A strategy has been adopted that maximizes the lengths of radial sections of the track subject to meeting minimum clearance requirements between tracks. This is achieved by keeping the track sections parallel on the inner radius side of arc XQ whose radius is defined by equations (3.1) or (3.2). Radius R_x is defined in exactly the same way as in section 3.2.1. Arc XQ is shown in figure 3.5. On the outer side of arc XQ, track sections are radial. The positions of all track sections are fully defined if R_i, R_o, w and c are known. The adopted algorithm to produce the tracks starts with the positioning of the inner arc sections and the parallel sections. The inner end-points of the radial sections are then known since they are where the parallel sections meet arc XQ. The radial sections can then be positioned since they lie on straight lines defined by the centre of the circle and the points where the parallel sections meet arc XQ.

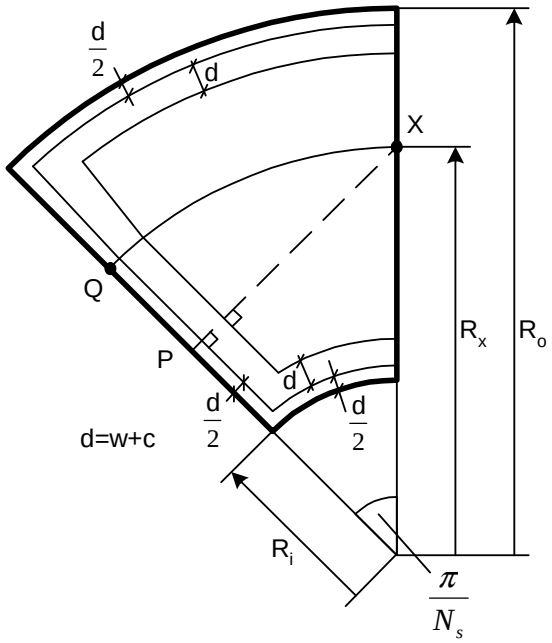

Figure 3.5 : Section of Substrate (Mixed Track Sections)

3.3 **Predicting Coil EMF's**

Back EMF per phase is an important measure of performance for a motor. The back EMF waveform allows deduction of the motor's torque capability and its torque quality. Prediction of back EMF waveforms requires knowledge of the flux density distribution. Depending on the level of accuracy required, this can be determined analytically or numerically. The machines being considered in this thesis project have relatively complex coil and magnetic circuit geometries and parts of the rotor iron may saturate magnetically. Consequently it is not possible to arrive at analytical expressions that will allow prediction of rotational EMF with better than

ten per-cent accuracy. Therefore there is a need to rely on numerical methods. The adopted numerical techniques are presented in section 3.3.2.

In spite of its limited accuracy, an analytical technique can be valuable to those who have to shortlist design configurations that deserve detailed analysis. An equation is suggested in section 3.3.1 that can be used to evaluate the rotational EMF to a first approximation. In both sections 3.3.1 and 3.3.2 it has been assumed that the number of rotor poles (P) is equal to the number of spirals (N_s) per printed circuit layer. It is possible to construct three phase motors with N_s not equal to P, but such motors are not considered in this work. Every stator under consideration was made up of three sets of printed layers circumferentially displaced from each other by 120 electrical degrees. This results in a small degree of asymmetry since the phase that is sandwiched between the other two has a slightly lower EMF. Theoretical and experimental results that are to be presented have allowed the practical significance of this asymmetry to be assessed.

An exploded view of one of the prototype motors is given in figure 3.6. All motors that were constructed are of the central stator dual rotor type. The single rotor option was not chosen because:

(a) A laminated back iron disk will be needed on which to mount the printed circuit boards.

(b) There would be increased asymmetry.

(c) Without the magnet, the relative amount of leakage flux will increase.

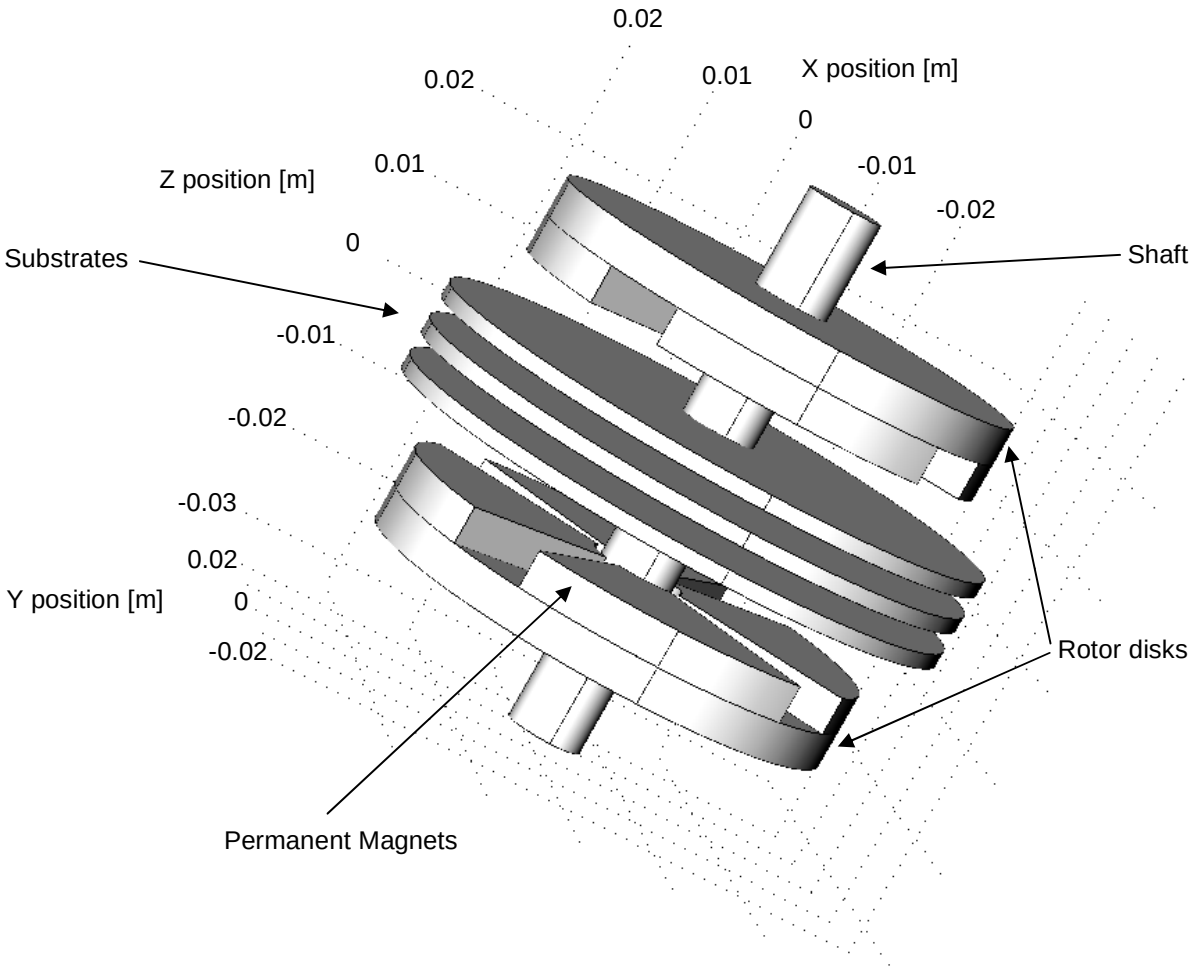

Figure 3.6 : Exploded View of one of six Test Motors

3.3.1 Approximate Analytical Modelling

The major simplifying assumptions that had to be made to arrive at an analytical expression for rotational EMF are:

(a) active track sections are in the radial directions and their lengths change linearly with angular position from (R_o-R_i) at the coil's edge to zero at its centre;

(b) the rotor iron has infinite permeability;

(c) flux outside the rotor iron flows in the axial direction only;

(d) flux density in the airgap is independent of radial and axial positions;

Equation (11) is based on the above assumptions.

$$E = \frac{\sqrt{2}NP(R_o + R_i)(R_o - R_i)B_{pk}\omega_m S_c}{2} \tag{3.11}$$

where:

E = EMF per spiral

ω_m = rotational speed

N = number of turns per spiral.

P = number of poles.

B_{pk} = airgap peak flux density = $\dfrac{B_r t_m}{\left(t_m + \frac{g}{2}\right)}$ (3.12)

B_r = remanence of permanent magnet.

t_m = magnet thickness

g = airgap length measured axially between opposite magnet surfaces

S_c = combined length, spread and pitch factors of coil

$$= \frac{2}{\pi}\int_0^{\frac{\pi}{2}}\left(1 - \frac{2\theta}{\pi}\right)\cos\theta d\theta = \frac{4}{\pi^2}$$

θ = electrical angle

Equation (3.12) has been derived using a 1-D magnetic model. Details on that model can be found in Appendix A. The 1-D model is based on the assumptions that:

a) Iron Permeability = infinity

b) Permanent Magnet Permeability = $\mu_0 = 1$

It has been assumed that the airgap flux density varies sinusoidally in the angular direction. This is a reasonable assumption because the effect of higher harmonics is significantly reduced as a result of the coils being distributed and short-pitched.

An approximate technique for determination of axial dimensions can be based on equations (3.13) and (3.14).

t_i = axial thickness of rotor = $\dfrac{\pi B_{pk} S_m (R_o + R_i)}{2PB_s}$ (3.13)

where:

B_s = maximum allowable flux density in the rotor iron

S_m = pitch factor magnet

t_a = total axial length = $2\left(t_i + t_{ag} + t_m\right) + 3t_s$ (3.14)

where:

t_s = stator thickness per phase.

t_{ag} = clearance between magnet surface and stator surface

3.3.2 Predicting Coil EMFs Numerically

This section provides details of a numerical solution to the problem of predicting the phase EMF waveforms. For the purpose of determining motional induced EMF, the plane of the substrate is divided into cells as shown in figure 3.4. Each cell is bounded by a pair of radial reference lines and a pair of angular reference lines. The total EMF corresponding to a given rotor position is generally made up of contributions coming from each cell. The number of active track segments within a cell may be zero, one or two. Contributions to the total EMF are separately calculated for each segment by using equation (3.15).

$$dE = B^* \omega_m r dr \tag{3.15}$$

where:

dE = contribution to total EMF from each track segment

B* = estimated flux density at point C in figure 3.7

r = radial distance as shown in figure 3.7

dr = $(r_o - r_i)$ as shown in figure 3.7

ω_m = rotational speed

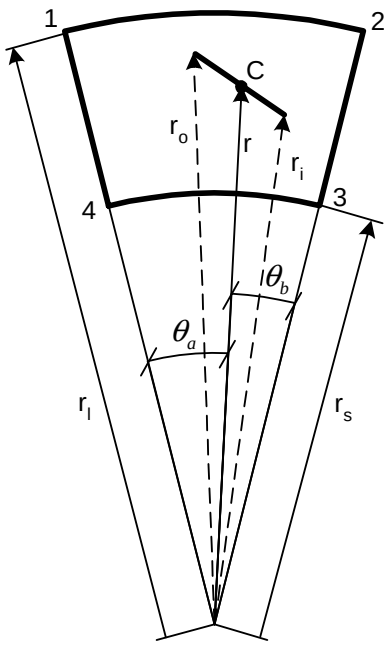

Figure 3.7 : Track Segment in a Cell (segment centred at point C)

The estimated value (B*) of flux density is obtained by using:

$$B^* = B_1 w_o w_l + B_2 w_o w_r + B_3 w_i w_r + B_4 w_i w_l \tag{3.16}$$

where:

$$w_o = \frac{(r - r_s)}{(r_l - r_s)}$$

$$w_i = \frac{(r_l - r)}{(r_l - r_s)}$$

$$w_l = \frac{\theta_b}{(\theta_a + \theta_b)}$$

$$w_r = \frac{\theta_a}{(\theta_a + \theta_b)}$$

It is assumed that the flux density at the four corners of every cell (B1-B4 in figure 3.7) is known. In general flux density (B) is a function of all spatial coordinates. Variation in the axial direction does not have to be considered since, for the purpose of coil EMF evaluation, it is reasonable to assume that all track segments making up a coil are at the same axial position. Flux distributions were obtained from finite element analysis. This has been done for a number of configurations with different values of P, R_o and R_i.

As shown in figure 3.8, finite element modeling was carried out using FEMLAB®.

Motors from 4 to 12 poles with dual rotor and central stator construction were considered. Existence of axial and circumferential symmetry meant that only half a pole pitch of one rotor had to be modeled. Figure 3.8 shows the model for a four pole motor.

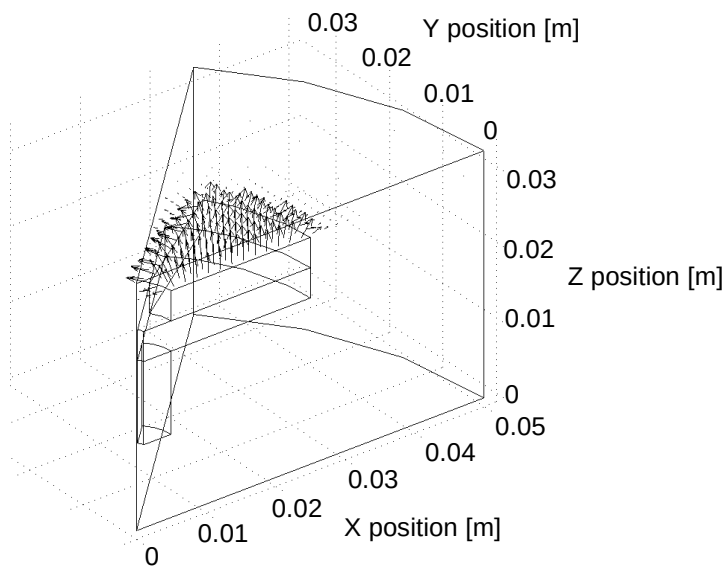

Figure 3.8 : FEMLAB® Model of the Rotor (Half Pole Pitch)

A plane of symmetry exists at z = 32.7 mm. The axial flux density distribution on that plane is used to evaluate the EMF of the middle phase. There is no need for explicit modeling of the stator since all the materials making up the stator are assumed to have relative permeability equal to one and no stator current flows. In addition to the air subdomain whose relative permeability is taken to be one, there are three other subdomains that have been considered. These are the permanent magnet subdomain which in figure 7 is between z = 26 mm and z = 30 mm, the rotor back-iron subdomain which is between z = 22 mm and z = 26 mm and the sub-domain representing the non-magnetic shaft. Based on the manufacturer's data, a value of 1.01e6 H/m was used for the magnetization of the NdFeB permanent magnet.

The rotor back-iron has been characterized by its magnetization curve which was determined experimentally since no reliable data were available. Measurement has been carried out on ring core shaped samples. A 50 Hz sinusoidal current (increased stepwise) was injected in the 'primary' winding. This current is directly proportional to magnetic strength H. Due to the imposed current a voltage v(t) is induced. Since:

$$v(t) = -\frac{d\psi_m}{dt} \tag{3.17}$$

with ψ_m = flux through the core cross-sectional area, the flux density B is:

$$B = \frac{\int v(t)dt}{A_{core}} \tag{3.18}$$

For every current level a B-H loop was generated, as shown in figure 3.9. To compute the relative iron permeability, the maxima values of B and H were used. These values are represented by the dots in figure 3.9.

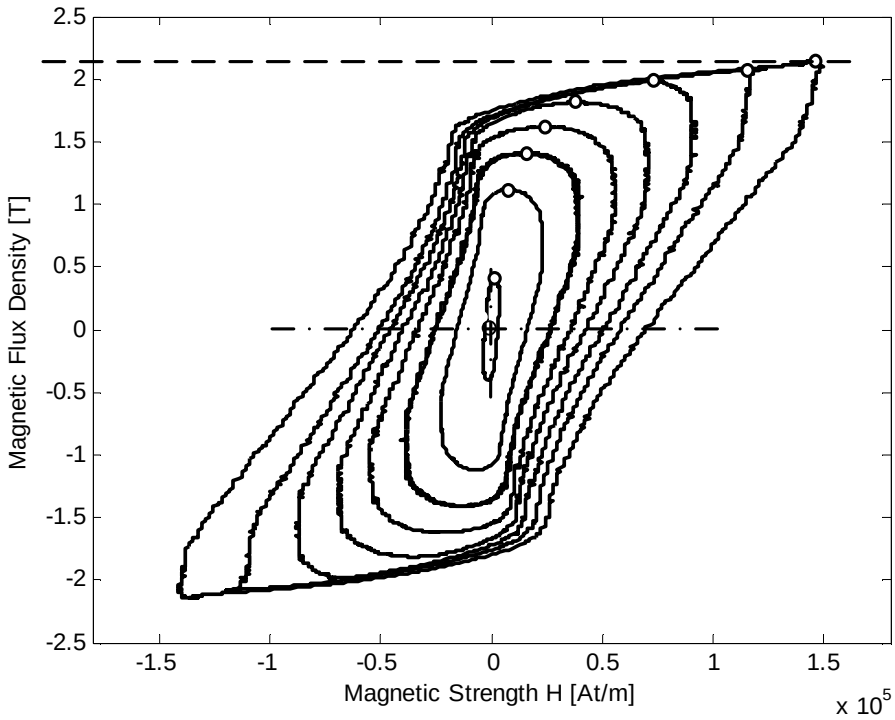

Figure 3.9 : B-H Loops of Rotor Material

The relative permeability of the shaft was taken as one. A typical axial flux density distribution obtained from finite element results is shown in figure 3.10.

As the rotor moves the flux distribution shown in figure 3.10 rotates relative to the radial reference lines shown in figure 3.4. As part of the algorithm that determines the rotational EMF waveform, the rotor position is changed in incremental steps and for each step a phase EMF value is calculated based on equation (3.15). A set of EMF values corresponding to one electrical cycle represents an EMF waveform. EMF waveforms for different phases are calculated using axial flux densities at the axial location of that phase.

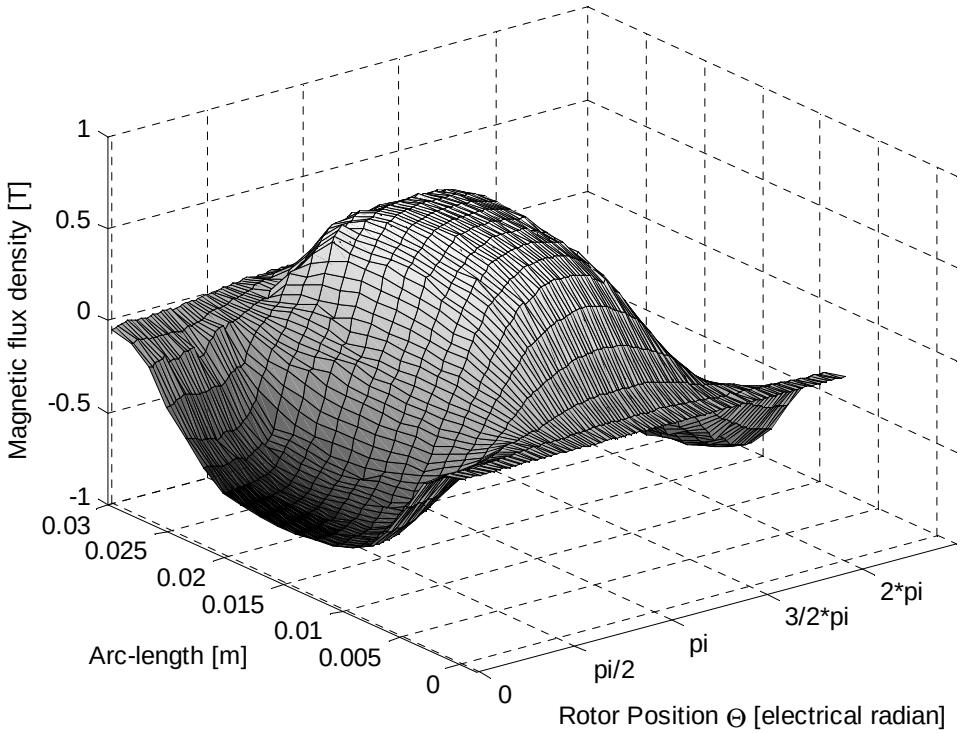

Figure 3.10 : Output from Finite Element Analysis (Axial Flux Density)

Before introducing the experimental results (section 3.4), some considerations on rhomboidal shaped spirals will follow. As expected the rhomboidal geometry presents lower resistance and lower EMF than the mixed track sections or the parallel track section designs. A comparison based on the torque capability factor $\left(\frac{E}{\omega_m}\right)\sqrt{\frac{P_l}{R}}$ (explained in section 3.4), clearly shows that the rhomboidal approach does not perform as well as the other two. The resulting difference is about 10%. Different rhomboidal shapes have been analyzed, two of them are presented in figures 3.11 and 3.12.

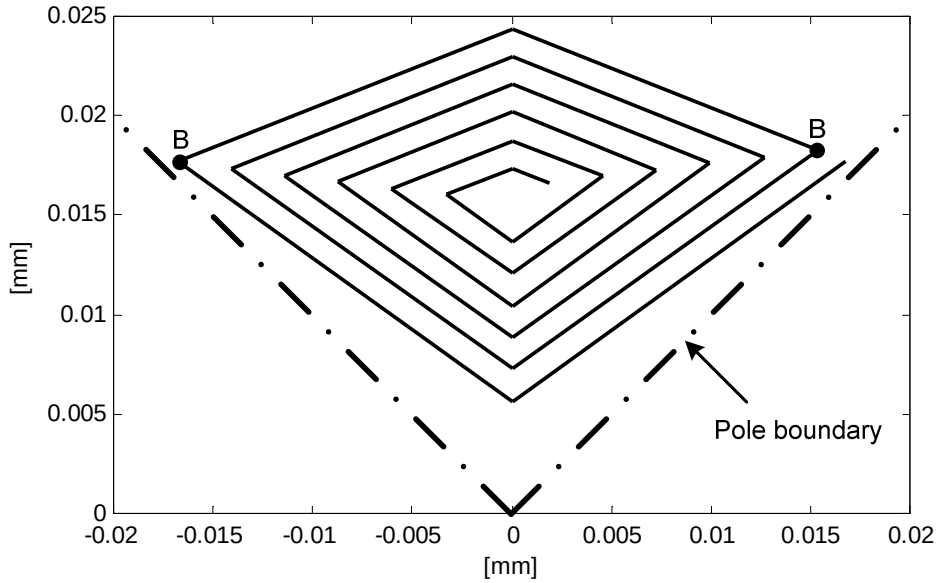

Figure 3.11 : “B” Point “max shift” in Direction Outer Radius

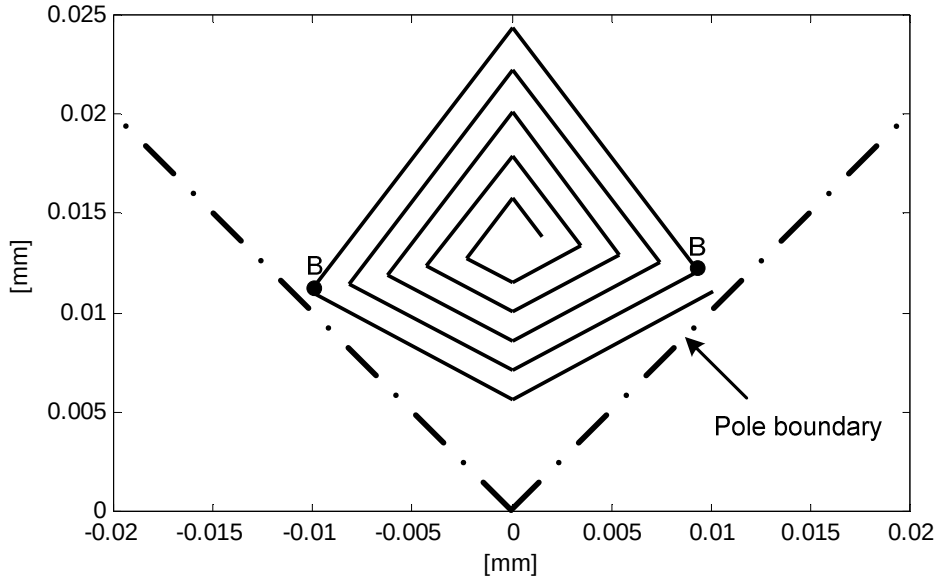

Figure 3.12 : “B” Point in Intermediate Position between Outer and Inner Radius

The best performing “rhomboidal” design, from a point of view of EMF is the one where the position of the B points (vertices) is maximized (maximal shift toward the outer radius). This particular B point configuration also results in near to sinusoidal EMF waveform. If the B points are shifted towards the inner radius the waveform gets quite distorted.

3.4 Experimental Verifications

Six motors were built to validate the coil design and EMF prediction procedures that have been proposed. Details of the motors are given in table 3.1. All motors have an outer radius of 25 mm, a rotor iron thickness of 4 mm, a magnet thickness of 4mm, a nominal track width of 1 mm and a track clearance of 0.3 mm. The outer dimensions were made equal to those of an existing commercial motor so that meaningful performance comparison could be made.

3.4.1 EMF Waveforms

A set of EMF waveforms for one of the prototype motors is shown in figure 3.13. For all six test motors, there is very good agreement between the predicted and measured waveforms. RMS values of the waveforms are given in table 3.1.

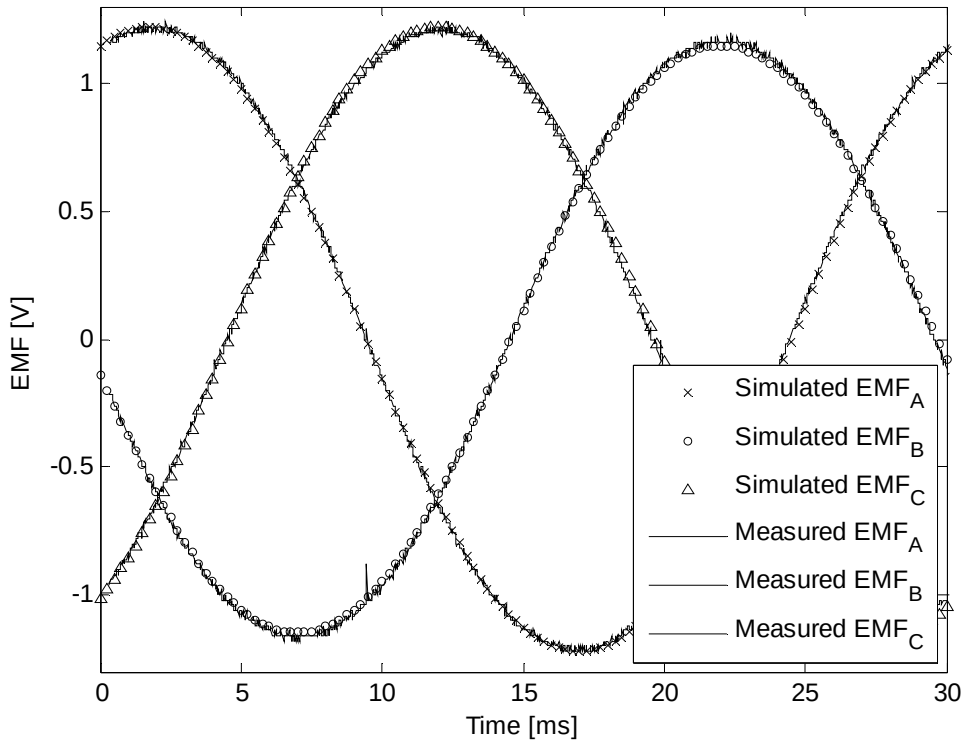

Figure 3.13 : Phase EMF Waveforms (Test Motor No. 1, 1000 r/min)

The sine wave approximation for the EMF waveform is well-justified since the total harmonic distortion is less than 2%.

Table 3.1 : Motor Test Data

	$\frac{R_i}{R_o}$	P	Track Type	N	B_{peak} [T]	E [V_{rms}]			R [Ω]		$\left(\frac{E}{\omega_m}\right)\sqrt{\frac{P_l}{R}}$ [mNm]
						(pred.) (eq. 3.11)	(pred.) FEM	(meas.)	(pred.)	(meas.)	(meas.)
1	0.20	4	Parallel	7	0.708	0.757	0.816	0.846	0.092	0.092	40.3
2	0.20	4	Mixed	7	0.708		0.810	0.840	0.085	0.084	42.0
3	0.36	4	Parallel	6	0.702	0.597	0.675	0.689	0.087	0.086	34.0
4	0.36	4	Mixed	6	0.702		0.672	0.687	0.084	0.083	34.5
5	0.20	8	Parallel	5	0.655	0.965	0.987	1.000	0.093	0.095	47.0
6	0.20	8	Mixed	5	0.655		0.975	0.987	0.090	0.091	47.4

As expected, the EMF waveform of the middle phase within the stator stack has slightly lower magnitude than the outer phases. The difference is typically less than 3.5% and does not represent any significant problem to motor performance. EMF predictions by the first order model in section 3.3.1 are within ten percent of those based on finite element.

3.4.2 Thermal Considerations

Both from the point of view of stator temperature rise and from the point of view of efficiency a reduction of printed circuit coil resistance is desirable. However a reduction in phase resistance should not be at the expense of an excessive reduction in EMF. An objective assessment of different strategies to reduce phase resistance may be based on the value of $\left(\frac{E}{\omega_m}\right)\sqrt{\frac{P_l}{R}}$ where P_l is the allowable stator power loss per phase. The term $\left(\frac{E}{\omega_m}\right)\sqrt{\frac{P_l}{R}}$ is proportional to the torque capability of the motor. The constant of proportionality depends on the shape of the phase current which would be sinusoidal for synchronous motor mode of operation or quasi-square for brushless DC mode of operation. Comparison of the torque capabilities of different motors using the single term $\left(\frac{E}{\omega_m}\right)\sqrt{\frac{P_l}{R}}$ is justified if armature reaction is neglected. Since the motors being considered have ironless stators, armature reaction is negligible. In the case of the prototype motors peak flux density due to rated stator current was less than 10 mT compared to the peak airgap flux density which was typically more than 0.5 T.

Allowable stator power loss can be estimated by thermal modeling or stator temperature rise test or both. For the prototype motors it was found by both thermal modeling and by test that, to keep substrate temperature rise below the acceptable level of 65°C, P_l has to be kept below 2.3 W. From the thermal investigations it was found that the temperature difference between the middle substrate and the exposed stator surface was less than 8°C. Table 3.1 provides $\left(\frac{E}{\omega_m}\right)\sqrt{\frac{P_l}{R}}$ values for the six prototype motors, with P_l assumed to be 2.3 W. The adopted thermal model, introduced by figure 3.14, is a simplified first order 1-D model.

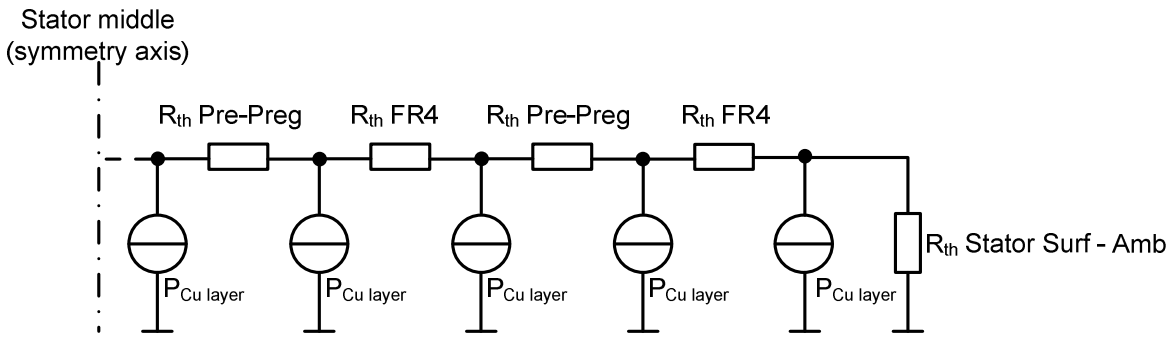

Figure 3.14 : The 1-D Thermal Model

The following assumptions have been made:

- No lateral / radial heat flow, since the cross sectional surface in lateral / radial direction is small compared to the one in axial direction. This assumption is conservative and will generate an overestimation of the increase in temperature

- Since the thermal conductivity of copper is approximatively 1600 times bigger than the one of the bulk materials (FR4 or Prep-Preg), the thermal resistivity of the copper layers has been neglected.

- A symmetry plane was assumed to exist in the middle of the central substrate. For many applications this is a reasonable assumption (for example for machines having a good thermal conducting housing). If it is not the case, the model has to be expanded to cover both sides, including, if necessary, different surface to ambient thermal resistances.

- The stator is made up of three substrates. The internal structure of these substrates is identical and consists of 8 copper layers (track layers) and 8 bulk material layers. The multilayer structure is:

  100 μm = copper layer,

  100 μm = bulk layer (FR-4),

  100 μm = copper layer,

  100 μm = bulk layer (FR-4),

  ...,

  resulting in a final substrate thickness of 1.6mm.

The following paragraph introduces the model in detail:

- R_i = 5mm =inner radius of the substrate
- R_o = 25mm =inner radius of the substrate
- $c_{pre\text{-}preg} \sim c_{FR\text{-}4}$ = 0.25 W/(m°C) = FR-4 thermal conductivity
- I_{phase} = 5 A = phase current *

  *All three phases carry I_{phase} (in normal BLDC operation only two are energized at the same time)

  R_{stator} = 300 mΩ = total three-phase stator resistance (series connected)

- Based on information from reference [53], a typical heat transfer coefficient for a planar disc in still air conditions was found to be approximatively 33.

  α = 33 W/(Km^2) = typical heat transfer coefficient

At first the thermal resistance of the bulk material can been computed by equation 3.19:

$$Rth_{FR-4} = \frac{l_{BaseCu}}{\left(R_o^{\,2}\pi - R_i^{\,2}\pi\right)c_{FR-4}} k_f \,, \tag{3.19}$$

where $k_f = \frac{w-c}{w} = 0.7$ is the copper fill factor. Then, by means of equation 3.20, the thermal resistance surface to ambient is worked out:

$$Rth_{S-A} = \frac{1}{\alpha\left(R_o^{\,2}\pi - R_i^{\,2}\pi\right)} \tag{3.20}$$

Finally the temperature difference between the middle of the central substrate and ambient can be derived by equation (3.21).

$$\Delta T = \left(\sum_{n=1}^{n=\frac{n_{used}}{2}-1} nRth_{FR-4} \frac{I_{phase}^{\;2} * R_{stator}}{n_{used}} \right) + n_{used} Rth_{S-A} \frac{I_{phase}^{\;2} * R_{stator}}{n_{used}} \tag{3.21}$$

$$\Delta T = 66.5[°C]$$

where n_u is the number of used layers

The measurement, carried out at ambient temperature of 26° celsius and still air conditions, delivered the following results:

- The stabilized temperature rise is around 65° celsius, as shown in figure 3.15. This rise, if using a standard FR-4 (no special high glass transition temperature), does not pose any problem.
- No significant voltage difference has been recorded between the top (A) and middle (B) phase, as presented in figure 3.16, which means both substrates experience approximately the same temperature.

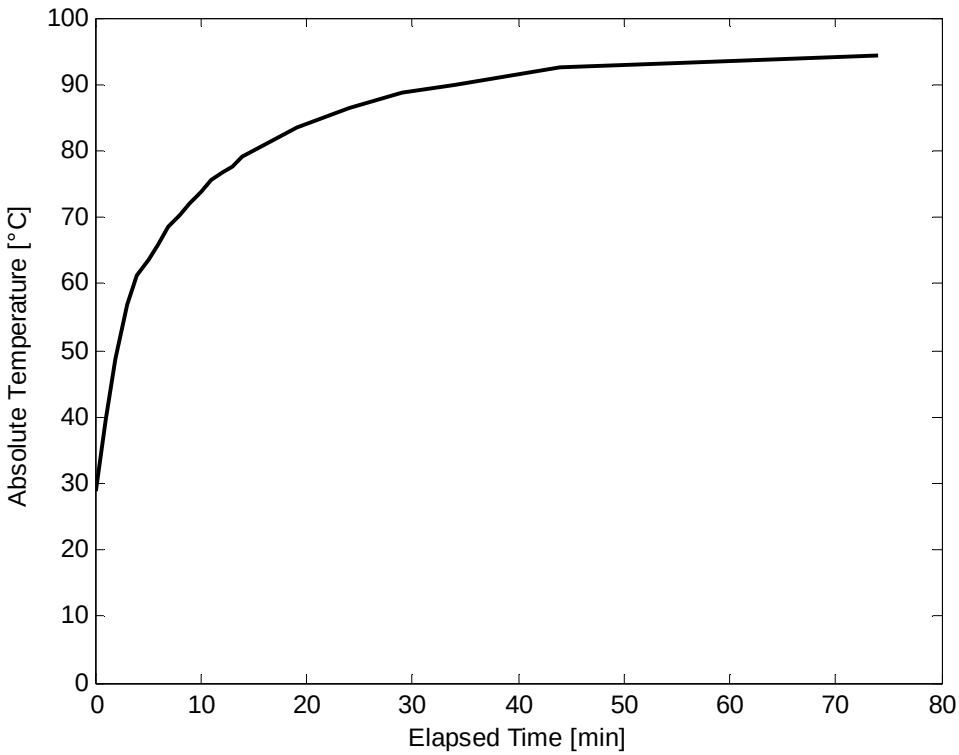

Figure 3.15 : Phase A (top phase) Temperature Rise on Time

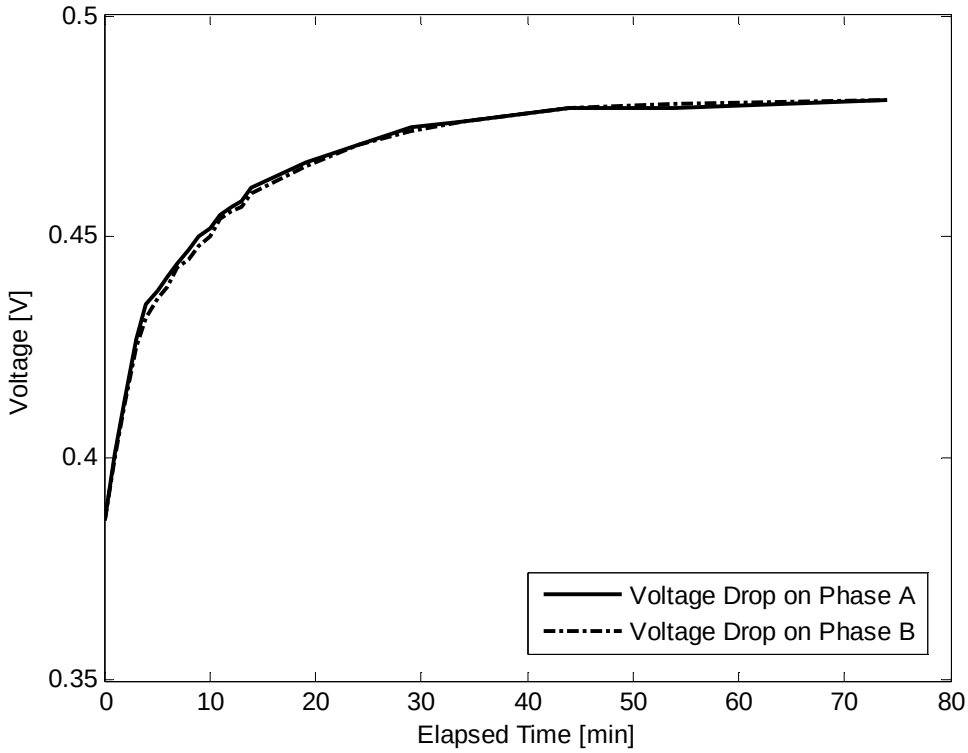

Figure 3.16 : Phases Voltage Drop

3.4.3 Resistance Optimization

There are a number of opportunities to reduce phase resistance:

- First opportunity is the use of mixed track, which is covered in section 3.4.4 and illustrated in table 3.1
- Second opportunity, which is not apparent in table 3.1, arises because the number of turns (N) when calculated using the equations in section 3.2 is usually not an integer.

The actual number of turns adopted is the next lower integer. Some substrate area is left and, as suggested in section 3.2.1, can be reallocated to increase track width to reduce resistance. This area could be substantial when N is low and in such cases phase resistance reduction could be very significant. The new optimized width is computed by equations (3.22) or (3.23)

$$w_{new} = \frac{(R_o - N \cdot c)\sin\left(\frac{\pi}{N_s}\right) - (N \cdot c)}{\sin\left(\frac{\pi}{N_s}\right) \cdot N} \tag{3.22}$$

Equation (3.22) is valid if inequality (3.4) is respected

$$w_{new} = \frac{\frac{(R_o - R_i)}{2} - (N \cdot c)}{N} \tag{3.23}$$

Equation (3.23) is valid if inequality (3.6) is respected

- Third opportunity is embedded in the design optimization algorithm. Since the following section is entirely dedicated to this algorithm, only the basic idea behind this possibility is introduced at this point. The previous opportunity is based on the reallocation of the leftover substrate area, in this one the leftover axial stator space is filled up by additional layers connected in parallel with the other coils (figure 3.17). Equations (3.24) to (3.29) are included in the optimization algorithm, allowing phase resistance optimization.

$$k_{series} = round\left(EMF_{total} / EMF_{element}\right) \tag{3.24}$$

where k_{series} = series connection coefficient (of 2-layer elements)

EMF_{total} = total desired phase EMF

$EMF_{element}$ = total EMF of 2-layer element

round (X) = rounds X to the nearest integer

$$n_{\max} = floor\left(\frac{t_a}{t_{layer}}\right) \tag{3.25}$$

where n_{max} = maximal number of layer

t_a = stator total axial length

t_{layer} = layer thickness = Base cu thickness + Pre-Preg thickness

floor (X) = rounds X to the lower nearest integer

$$n_{parallel} = floor\left(\frac{n_{\max}}{2k_{series}}\right) \tag{3.26}$$

where $n_{parallel}$ = number of parallel layers

$$n_u = 2n_{parallel}k_{series} \tag{3.27}$$

where n_{used} = number of used layers without optimization

$$R_{spiral} = \rho_{cu}\frac{l_{spiral}}{A_{spiral}} \tag{3.28}$$

where l_{spiral} = length of the spiral

A_{spiral} = cross sectional area of the spiral

$$R_{phase} = \left(\frac{R_{spiral}}{n_{parallel}+1}\left(n_{\max} - n_{used}\right) + \frac{R_{spiral}}{n_{parallel}}\left(\left(2k_{serie}\right) - \left(n_{\max} - n_{used}\right)\right)\right) P \qquad (3.29)$$

where P = number of stator poles

n_{max} = maximal number of layer

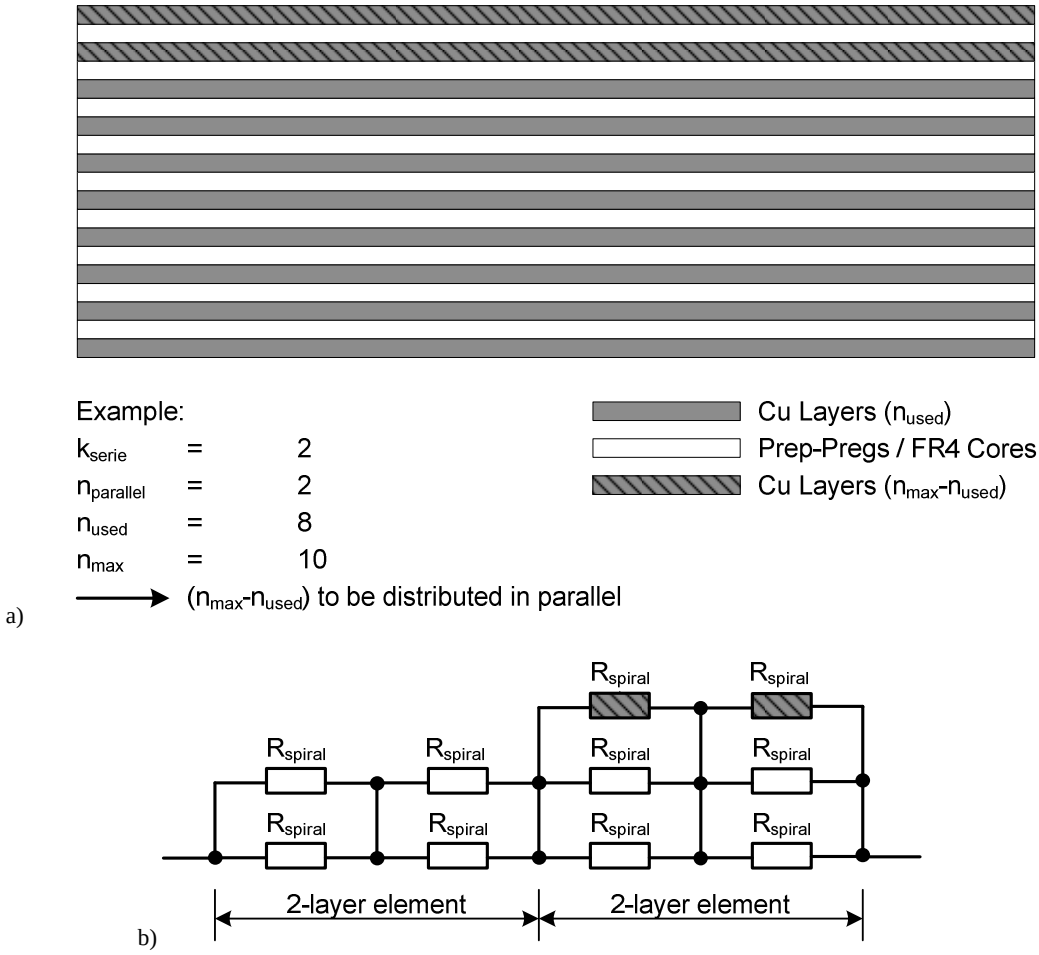

Figure 3.17 : a) Layers Structure; b) Resistive Structure

Note that difference on axial magnetic flux density between two layers is less than 0.4%.

3.4.4 Parallel Track Sections versus Mixed Track Sections

As shown in table 3.1 and in figure 3.18 the main advantage of coils with mixed track sections is lower phase resistance without substantially sacrificing the magnitude of rotational EMF. As expected, of the motors being considered, the four pole motors benefit the most from coils with mixed track sections because they have the highest effective curvature and therefore the highest ratio of non-active to active conductor length.

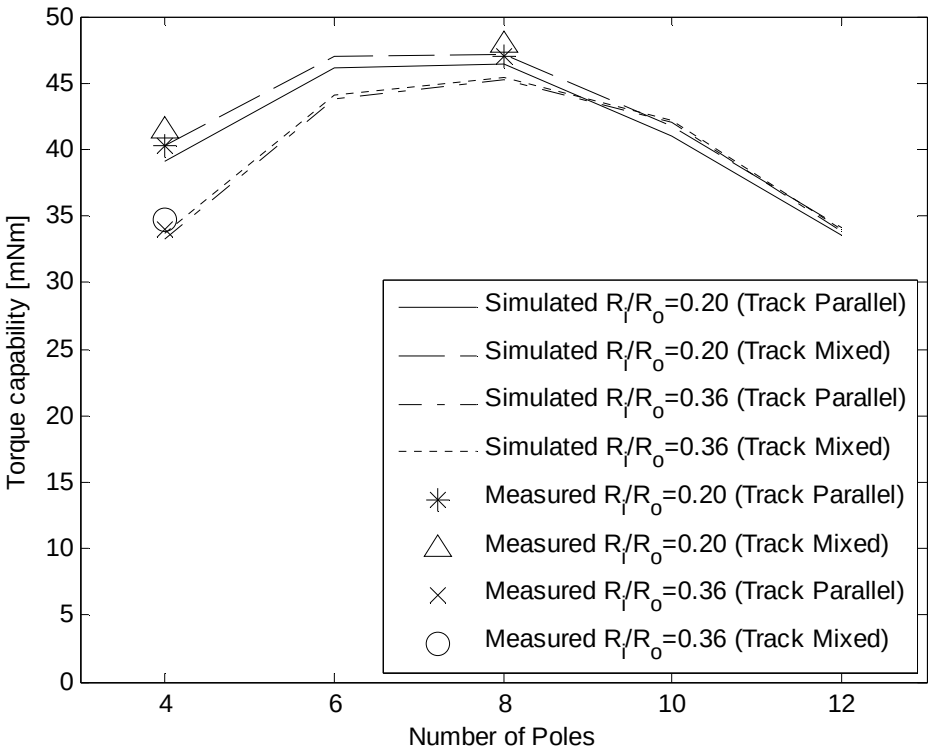

Figure 3.18 : Torque Capability versus Number of Poles

Table 3.1 also shows that the coils with fully parallel track sections have the higher EMF compared to coils with mixed sections. Parallel track sections have lower skew factors compared to radial track sections which have a skew factor of 1. But the coils with parallel sections have better pitch factors which more than compensate for the effect of their lower skew factors.

3.4.5 Single Layer Machines

In chapter 1, section 1.3, the possibility to have coils on a printed layer shared between phases has been pointed out. Experiments have been carried out on stators with this configuration. For fair comparison the same rotor was used as with other configurations. Since at least 6 coils must be fitted into the layer to build a three phase machine, it is evident, that the coil pitch differs from the magnet pitch. This results in a non sinusoidal EMF waveform (figure 3.19) and in a non sinusoidal inductance variation (figure 3.20). Sinusoidal variation of inductance is an important requirement of the equal inductance method which is planned to be used. From a point of view of EMF this configuration does not achieve the same performance level as stators with mixed track sections.

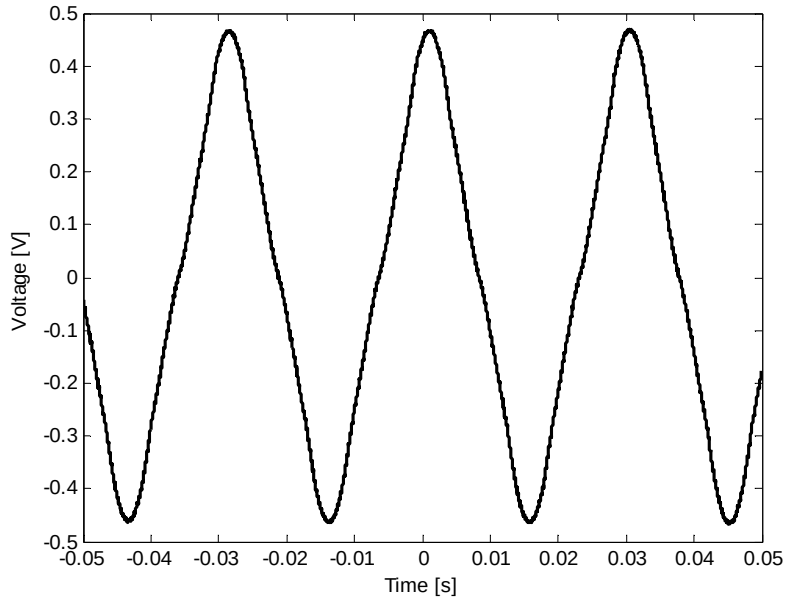

Figure 3.19 : Single Layer Machine Phase EMF Waveform at 1000 r/min

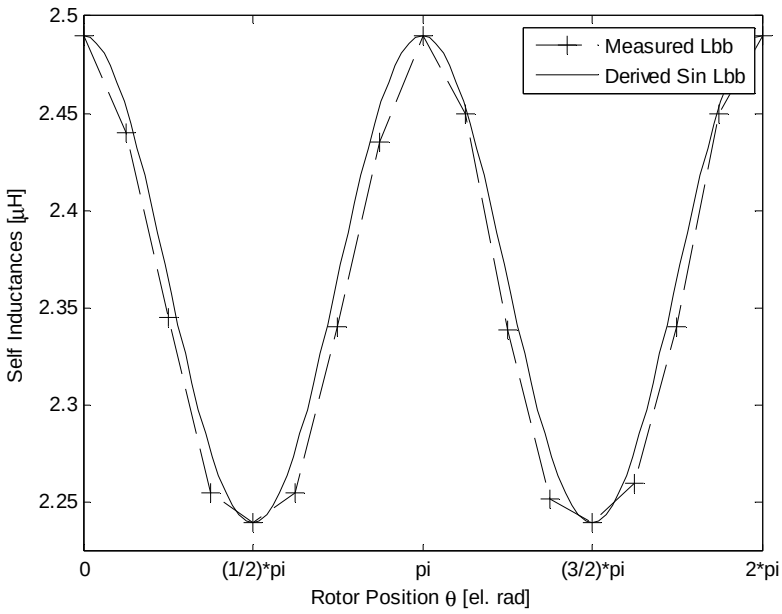

Figure 3.20 : Self-inductance L_{bb} Single Layer Stator

Based on these result the single layer machine configuration has not been considered any further.

3.4.6 Number of Poles

Predictions and test results shown in table 3.1 and in figure 3.18 suggest that benefits of higher EMF and lower phase resistance are possible if the number of poles is carefully chosen. There are two major factors affecting the magnitude of the phase EMF. These are the magnitude of the air-gap flux density and the total number of turns. Since the circumferential gap between magnets, measured in electrical degrees, was kept the same irrespective of the number of poles, there is increased leakage between neighbouring magnets as the number of poles goes up. The consequence, as can be seen in table 3.1, is a decrease in the axial component of air-gap flux density with higher pole numbers. The number of turns and the skew factor both go up with number of poles. From the point of view of phase EMF, the combination of those factors results in the existence of an optimal value for the number of poles. This optimum value is dependent on variables such as R_i and R_o. As shown if figure 3.18, in the case of the motors being considered, the optimum number of poles is eight.

3.4.7 Ratio of Inner Radius to Outer Radius

In the case of wound axial flux machines a well-known theoretical result stipulates that making R_i/R_o less than $\frac{1}{\sqrt{3}}$ is counter productive. However this result is based on the assumption that active sections of conductors are radial and there is a limit on the number of conductors per meter in the circumferential direction. In the present case the active conductor sections, at least

near the inner radius, are not radial and therefore the $\frac{1}{\sqrt{3}}$ rule does not apply. Both table 3.1 and figure 3.18 show that EMF magnitudes go up as R_i/R_o goes down, but at a decreasing rate. It has been found that, for the chosen value of R_o, the magnitude of the phase EMF is practically constant for values of R_i/R_o which are below about 0.2. A general conclusion would be that there is no benefit in reducing R_i below a certain value. However that value is lower than the shaft radius and would therefore have no practical relevance.

3.5 **Design Optimization**

The experimentally validated EMF evaluation method and the suggested track plotting procedure can form the basis for a design optimization algorithm for printed circuit motors. In the example that follows, the design objective would be to maximize torque output capability subject to a number of constraints which are listed in Table 3.2.

The torque developed by the printed circuit motor is proportional to the product of the airgap flux density and the stator current. At one extreme, if the entire available axial length was allocated to the field system, torque will be zero because there would be no room left for the stator and stator current will be zero. The other extreme would be if the entire available axial length was allocated to the stator, excitation would be zero and again torque production would be zero because the field flux density would be zero. As the axial length allocated to the magnet and rotor iron is increased from zero, the output torque will rise to a maximum and then fall and

reaches zero again when no room is left for the stator. The aim of the algorithm is to find this maximum.

For a given maximum stator power loss P_l, a lower phase resistance, achievable with a higher value of t_s, signifies a higher allowable stator current. Magnet axial thickness t_m and phase resistance R may be considered to be independent variables under the control of the designer. Design optimization means identifying the (t_m,R) pair that results in highest torque capability.

A design requirement is for the back EMF per unit speed to be within tight limits. Thus the number of turns per phase, is relatively constant. In a multilayer PCB design the total number of turns per phase, assuming all spirals are series connected, is N x L x P where N is the number of turns in a spiral, L is the number of layers and P is the number of poles. For a given copper foil, different (N,L) pairs satisfy the EMF requirement. For every given value of tm, a sub-optimum is found which would correspond to the (N,L) pair that results in the highest output torque. In cases where there is more than enough axial space to meet the EMF requirement, the algorithm automatically increases the number of layers. The coils on the additional layers are connected in parallel with the other coils. By paralleling the additional coils as uniformly as possible to the other coils overall phase resistance is minimized (as introduced in section 3.4.3).

The algorithm consists of the following steps:

(a) Set t_m equal to its minimum allowable value.

(b) Make an initial estimate for t_i by simultaneous solution of equations (3.11) and (3.14).

(c) Use finite element analysis to obtain the flux density distribution and, if necessary, repeat the FEM analysis with t_i re-adjusted until the peak flux density in the rotor iron is close to B_s.

(d) Use equation (3.14) to calculate t_s.

(e) For the copper foil being considered, calculate the maximum value of N using equation (3.3) or (3.5).

(f) For each integer value of N between 1 and its maximum value, calculate if the constraints in Table 3.2 allow, $\left(\frac{E}{\omega_m}\right)\sqrt{\frac{P_l}{R}}$.

(g) Select and plot against the current tm the highest value of $\left(\frac{E}{\omega_m}\right)\sqrt{\frac{P_l}{R}}$ from the current set of values obtained from step (f).

(h) Increment tm and go to step (b) if the maximum allowable value of t_m is not exceeded.

(i) Repeat steps (a) to (h) for all candidate copper foil thicknesses

(j) Read the graph from step (g) to obtain the maximum torque capability.

The graphical output from step (g) is shown in figure 3.21.

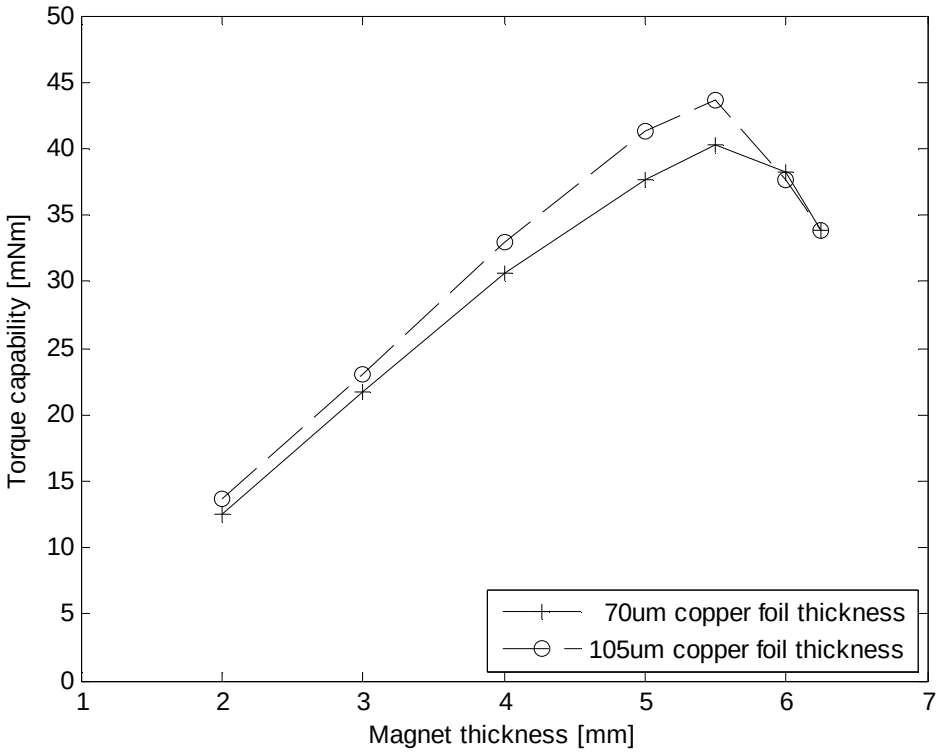

Figure 3.21 : Torque Capability versus Magnet thickness

Table 3.2 : Printed Circuit Motor Design Example

Design Parameter	*Degree of Flexibility*
Outer Radius (R_o)	R_o = 25 mm (R_o defined in section 1)
Inner Radius (R_i)	R_i = 5 mm
Number of poles (P)	P = 4 (Chosen on basis of mechanical requirement and drive switching frequency)
Total thickness (t_a)	t_a = 28 mm
Rotor Iron thickness (t_i)	t_i > 1 mm (for mechanical stability)
Rotor peak flux density (B_s)	B_s =1.4 T $\pm$ 0.1
Stator/Magnet Clearance (t_c)	0.3 mm
Insulation layer thickness	Foil 1: 100 um ; Foil 2: 100 um
Track thickness	Foil 1: 70 um ; Foil 2: 105 um
Clearance between tracks	Foil 1: 230 um ; Foil 2: 300 um
Minimum track width	Foil 1: 200 um ; Foil 2: 300 um
Maximum track width	Foil 1: 2.5 mm ; Foil 2: 2.5 mm (to avoid stator eddy currents)
Max allowable stator power loss (P_l)	P_l = 2.3 W
Magnet thickness	1mm < t_m< t_{max}; (t_{max} determined by minimum t_s)
Minimum Magnet thickness delta	0.25 mm
Remanence (B_r)	B_r = 1.24 T
EMF (at 1000 rpm)	1V $\pm$ 10%

3.6 **Conclusions**

A track plotting procedure has been developed for the design of coils in printed circuit brushless motors. The procedure maximizes the number of turns in the printed spiral shaped coil for given values of substrate inner radius, substrate outer radius, minimum track thickness and inter-track clearance. Active sections of the tracks may be purely radial, parallel with each other or may be partly radial and partly parallel. Computer programs, that implement the procedure, automatically produce track plots which can be used directly by the printed circuit production process.

By combining the track plotting procedure with the finite element method, a technique has been developed to predict rotational EMF waveforms of printed circuit motors. The technique, which has been validated by experimental results from six different prototype motors, has been used for printed circuit motor design optimization.

.

Chapter 4

Sensorless Commutation Technique for Brushless DC Motors

4.1 Introduction

The aim of this chapter has been to investigate the possibility of a sensorless technique which is as cost effective as the back EMF method but with a performance at start-up comparable with that obtained when Hall sensors are used. Initial investigations led to a saliency based method. Unlike other proposed methods, no special signal injection is needed. The technique is based on the detection of rotor positions where the two energised phases have equal inductances. It has therefore been termed the *equal inductance method* [2]. Theoretical analysis is presented which shows that the method is insensitive to variations in operational parameters such as load current

and speed or circuit parameters such as power device voltage drops and winding. Test results are presented which demonstrate practical application of the method.

Gambetta [3] required a neutral connection for practical implementation of a version of the equal inductance method. It is shown in this chapter that connection to the neutral is not necessary.

An initial position detection and start-up method based on saliency related measurement is also proposed and practically implemented. This method offers starting performance as good as Hall sensor based techniques.

4.2 Relationship between Equal Inductance Positions and Commutation Positions

Electrical machines that exhibit saliency may be analysed using the well established two-axis theory. This theory leads to the following expressions for the three-phase winding inductances and mutual inductances:

$$L_{aa} = L_{aa0} + L_{al} + L_{g2}\cos(2\theta) \tag{4.1}$$

$$L_{bb} = L_{aa0} + L_{al} + L_{g2}\cos\left(2\theta + \frac{2\pi}{3}\right) \tag{4.2}$$

$$L_{cc} = L_{aa0} + L_{al} + L_{g2}\cos\left(2\theta - \frac{2\pi}{3}\right) \tag{4.3}$$

$$L_{ab} = L_{ba} = -0.5L_{aa0} + L_{g2}\cos\left(2\theta - \frac{2\pi}{3}\right) \tag{4.4}$$

$$L_{bc} = L_{cb} = -0.5L_{aa0} + L_{g2}\cos\left(2\theta\right) \tag{4.5}$$

$$L_{ac} = L_{ca} = -0.5L_{aa0} + L_{g2}\cos\left(2\theta + \frac{2\pi}{3}\right) \tag{4.6}$$

where θ is the electrical angle between the magnetic axis of phase A and the rotor direct axis or the rotor quadrature axis; L_{ii} is the self inductance of phase i; L_{ji} is the mutual inductance between phase i and phase j; L_{aa0}, L_{a1} and L_{g2} are positive constants which are independent of θ and, if the effects of saturation are ignored, they are also independent of winding currents. By definition the direct axis (d-axis) of the rotor is coincident with the magnetic axis of the rotor permanent magnet. The quadrature axis (q-axis) is ninety electrical degrees away from the d-axis.

Equations (4.1) to (4.6) are good representation of phase inductances of BLDC motors with surface mounted magnets or surface inset magnets. This conclusion was based on inductance measurements performed at 20 kHz or higher on a number of test machines. Figure 4.1 shows the phase inductance profiles for one of those machines.

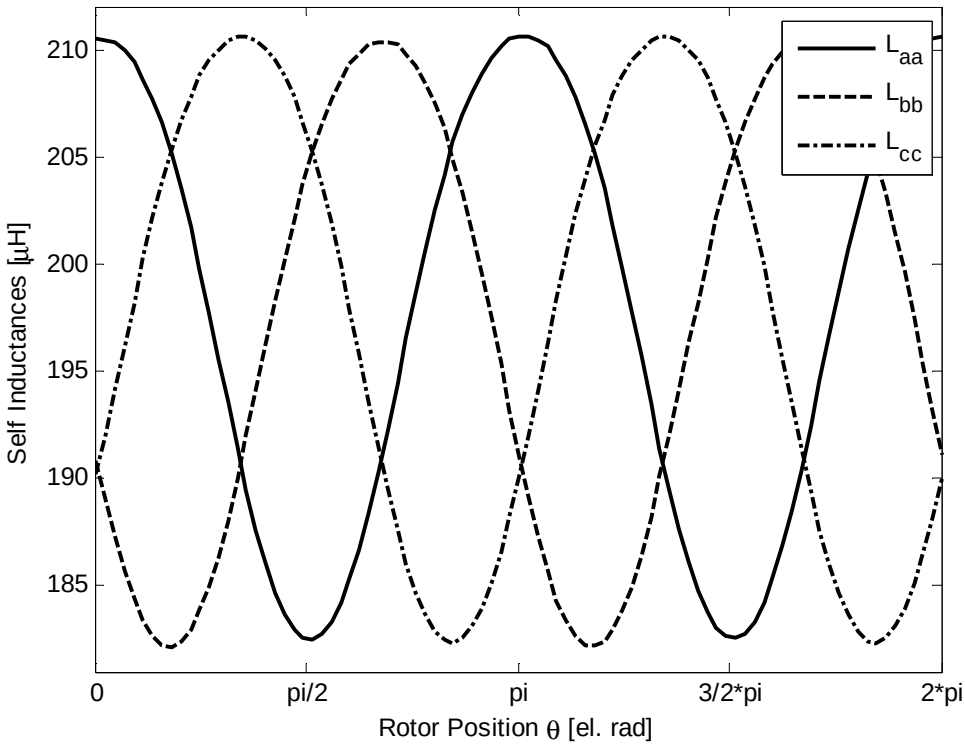

Figure 4.1 : Measured Self-Inductances

It is important to point out that the self-inductances and the mutual inductances that are referred to here are only effective values rather than actual values. The actual value of L_{aa} , for example, can only be obtained by measurement if all circuits that are magnetically linked to phase A were open-circuited. But that is not possible. Whilst the other two stator windings were open-circuited, the influence of eddy-currents in the magnets and other parts of the machine could not be eliminated. Thus the measured winding inductances are lower than their true values. They may be regarded as effective values that take into consideration the effect of eddy-currents, in a similar manner that the use of sub-transient inductances in synchronous machine analysis is a

way of accounting for the effect of damper windings and other induced current paths on the rotor. In the case of the test motors, induced eddy currents in the magnets result in a lower phase inductance when the magnetic axis of that phase lines up with the magnetic axis of a rotor magnet (direct axis). Conversely, phase inductance is a maximum when the magnetic axis of the phase winding lines up with a quadrature axis. The reluctance is effectively less along the q-axis because the flux cancelling effect of eddy-currents is less along that axis since the gap between adjacent magnets breaks the eddy-currents paths. Thus the zero degree position in figure 4.1 or in table 4.1 corresponds to alignment of the phase A magnetic axis with the rotor quadrature axis.

Table 4.1 : Equal Inductance Positions and Commutation Intervals

Rotor position range (electrical degrees)	0° to 60°	60° to 120°	120° to 180°	180° to 240°	240° to 300°	300° to 360°
Energised pair in each commutation interval	CA	CB	AB	AC	BC	BA
Equal inductance position before next commutation event	30°	90°	150°	210°	270°	330°
Next commutation position	$\theta_1 = 60°$	$\theta_2 = 120°$	$\theta_3 = 180°$	$\theta_4 = 240°$	$\theta_5 = 300°$	$\theta_6 = 360°$

The BLDC motor is normally operated with only two phases energised at any one time. Each phase is energised for a 120 electrical degree interval after which it is de-energised for a 60 electrical degree interval. The ideal commutation positions, θ_1 to θ_6, are shown in table 4.1. These commutation positions lead to the highest electromagnetic torque per unit ampere as well

as the lowest torque ripple. The reason for this is that each phase is energized during the 120 degree intervals centred about the peak value of the phase back EMF. There are six distinct commutation intervals. They have been labelled in figure 4.1 according to the phase pair that is energised and supply voltage polarity. For example CA corresponds to inverter transistors TB+ and TB-, shown in figure 4.2, being kept off and the other four transistors switched so that, on average over a PWM cycle, phase terminal *c* is kept at a higher potential relative to phase terminal *a*.

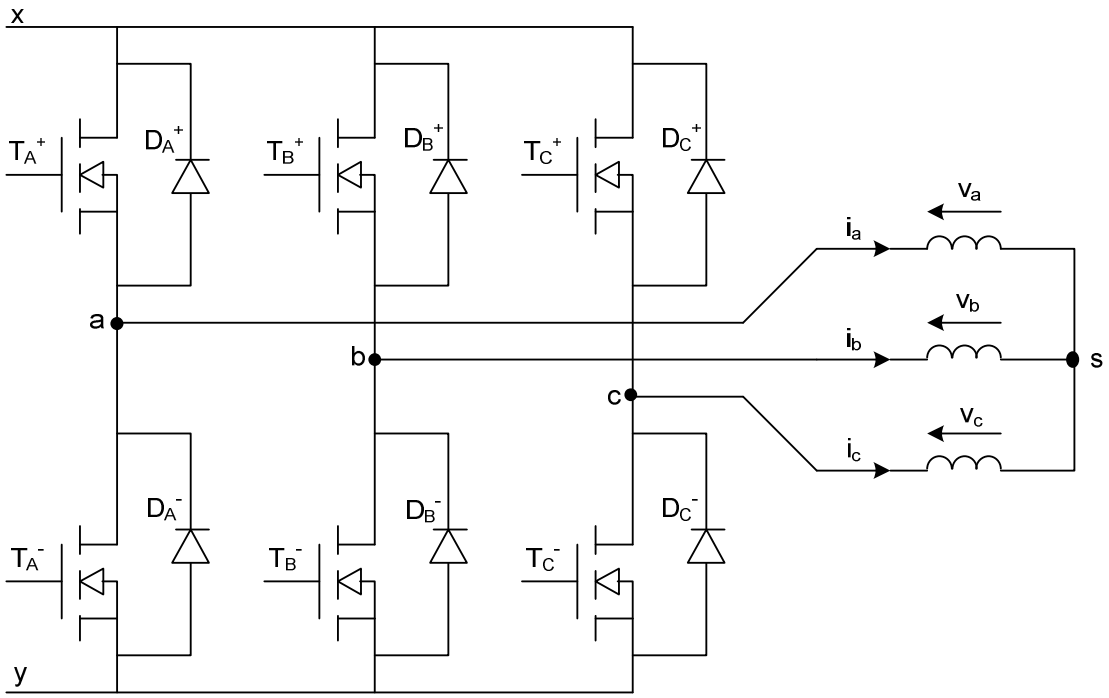

Figure 4.2 : Inverter Bridge Supplying a Brushless DC Motor

It follows from the previous paragraph that the zero-crossings of the back EMF of a particular phase occurs 30 electrical degrees before that phase is energized. But the zero crossing of the

back EMF of a phase winding also coincides with alignment of the magnetic axis of that winding with the d-axis of the rotor. Clearly at that position the self-inductance of that phase is a minimum, whereas the inductances of the two other phases will, because of geometric symmetry, be equal to each other. In other words, wherever the rotor d-axis aligns with the magnetic axis of the A-phase winding, back EMF E_a is equal to zero and $L_{bb} = L_{cc}$. Similar statements can be made about the B-phase winding and the C-phase winding. Thus the positions of equal inductance of the energized phases, just like the zero-crossings of the back EMF of the non-energised phase occur 30 electrical degrees before the next commutation position.

There are twelve positions of equal inductance over each electrical cycle (360 electrical degrees). Six of them correspond to the rotor q-axis coinciding with the magnetic axis of each one of the phase windings. The other six correspond to the rotor d-axis coinciding with the magnetic axis of each one of the phase windings. Only six of these, the ones associated with the rotor d-axis aligning with stator phase windings will be used to help determine commutation positions. They are specified in table 4.1. Note that while the frequency of commutation is proportional to speed, rotor position at which commutation is initiated does not change as speed changes.

4.3 Detection of Equal Inductance Positions

As mentioned before there are six commutation intervals. During each interval the aim is to have only two phases active. In table 4.1 the six intervals have been labelled according to the phases

that are active. Transition from one interval to the next involves de-energising of one phase and energising of the next one. This transition is complete only after the current in the outgoing phase has decayed to zero. Decay of the current occurs through a diode and takes finite time. For example the transition from interval AC to interval BC involves decaying current through the diode D_A^-. Therefore each interval involves two sub-intervals, one during which all three-phase currents are present and one during which the non-active phase current is equal to zero. In total there are twelve sub-intervals and twelve corresponding inverter states. The inverter states are labelled according to the polarity of the DC supply terminal to which the motor phase terminals are connected. For example inverter state $c^+a^+ b^-$ implies the “c” and “a” phase terminals are connected, through transistors or diodes to the positive DC rail whereas the “b” terminal is connected to the negative DC rail. Since bipolar PWM is used, during any one of the commutation intervals, the inverter may be in one of six possible states. For example during interval AB, the inverter may be in state $a^+c^+b^-$, or $a^+c^-b^-$, or $a^-c^+b^+$, or $a^-c^-b^+$, or a^+b^-, or b^+a^-.

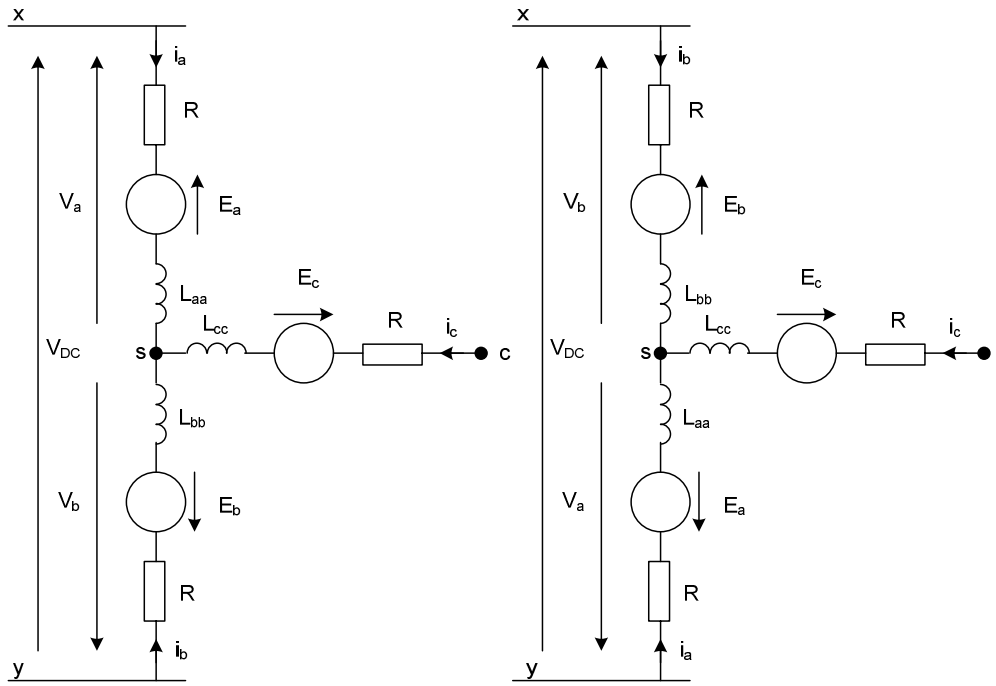

Figure 4.3 : Equivalent Circuits for Inverter States a^+b^- and b^+a^-

(Switching device voltage drop not shown)

The aim is to use inductive saliency to determine the correct commutation instants for the motor. The method is based on the sensing of the potential at the non-energised phase winding terminal after the current in that phase has decayed to zero. Consider commutation interval AB. Assuming current i_c has decayed to zero, the inverter will revert alternately between the states a^+b^- and b^+a^-. These are represented by the equivalent circuits in figure 4.3.

Voltage measurements v_{cy}^+ and v_{cy}^- are carried out while the inverter is respectively in states a^+b^- and b^+a^-. For consistency, as shown in figure 4.4, measurements are carried out near the middle of the applied voltage pulses. Consecutive measurements v_{cy}^+ and v_{cy}^- are compared. It is shown, in the next paragraphs that those two values are equal to each other at precisely the position of

equal inductance independent of the value of phase current, supply voltage or speed. Thus, by cyclic monitoring of voltage signals v_{cy}, v_{ay} and v_{by}, commutation instants can be pre-determined with very little computational effort.

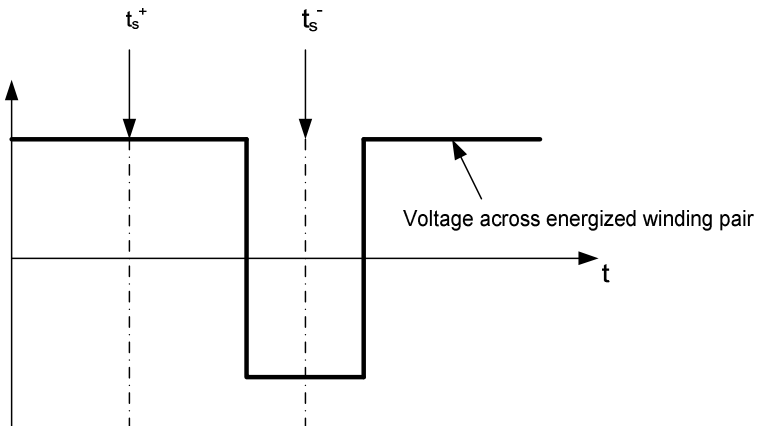

Figure 4.4 : Voltage Sampling Instants (t_s^+ and t_s^-)

Consider operation during commutation interval AB. With the inverter in state a^+b^- we have:

$$v_{sy}^+ = \frac{1}{2}\left(V_{dc} - v_{ay}^+\right) - \frac{1}{2}v_{by}^+ \tag{4.7}$$

Since i_a=-i_b, equation (4.7) gives:

$$v_{sy}^+ = \frac{V_{dc}}{2} + \left(\frac{L_{bb} - L_{aa}}{2}\right)\left(\frac{di_a}{dt}\right)^+ + \frac{i_a^+}{2}\frac{d\left(L_{bb} - L_{aa}\right)}{dt} - \left(\frac{E_b + E_a}{2}\right) \tag{4.8}$$

Adding v_{cs}^{+} to v_{sy}^{+} yields:

$$v_{cy}^{+} = \frac{V_{dc}}{2} + \left(\frac{L_{bb} - L_{aa} + 2L_{ca} - 2L_{cb}}{2}\right)\left(\frac{di_a}{dt}\right)^{+} + \frac{i_a^{+}}{2}\frac{d\left(L_{bb} - L_{aa} + 2L_{ca} - 2L_{cb}\right)}{dt} - \left(\frac{E_a + E_b - 2E_c}{2}\right) \quad (4.9)$$

Also,

$$\left(\frac{di_a}{dt}\right)^{+} = \frac{\left(V_{dc} - i_a^{+}\frac{d\left(L_{aa} + L_{bb} - 2L_{ab}\right)}{dt} - E_a + E_b - 2V_t^{+} - 2i_a^{+}R\right)}{\left(L_{aa} + L_{bb} - 2L_{ab}\right)} \quad (4.10)$$

where $2V_t^{+}$ is the total switching device voltage drop.

With the inverter in state $b^{+}a^{-}$ we have:

$$v_{sy}^{-} = \frac{1}{2}\left(V_{dc} - v_{by}^{-}\right) - \frac{1}{2}v_{ay}^{-} \quad (4.11)$$

Since i_a=-i_b, equation (4.11) gives:

$$v_{sy}^{-} = \frac{V_{dc}}{2} + \left(\frac{L_{bb} - L_{aa}}{2}\right)\left(\frac{di_a}{dt}\right)^{-} + \frac{i_a^{-}}{2}\frac{d\left(L_{bb} - L_{aa}\right)}{dt} - \left(\frac{E_b + E_a}{2}\right) \quad (4.12)$$

Adding v_{cs}^{-} to v_{sy}^{-} yields:

$$v_{cy}^{-} = \frac{V_{dc}}{2} + \left(\frac{L_{bb} - L_{aa} + 2L_{ca} - 2L_{cb}}{2} \right) \left(\frac{di_a}{dt} \right)^{-} + \frac{i_a^{-}}{2} \frac{d\left(L_{bb} - L_{aa} + 2L_{ca} - 2L_{cb} \right)}{dt} - \left(\frac{E_a + E_b - 2E_c}{2} \right) \quad (4.13)$$

Also,

$$\left(\frac{di_a}{dt} \right)^{-} = \frac{\left(-V_{dc} - i_a^{-} \frac{d\left(L_{aa} + L_{bb} - 2L_{ab} \right)}{dt} - E_a + E_b - 2V_t^{-} - 2i_a^{-} R \right)}{\left(L_{aa} + L_{bb} - 2L_{ab} \right)} \quad (4.14)$$

where $2V_t^{-}$ is the total switching device voltage drop. There may be a small difference between V_t^{+} and V_t^{-} because, for example, in the a^+b^- state a pair of inverter transistors may be conducting whereas in b^+a^- state it may be a pair of inverter diodes that carries the phase currents.

In equations (4.7) to (4.14) superscript "+" denotes values sampled while the inverter in the a^+b^- state (t_s^{+} in figure 4.4) whereas the superscript "-" denotes values sampled while the inverter is in the b^+a^- state (t_s^{-} in figure 4.4). If PWM frequency is high enough, say about 20 kHz, and speed is low enough, say one tenth of rated, then it is reasonable to assume that there is negligible change in currents, inductances and back emfs from time t_s^{+} to time t_s^{-}. Therefore no superscripts have been used for those variables.

If the reasonable assumption is made that (V_t^+ - V_t^-) is negligible compared to V_{dc}, it can be deduced from equations (4.9), (4.10), (4.13) and (4.14) that:

$$v_{cy}^+ - v_{cy}^- = V_{dc}\left(\frac{L_{bb} - L_{aa} + 2L_{ca} - 2L_{cb}}{L_{aa} + L_{bb} - 2L_{ab}}\right) \tag{4.15}$$

Equation (4.15) confirms that, independent of all operating and machine parameters, the rotor position at which v_{cy}^+ and v_{cy}^- are equal coincides with the position equal inductance ($L_{aa} = L_{bb}$ and $L_{ca} = L_{cb}$).

Equation (4.15) may be written as:

$$v_{cy}^+ - v_{cy}^- = \frac{V_{dc}\left(\sqrt{3}\left(L_q - L_d\right)\cos\left(2\theta + \frac{5\pi}{6}\right)\right)}{\left(L_q + L_d + (L_q - L_d)\cos\left(2\theta + \frac{\pi}{3}\right)\right)} \tag{4.16}$$

where:

$$L_q = L_{al} + \frac{3}{2}\left(L_{aa0} + L_{g2}\right) \tag{4.17}$$

and

$$L_d = L_{al} + \frac{3}{2}\left(L_{aa0} - L_{g2}\right) \tag{4.18}$$

For reasonable saliency ratios, of around 1.2, a good approximation for ($v_{cy}^+ - v_{cy}^-$) is:

$$v_{cy}^{+} - v_{cy}^{-} = \frac{V_{dc}\left(\sqrt{3}\left(S-1\right)\cos\left(2\theta + \frac{5\pi}{6}\right)\right)}{\left(S+1\right)} \tag{4.19}$$

S is the saliency ratio, which for the purpose of this thesis is defined as $\frac{L_q}{L_d}$. This definition has been adopted because for the machines being considered L_q is greater than L_d.

Similarly:

$$v_{ay}^{+} - v_{ay}^{-} = \frac{V_{dc}\left(\sqrt{3}\left(S-1\right)\cos\left(2\theta - \frac{\pi}{2}\right)\right)}{\left(S+1\right)} \tag{4.20}$$

and

$$v_{by}^{+} - v_{by}^{-} = \frac{V_{dc}\left(\sqrt{3}\left(S-1\right)\cos\left(2\theta + \frac{\pi}{6}\right)\right)}{\left(S+1\right)} \tag{4.21}$$

Assuming a saliency ratio of 1.2 the maximum error in approximating using equation (4.19) instead of equation (4.16) is 2.9%. It is deduced from equation (4.19) (or (4.20) or (4.21)) that the sensitivity and precision of the equal inductance method of pre-determination of commutation instants is dependent only on saliency ratio and the DC supply voltage. Figure 4.5 represents practical confirmation of equations (4.19) to (4.21).

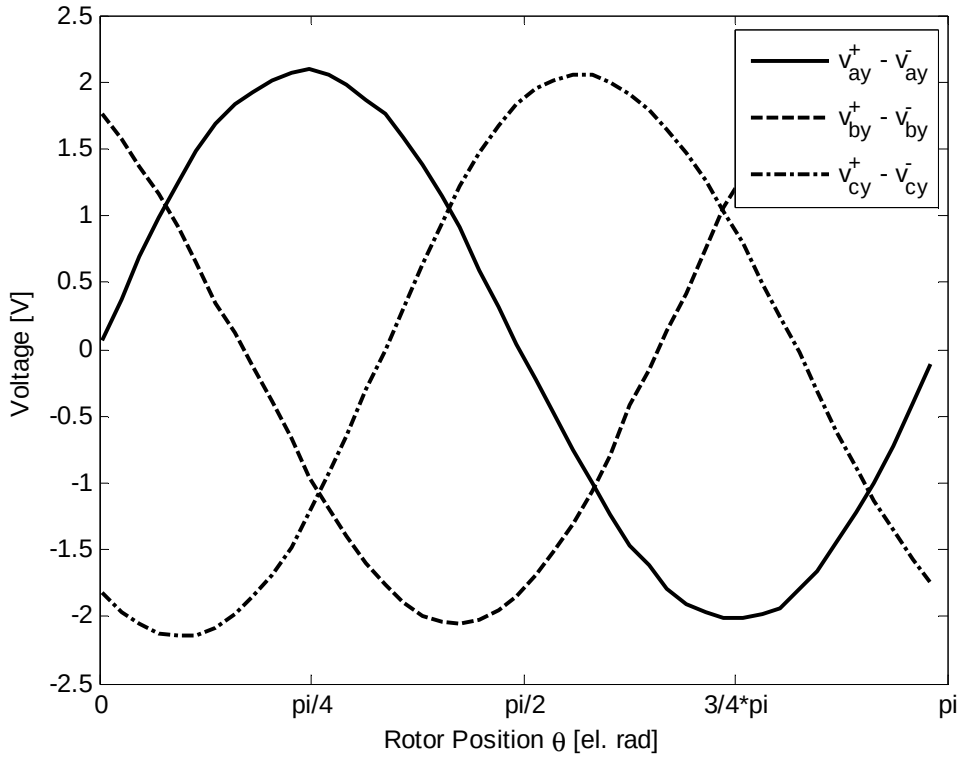

Figure 4.5 : Measured Voltage Differences (eqs 19 - 21)

4.4 Initial Position Detection and Start-Up

Assuming the rotor is initially at standstill, the start-up procedure using the newly proposed sensorless method consists of the following steps:

(a) Determine, by solving any two of equations (4.19) to (4.21), the two possible values for θ_i, the rotor initial position.

(b) Identify the phase pair that on energisation will provide the maximum driving torque.

(c) Energise the selected phase pair until θ_i changes by a small (typically less than one mechanical degree) but measurable amount.

(d) Depending on whether θ_i increased or decreased in step (c), determine the actual value of θ_i .

(e) Use one of equations (4.19) to (4.21) to evaluate P where:

$$P = \frac{V_{dc}\sqrt{3}(S-1)}{(S+1)} \tag{4.22}$$

(f) Identify the phase pair and polarity that will provide maximum driving torque for rotation in the desired direction.

(g) Energise the phase pair identified in step (f) and initiate commutation to the next phase pair when the value of the measured voltage difference (left hand side of equation (4.19) or (4.20) or (4.21)) reaches $\sqrt{3}P/2$.

(h) Activate the normal commutation algorithm straight after initiation of the first commutation event.

Step (a) requires at least two phase pair energisations to be done with 50 percent PWM to avoid rotation. Any two or more of the six possible phase pair combinations could be used. A good strategy would be to use the three pairs and polarities corresponding to equations (4.19) to (4.21) and select two for the determination of θ_i. The third equation can be used for verification purposes. If, for example, equations (4.19) and (4.20) were chosen to determine the rotor initial position θ_i, then we have:

$$\theta_d = \tan^{-1}(P_s / P_c) \tag{4.23}$$

where:

$$\begin{pmatrix} P_s \\ P_c \end{pmatrix} = \begin{pmatrix} P\sin(2\theta_i) \\ P\cos(2\theta_i) \end{pmatrix} = \begin{pmatrix} -1/2 & -\sqrt{3/2} \\ 1 & 0 \end{pmatrix}^{-1} \begin{pmatrix} v_{cy}^{+} - v_{cy}^{-} \\ v_{ay}^{+} - v_{ay}^{-} \end{pmatrix} \tag{4.24}$$

In applying equations (4.19) to (4.24) together with measured voltage differences ($v_{cy}^{+} - v_{cy}^{-}$) and ($v_{ay}^{+} - v_{ay}^{-}$), a unique value for θ_d is obtained in the zero to 360 electrical degree range. The initial rotor position θ_i, however is either equal to $\theta_d / 2$ or $\theta_d / 2$ plus 180 electrical degrees. The purpose of steps (b), (c) and (d), listed above, is to determine whether θ_i is equal to $\theta_d / 2$ or to $(\theta_d + 2\pi)/2$. The phase pair combination to be selected in step (b) should be according to the following:

CA if $0^\circ \leq \theta_d / 2 \leq 60^\circ$;

CB if $60^\circ \leq \theta_d / 2 \leq 120^\circ$; and

AB if $120^\circ \leq \theta_d / 2 \leq 180^\circ$.

During step (c) the PWM duty ratio is deviated from 50% just enough to allow a small but measurable change in θ. If θ increases then it can be deduced that $\theta_i = \theta_d / 2$ otherwise it is concluded that $\theta_i = (\theta_d + 2\pi)/2$.

Step (f) is about choosing the optimum phase pair for initial movement in the right direction. This can be done according to table 4.1. For example, if the motor initial position is between 60° and 120° and backward rotation was desired, then the phase pair to be energised should be

BC. After the first commutation event, performed according to step (g) above, subsequent commutation control is carried out by executing the algorithm in figure 4.6.

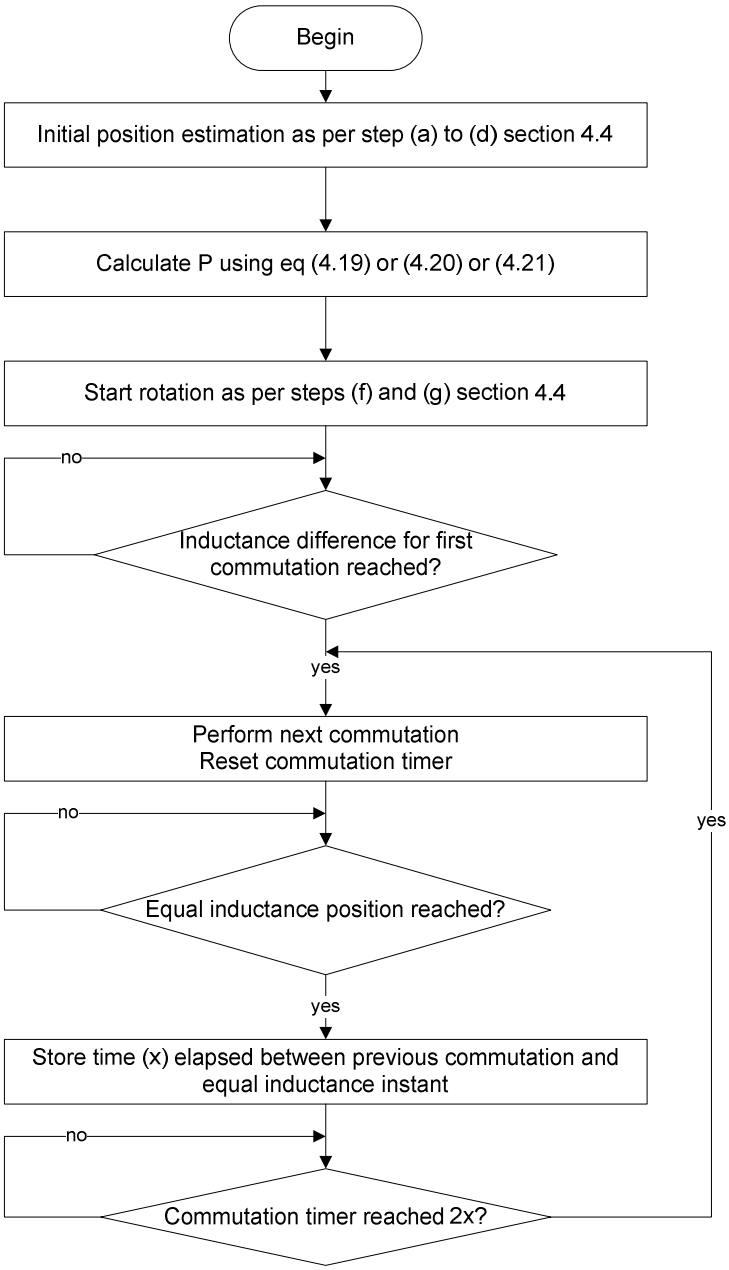

Figure 4.6: Commutation Algorithm Based on the Equal Inductance Method

4.5 Test Results

BLDC commutation based on the equal inductance method was implemented and tested using an 8 pole 12V / 2A motor (rated speed 2400 rpm). The commutation algorithm was implemented using the 56F8013 digital signal controller.

As shown in figure 4.7(b) there is good agreement between the standstill rotor positions deduced by solving two of equations (4.19) to (4.21) (shown in figure 4.7(a)) and the actual rotor position. This is in spite of the existence of a small imbalance in phase inductances. The maximum deviation between actual position and estimated position was found to be 1.4 electrical degrees.

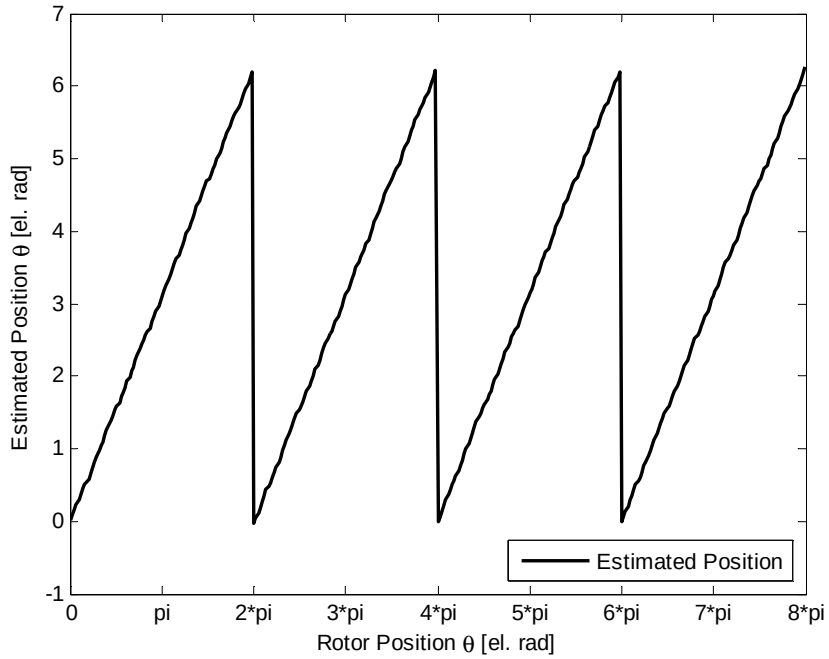

Figure 4.7(a) : Estimated Rotor Position (360° Mechanical)

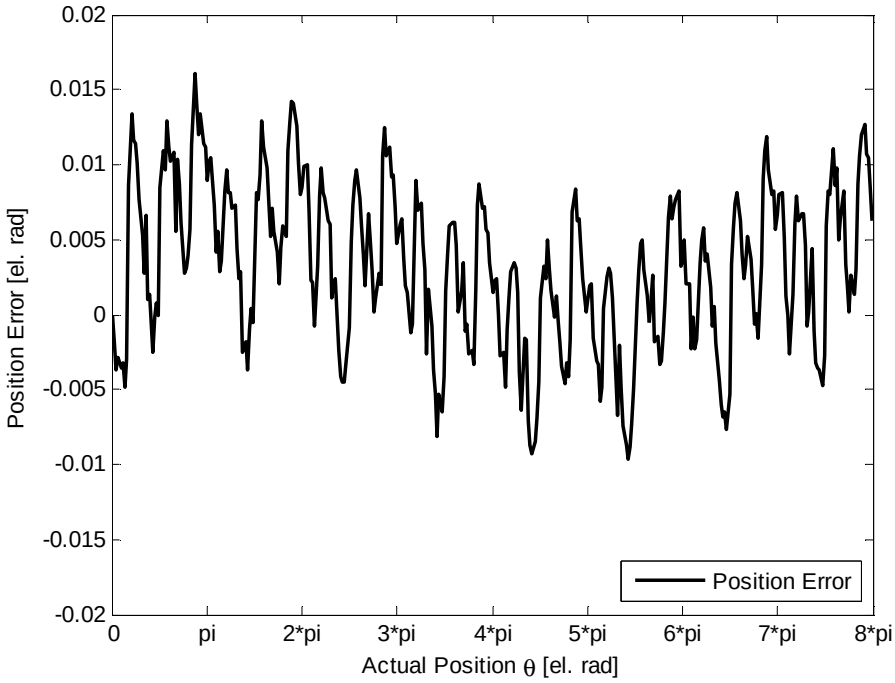

Figure 4.7(b) : Position Error (360° Mechanical)

Figure 4.8 shows oscillograms of phase A voltage (v_{ay}), phase A current, the *equal inductance flag* and the *commutation flag*. The control software operates such that the *equal inductance flag* changes state whenever the rotor passes through a position where the energised phases have equal inductances. Thus, as expected, the *equal inductance flag* changes state every 60 electrical degrees. By design the *commutation flag* lags the equal inductance flag by 30 electrical degrees. The waveforms in figure 4.8 confirm correct commutations since commutation events occur every sixty electrical degrees and disturbance of the non-commutating phase current is small. Figure 4.9 confirms that the equal inductance method works well at higher current and higher speed. Please note that the presented waveforms sequence (in figure 4.8 and 4.9) is identical to the legend entries sequence.

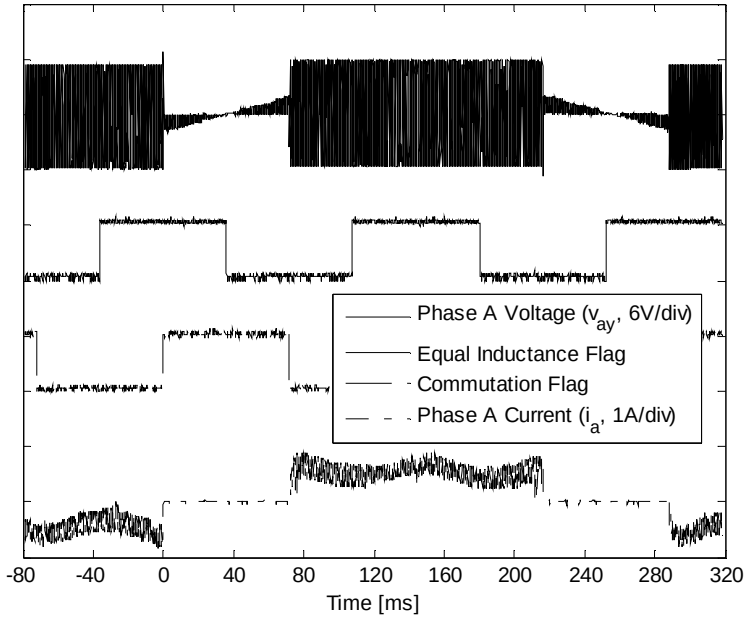

Figure 4.8 : BLDC Commutation using the Equal Inductance Method (139 r/min)

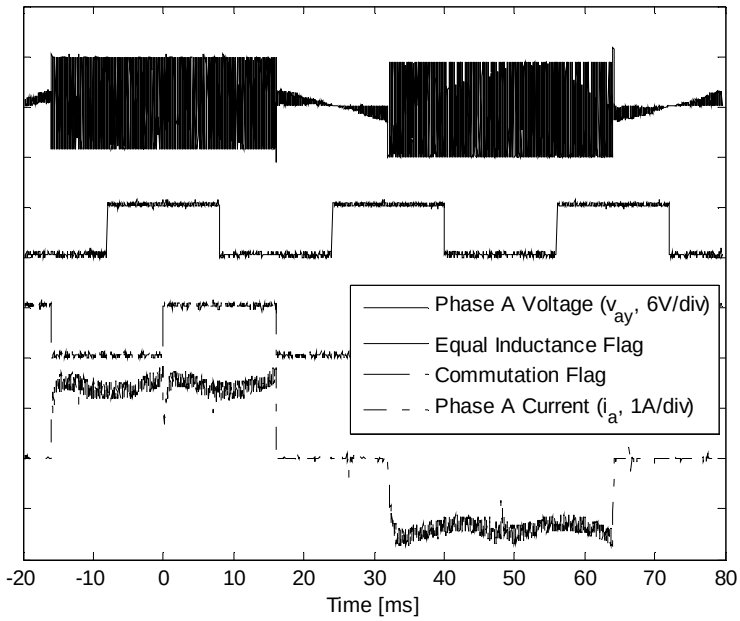

Figure 4.9 : BLDC Commutation using the Equal Inductance Method (630 r/min)

The equal inductance method is used to pre-determine all commutation instants except the first one. The *first commutation flag*, displayed in figure 4.10, is set when the voltage difference (left hand side of equation (4.19) or (4.20) or (4.21)) reaches the pre-calculated value of $\sqrt{3}P/2$. The test results in figure 4.10 confirm correct operation of the proposed starting method since the timing of the instant of the first commutation event determined by the *first commutation flag* is consistent with the timing of subsequent commutation event which are determined by the normal *commutation flag*.

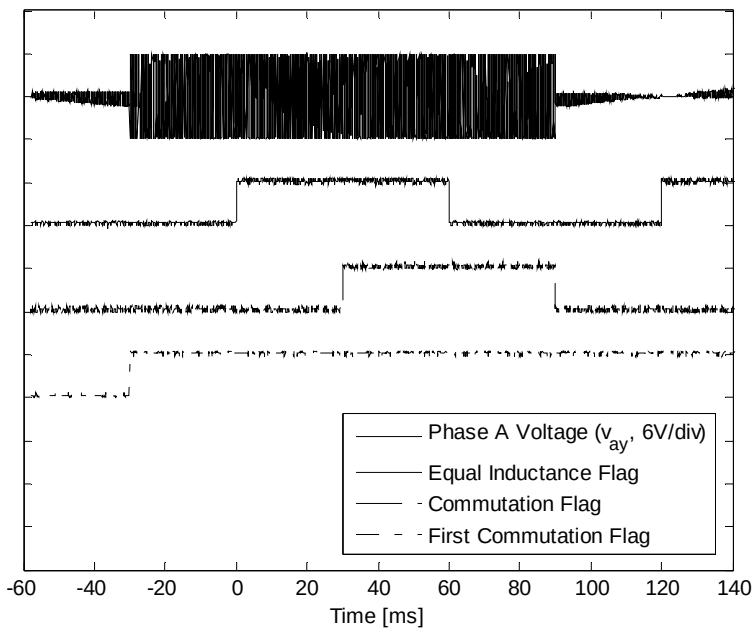

Figure 4.10 : First Commutation Event

4.6 **Discussion**

Performance of the *equal inductance method* is best near zero speed since both positive and negative PWM voltage pulses applied to the active phase pair are relatively wide. Under those conditions, there is sufficient time for transients to settle before measurements are made. Also there is sufficient time to perform computations. However, as speed rises either the positive voltage pulse or the negative pulse within a PWM cycle becomes shorter and eventually there may not be sufficient time for transients [3] to settle and for calculations to be performed. Thus there exists an upper limit of satisfactory performance of the *equal inductance method*. It is not possible to arrive at a general conclusion regarding this limit. It depends on supply voltage, saliency, resolution and speed of the selected digital signal processor and the effect of switching noise. With a saliency ratio of 1.1 or more, 12V DC supply and a low cost DSP with 8-bit resolution, it is estimated that performance as good as that obtained with the back EMF zero crossing is achievable at about 25% of full speed. Well above that speed the back EMF method is better, whereas well below that speed the equal inductance method gives superior performance. Thus the *equal inductance method* complements the back EMF very well.

The *equal inductance method* is based on voltage measurements made as voltage pulses are applied to active winding pairs during bipolar operation. There is no practical advantage in adapting the method to unipolar operation. With unipolar operation, correct measurement at very low speed is not possible because the voltage pulse width is too short. Thus adapting the *equal inductance method* to unipolar operation will not result in a technique that complements the back

EMF zero crossing method. If unipolar operation is preferred for normal motor operation, it is recommended that the motor is started under bipolar operation and the *equal inductance method* up to a minimum speed. Above that speed, operation can be changed to unipolar with back EMF zero crossings used to determine commutation instants.

The *equal inductance method* has been found to perform very well with motors having surface inserted magnets. However, the method can be considered for motors with fully buried magnets. Qualitative analysis suggests that these motors would exhibit inductive saliency due to the cumulative effects of rotor geometry and eddy currents induced in their permanent magnets.

4.7 **Conclusion**

A low cost saliency based sensorless technique for BLDC motors has been proposed, physically implemented and tested. It offers performance that is equal to that obtained by systems relying on low resolution physical devices such as Hall sensors. Rotor position is deduced from the response of the BLDC motor un-energised phase terminal voltage, measured with respect to the negative DC supply rail, due to bipolar PWM voltage pulses that are normally applied to the other two phases. Theoretical analysis shows that this potential difference is made up of a DC component equal to the sum of half the DC supply voltage and the un-energised phase back EMF plus an AC component (non-sinusoidal) that is modulated by the rotor movement. In other words the peak to peak value of the AC component varies as rotor position changes. The fundamental frequency of the AC component is equal to the PWM frequency. The envelope of

that AC component is represented by the waveforms of figure 4.5. It was found, from the theoretical investigation, that a zero peak to peak value of the AC component corresponds to a rotor position that is thirty electrical degrees away from the next ideal commutation position. That rotor position is also the one where the energized phase windings have equal inductances. Hence the adopted sensorless commutation control method has been termed the 'equal inductance method'. Further theoretical analysis showed that the peak to peak value of the AC component depends only on the DC supply voltage and the saliency ratio. In other words the position of equal inductance deduced from voltage measurements at the un-energised phase terminal is insensitive to operational parameters such as load current and circuit parameters such as winding resistance.

It has been demonstrated that with sufficient saliency, standstill rotor position can be determined from the same measurements made to determine positions of equal inductance. The necessary phase winding energisations during those measurements may lead to some back-rotation. But this has been found to be less than a mechanical degree and is therefore considered negligible. Once the initial rotor position has been determined, the optimum phase pair to be energised can be selected. Voltage measurements allow the rotor position for the first commutation event to be identified, subsequent commutation instants being pre-determined by the 'equal inductance method'.

The back EMF method of commutation control relies on detection of zero-crossing instants of the back EMF signal from the unenergised phase. It has been shown that the instant at which the rotor reaches the equal inductance position coincides with the zero-crossing instant of the back

EMF of the unenergised phase. There is, therefore, a close parallel between the equal inductance method and the back EMF method. For operation over a wide speed range it may be advantageous to operate using the equal inductance method at low speed and the back EMF method at high speed. The close parallel between the two methods makes it easy to implement changeover strategies from one to the other as the motor speed crosses the chosen boundary between low speed and high speed operation.

As pointed out in section 2.1.2 other researchers have used saliency as a basis for rotor position detection. However, the literature review carried out the author revealed that all techniques proposed before this thesis project were based on explicit injection of signals for the purpose of using saliency to determine rotor position. In contrast the new method proposed in this dissertation relies on information extracted from the normal currents and voltages of the motor.

In summary the *'equal inductance method'* is easy to implement, is very cost competitive and offers commutation and starting performance equal to that obtained with Hall sensors. Also, its close parallel with the back EMF method allows seamless changeover to that method at high speeds.

Chapter 5

Sensorless Commutation of Printed Circuit Brushless DC Motors

5.1 Introduction

The technique proposed in chapter 4 termed the ‘equal inductance method’ offers commutation control and starting performance equal to that obtained when using Hall sensors. However, the method applies to nominally symmetrical machines with high enough phase winding time constants. This chapter is about sensorless commutation of a class of motors which is characterized by significant asymmetry and relatively low phase winding time constants. The motors in question are axial flux machines with iron-less stators that may be wound or made up of printed circuits. The basic reason for the asymmetry is that the three stator phases are stacked

with each one of them located at a different axial distance from the rotor. The low phase time constant is due to the iron-less nature of the stator. The focus in this chapter is on the printed circuit version of the motor. A new sensorless commutation technique has been developed, which is effectively a generalization of the originally proposed equal inductance method. The theoretical basis behind the technique and practical results demonstrating its effectiveness are presented.

5.2 Characteristics of Test Motors

As illustrated in chapter 3, figure 3.6, the test machines used for this thesis project had each phase winding on separate substrates. On each substrate there is a multilayer printed circuit which is essentially a set of spirally wound coils forming one phase of the stator.

The three substrates are nominally identical. However the magnetic axes of each substrate are displaced from those of the other substrates by 120 electrical degrees. Details of typical printed circuit stators were provided in chapter 3.

Two different test motors with identical rotors were used. They were both of four-pole construction. Each substrate of both motors was made up of 8 winding layers. For test motor 1, the spirally wound coils were arranged so that they formed two series connected groups, each group made up of the parallel connection of half the total number of coils. For test motor 2, the coils were arranged so that they formed two parallel connected groups, each group made up of the series connection of half of the total number of coils. Thus, although the two test motors had

practically the same winding time constant, the inductance and resistance of test motor 2 were higher by a factor of approximately 4. Phase resistances of motors 1 and two were, respectively, 0.089 ohm and 0.362 ohm.

Motor inductance characteristics are of primary importance to the sensorless method being considered. Figures 5.1 and 5.2 respectively show measured self and mutual inductances of motor 2. As expected the self-inductance of the sandwiched or middle phase, which is phase *b* is different from the self inductance of the other two phases. The two outer phases, that is phase *a* and phase *c*, have the practically equal self–inductances. The inductances of test motor 1 behave similarly, except as expected they are significantly smaller. As will be explained later motor 2 turned out to be a better choice because of its higher inductance. Hence it was used for most of the subsequent tests that were carried out.

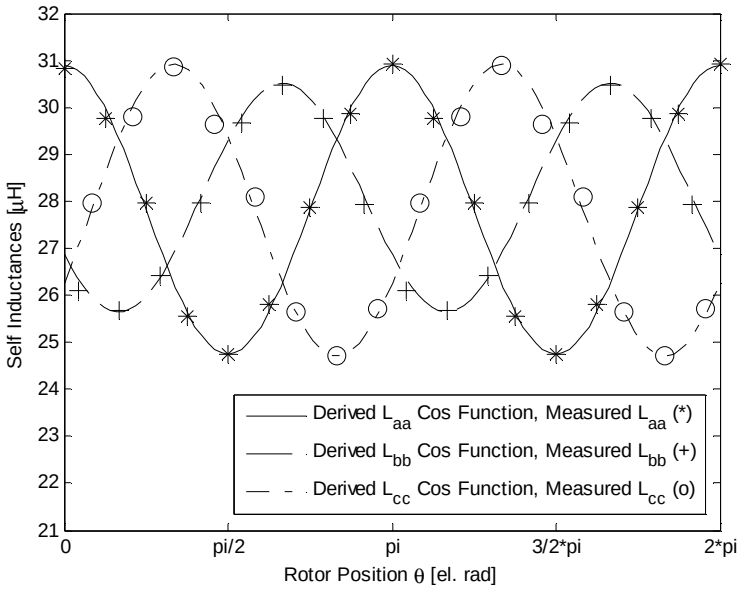

Figure 5.1 : Self-inductances of Test Motor 2

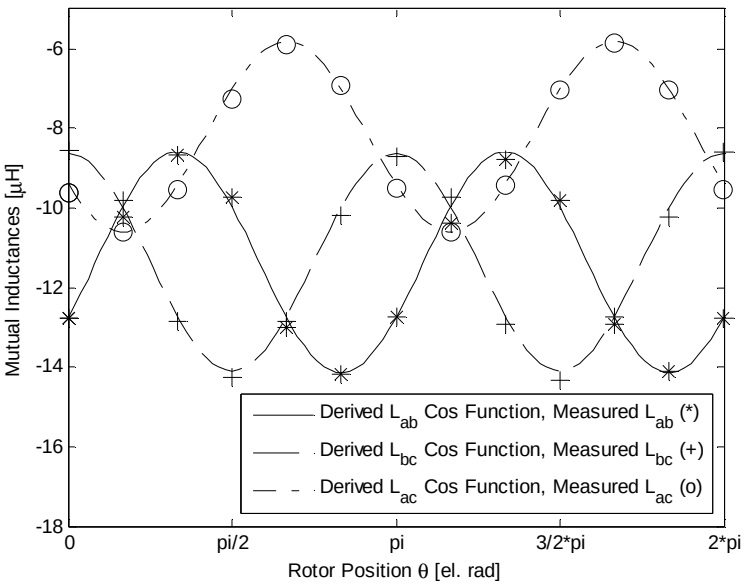

Figure 5.2 : Mutual-inductances of Test Motor 2

Each set of three phase measurements of self and mutual inductances were taken for a fixed rotor position relative to the magnetic axis of phase *a*. A small sinusoidal current (50mA @ 20kHz) was injected into one phase while the other two phases were left open-circuited. The injected current and the three line to star-point voltages were recorded. From the measurements, effective self-inductances and mutual inductances were evaluated. As stated in chapter 3, it should be pointed out that the self-inductances and the mutual inductances are only effective values rather than actual values because they incorporate the effect of eddy-currents in permanent magnets and the rotor iron.

Electrical machines that exhibit saliency and that are symmetrical may be analyzed using the well established two-axis theory. Equations (5.1) to (5.6) below are modified versions of the

classical equations that are based on the two-axis theory. The modifications allow for the asymmetry that is characteristic of the class of machines under consideration. The terms ΔL_{s2}, ΔL_{s0}, ΔL_{m0} and ΔL_{m2} that appear in the equations represent the necessary modifications. For test motor 2, in µH, L_{s0}=27.82; L_{s2}=3.08; ΔL_{s0}=0.27; ΔL_{s2}=6.46; L_{m0}=1.14; L_{m2}=2.76; ΔL_{m0}=3.15 and ΔL_{m2}=0.36.

$$L_{aa} = L_{s0} + L_{s2}\cos(2\theta) \tag{5.1}$$

$$L_{bb} = (L_{s0} + \Delta L_{s0}) + (L_{s2} - \Delta L_{s2})\cos\left(2\theta + \frac{2\pi}{3}\right) \tag{5.2}$$

$$L_{cc} = L_{s0} + L_{s2}\cos\left(2\theta - \frac{2\pi}{3}\right) \tag{5.3}$$

$$L_{ab} = L_{ba} = -L_{m0} + L_{m2}\cos\left(2\theta - \frac{2\pi}{3}\right) \tag{5.4}$$

$$L_{bc} = L_{cb} = -L_{m0} + L_{m2}\cos(2\theta) \tag{5.5}$$

$$L_{ca} = L_{ac} = -(L_{m0} - \Delta L_{m0}) + (L_{m2} - \Delta L_{m2})\cos\left(2\theta + \frac{2\pi}{3}\right) \tag{5.6}$$

5.3 Determination of commutation positions

Figure 5.3 represents the printed windings of a BLDC motor connected to a three-phase bridge. The commutation intervals are defined in table 5.1. The rotor is considered to be at zero angular

position when its q-axis lines up with the magnetic axis of stator phase *a*. The d-axis of the rotor coincides with the magnetic axis of its permanent magnet.

During normal operation the inverter transistors are switched in turn so that the phase windings are energised cyclically in accordance to table 5.1. For commutation interval AB, for example, transistors T_A^+, T_A^-, T_B^+ and T_B^- will be pulse width modulated whereas transistors T_C^+ and T_C^- will be kept off.

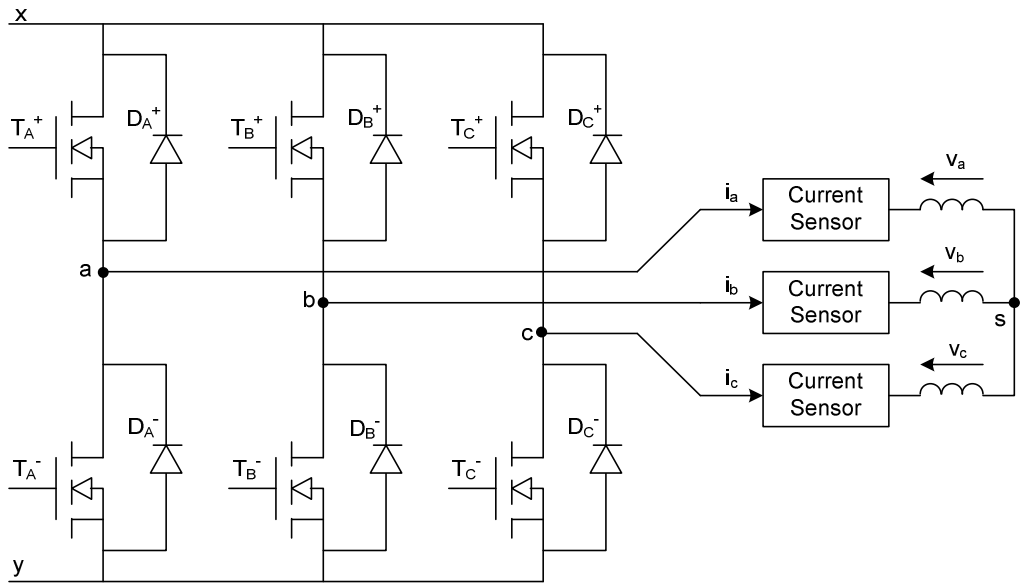

Figure 5.3 : Inverter Bridge and Stator Winding

Table 5.1 : Commutation Intervals

Rotor position range (electrical radians)	0 to π/3	π/3 to 2π/3	2π/3 to π	π to 4π/3	4π/3 to 5π/3	5π/3 to 2π
Energised phase pair	CA	CB	AB	AC	BC	BA

As for the equal inductance method presented in chapter 4, bipolar pulse width modulation (PWM) is assumed. The selected PWM frequency was 20 kHz. This means that a relatively large number of PWM cycles fits into one commutation interval. During interval AB, T_A^+ and T_B^- are normally turned on for a longer portion of the PWM period to achieve a positive average for v_{ab}. Conversely during interval BA, T_A^- and T_B^+ are normally turned on for a larger portion of the PWM period to achieve a negative average value for v_{ab}. Voltage v_{ab} is defined in figure 5.4. Assuming conduction takes place through two legs of the inverter, there would be six states that the inverter could be in. These are labelled a^+b^-, b^+a^-, b^+c^- and c^+b^-, c^+a^- and a^+c^-. For example during state a^+b^-, transistors T_A^+ and T_B^- are turned on. Figure 5.4 shows the motor equivalent circuits for inverter states a^+b^- and b^+a^-.

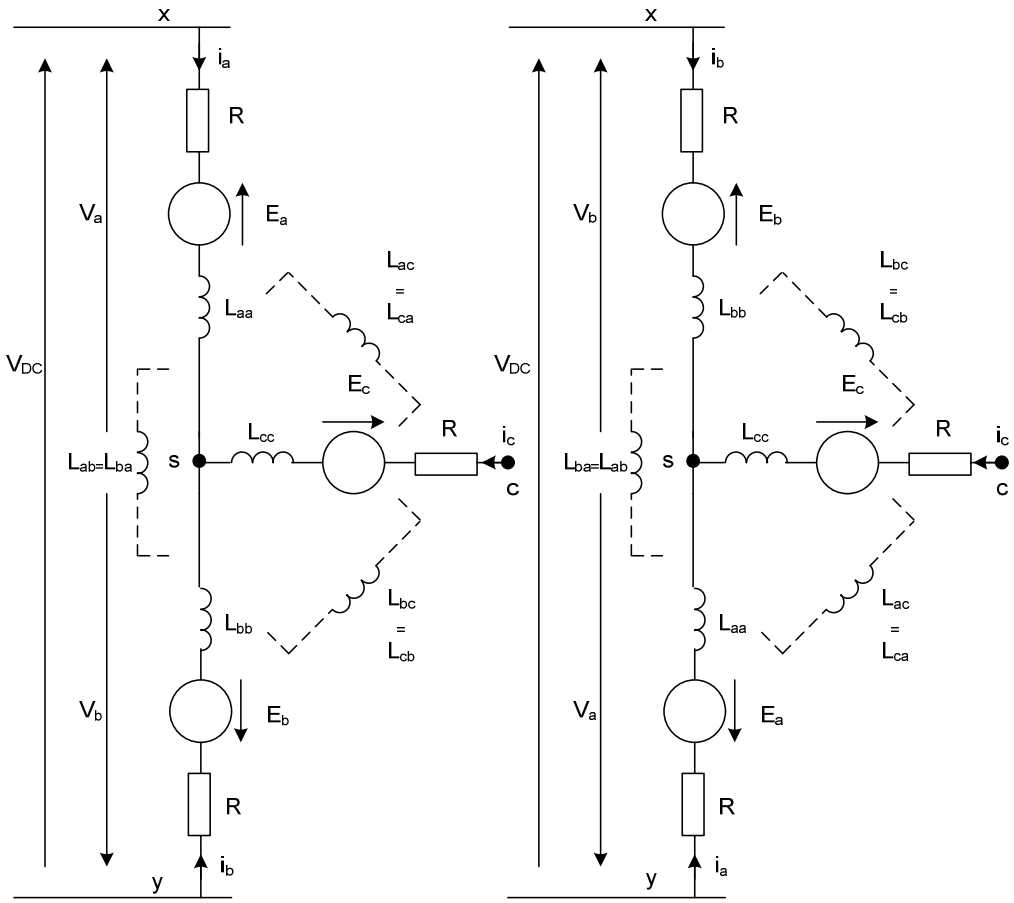

$v_{ab} = v_a - v_b$

Figure 5.4 : Equivalent Circuits for Inverter States a^+b^- and b^+a^-

(Switching Device Voltage Drop not shown)

It can be shown [11] that during inverter state a^+b^-:

$$v_{cy}{}^{+} = \frac{v_{dc}}{2} + \left(\frac{L_{bb} - L_{aa} + 2L_{ca} - 2L_{cb}}{2}\right)\left(\frac{di_a}{dt}\right)^{+} + \frac{i_a{}^{+}}{2}\,\frac{d\left(L_{bb} - L_{aa} + 2L_{ca} - 2L_{cb}\right)}{dt} - \left(\frac{E_a + E_b - 2E_c}{2}\right) \tag{5.7}$$

$$\left(\frac{di_a}{dt}\right)^{+} = \frac{\left(v_{dc} - i_a^{+}\frac{d\left(L_{aa}+L_{bb}-2L_{ab}\right)}{dt} - E_a + E_b - 2v_t^{+} - 2i_a^{+}R\right)}{\left(L_{aa}+L_{bb}-2L_{ab}\right)} \tag{5.8}$$

Similarly during inverter state $b^{+}a^{-}$:

$$v_{cy}^{-} = \frac{v_{dc}}{2} + \left(\frac{L_{bb}-L_{aa}+2L_{ca}-2L_{cb}}{2}\right)\left(\frac{di_a}{dt}\right)^{-} + \frac{i_a^{-}}{2}\frac{d\left(L_{bb}-L_{aa}+2L_{ca}-2L_{cb}\right)}{dt} - \left(\frac{E_a+E_b-2E_c}{2}\right) \tag{5.9}$$

$$\left(\frac{di_a}{dt}\right)^{-} = \frac{\left(-v_{dc} - i_a^{-}\frac{d\left(L_{aa}+L_{bb}-2L_{ab}\right)}{dt} - E_a + E_b - 2v_t^{-} - 2i_a^{-}R\right)}{\left(L_{aa}+L_{bb}-2L_{ab}\right)} \tag{5.10}$$

In equations (5.7) to (5.10), superscript '+' denotes values sampled while the inverter is in state $a^{+}b^{-}$whereas superscript '-' denotes values sampled while the inverter is in state $b^{+}a^{-}$. The values of currents and voltages referred to in equations (5.7) to (5.10) are sampled within a single PWM cycle. Total switching device voltage drop is denoted by $2v_t^{+}$ for inverter state $a^{+}b^{-}$ and by $2v_t^{-}$ for inverter state $b^{+}a^{-}$. It is reasonable to assume that rotational back EMFs E_a, E_b and E_c remain unchanged during a PWM cycle.

If, as shown in figure 5.5, voltage is sampled at the same level of winding current during inverter state $a^{+}b^{-}$ and $b^{+}a^{-}$, we can deduce, from equation (5.7) to (5.10), that:

$$v_{cy}^{+} - v_{cy}^{-} = v_{dc}\left(\frac{L_{bb}-L_{aa}+2L_{ca}-2L_{cb}}{L_{aa}+L_{bb}-2L_{ab}}\right) \tag{5.11}$$

$$v_{cy}^{+} - v_{cy}^{-} = \frac{v_{dc}\left[\left(\Delta L_{so} + 2\Delta L_{mo}\right) + \sqrt{3}\left(L_{s2} + 2L_{m2}\right)\cos\left(2\theta + \frac{5\pi}{6}\right) - \left(\Delta L_{s2} + 2\Delta L_{m2}\right)\cos\left(2\theta + \frac{2\pi}{3}\right)\right]}{\left[\left(2L_{s0} + 2L_{m0} + \Delta L_{s0}\right) + \left(L_{s2} + 2L_{m2}\right)\cos\left(2\theta + \frac{\pi}{3}\right) - \Delta L_{s2}\cos\left(2\theta + \frac{2\pi}{3}\right)\right]} \quad (5.12)$$

Equation (5.11) is based on the reasonable assumption that $|v_t^+ - v_t^-|$ is much smaller than v_{dc}. Also inspection of equation (5.7) and (5.10) reveals that, theoretically, making i_a^+ equal to i_a^- results in complete insensitivity of the measured voltage difference to phase resistance.

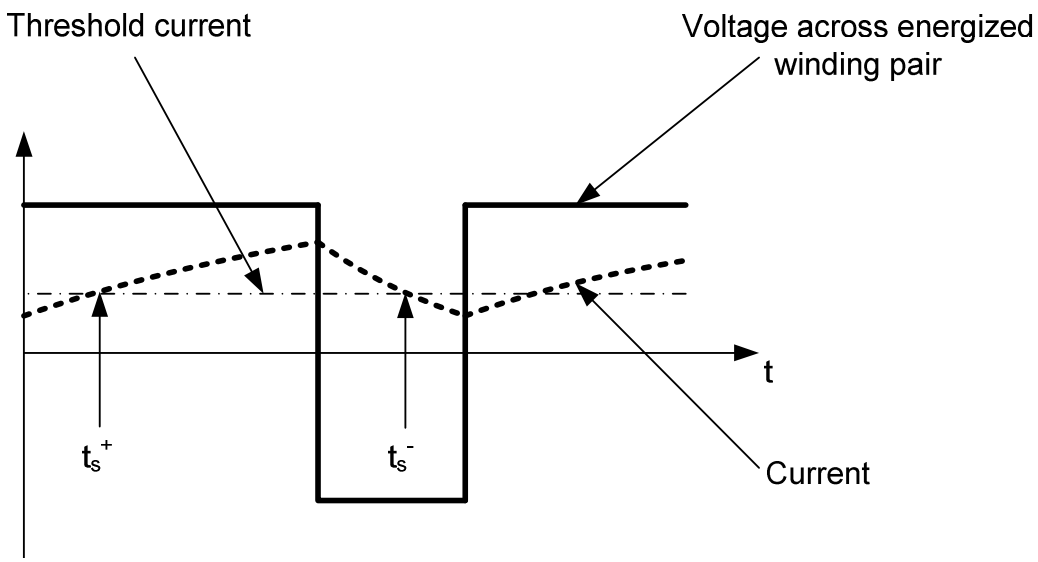

Figure 5.5 : Voltage Sampling Instants (t_s^+ and t_s^-)

Figure 5.5 illustrates the fundamental difference between the equal inductance method introduced in chapter 4, and the method proposed in this chapter. Voltage v_{cy} is first sampled at time instant t_s^+ during inverter state a^+b^-. The current i_a^+, also sampled at t_s^+, is termed the threshold current. In practice, to avoid errors associated with ringing caused by parasitic

capacitances and inductances, t_s^+ must be sufficiently delayed from the instant that the inverter changes state. Voltage v_{cy} is then sampled at t_s^-, at which instant current i_a must be equal to the threshold value recorded at t_s^+. In contrast, with the equal inductance method, t_s^+ and t_s^- were chosen to be in the middle of the applied voltage pulses, the implicit assumption being that the winding current was practically equal at those two instants. This assumption is only true if the winding time constant is long compared with the PWM period.

In practice identification of t_s^- is carried out by continuous sampling of v_{cy} and the winding current before the latter crosses the threshold current. Each current sample is compared with the threshold current. When the sampled current goes below the threshold current, sampling is stopped, t_s^- is deemed to have been identified and v_{cy}^- is taken to be equal to the average of the last two samples of v_{cy}.

While equations (5.11) and (5.12) are applicable when phase *c* is idle, equations (5.13) and (5.14) apply when phase *a* is idle and equations (5.15) and (5.16) apply when phase *b* is idle.

$$v_{ay}^{+} - v_{ay}^{-} = v_{dc}\left(\frac{L_{cc} - L_{bb} + 2L_{ab} - 2L_{ac}}{L_{bb} + L_{cc} - 2L_{bc}}\right) \tag{5.13}$$

$$v_{ay}^{+} - v_{ay}^{-} = \frac{v_{dc}\left[\left(-\Delta L_{so} - 2\Delta L_{mo}\right) + \sqrt{3}\left(L_{s2} + 2L_{m2}\right)\cos\left(2\theta - \frac{\pi}{2}\right) + \left(\Delta L_{s2} + 2\Delta L_{m2}\right)\cos\left(2\theta + \frac{2\pi}{3}\right)\right]}{\left[\left(2L_{s0} + 2L_{m0} + \Delta L_{s0}\right) - \left(L_{s2} + 2L_{m2}\right)\cos\left(2\theta\right) - \Delta L_{s2}\cos\left(2\theta + \frac{2\pi}{3}\right)\right]} \tag{5.14}$$

$$v_{by}^{+} - v_{by}^{-} = v_{dc}\left(\frac{L_{aa} - L_{cc} + 2L_{bc} - 2L_{ba}}{L_{cc} + L_{aa} - 2L_{ca}}\right) \tag{5.15}$$

$$v_{by}^{+} - v_{by}^{-} = \frac{v_{dc}\sqrt{3}\left(L_{s2} + 2L_{m2}\right)\cos\left(2\theta + \frac{\pi}{6}\right)}{\left[\left(2L_{s0} + 2L_{m0} - 2\Delta L_{m0}\right) + \left(L_{s2} + 2L_{m2} - 2\Delta L_{m2}\right)\cos\left(2\theta - \frac{\pi}{3}\right)\right]} \tag{5.16}$$

It is now shown that there are unique relationships between the phase voltage differences defined by equations (5.12), (5.14) and (5.16) and the commutation positions given in figure 5.6.

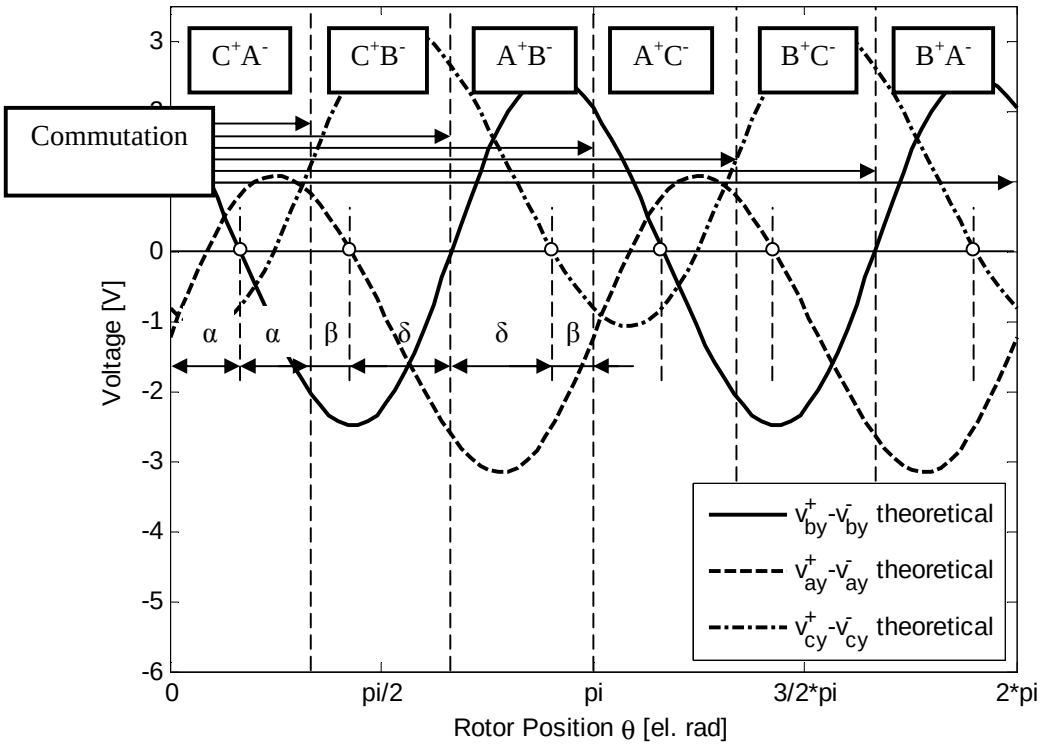

Figure 5.6 : Relationship between Voltage Zero Crossings and Commutation Positions

Equation (5.16) will be considered first. With v_{by}^{+} equal to v_{by}^{-} we have:

$$\cos\left(2\theta + \frac{\pi}{6}\right) = 0 \tag{5.17}$$

Within the range from 0° to 360°, the solutions to equation (5.17) are 30°, 120°, 210° and 300°. Those four solutions appear in figure 5.6. It is clear that two of the solutions, θ=120° and θ=300°, are not applicable to the detection of the commutation instant because at these positions v_{by} is not being measured. On the other hand, as shown in figure 5.6, v_{by} is being measured during commutation intervals CA or AC. The points at which v_{by}^{+} equals v_{by}^{-} occur in the middle of those intervals respectively at θ=30° and at θ=210°. This means that by monitoring the voltage of the b-phase while the other two phases are energised, the next commutation instants can be determined. It is clear from figure 5.6 that if the motor is going through commutation interval CA and AC, the next commutation position is thirty electrical degrees away from the position when (v_{by}^{+} - v_{by}^{-}) is equal to zero. It is interesting to note that the position at which v_{by}^{+} is equal to v_{by}^{-} is also the position where L_{aa} is equal to L_{cc}. This is due to the fact that the middle phase, which is the b-phase, is symmetrically positioned relative to the other two phase windings. So detection of commutation positions while outer phases a and c are energised resembles the standard equal inductance method (chapter 4).

Determination of commutation positions at the end of commutation intervals AB and BA is based on the solution to equation (5.12). Samples of voltage v_{cy} are taken until v_{cy}^{+} is found to be equal to v_{cy}^{-}. Under that condition equation (5.12) reduces to:

$$\left(\Delta L_{so}+2\Delta L_{mo}\right)+\sqrt{3}\left(L_{s2}+2L_{m2}\right)\cos\left(2\theta+\frac{5\pi}{6}\right)-\left(\Delta L_{s2}+2\Delta L_{m2}\right)\cos\left(2\theta+\frac{2\pi}{3}\right)=0 \qquad (5.18)$$

The solution to equation (5.18) is given by:

$$\theta = \delta = \frac{\sin^{-1}\left(\dfrac{\left(-\Delta L_{so} - 2\Delta L_{mo}\right)}{\sqrt{\left(\sqrt{3}\left(\dfrac{-\left(L_{s2}+2L_{m2}\right)+\left(\Delta L_{s2}+2\Delta L_{m2}\right)}{2}\right)\right)^2 + \left(\dfrac{-3\left(L_{s2}+2L_{m2}\right)+\left(\Delta L_{s2}+2\Delta L_{m2}\right)}{2}\right)^2}}\right)}{2} - \frac{\tan^{-1}\left(\dfrac{\left(\dfrac{-3\left(L_{s2}+2L_{m2}\right)+\left(\Delta L_{s2}+2\Delta L_{m2}\right)}{2}\right)}{\left(\sqrt{3}\left(\dfrac{-\left(L_{s2}+2L_{m2}\right)+\left(\Delta L_{s2}+2\Delta L_{m2}\right)}{2}\right)\right)}\right)}{2} \tag{5.19}$$

Similarly determination of commutation positions at the end of commutation intervals CB or BC is based on the solution to equation (5.14). Samples of voltage v_{ay} are taken until v_{ay}^{+} is found to be equal to v_{ay}^{-}. Under that condition equation (5.14) reduces to:

$$\left(-\Delta L_{so} - 2\Delta L_{mo}\right) + \sqrt{3}\left(L_{s2}+2L_{m2}\right)\cos\left(2\theta - \frac{\pi}{2}\right) + \left(\Delta L_{s2}+2\Delta L_{m2}\right)\cos\left(2\theta + \frac{2\pi}{3}\right) = 0 \tag{5.20}$$

The solution to equation (5.20) is given by:

$$\theta = \beta = \frac{\sin^{-1}\left(\dfrac{\left(+\Delta L_{so} + 2\Delta L_{mo}\right)}{\sqrt{\left(\sqrt{3}\left(\left(L_{s2} + 2L_{m2}\right) - \dfrac{\left(\Delta L_{s2} + 2\Delta L_{m2}\right)}{2}\right)\right)^2 + \left(-\dfrac{\left(\Delta L_{s2} + 2\Delta L_{m2}\right)}{2}\right)^2}}\right)}{2} - \frac{\tan^{-1}\left(\dfrac{-\dfrac{\left(\Delta L_{s2} + 2\Delta L_{m2}\right)}{2}}{\left(\sqrt{3}\left(\left(L_{s2} + 2L_{m2}\right) - \dfrac{\left(\Delta L_{s2} + 2\Delta L_{m2}\right)}{2}\right)\right)}\right)}{2} \tag{5.21}$$

The angular positions at which equations (5.18) and (5.20) are satisfied are shown on figure 5.6. Equations (5.19) and (5.21) emphasize that those positions are independent of operating conditions. Since the positions at which equations (5.18) and (5.20) are satisfied are fixed, measurements of v_{ay} and v_{cy} can be used to determine commutation positions. Referring to figure 5.6, during commutation interval AB or BA, the commutation controller can be programmed to carry out the next commutation ($\Pi/3 - \delta$) or β radians from the instant when equation (5.18) is satisfied. Similarly during interval BC or CB, the commutation controller can be programmed to carry out the next commutation ($\Pi/3 - \beta$) or δ radians from the instant when equation (5.20) is satisfied.

5.4 Initial Position Detection

Determination of initial position by the equal inductance method (presented in chapter 4) is entirely based on on-line measurements. The controller does not have to rely on stored motor data. However a basic assumption is that motor is symmetrical. In the case of a motor that is not symmetrical it is impossible to determine the initial rotor position solely from measured voltages such as those defined by equations (5.12), (5.14) and (5.16). One solution to the problem is to pre-load five motor constants into the controller memory.

These are:

$$k_1 = \frac{\sqrt{3}\left(L_{s2} + 2L_{m2}\right)}{\left(2L_{s0} + 2L_{m0} - 2\Delta L_{m0}\right)}; \tag{5.22}$$

$$k_2 = \frac{\sqrt{3}\left(L_{s2} + 2L_{m2}\right)}{\left(2L_{s0} + 2L_{m0} + \Delta L_{s0}\right)}; \tag{5.23}$$

$$k_3 = \frac{\left(\Delta L_{s2} + 2\Delta L_{m2}\right)}{\left(2L_{s0} + 2L_{m0} + \Delta L_{s0}\right)}; \tag{5.24}$$

$$k_4 = \frac{\left(\Delta L_{s0} + 2\Delta L_{m0}\right)}{\left(2L_{s0} + 2L_{m0} + \Delta L_{s0}\right)} \text{ and} \tag{5.25}$$

$$k_5 = \beta \text{ which is defined in figure 5.6.} \tag{5.26}$$

Motor constants k_1 to k_4 are coefficients from the right hand side of equations (5.12), (5.14) and (5.16). They are derived under the assumption that the cosine terms in the denominator of those equations are negligible. Figure 5.7 compares waveforms calculated using equations (5.12), (5.14) and (5.16) with and without the cosine terms in the denominator.

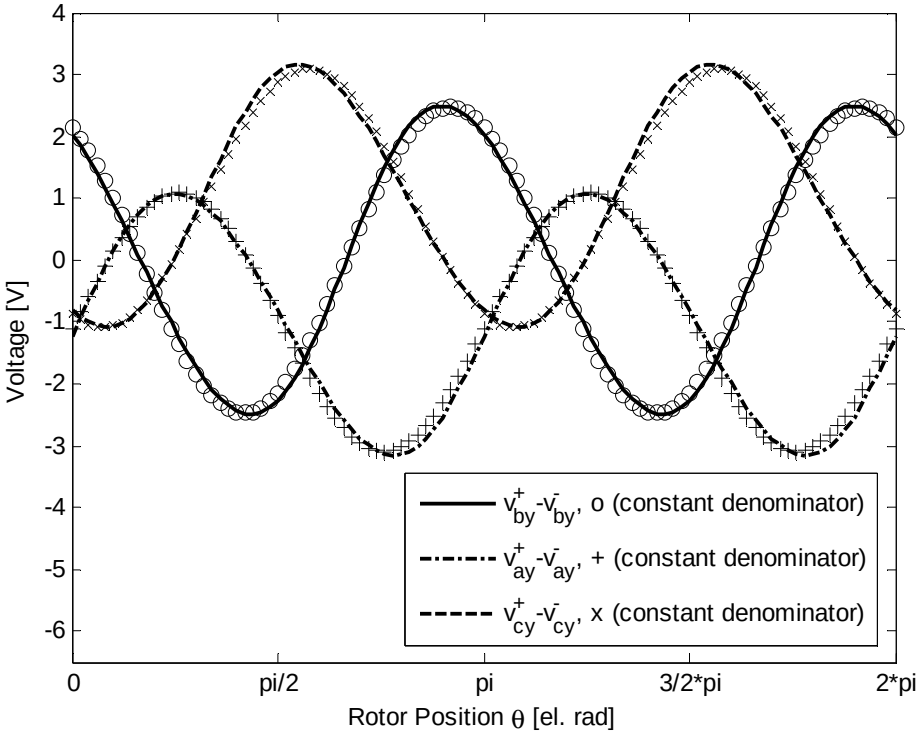

Figure 5.7 : Voltage Difference Waveforms (full equations and simplified)

It has been found that neglecting the cosine term leads to a maximum starting position estimation error of 4 electrical degrees. It does not however contribute to any error in the determination of commutation positions after start-up, since at the “zero crossing” positions, the error disappears. There is a possibility to avoid this error, by implementing bi-dimensional look-up tables representing equations (5.12), (5.14) and (5.16) in discrete from. If the acquired voltage samples are properly scaled, they define the indices to directly access the look-up tables. Doing this the method will lose some flexibility but would still keep the computation burden to an acceptable level. However the pre-operative operations to generate and link the look-up tables will be significant. This possibility has also been tested, but not further considered, due to the above mentioned drawbacks.

Motor constants k_1, k_2 and k_3 are coefficients of the cosine terms in equations (5.16), (5.12) and (5.14) respectively. Motor constant k_4 is the first bracketed term of equation (5.12). The determination of constants k_1 to k_5 off-line and their pre-loading into the digital controller greatly reduces the computational burden during on-line calculations. Experimental methods to determine the motor constants are presented in chapter 7. Sensitivity analysis can be carried out based on differences between predicted values and measured values.

Assuming the rotor is initially at standstill, start-up would consist of the following steps:

a) Determine, by solving any two of equations (5.12), (5.14) and (5.16), the two possible values for θ_i, the rotor initial position.
b) Identify the phase pair that on energisation will provide the maximum driving torque.
c) Energise the selected phase pair until θ_i changes by a small (typically less than one mechanical degree) but measurable amount.
d) Depending on whether θ_i is increased or decreased in step (c), determine the actual value of θ_i.
e) Identify the phase pair and polarity that will provide maximum driving torque for rotation in the desired direction.
f) Energise the phase pair identified in step (e) and initiate commutation to the next phase pair when the value of the measured voltage difference reaches the value specified in table 5.2.
g) Activate the normal commutation algorithm straight after initiation of the first commutation event.

Table 5.2: Value of sensed Voltage Differences at First Commutation Positions

Phase pair first energised as per step (e)	Voltage difference sensed	Voltage value at first commutation position (forward)	Voltage value at first commutation position (reverse)
CA or AC	$\frac{v_{by}^{+} - v_{by}^{-}}{v_{dc}}$	$k_1 \sin\left(\frac{5\pi}{6}\right)$	$k_1 \sin\left(\frac{\pi}{6}\right)$
CB or BC	$\frac{v_{ay}^{+} - v_{ay}^{-}}{v_{dc}}$	$-k_4 + k_1 \cos\left(\frac{5\pi}{6}\right) + k_3$	$-k_4 + k_1 \cos\left(\frac{\pi}{6}\right) - k_3 \cos\left(\frac{2\pi}{3}\right)$
AB or BA	$\frac{v_{cy}^{+} - v_{cy}^{-}}{v_{dc}}$	$k_4 + k_1 \cos\left(\frac{5\pi}{6}\right) - k_3 \cos\left(\frac{2\pi}{3}\right)$	$-k_4 + k_1 \cos\left(\frac{\pi}{6}\right) - k_3$

As in the case of the standard equal inductance method, step (a) requires at least two phase pair energisations to be carried out with 50 percent PWM duty cycle to avoid rotation. Any two of the six possible phase pair combinations could be used. A third one can be used for verification purposes. If, for example, phase pair AB and BC were used equations (5.12) and (5.14) would apply and we would have:

$$\theta_d = \tan^{-1}\left(\frac{P_s}{P_c}\right) \tag{5.27}$$

$$\begin{bmatrix} P_s \\ P_c \end{bmatrix} = \begin{bmatrix} \sin(2\theta_i) \\ \cos(2\theta_i) \end{bmatrix} = \begin{bmatrix} -k_2 \sin\left(\frac{5\pi}{6}\right) + k_3 \sin\left(\frac{2\pi}{3}\right) & k_2 \cos\left(\frac{5\pi}{6}\right) - k_3 \cos\left(\frac{2\pi}{3}\right) \\ k_2 - k_3 \sin\left(\frac{2\pi}{3}\right) & k_3 \cos\left(\frac{2\pi}{3}\right) \end{bmatrix}^{-1} \begin{bmatrix} \frac{v_{cy}^{+} - v_{cy}^{-}}{v_{dc}} & -k_4 \\ \frac{v_{ay}^{+} - v_{ay}^{-}}{v_{dc}} & +k_4 \end{bmatrix} \tag{5.28}$$

Equations (5.27) and (5.28) define a unique value for θ_d in the zero to 360 electrical degree range. The initial rotor position θ_i, however is either equal to $\theta_d/2$ or $(\theta_d+2\pi)/2$. The purpose of steps (b), (c) and (d), listed above, is to determine whether θ_i is equal to $\theta_d/2$ or $(\theta_d+2\pi)/2$.

The phase pair combination to be selected in step (b) should be:

CA if $0 \le \frac{\theta_d}{2} < \pi/3$;

CB if $\pi/3 \le \frac{\theta_d}{2} < 2\pi/3$; and

AB if $2\pi/3 \le \frac{\theta_d}{2} < \pi$.

Step (c) requires the PWM duty ratio to be deviated from 50% just enough to allow a small but measurable change in rotor position. It can be deduced that $\theta_i = \theta_d/2$ if θ increases, otherwise $\theta_i = (\theta_d+2\pi)/2$.

Step (e) is about the choice of the first phase pair to be energised. This can be done with the help of table 5.2. For example, if the rotor initial position is between 120° and 180° and backward rotation was desired, then the phase pair to be energised should be BA. The first commutation event is performed according to step (f) above and subsequent commutation is carried out as described in section 5.3.

The procedure for the determination of the initial position has, by design, very much the same structure as the one presented in the previous chapter.

5.5 Practical Investigations and Test Results

Equations (5.12), (5.14) and (5.16) form the basis of the sensorless technique proposed in this chapter. Figure 5.8 represents experimental verification of those equations. Tests were done with the rotor held stationary at a known angular position. While at that position phase pairs AB, BC and CA were energized in the normal way through the inverter and with a PWM duty cycle of 50%. Voltage differences as defined by equations (5.12), (5.14) and (5.16) were measured and graphed against rotor position. Simultaneous sampling was carried out at 500 kHz. The voltage transducer was a simple resistive voltage divider. Agreement between measured and predicted values was found to be within 3.5%.

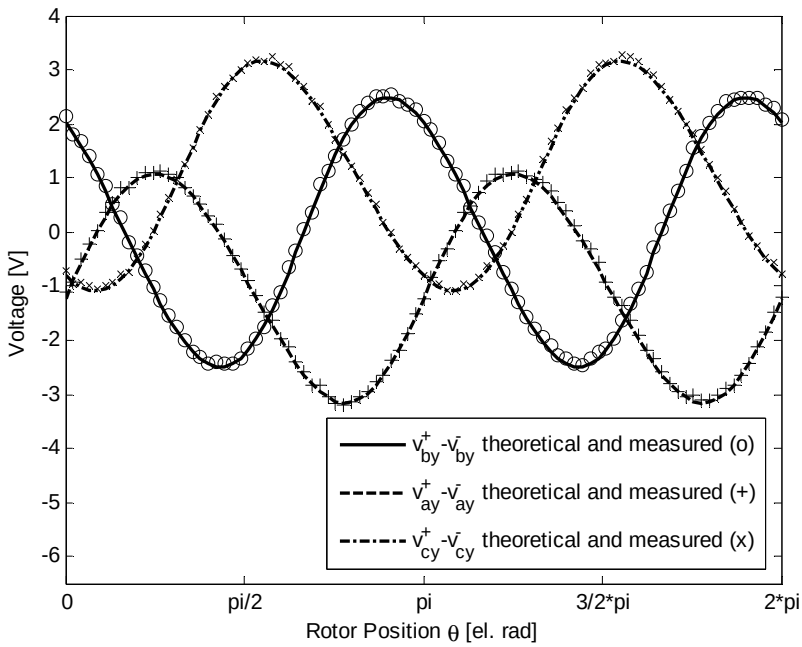

Figure 5.8: Experimental Verification of Equations 12, 14 and 16 (on motor 1)

Figure 5.9(a) shows the estimated positions. Estimation of rotor position is part of the motor starting process and is carried out by going through steps a) to d) of section 4, which involves equations (5.27) and (5.28). The experimental results of figure 5.9(b) show that over the entire range of possible starting positions, the maximum error between estimated and actual initial position was 5.4 electrical degrees.

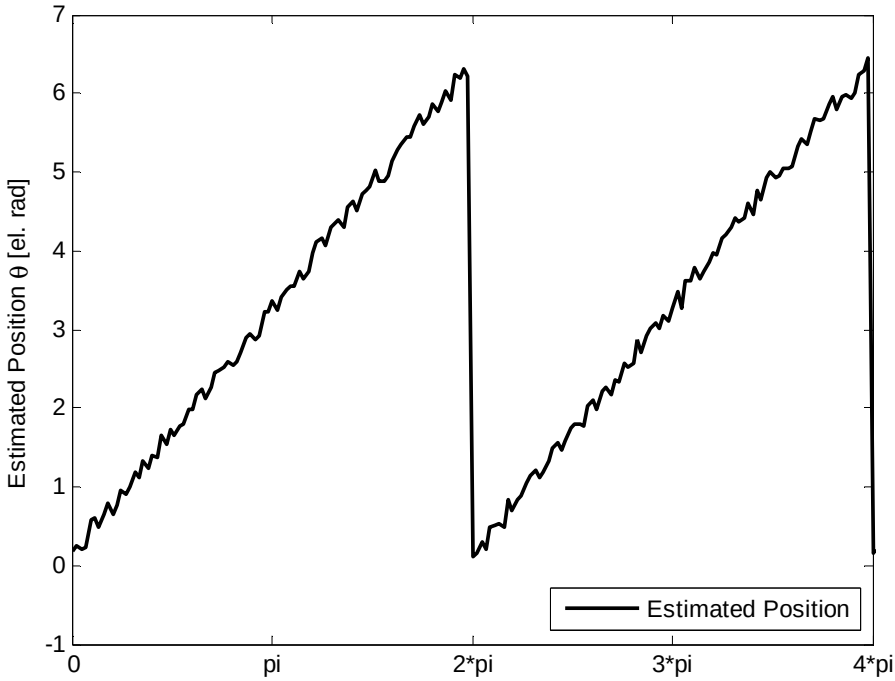

Figure 5.9(a) : Estimated Rotor Position (Test Motor 2)

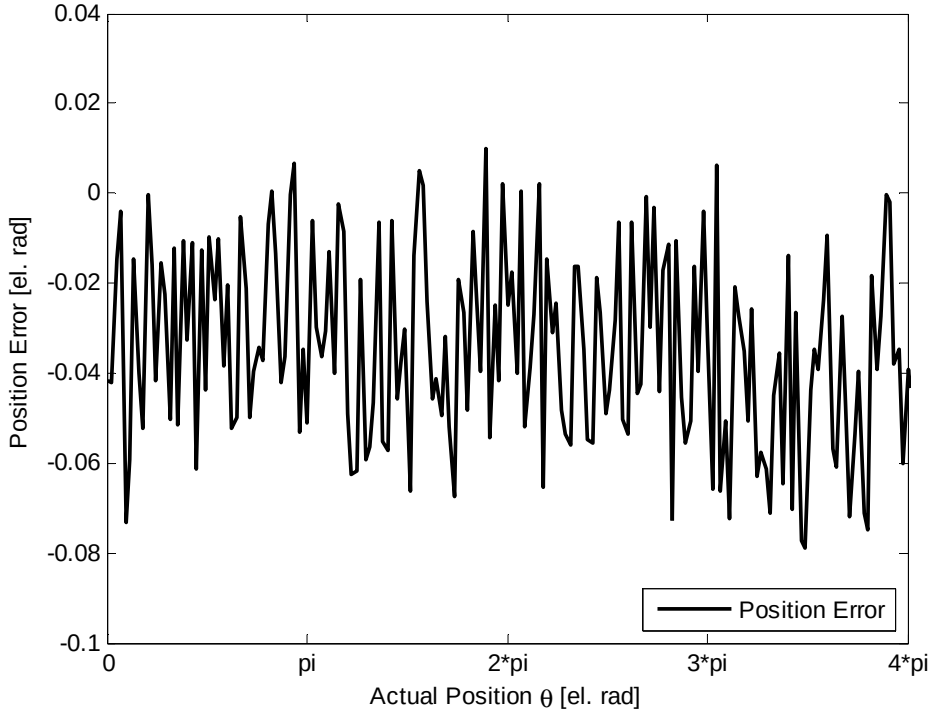

Figure 5.9(b) : Position Error (Test Motor 2)

The proposed sensorless commutation technique has been used successfully on a number of test motors including test motors 1 and 2. The control algorithm was implemented using the 56F8037 digital signal controller. Figure 5.10 illustrates the control algorithm. In general if x is the time interval from a commutation instant to the instant of zero sensed voltage difference, the time between consecutive commutations is given by $x\ (1+\gamma)$. The time multiplication factor γ is defined in table 5.3.

The algorithm has been written partially in assembly and partially in C language. Freescale Codewarrior has been chosen as development suite. Different macros, as well as inherent

functionalities of the Freescale 56F8XXX DSC family, have been used, for example to access the ad converter module.

Figure 5.11 shows the waveforms of the current of phase b captured while the test motors were operating at 750 rpm. The current waveform provides evidence of correct operation of the proposed sensorless technique with commutation events taking place every 60 electrical degrees. Figure 5.11 also shows the relationship between actual commutation instants and the instants of detecting of zero voltage differences. Note that t_α, t_β and t_δ corresponds respectively to angles α, β and δ of figure 5.6. The higher ripple content in the current waveform of test motor 1 is a reflection of its lower inductance.

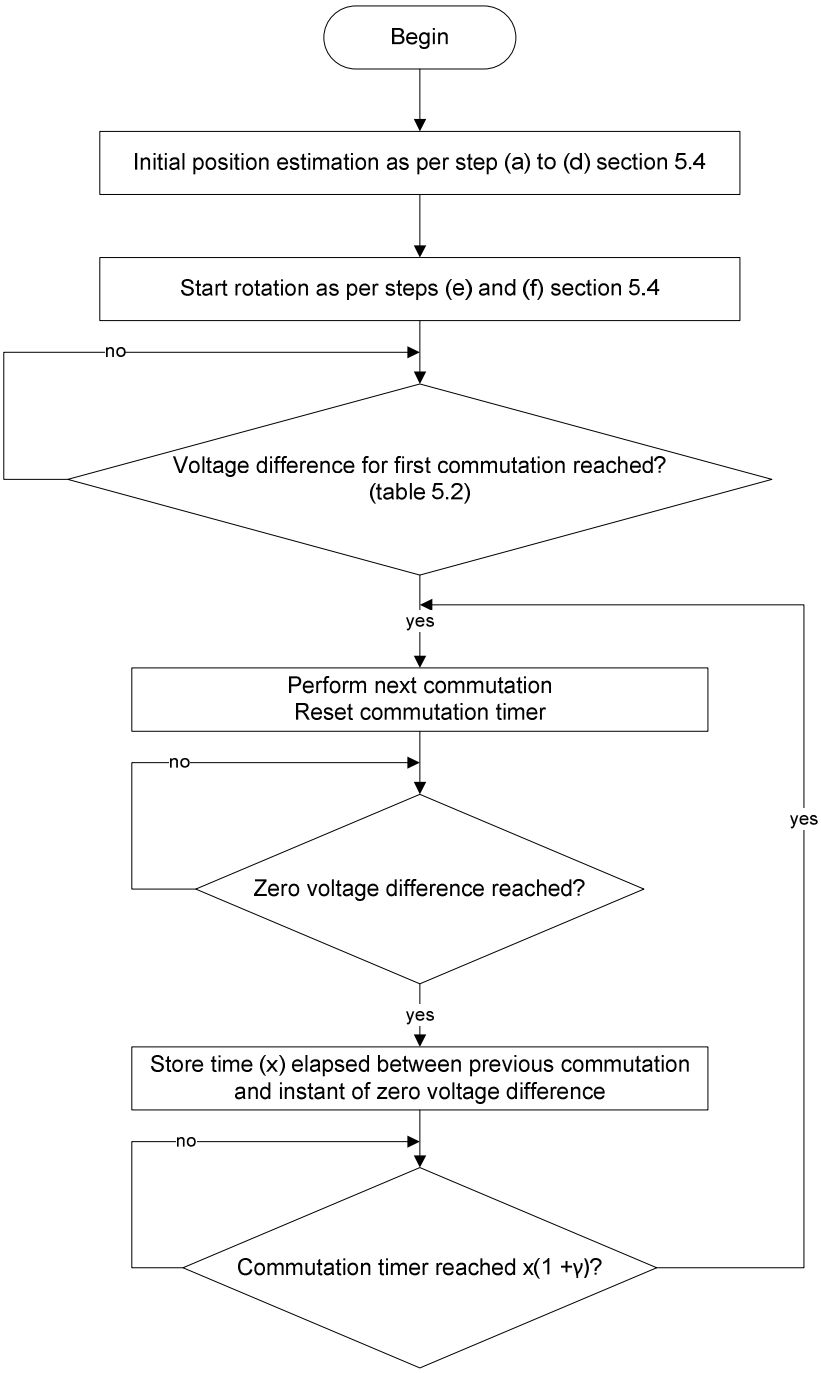

Figure 5.10 : Commutation Control Algorithm

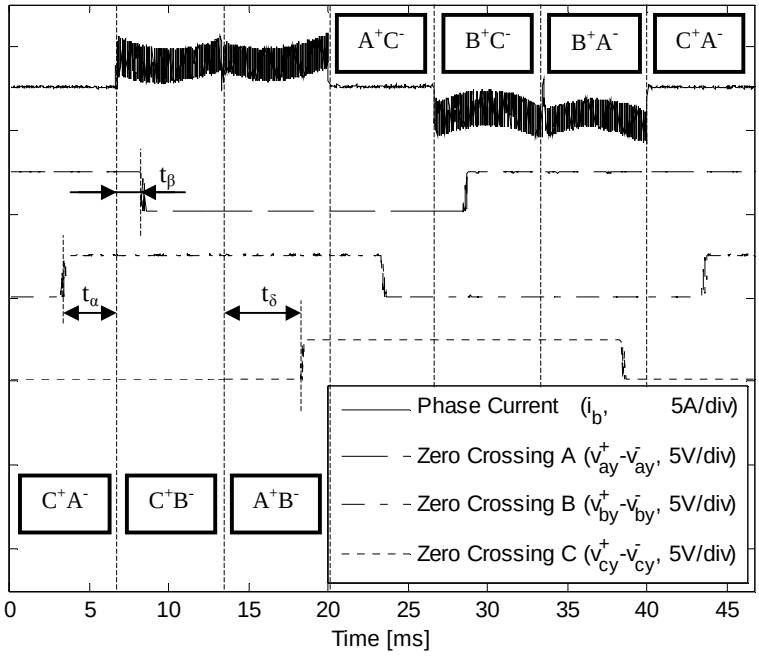

a)

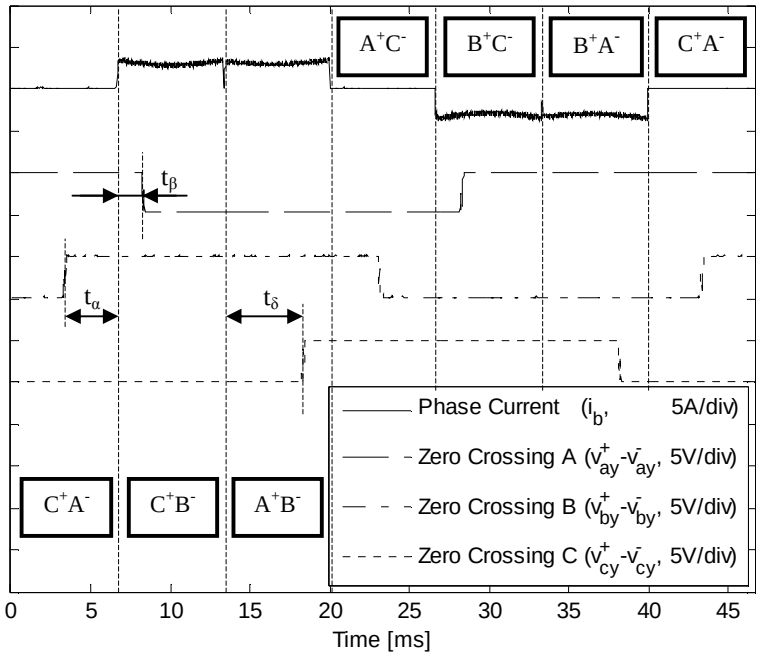

b)

Figure 5.11 : Commutation under Load at 750 rpm, a) Motor 1, b) Motor 2

Table 5.3 : Commutation Time Multiplier γ $\left(\beta = \frac{\pi}{3} - \delta\right)$

Commutation interval	CA or AC	CB or BC	AB or BA
γ forward rotation	1	$\frac{\delta}{\beta}$	$\frac{\beta}{\delta}$
γ reverse rotation	1	$\frac{\beta}{\delta}$	$\frac{\delta}{\beta}$

It is important to mention that the first commutation is much easier than a commutation during the running mode because the commutation take place immediately after the pre-loaded voltage threshold (table 5.2) is reached. This is done in hardware by a dedicated interrupt subroutine, called automatically after crossing of the pre-loaded voltage threshold value.

While successful commutation and start-up were obtained with both test motor 1 and test motor 2, it was noted that test motor 1, because of its lower inductance and resistance presented a higher burden on the inverter and power supply during start-up. The technique used to determine initial position relies on the application of what is essentially a square wave to winding pairs (essentially an R-L circuit) and this results in a non-sinusoidal AC component in the winding current (rising and falling exponential). Figure 5.12 presents the waveform on motor 1 during start-up. There is a need to ensure that the inverter transistors and the DC source are rated to supply this AC current component.

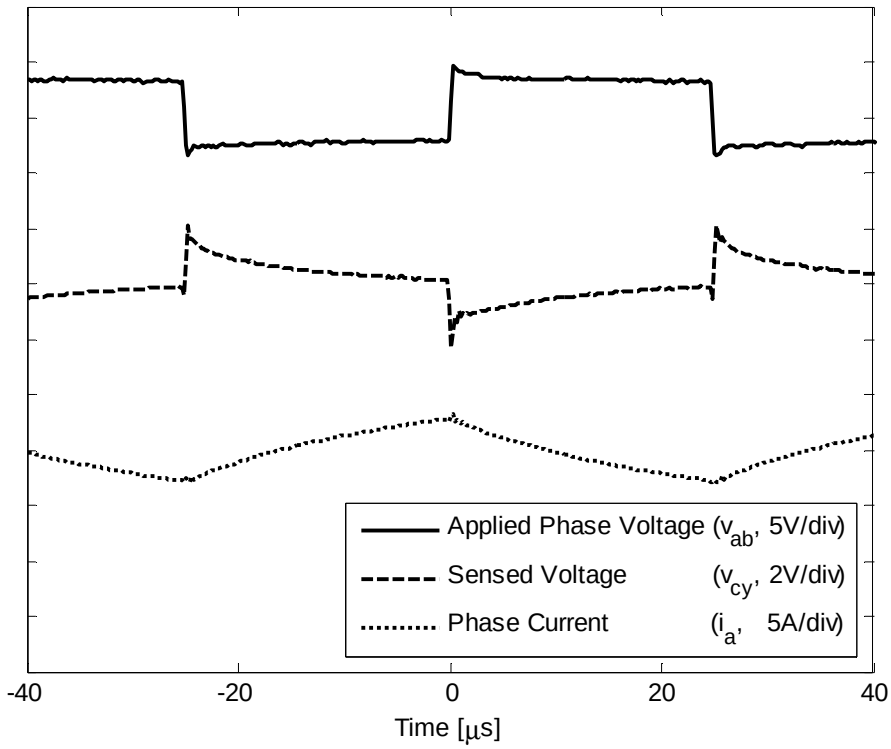

Figure 5.12 : Motor 1 Waveforms

5.6 Practical Considerations

5.6.1 Motor Stiction

BLDC sensorless control strategies are useful and justified in applications where no holding torque at 0 speed is required for example in the case of fans and pumps. During the first two steps of the start-up procedure, the proposed method is not sensitive to the load conditions, since a 50% duty cycle is applied, which does not result in any rotation. However in step c), if the load

is too heavy, the rotor will not move. In order to prevent serious damage to the inverter, a fault / warning signal (over current) will be automatically generated.

5.6.2 Power Semiconductor Voltage Drops Compensation

Equation (5.11) which is obtained from equations (5.7) to (5.10), shows that voltage drop across power switches do not have any significant influence as long as the difference in voltage drop across the power switches during the two states of a PWM cycle is small compared to the DC supply voltage. However, a part of the control algorithm is dedicated to a direct compensation of these voltage drops, regardless of their amplitude.

The coreless nature of the machine being considered means they have relatively short time constants. Consequently the current in the outgoing phase decays to zero in the first few PWM pulses after commutation. Generally speaking, after commutation, the first few pulses can be discarded without influencing the drive performance, since the PWM frequency is much higher than the phase winding commutation frequency. The choice of the PWM frequency is not only important for that aspect but also from a point of view of the sampling resolution, since, as introduced above, the simultaneous sampling frequency is 500 kHz. If the selected PWM frequency is too high, the resolution could significantly decrease, affecting drive performance. The sampling frequency of 500 kHz is limited by the bandwidth of the DSC analog to digital converter. Simultaneous sampling is fundamental in order to have time consistent data to process.

The following list introduces the main sampling characteristics:

- Sampling enabled 3.75 µs (approximately 7.5% of PWM period) after commutation to avoid "ringing"
- Three values are acquired simultaneously (for example: i_a, v_{ab} and v_{cy})
- Per definition, in the "first pulse", the samples are acquired "only" at time instant = 5 µs (10% of PWM period)
- The acquired value of i_a sets the "current threshold" for "second pulse" acquisition
- In the "second pulse", samples are taken every 2 µs (max. sampling rate)
- Sampling is stopped once the sampled (actual) i_a crosses the "current threshold"; values of actual sampling instant and of (instant-1) are considered and linearly interpolated to increase precision
- Special hardware functionalities of the DSC are used. They notably accelerate data processing, e.g. automatic interrupt ISR call on threshold value crossing.

After having introduced the sampling characteristics, the focus is set back to the voltage drop cancellation strategy.

Consider figure 5.13: in every pulse (t_{ON} or t_{OFF} of the applied PWM pulse) two different intervals can be distinguished:

a) Current fast (forced) decaying through the free-wheeling diodes. During this interval the voltage level at motor phase terminals are pushed above / below (symmetrically) the dc-rails references voltages because of the freewheeling diodes voltage drops. As the current decays the voltage shift is reduced following the diode's characteristics.

b) "Normal" driving current. During this phase R_{DSon} of the power semiconductors influences the applied voltage at the at motor phase terminals

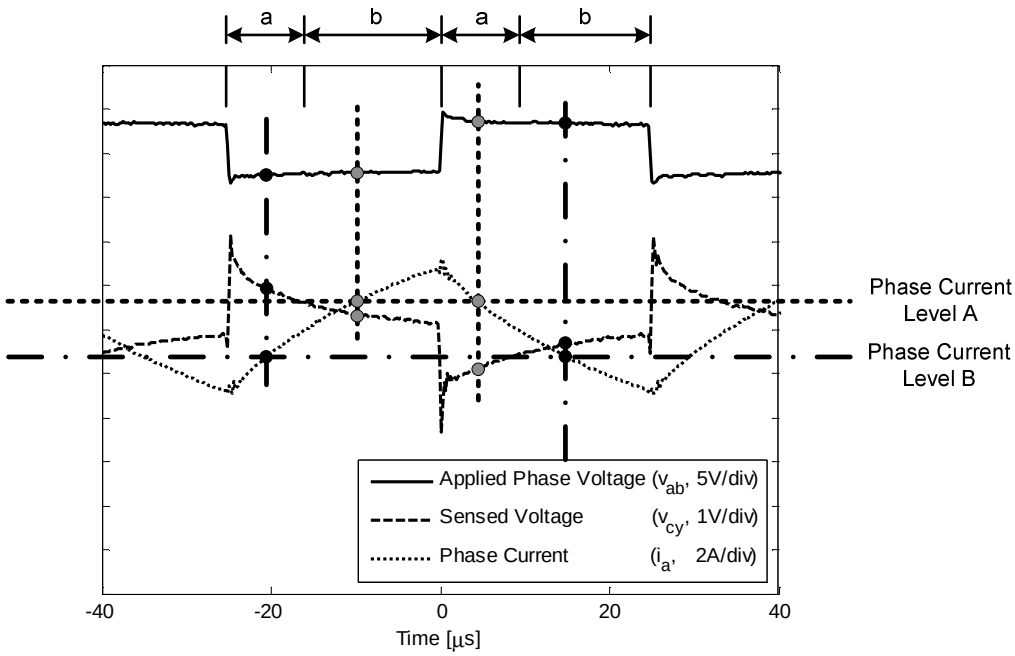

Figure 5.13 : Measurements on Motor 1

It is important to sample at the same level of current (for example "Phase Current Level A" or "B" in figure 5.13), this way the algorithm is not sensitive to the phase resistance, as already pointed out after equation (5.12).

The algorithm is able to sense the voltage drops at both terminals of the actual energized phase pair. A pre-process stage automatically process the acquired voltage samples, in order to eliminate the actual voltage shift (regardless if the actual interval is a) or b)) having as reference the dc bus voltage, which is sampled as well. Consequently the data processed by the algorithm

are consistent with the value computed with the dc-bus voltage as a reference. Due to this easy pre-processing step there is no need to modify any of the presented equations, giving full system stability also if a low cost semiconductor presenting a large value of R_{DSon} is used.

If the voltage shifts (on the motor terminals) are be considered as dc-bus voltage ripple, the pre-process stage can be considered as a dc-bus ripple cancellation stage.

5.6.3 Computation Burden and Speed Range

During rotation, multiplication factor γ is used (Table 5.3 and Figure 5.11). This way the DSC is not loaded with "heavy" computations, since the multiplication factors are determined off-line based on equations (5.19) and (5.21). An online computation would not be possible with the proposed DSC, since the MIPS (Million instructions per second) value is too low. Solution of equation (5.28) is relatively easy and is performed on-line only at start-up when there is ample time to do so. It has been proven that the method works well from zero speed to hundreds of rpm. Beyond a few hundreds of rpm, there is always the option of shifting to the back EMF zero crossing method.

The constants k_1 to k_5 (equations (5.22) to (5.26)) and the different discrete trigonometric functions (as indexed look-up tables) are as well preloaded onto the controller. As stated above, equations (5.12), (5.14) and (5.16) are definitely too heavy to be solved in a closed form (also during the initial position detection, where there are no timing problems). The author was forced to find a way to substantially reduce the computational effort. The simplification can be seen in

Equation (5.28). This way the computation burden is reduced to the minimum (not far from what is needed in the method presented in the previous chapter).

5.7 **Conclusions**

Whereas the previously proposed equal inductance method for sensorless commutation of BLDC motors is restricted to machines that are designed to be symmetrical, the sensorless technique presented in this chapter has been proven to work very effectively for an increasingly important class of non-symmetrical motors. These are multi-layered printed circuit or wound axial flux motors, with ironless stators, where the three separate single phase layers are stacked so that they are located at slightly different axial positions. In the case of the equal inductance method, commutation control, except for the assumption of three-phase symmetry and relatively high phase winding time constant, does not rely on any knowledge of the motor parameters or the value of DC supply voltage and current. In contrast, the more general technique being proposed requires values for the DC supply voltage and current and five other dimensionless constants which are known functions of the motor self and mutual inductances. The dimensionless constants have to be pre-loaded into the motor controller and this is a disadvantage compared to the case of the equal inductance method used with symmetrical motors. It is also assumed that the preloaded dimensionless values remain constant throughout the operating life of the motor. This is a reasonable assumption for mechanically and thermally well designed motors that operate within their ratings since the pre-loaded values are only dependent on motor geometry and the magnetic and electric properties of the rotor.

In common with the equal inductance method, the commutation position determined by the proposed technique is insensitive to operational parameters such as load current and circuit parameters such as phase resistance. The technique is also cost competitive and it offers commutation and starting performance equal to that obtained with Hall sensors.

Chapter 6

Stator Eddy Current Losses in Printed Circuit Brushless Motors

6.1 Introduction

Eddy-current losses in the conducting tracks of printed circuit stators of brushless motors may be significant for cases where tracks are relatively wide and speed is high. This chapter presents a numerical technique that will allow estimation of losses due to eddy currents flowing within the tracks of a printed circuit stator. It is based on a hybrid between 3-D finite elements analysis and 2-D finite difference. Estimation of this component of power loss is an important part of the stator design process especially if high speed operation is intended. Stator power loss, of which eddy current loss may be a significant part, determines the stator operating temperature which

has to be kept below a safe level to avoid thermally induced damage and life reduction. Experimental validation of the proposed model is based on measurement of the parasitic braking caused by the induced currents. This validated technique is fast, reasonably accurate and its computing resource requirements are very modest.

6.2 Characteristics of Test Motors

A prototype three-phase motor rated at about 20 watts per krpm was used to validate the electromagnetic model specially developed for prediction of eddy current losses in the stator. An exploded view of the motor was shown in chapter 3, figure 3.6. Axial lengths of the rotor disks, permanent magnets and mechanical air-gaps are respectively 4 mm, 4mm and 0.3mm. The stator is made up of a stack of three printed circuit boards. The printed coil shape that designers can choose includes, for example, the rhomboidal coil and the mixed parallel and radial coil. It will be clear in the next section that the numerical model being suggested for working out eddy current loss is applicable to any printed coil shape. The coil shape used for the machine's stator is shown in figure 6.1.

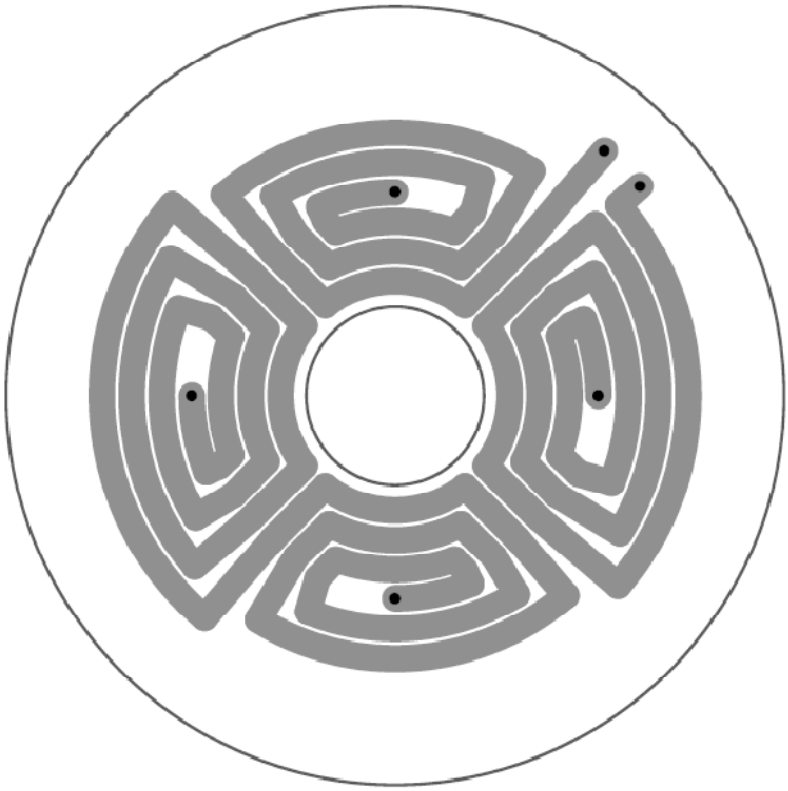

Figure 6.1 : Coil Shape used for the Machine's Stator (2.4 mm Track Width)

Each substrate was made up of two layers of track. Track dimensions and other stator information are given in table 6.1. Each printed layer of the stator belongs to only one phase and the coil pitch is equal to the rotor pole pitch.

Table 6.1 : Test Motor Details (inner radius = 8 mm, outer radius = 25 mm)

Track Width (Base Cu = 35 μm) [mm]	Stator Axial Thickness [mm]	Comments
1	1.6	Single phase test
1	4.8	Full stator test
2.4	1.6	Single phase test
2.4	3.2	Dual phase test
2.4	4.8	Full stator test
3.7	1.6	Single phase test
3.7	4.8	Full stator test

The presented eddy current modelling method is applicable whether printed circuit layers are shared among phases or belong to a single phase. In this test motor the two printed layers making up one phase reside on one substrate. Similarly printed layers belonging to the other two phases reside on two other separate substrates. The three substrates are nominally identical. However they are displaced circumferentially so that their magnetic axes are separated by 120 electrical degrees. The printed circuit test motor can be operated as a brushless DC motor or as a synchronous motor.

6.3 Eddy Current Modelling

This section presents a formal definition, based on Maxwell laws, of the eddy current problem being investigated. The simplifying assumptions that were necessary to arrive at a practical solution to the problem are explained. The mains aspects of the proposed solution procedure are also presented.

6.3.1 Formulation of the Eddy Current Problem

In general the determination of eddy currents is regarded as a quasi-static problem and requires the simultaneous solution of three of Maxwell's equations together with the constitutive equations for each material within the domain of interest. The equations to be solved are given below.

$$\text{curl } H = J \tag{6.1}$$

$$\text{div } B = 0 \tag{6.2}$$

$$\text{curl } E = -\frac{\partial B}{\partial t} \tag{6.3}$$

$$B = \mu H \tag{6.4}$$

$$J = J_m + J_e + J_i \tag{6.5}$$

$$J_e = \sigma E \tag{6.6}$$

$$J_m = \text{curl } M \tag{6.7}$$

where:

H is magnetic flux intensity;

J is current density;

E is the electric field induced within printed tracks;

B is magnet flux density;

J_i is the imposed current density;

J_e is the induced current density;

J_m is the magnetisation current density;

μ is magnetic permeability;

σ is electric conductivity; and

M is magnetisation of permanent magnets.

The problem of determining eddy current loss distribution in the stator would be excessively complex if reasonable simplifying assumptions are not made. The main reasons are the complex geometries involved and the aspect ratios of important sub-domains such as airgaps and copper tracks. An important assumption on which the proposed model is based is that the inductive effect of the eddy currents is insignificant. In other words the induced eddy currents have practically no effect on the flux density distribution set up by the permanent magnets. In mathematical terms J_e is being removed from the right hand side of equations (6.5) and (6.1) because the effect of J_e on B or H is insignificant compared to that of J_m. Very little flux results from the induced eddy currents because in general they are restricted to loop within a track thickness.

Neglecting the inductive effect of eddy currents decouples equation (6.3) from equations (6.1) and (6.2). This greatly simplifies the problem of determination of eddy current loss distribution since equations (6.1) and (6.2), together with constitutive relations (6.4) and (6.7), can be solved

as a magnetostatic problem. The magnetostatic solution can then be used, together with equations (6.3) and (6.6), to determine the induced current distribution.

6.3.2 Determination of Magnetic Flux Density Distribution

A three dimensional magnetostatic solution for the test machine was arrived at based on the finite element method (FEM). As shown in figure 6.2, symmetry planes allowed the full 3-D problem to be reduced and only one sixteenth of the full geometry needed to be considered, following the same approach adopted in chapter 3

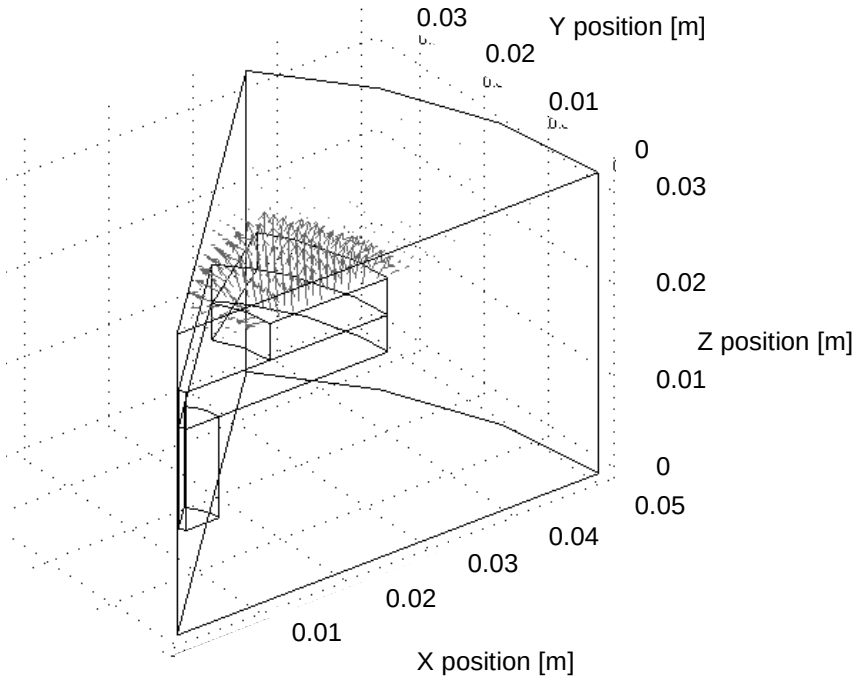

Figure 6.2 : FEMLAB® Model of the Rotor (Half Pole Pitch, inner Radius of Permanent Magnet = 11 mm)

The ironless nature of the stator allowed a single magnetostatic solution to be used for the entire eddy current evaluation procedure. In other words armature reaction is neglected and the flux density distribution set up by the permanent magnets is assumed to be undisturbed by rotor movement or stator currents. Equation (6.8) expresses this assumption mathematically in terms of spatial co-ordinates r, θ and z.

$$B(r, \theta, z, t) = B(r, \theta-\omega t, z, 0) \tag{6.8}$$

where:

$B(r, \theta, z, t)$ = flux density seen, at time t, by an observer fixed to the stator at location (r, θ, z)

ω = speed of the rotor in mechanical radians per second

Equation (6.8) is justified by the fact that the stator is ironless. It is also a consequence of the assumption that flux due to eddy currents is negligible.

6.3.3 Induced Current Evaluation

It is well-known that if a magnetic field is static and a straight conductor of length 1 metre moves relative to the magnetic field then the induced electromagnetic force (EMF) across that conductor is given by:

$$E = B_z v \sin(\lambda) \tag{6.9}$$

where:

B_z is the component of flux density that is normal to the plane in which the conductor lies;

$v = \omega r$ = relative speed between the magnetic field and the conductor; and

λ is the angle between the conductor and the direction of relative motion.

Equation (6.9) can be used to find the induced voltage around a conducting loop as a result of relative movement between the conducting loop and a static magnetic field. In order to do this, the conducting loop should be discretised into sufficiently small elements. Equation (6.9) can then be applied to each of the elements. The sum of the calculated induced voltages will be equal to the loop EMF. The loop current flowing as a result of the induced voltage can be assumed to be equal to the induced voltage divided by the loop resistance. The preceding sentence is based on the following assumptions:

(a) The induced current does not significantly influence the magnetic field causing the induced voltage.

(b) The effect of the conducting loop inductance is negligible compared to the effect of its resistance.

(c) The conducting loop is not electrically connected to anything else.

The proposed eddy current evaluation procedure is based on the basic idea presented in the previous paragraph. However, while for the purposes of eddy current evaluation, the stator printed tracks may be regarded as a large number of conducting loops, those loops are interconnected which means that assumption (c) above is not valid. It will be shown that, by application of standard circuit theory to the collection of interconnected loops representing the stator printed coil, assumption (c) becomes unnecessary.

The validity of assumption (a) relies on the fact that the induced currents are resistively limited. The eddy currents within the printed copper tracks may, to a first approximation, be assumed to experience a resistance which is at least twice the resistance seen by normal load currents. Thus the eddy current path resistance would be of the order of tens of milliohms per metre. Similarly the inductance of the eddy current paths within a track may be taken to be approximately equal to the loop inductance of a two-wire transmission line where the two wires are in very close proximity. Based on this, the eddy current loop inductance would be of the order of one microhenry per metre. With an estimated eddy current loop time constant of about 0.1 millisecond, the assumption of resistively limited eddy currents would be valid well beyond 15 krpm, which is outside the speed range of the type of machine being considered.

6.3.4 Stator Track Discretization

Subdivision of the printed copper track was done as shown in figure 6.3. For clarity, figure 6.3 is only a partial representation of the spiral shaped coil which is shown fully in figure 6.1. The track has been split into three types of standard sections which are radial, circumferential or 'parallel'. The 'parallel' sections are parallel to the mid-line between neighbouring spirals. Each section of the track has been divided into what has been termed 'filaments' and 'segments'.

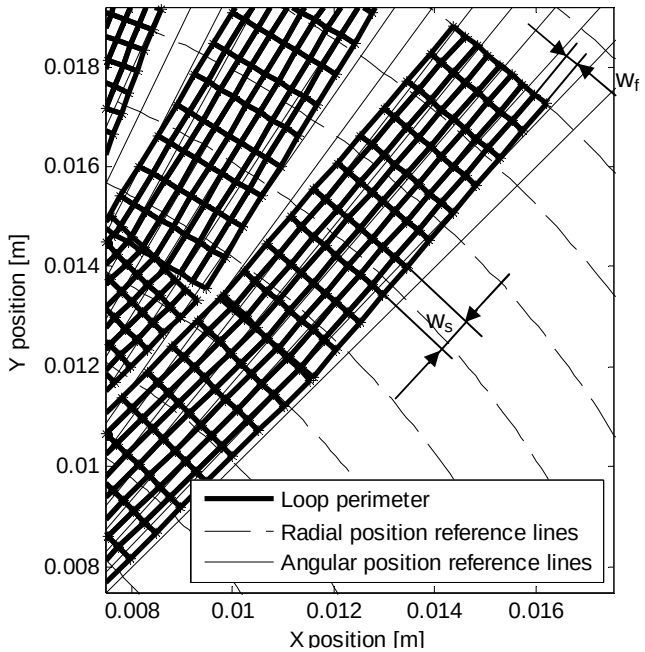

Figure 6.3 : Subdivision of the Printed Copper Tracks

For example, the right most track section in figure 6.3 is divided into eight filaments and ten segments. Filaments run along the tracks in the direction of flow of normal current. A segment runs across the track. For the purpose of evaluation of induced eddy currents, the printed copper track is represented by purely resistive grids which spatially coincide with the filament and

segment boundaries. The resistance of each of the branches forming a grid is determined according to equations (6.10) and (6.11).

$$R_{ia} = w_s/(\sigma t_c w_f) = R_{ea}/2 \quad (6.10)$$

$$R_{ib} = w_f/(\sigma t_c w_s) = R_{eb}/2 \quad (6.11)$$

where:

R_{ia}= resistance of internal branch along the track;

R_{ea}= resistance of branch along the track on the grid edge;

R_{ib}= resistance of internal branch across the track;

R_{eb}= resistance of branch across the track on the edge of the grid;

w_s = width of segment;

w_f = width of filament;

t_c = track thickness; and

σ= electrical conductivity of track;

As long as the number of filaments and segments are sufficiently large, the replacement of the actual printed coil by a number of resistive grids is considered to be a reasonable approximation. As shown in figure 6.3, in the neighbourhood of the edges of the grids there are small sections of tracks that are not directly represented. However any error arising because of this non-representation is insignificant because only a relatively small part of the track is involved and for each non-represented area there is an approximately equal area in the same neighbourhood that is doubly represented. Node pairs at the edges of adjacent grids are considered to be electrically connected.

The model that is being suggested is only a two dimensional representation of the printed circuit coil. In other words the assumption is that induced current density is uniform within the printed track in the axial direction. This assumption is justified because:

(a) track thicknesses that are being considered are no greater than 100 μm whereas the track widths are typically greater than 1 mm;

(b) there is practically no change in the axial component of the flux density due to the permanent magnet over a distance of 100 μm in the neighbourhood of the printed coil; and

(c) the highest track thickness that is of interest is much smaller than one skin depth at the highest relevant eddy current frequency.

The question of sufficiency of number of filaments (n_f) and number of segments (n_s) needed to be addressed. Generally higher values of n_f and n_s leads to better accuracy but at the expense of higher memory requirement and computation time. One basic requirement is to ensure that n_f and n_s are chosen such that both w_s and w_f are significantly smaller than one skin depth at the highest eddy current frequency of interest. It has been quite easy to meet this requirement while staying well under computer memory limitations. Sufficiency of number of filaments and segments were verified by comparing solutions obtained using nominal values for n_f and n_s with those obtained when significantly higher values are used.

6.3.5 Determination of Eddy Current Loss Distribution

According to the proposed model induced eddy currents within the stator printed tracks are approximated by currents flowing in the resistive grids of figure 6.3. For clarity, it may be assumed that the stator winding is open-circuited. The grid currents can be determined by standard loop analysis which is based on the following matrix equation.

$$I_{loop}=(R_{loop})^{-1}E_{loop} \tag{6.12}$$

where:

I_{loop} is the array of loop currents;

E_{loop} is array of loop EMFs; and

R_{loop} is the loop resistance matrix

Examples of loops and the adopted loop numbering system are shown in figure 6.4. It is well known that construction of the loop resistance matrix is based on Kirchhoff's voltage law.

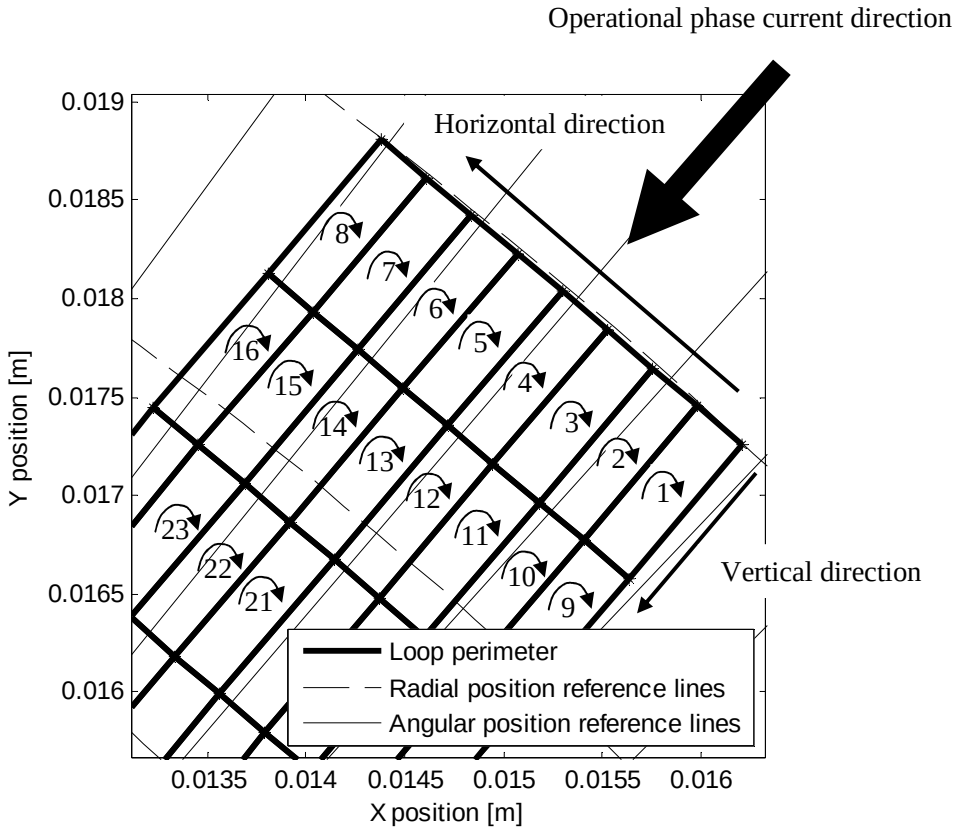

Figure 6.4 : Examples of Loops and the adopted Loop Numbering System

Determination of the elements of E_{loop} is based on equation (6.9). For each rotor position and for each loop the equation is applied four times since each loop is comprised of four conducting branches. For a particular branch, the value of B at the mid-point of the branch is taken to be the flux density for the whole branch. That value of B is a function of the rotor position. It is evaluated by using the FEA results. Since the FEA results are available in discrete form, linear interpolation is necessary to obtain the value of B at the mid-point of each branch. For each branch the radius that is used with equation (6.9) is taken to be the radial co-ordinate of the mid-

point of the branch. Any element of E_{loop} is the sum of four values calculated using equation (6.9) taking into consideration the polarity of the calculated EMFs.

For each rotor position I_{loop} can be determined by using equation (6.10). Branch currents can be deduced from loop currents by using the loop to branch incidence matrix A. Equation (6.13) expresses the relationship between loop currents and branch currents. I_{branch} is the array of branch currents.

$$I_{branch} = AI_{loop} \tag{6.13}$$

The spatial distribution of eddy current loss can be determined by evaluating the resistive loss for each resistive branch. Summation of the resistive losses of all the branches of the resistive grids representing a printed coil gives the total eddy current loss for that printed coil.

6.4 Theoretical Predictions

6.4.1 Effect of Track Width and Number of Turns

Figure 6.5 represents calculated eddy current loss for three printed stator substrates that were made for the test motor of figure 3.6, chapter 3. The three printed stators were nominally identical in all respects except for the track widths and the number of turns per spiral.

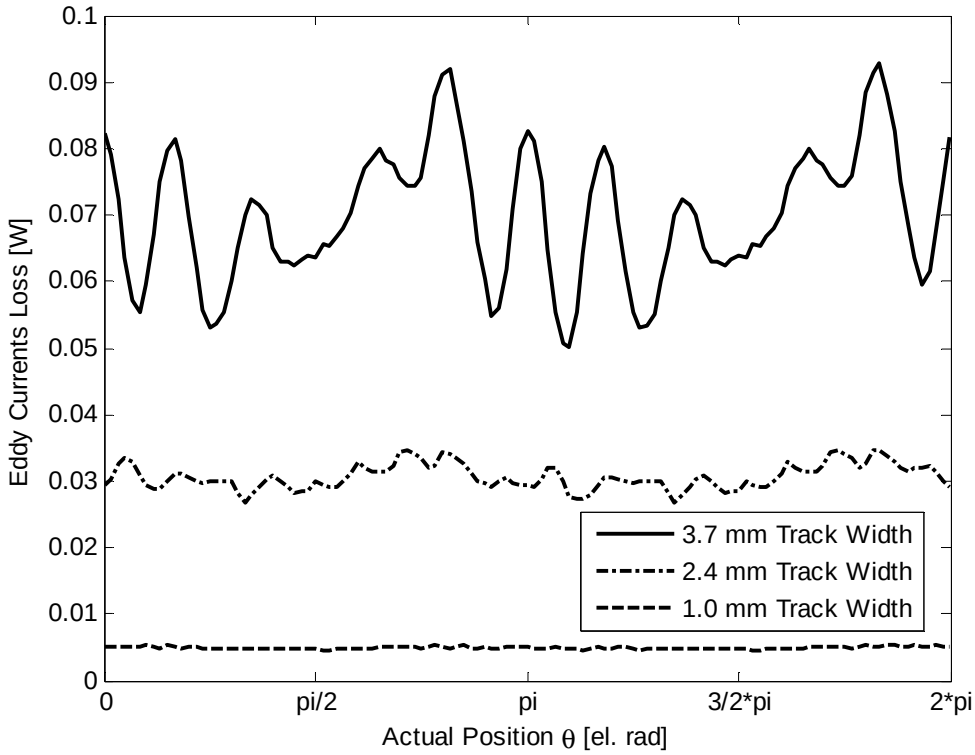

Figure 6.5 : Calculated Eddy Current Loss for Different Track Widths

(for the Middle Phase at 1000 rpm)

With the widest track of 3.7 mm only 2 turns per spiral are able to be accommodated on the substrate. The number of turns per spiral for the other two stator substrates were respectively 6 (1 mm track) and 3 (2.4 mm track). As expected the eddy current loss was found to be a strong function of track width. The induced EMF that drives the eddy current within the active section of each track is, to a first approximation, proportional to track width. The eddy current loss is proportional to the square of that induced EMF and inversely proportional to the track resistance.

Thus a wider track suffers more from eddy currents because its induced EMF is higher and its resistance is lower.

Figure 6.5 shows that there is variation in the level of eddy current loss as the rotor position changes. This is specially the case when the number of turns is small. Each turn in the spiral may be considered to have a component of eddy current loss that is independent of rotor position and a ripple component. The spatial frequencies present in the ripple component result from the spatial harmonic frequencies in the air-gap flux density distribution set up by the rotor permanent magnets. The total eddy current loss for a spiral is the sum of eddy current loss of the individual turns making up that spiral. The ripple components in the eddy current loss of individual turns of a spiral may not be in phase and may cancel or partially cancel each other as a result of summation. These two important statements find their justification in a turn by turn analysis. All presented cases from 1 mm to 3.7 mm have been analysed turn by turn and results are presented in figures 6.6 to 6.8. Since the spiral turns have a different pitch, the axial flux density experienced by every turn is different. In cases where the circumferential displacement between coil sides is large enough, complete phase reversal of the ripple component appears. The reversal can clearly be observed in all analysed track widths. In the 3.7 mm case, with only two turns on the substrate, ripple cancellation is small but still significant. With decreasing track width, there is a smoother transition, because of the gradual change in position of the spiral turns. In the 1 mm case this transition is very visible. It is interesting to point out, that in cases where the turn span is close to half-pitch, the waveform, except for the ripple caused by the spatial harmonics, is quite flat (for example turn 3 in the 1 mm case or turn 2 in the 2.4 mm case).

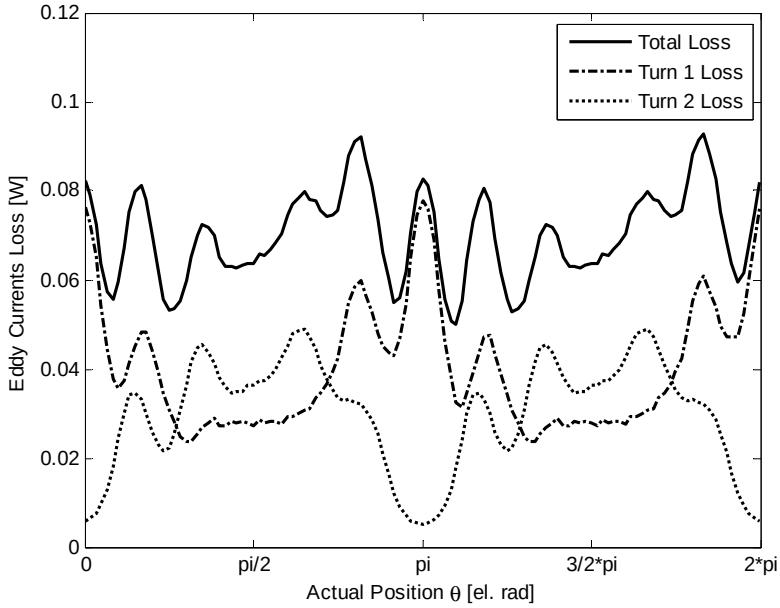

Figure 6.6 : Per Turn Loss with 3.7 mm Wide Tracks at 1000 rpm

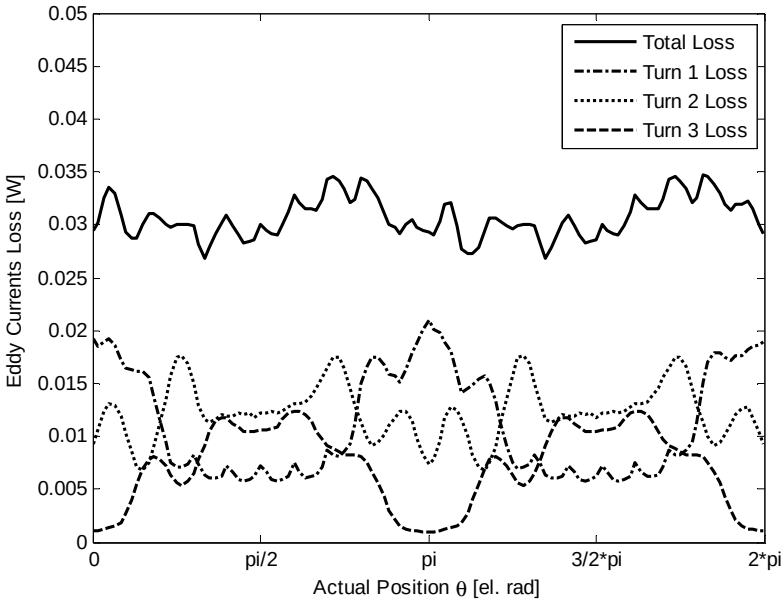

Figure 6.7 : Per Turn Loss with 2.4 mm Wide Tracks at 1000 rpm

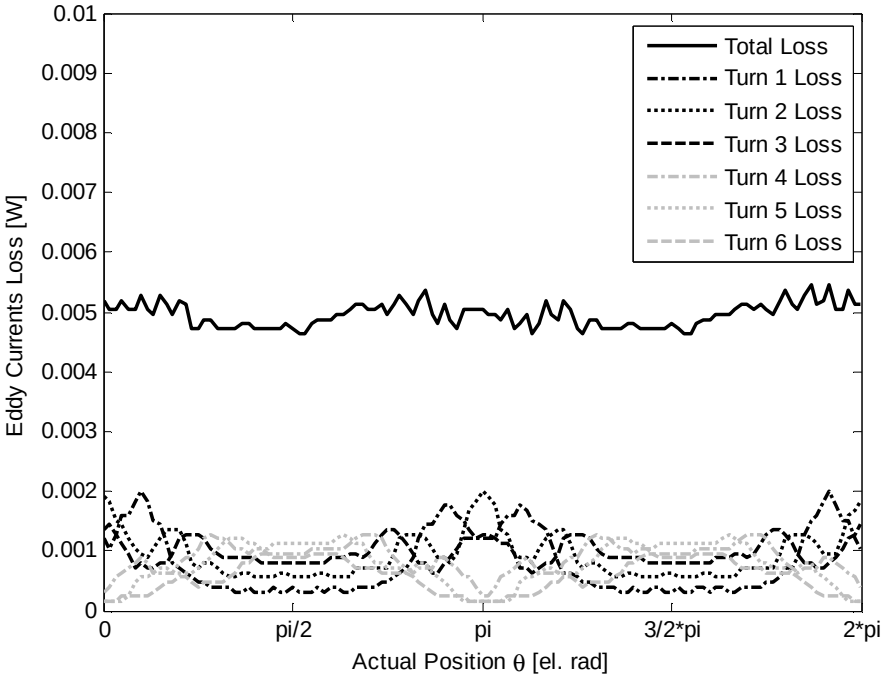

Figure 6.8 : Per Turn Loss with 1 mm Wide Tracks at 1000 rpm

Summarizing, based on figures 6.5, the ripple in eddy current loss curves is less prominent in the case of the narrower tracks. There are two reasons for this. Firstly the ripple component of eddy current losses, just like the rotor position independent component of eddy current losses, is strongly dependent on track width. Secondly, as illustrated in figure 6.8, a higher number of turns in a spiral makes cancellation of the ripple components more likely.

6.4.2 Consideration on the Relation between Eddy Current Ripple and Axial Flux Distribution

In section 6.4.1, the following statement has been made: "The spatial frequencies present in the ripple component result from the spatial harmonic frequencies in the air-gap flux density distribution set up by the rotor permanent magnets".

This statement is justified by considering different axial flux density distributions (Bz). An overview is presented in figure 6.9.

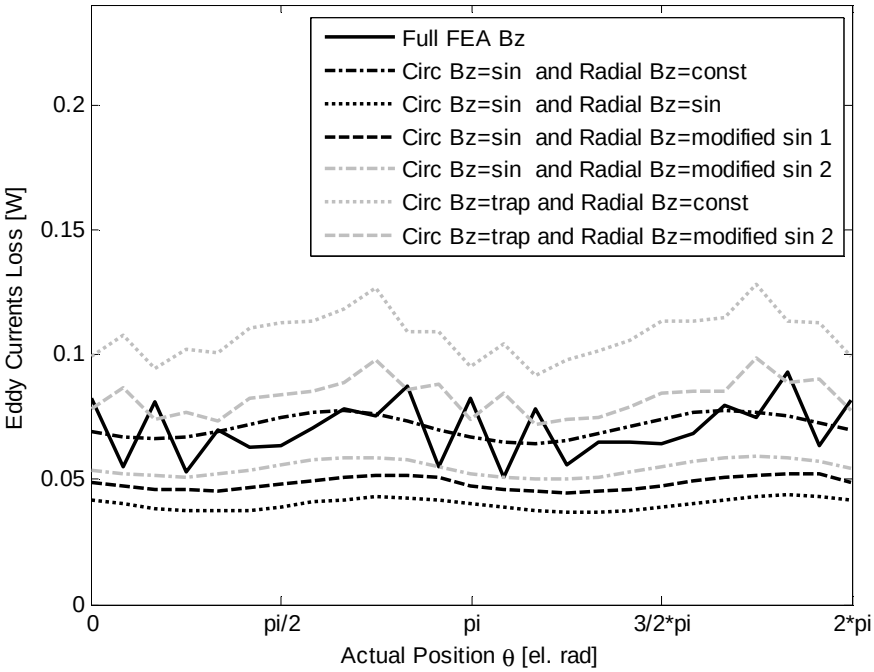

Figure 6.9 : Eddy Current Loss Waveforms under Different Axial Flux Density Distributions

The model, considering a track width of 3.7 mm and a mechanical speed of 1000 rpm, has been run with seven different axial flux density distribution (Bz). The first waveform, which represents the reference, was obtained using Bz resulting directly from FEMLAB®, without any modifications. For the next four waveforms, Bz is assumed to be sinusoidal in the circumferential direction. The following four variations in the radial direction have been considered:

- Bz kept constant from the inner radius towards the outer radius
- Bz varies sinusoidally from the inner radius to the outer radius; the resulting Bz is presented in figure 6.10.

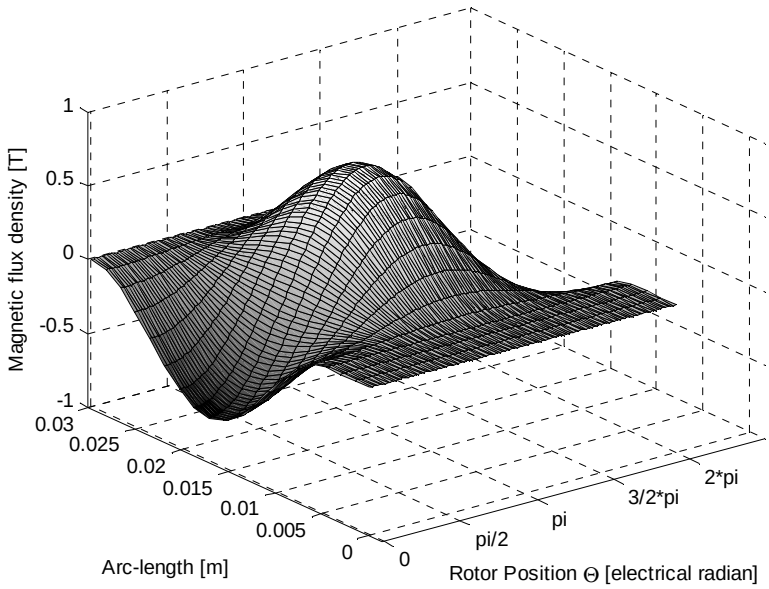

Figure 6.10 : Bz with Sinusoidal Variation in both Directions.

- Radial Bz varies quasi sinusoidally, since the waveform is slightly flat topped. The resulting Bz is presented in figure 6.11.

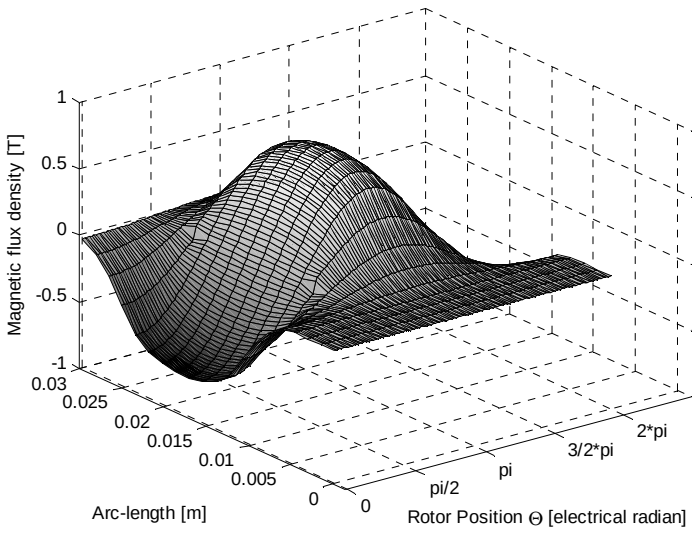

Figure 6.11 : Bz with modified Sinusoidal (flat topped) Variation in Radial Direction.

- Radial Bz varies approximately similarly to the radial variation of the full Bz resulting from FEMLAB. The resulting Bz is presented in figure 6.12.

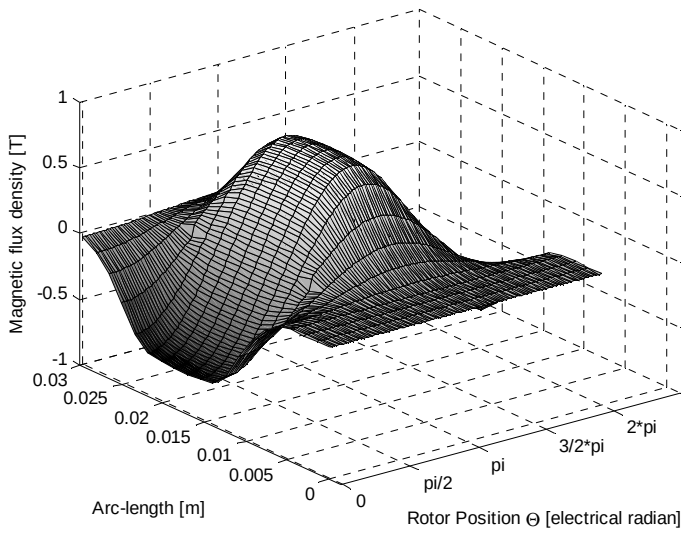

Figure 6.12 : Bz with modified Sinusoidal (approximately as Bz from FEMLAB) Variation in Radial Direction.

For the last two waveforms, Bz is assumed to be trapezoidal in the circumferential direction. The following two variations in the radial direction have been made:

- Bz kept constant from the inner radius towards the outer radius. The resulting Bz is presented in figure 6.13.

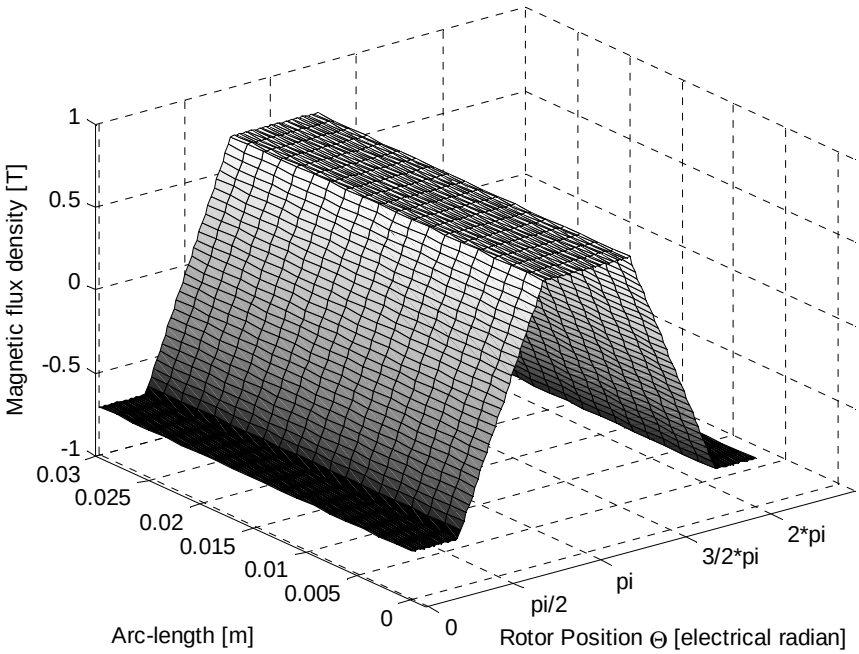

Figure 6.13 : Bz with Trapezoidal Variation in the Circumferential Direction.

- Bz varies approximately similar to the radial variation of Bz resulting from FEMLAB. The resulting Bz is presented in Figure 6.14.

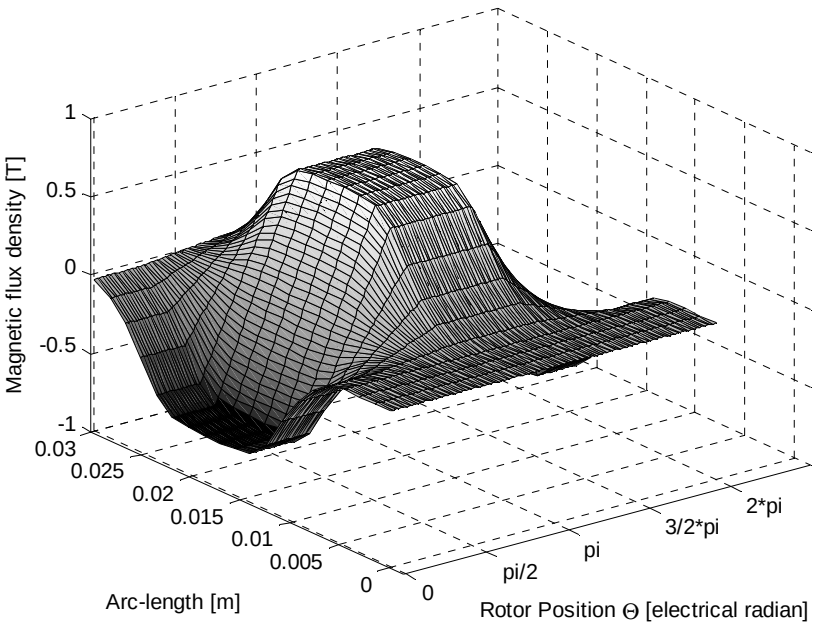

Figure 6.14 : Bz with modified Sinusoidal (approximately as from FEMLAB) Variation in Radial Direction.

The results presented in figure 6.9 led to following conclusions:

- The "high" frequency ripple component is mainly due to circumferential spatial harmonic frequencies in the air-gap flux density distribution. The radial active parts of the coil are the most exposed to these harmonics.
- The ripple component, similar to the 'dc-offset' is mainly influenced by the radial behavior of Bz. A radially constant Bz results in a bigger "dc offset", since the active parts experience the same Bz over the whole radial length.

- The word “mainly” has been intentionally used, since a clear and complete decoupling of the two effects is not possible.

6.4.3 Level of Discretisation

An important question is how sensitive the accuracy of the method is to the segment and filament discretization and the angular resolution. Figure 6.15 simply and clearly shows that discretization and resolution used were adequate.

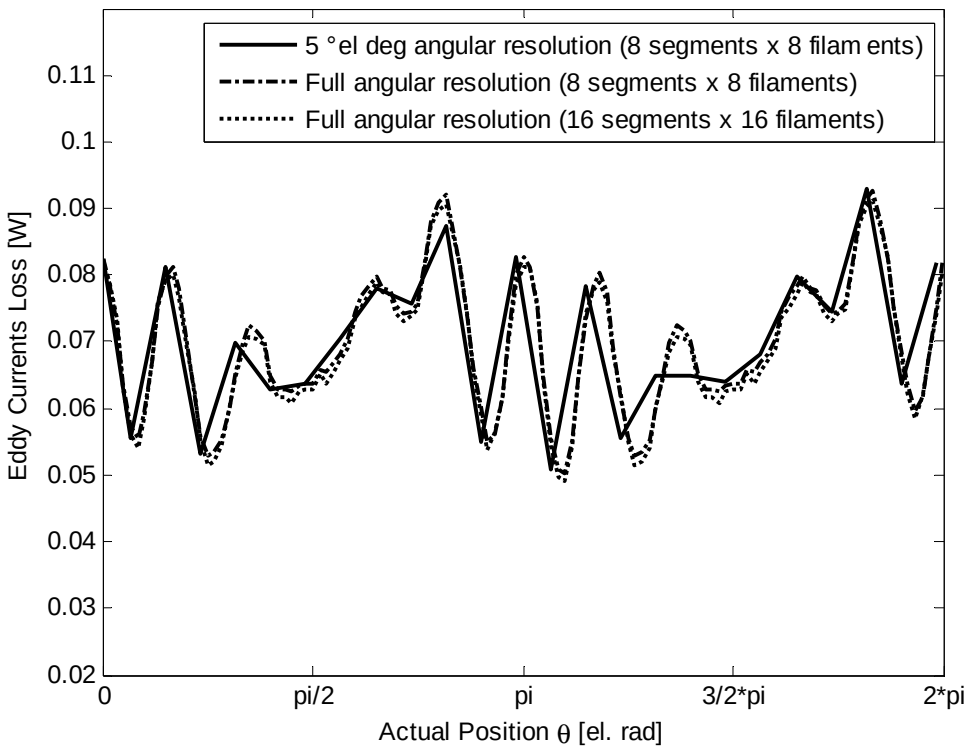

Figure 6.15 : Eddy Current Loss (3.7 mm wide tracks at 1000 rpm) under Different Levels of Discretization

6.4.4 Effect of Substrate Position

Figure 3.6 has shown that the stator of the test machine has its outer phases closer to the rotor magnets compared to the middle phase. As illustrated in figure 6.16 this gives rise to significantly higher eddy current losses in the outer phases. The substrates closer to the magnet are exposed to a higher flux density which gives rise to higher induced EMFs. Even a small difference in induced EMF leads to a relatively large difference in eddy current loss because the loss is a function of the square of the induced EMF.

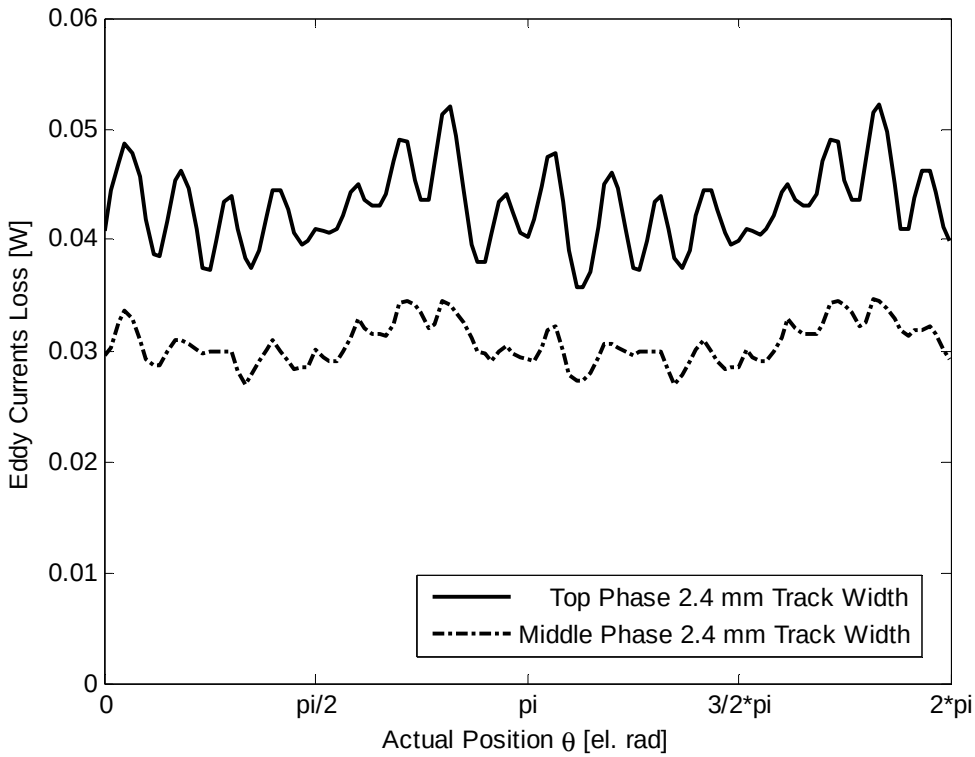

Figure 6.16 : Calculated Eddy Current Loss for different Phases (at 1000 rpm)

6.4.5 Eddy Current Paths

This section focuses on spatial distribution of the induced eddy currents. Before going into details definition of directions have to be made. Figure 6.17 presents the reference directions. The arrow is always taken as reference in order to define positive / negative horizontal and vertical currents, but it does not represent any eddy current path.

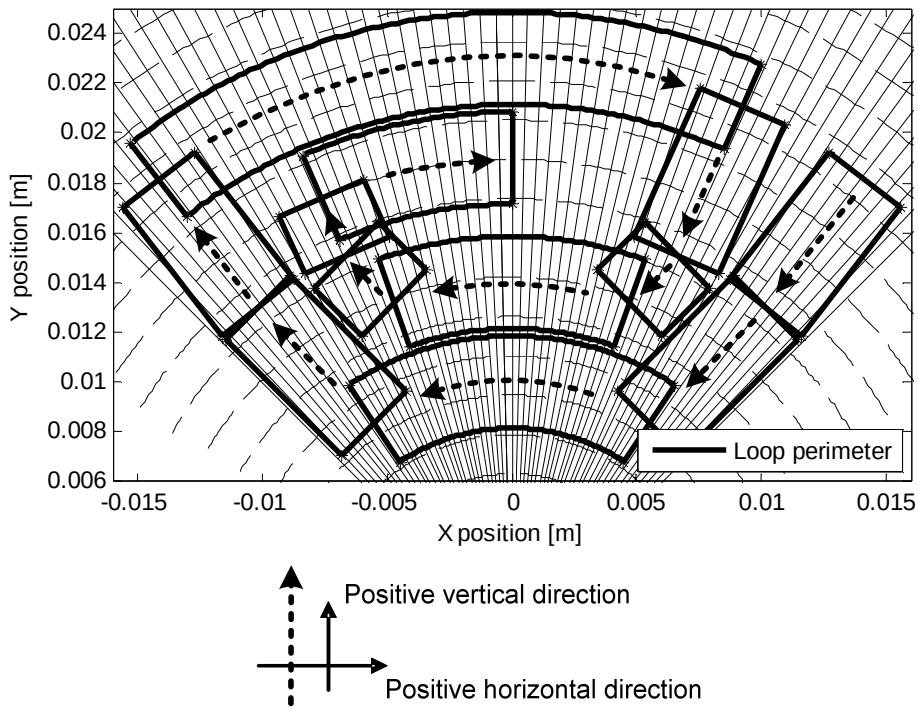

Figure 6.17 : Direction Definitions

Figures 6.18 and 6.20 present the eddy currents inside the spiral at two different rotor positions. The line width of each “branch-line” (horizontal and vertical) depends on the amplitude of the

eddy current flowing in this particular branch. The color of the "branch-line" depends on the sign of the eddy current: dark-gray represents positive currents, light-grey negative ones.

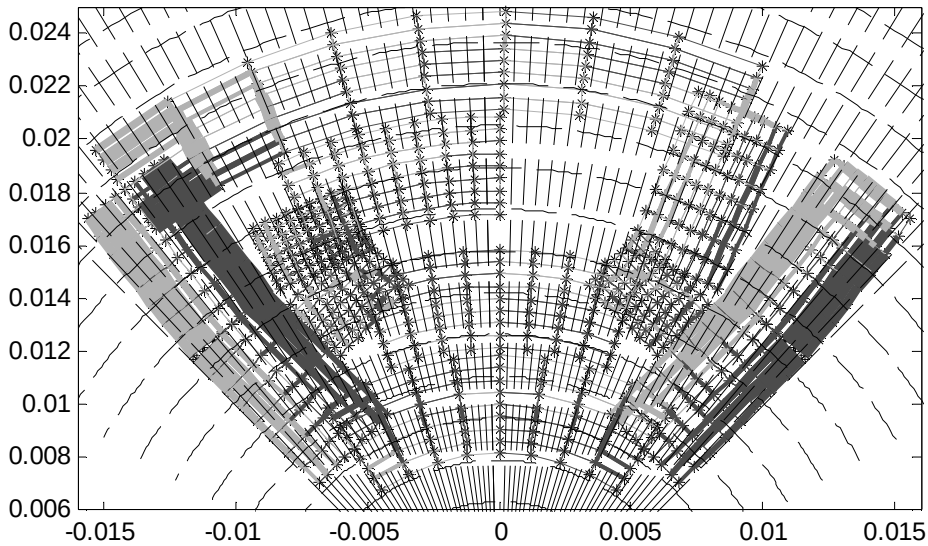

Figure 6.18 : Eddy Current Distribution at Position 0° (both rotor and stator axis are aligned)

To avoid misinterpretation of figures 6.18 and 6.20, it is important to present details on the boundaries, where the track changes from radial to circumferential. At first it could appear that there is break in the eddy current paths. That is not the case (would not be possible from an electrical point of view). This is only due to the adopted geometric model. Figure 6.19 presents how the broken lines are 'mathematically' connected. This connection is depicted by the dashed lines.

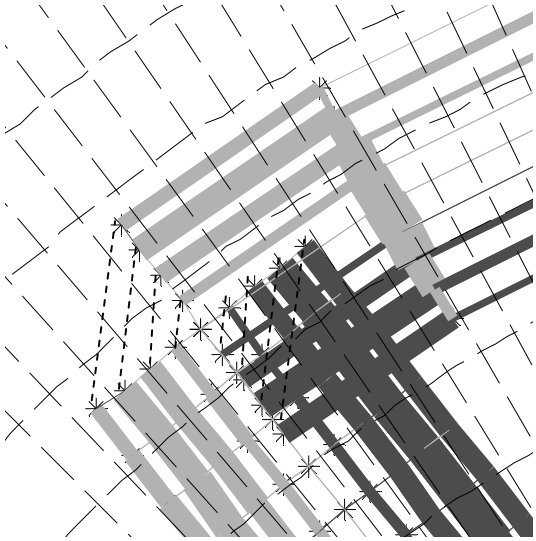

Figure 6.19 : Tracks Boundaries between Different Sections

Figures 6.18 and 6.20 clearly show how the eddy currents flow in “concentric loops” and mainly in “vertical” direction. There are also horizontal currents, mainly where the loops “end” (they are like “end-part connections” for the concentric loops). It is interesting to observe that a portion of the “arc”-sections can be part of the “concentric loops”, since there is no insulation and the eddy currents will flow there to “close” the loop. At this point it is important to mention, that eddy currents can also be induced in the arc sections, since two of the four loop edges (discretization loops) are still in the “active” direction. This can be seen in figure 6.20, where stator coil axis is aligned with rotor q-axis.

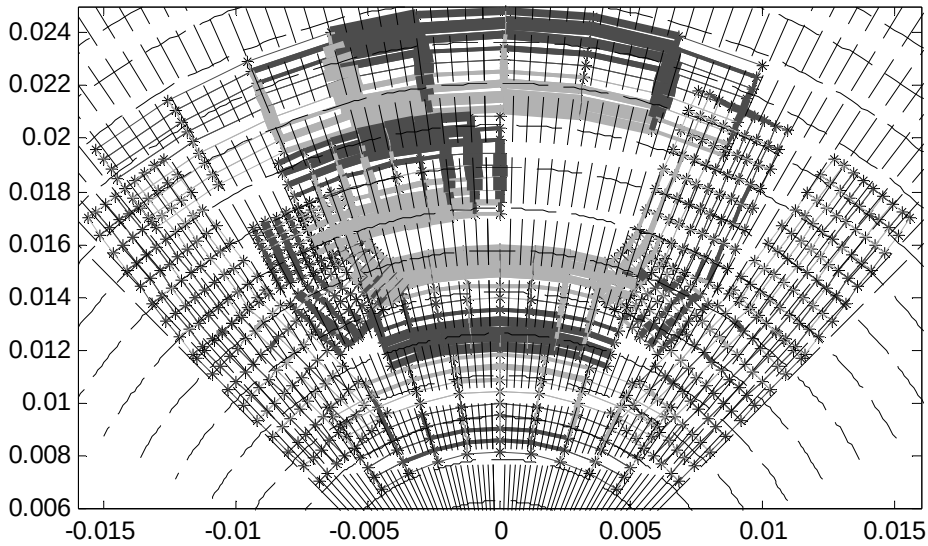

Figure 6.20 : Eddy Current Distribution at Position 90° electrical Degrees

6.4.6 Co-existence of Eddy and Load Currents

In practice the eddy currents induced in the printed coils will be superimposed onto normal load current flowing in those coils. An important question is whether this co-existence leads to additional losses. In order to analyse this question it is assumed that the normal load current flows through the grid branches totally along the printed track and not though the grid branches across the track. This means that if R is the resistance of a track section, I is the motor current and I_e is the eddy current then total resistive loss, to a first approximation, is given by:

$$2(I/2+I_e)^2R+2(I/2-I_e)^2R = I^2R + 4(I_e)^2R = \text{loss due to normal current+eddy current loss} \qquad (6.14)$$

Equation (6.14) predicts that the co-existence of normal machine currents and induced eddy currents within printed tracks does not cause additional losses.

In practice eddy currents will be induced simultaneously in all phases of the motor. As shown in figure 6.21, the eddy current loss for the stator is the sum of the eddy current loss of the three individual substrates. As expected this summation results in significant reduction in the ripple content of the eddy current losses. Indeed if the number of turns is high enough total eddy current losses can be assumed to be independent of rotor position.

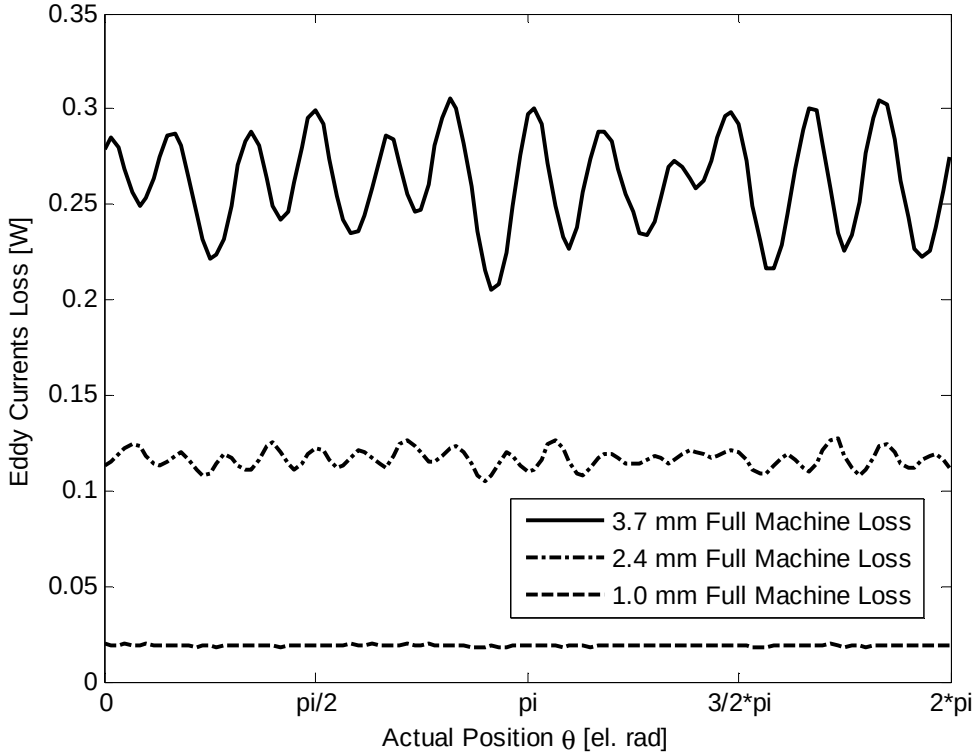

Figure 6.21 : Calculated Eddy Current Loss for Different Track Widths (full 3 Phase Machine at 1000 rpm)

6.5 Experimental Validation

The method of experimental validation is based on the fact that it is mechanical energy coming from the rotor that gets converted to eddy current losses. The preceding statement remains true irrespective of whether the brushless printed circuit machine operates as a motor or as a generator. For convenience tests were performed with the machine running as a generator.

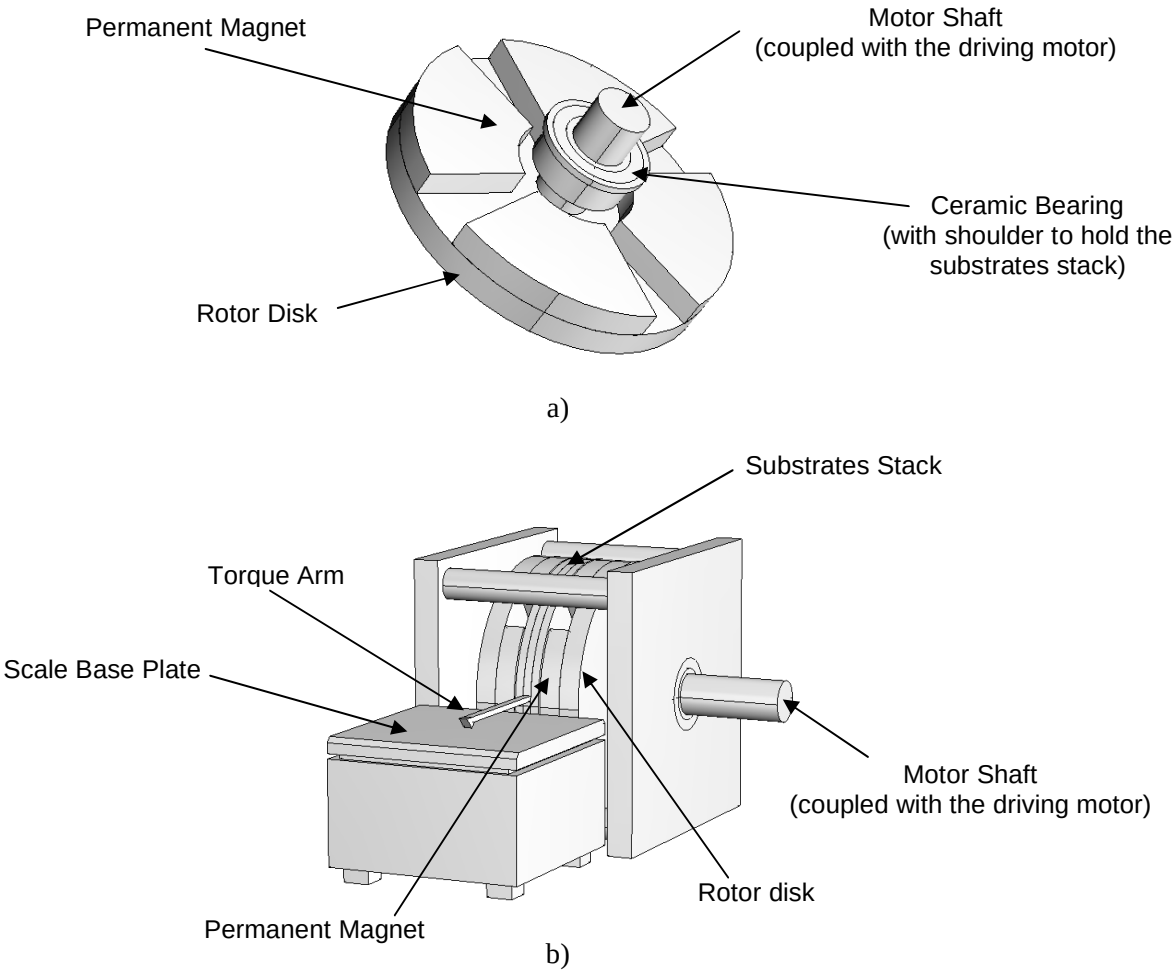

Figure 6.22 : a) Ceramic Bearing for Stator Support; b) Arrangement for Force Measurement

The arrangement illustrated in figure 6.22 (b) was used to carry out specially designed tests. The printed circuit machine under test was motor driven. The stator of the machine was bearing mounted (figure 6.22 (a)) onto the shaft effectively allowing the overall system to operate as a dynamometer. As shown in figure 6.22 a torque arm attached to the stator was made to rest on an electronic scale which had a resolution of 0.1 gram. The length of the torque arm was 0.050 m. An eddy current loss of P_e watts requires a rotor driving torque of T_e which is given by P_e/ω where ω is the rotor speed. This torque is measurable on the electronic scale as a force given by:

$$F_e = P_e/(L_a\omega) \tag{6.15}$$

where L_a is the length of the torque arm.

Assuming that the stator is open circuited, the actual measurement on the electronic scale will be due to a combination of bearing friction torque (F_rL_a) and the driving torque needed to generate the eddy currents. Special low friction ceramic bearings were used to mount the stator onto the shaft. Pre-tests were performed on the bearing to determine F_r at 1000 rpm and at 1600 rpm. The pre-tests were performed with the bearing mounted on the shaft without the stator and with the torque arm mounted on the outer race of the bearing. Subsequent tests on a number of different stators were performed at 1000 rpm and at 1600 rpm. It was assumed that F_r remains constant if speed remains constant. F_e was taken to be the difference between the reading on the electronic weighing scale and F_r whose value was 1.1 gram at 1000 rpm and 1.3 gram at 1600 rpm.

Table 6.2 shows good agreement between measured values of F_e and those predicted using the method described in section 6.4. The percentage discrepancy is less than 6% for the two wider tracks. For the 1 mm track the error is larger because the force being measured falls within the resolution of the electronic scale.

Table 6.2 : Force Measurements width Different Track Widths (Base Cu = 35 μm)

Track Width [mm]	Speed [rpm]	Middle Phase			Full stator		
		Measured [g]	Simulated [g]	Error [%]	Measured [g]	Simulated [g]	Error [%]
3.7	1000	1.4	1.363	2.64	5.2	5.097	1.98
	1600	2.3	2.181	5.17	8.4	8.155	2.92
2.4	1000	0.6	0.597	0.50	2.3	2.270	1.30
	1600	1.0	0.955	4.50	3.8	3.632	4.42
1.0	1000	0.1	0.096	4.00	0.4	0.368	8.00
	1600	0.2	0.153	23.50	0.6	0.588	2.00

Additional tests were performed to confirm the validity of equation (6.14) which states that co-existence of eddy-currents and normal operating currents does not result in increased stator loss beyond the sum of the separately calculated losses. Those tests were performed with the printed circuit machine running as a resistively loaded generator. Prediction for instantaneous phase EMFs was based on equation (6.9). From instantaneous phase EMFs, average power consumed by the resistive loads was evaluated and converted to an equivalent braking force as presented in figure 6.23. Table 6.3 shows that there is reasonable agreement between the measured total braking F_t and total force that was predicted using equation (6.14). The fundamental reason for

insignificant additional loss due to co-existence of eddy-currents and load current is the small ratio of width to length of the copper tracks.

Table 6.3 : Force Measurements (two substrates mounted, 2.4 mm track width)

Speed [rpm]	Load Resistance not Connected			Load Resistance (0.66 ohm) Connected		
	Measured [g]	Predicted [g]	Error [%]	Measured [g]	Predicted [g]	Error [%]
1000	1.5	1.433	4.47	8.3	8.034	3.25
1600	2.3	2.292	0.35	13.3	12.854	3.38

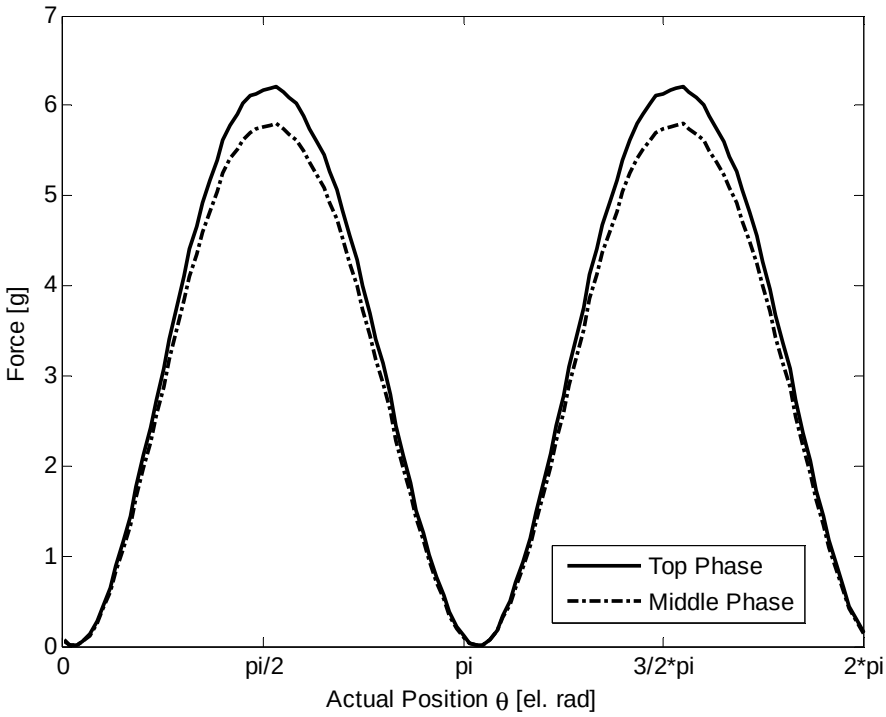

Figure 6.23 : Braking Force of the Middle and Top Phase at 1000 rpm

6.6 Comparison between I^2R and Eddy Current Loss

As for the optimization algorithm introduced in chapter 3, the phase EMF at a nominally fixed mechanical speed of 1000 rpm + / - 10% has been chosen as reference, in order to make meaningful comparisons. The axial length of the permanent magnet has been adapted for all cases in order to have exactly the same axial flux density in the stator air gap. The assumed phase current is 1 A.

1 mm track width (6 turns)

Phase I2R Losses =	1.22W
Phase Eddy Current Loss =	0.0048 W
Ratio= Eddy Loss / I2R =	0.39 %

2.4 mm track width (3 turns)

Phase I2R Losses =	0.5484W
Phase Eddy Current Loss =	0.060W
Ratio = Eddy Loss / I2R=	10.94 %

3.7 mm track width (2 turns)

Phase I2R Losses =	0.3027W
Phase Eddy Current Loss =	0.208W
Ratio= Eddy Loss / I2R=	68.71 %

From the above, it is clear that eddy current loss rises sharply with track width. Every application should be considered on its own merit when a decision on maximum track width is being made. Eddy current loss becomes an increasingly important consideration as speed increases. For the purpose of this thesis, as specified in table 3.2, track width was limited to 2.5mm.

6.7 **Conclusion**

During normal operation of a motor with a printed circuit stator, eddy currents are induced within the stator tracks. The significance of such currents depends mainly on speed and on the track width. A computationally efficient numerical method has been developed to evaluate eddy current losses within the stators of printed circuit brushless motors. The theoretical basis of the proposed technique has been presented. The technique has been experimentally validated by specially designed tests. It was found stator eddy current loss is independent of the flow of normal stator current.

Chapter 7

Prediction of Inductances of Printed Circuit Motors

7.1 Introduction

The variation of stator inductances with rotor position plays a crucial role in BLDC motor commutation control systems that are based on the equal inductance method. If a BLDC motor is being designed and the intention is to use the equal inductance method for sensorless commutation of that motor, then there is a need to ensure right at the design stage that the motor will have sufficient inductive saliency. While prototypes could be built and tested to determine inductances, it is much more economical and convenient to carry out theoretical predictions. However, the method of prediction should be accurate, easy to use and cost effective. This

chapter is about the development of such a method. The requirement for relatively high accuracy ruled out purely analytical methods. Consequently the adopted method was numerical. In this chapter the theoretical basis behind the method is explained and test results are presented which confirm its validity.

Stator inductance may also be required to estimate the size of current ripple at a particular PWM frequency. For this purpose, a first order estimation may be sufficient. A closed form formula for first order estimation of the stator inductance is given in appendix C.

7.2 Basic Principles

By definition the self inductance of a circuit is equal to the flux linking that circuit per ampere of current flowing through it with all other circuits, to which it is magnetically coupled, open-circuited. At first the impossibility of open-circuiting eddy current loops within the permanent magnets and the rotor iron appears to be a difficulty. But this is conveniently resolved by an alternative, but more appropriate, definition of stator self inductance. The inductance of a particular stator phase is defined, at a particular frequency, as flux linkage per ampere of sinusoidal current flowing through that phase with the other two phases open-circuited. This definition is appropriate for the application being looked at because the self-inductance evaluated or measured is based on flux distribution that closely resembles the one which would exist under normal operating conditions. The selected frequency is taken to be the PWM frequency that the BLDC motor drive would use.

Based on the above definition, the requirement for inductance calculation would be knowledge of the flux distribution in the BLDC motor when sinusoidal current flows in one of its phase windings. That flux distribution is influenced by eddy currents flowing in the magnets as well as in the rotor. Therefore the quasi static solution to Maxwell's equations is required. Due to the complexity of the geometry an analytical solution is not possible. A number of numerical techniques have been developed to solve the quasi-static form of Maxwell's equations. These include the finite element method (FEM), the finite difference time domain method, the coupled network method and the assumed flux path method. Each of those methods has advantages and disadvantages. For example the FEM has the advantage of giving accurate results, but it requires expensive software that can be hard to use and computation times can be long. The assumed flux path method is good as a first approximation, it is computer resource efficient and processing time is small. Its main disadvantages are that customised software has to be written for each problem and that good prior knowledge of the main flux paths is necessary. The technique being used is a combination the assumed flux path method and the coupled network method.

A number of simplifications were necessary to arrive at a solution that is satisfactory in terms of computer resource requirements, processing time, software development effort and accuracy. The actual geometry of the problem is represented in figure 7.1. The main difficulty is the three dimensional nature of the problem. It has been possible to reduce the actual problem to what is effectively a two dimensional problem by making three reasonable assumptions. These are:

(a) The stator coils which are in reality spirals, as shown in figure 7.2(a), have been replaced by a number of separate turns, as shown in figure 7.2(b).

(b) Throughout the region of interest the magnetic flux density component along the direction of the conductors shown in figure 7.2(b) is equal to zero.

(c) Phase inductances are made up of an offset component and a sinusoidal component with extrema at locations where the magnetic axis of the phase winding aligns with the rotor direct and quadrature axes.

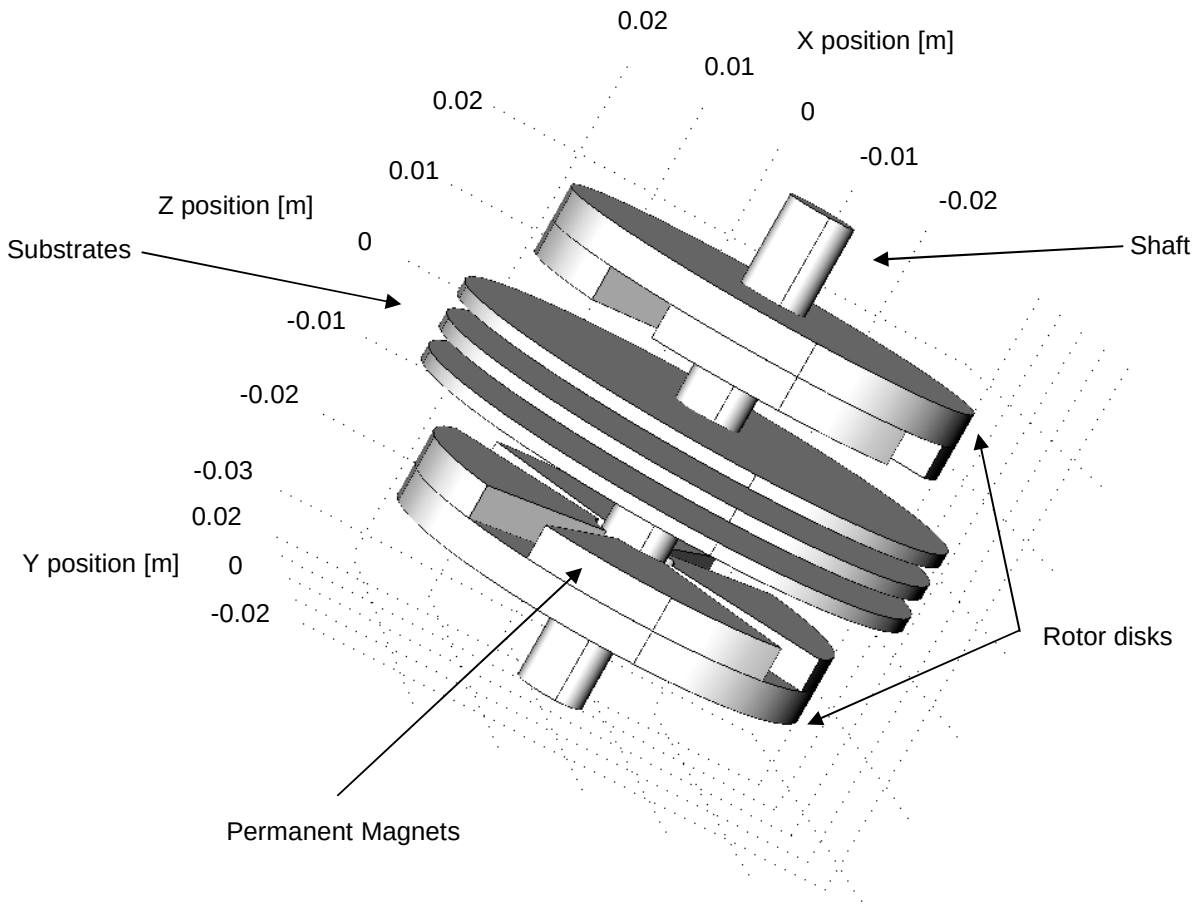

Figure 7.1 : Overall Problem Geometry

As a consequence of the last assumption the inductance at any rotor position may be deduced from two inductance values evaluated at two different rotor positions. The chosen rotor positions for inductance evaluation give the direct axis inductances and the quadrature axis inductances.

7.3 Prediction of Direct Axis Inductances

7.3.1 The Coupled Network Model

As shown in figure 7.2(b), the phase winding has been replaced by a set of infinitely thin conductors.

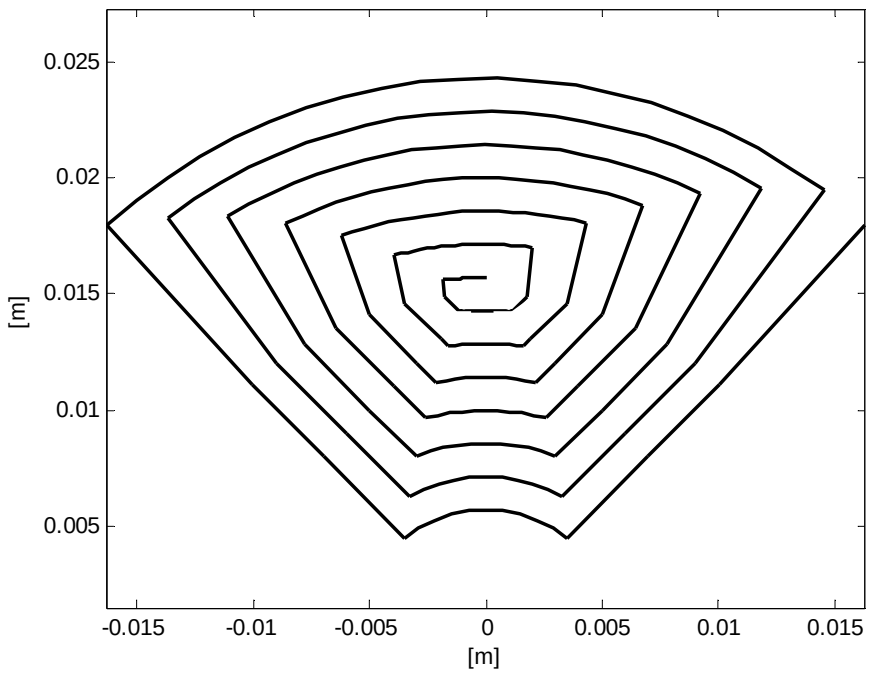

a)

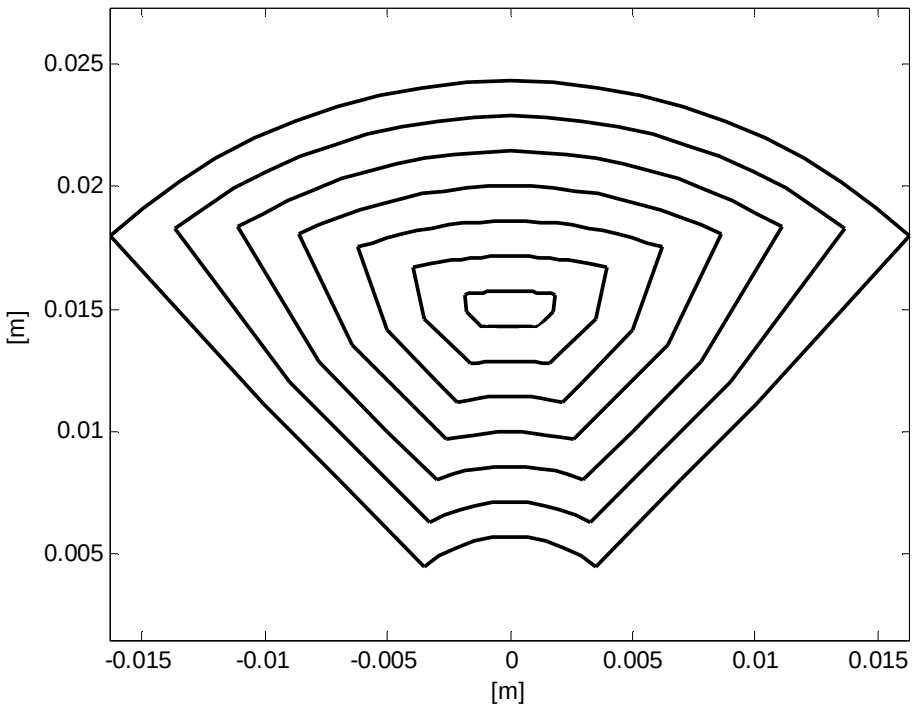

b)

Figure 7.2(a) : Actual Spiral, (b): Current Loop Approximation

The coupled network method is essentially about replacing a physical electromagnetic structure by a reluctive network which is mutually coupled with a resistive network. In general the reluctive network is made up of a set of nodes with reluctive branches connecting neighbouring nodes. The diagram in figure 7.3 includes a layer of magnetic nodes that are just above the conductors representing the stator coils. There are layers of nodes in equally spaced planes parallel to the coil plane. In particular there is a plane of nodes just below the plane of the stator coil. Every plane has the same number of nodes and the nodes line up in the axial direction. Note that there are no magnetic nodes on the plane of the coil.

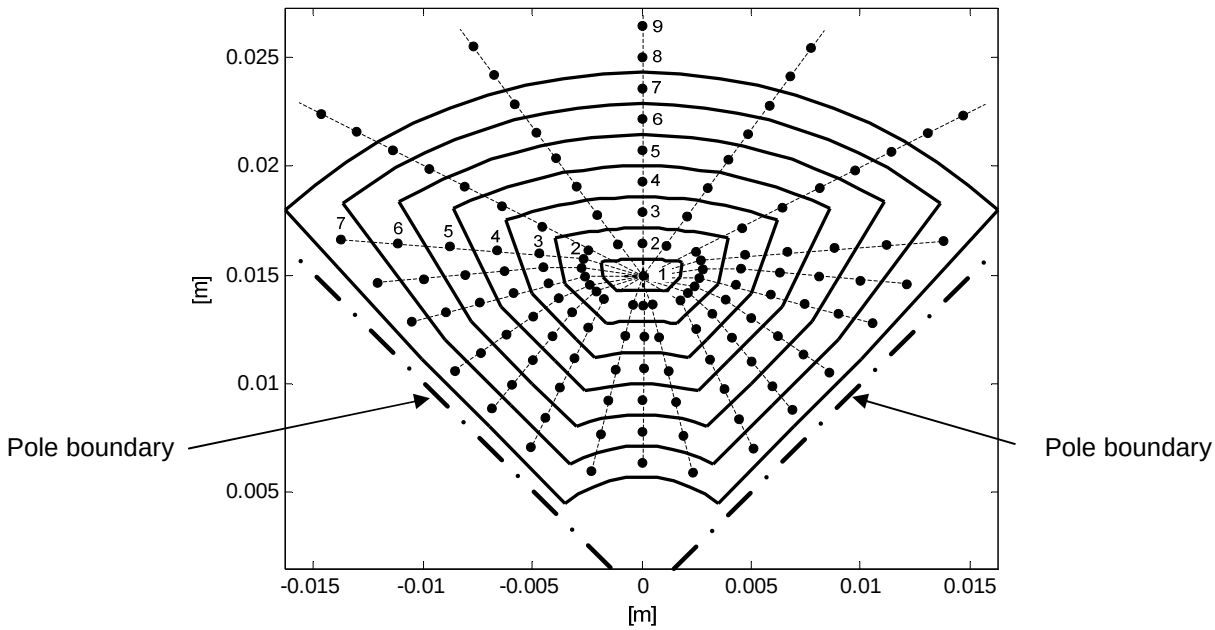

Figure 7.3 : Magnetic Nodes

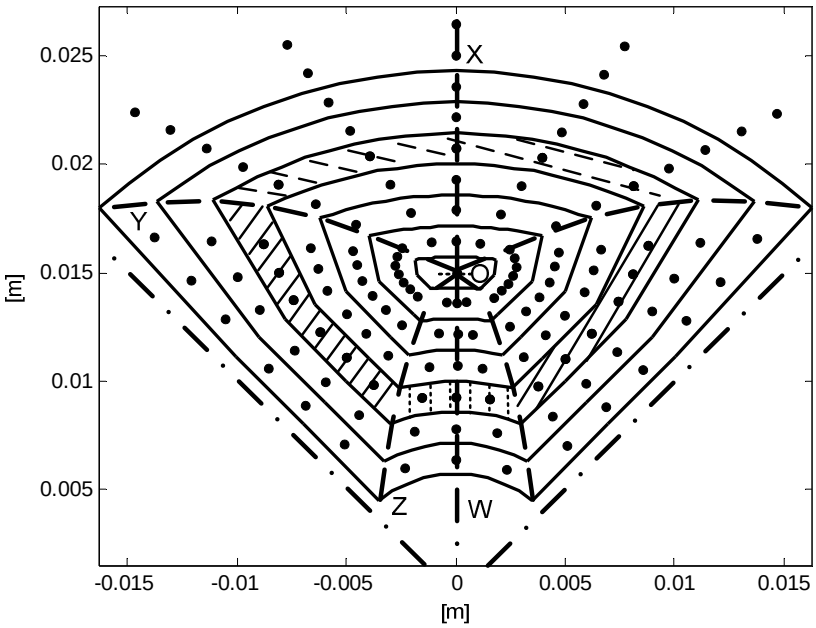

Figure 7.4 : Grouping of Magnetic Nodes

Assumption (b) in section 7.2 states that there is zero flux along branches between neighbouring nodes that lie between two conductors and that fall in the same plane. For example there is no flux in the branches joining neighbouring pairs of the nodes that are shown in the shaded area of figure 7.4. This means that those nodes are at the same magnetic potential and therefore they can be joined together to form single nodes. As shown in figure 7.5, the nodes have been joined to form three planar networks. In section 7.3.1, it is shown that the use of three networks rather than a single one allows flexibility in setting realistic boundary conditions. All the nodes between 0W and 0Z in figure 7.4 have been joined appropriately to form the planar network in figure 7.5(a). For example all nodes between those lines have been joined to form nodes a1, a2, a3, a4, a5, a6 and a7.

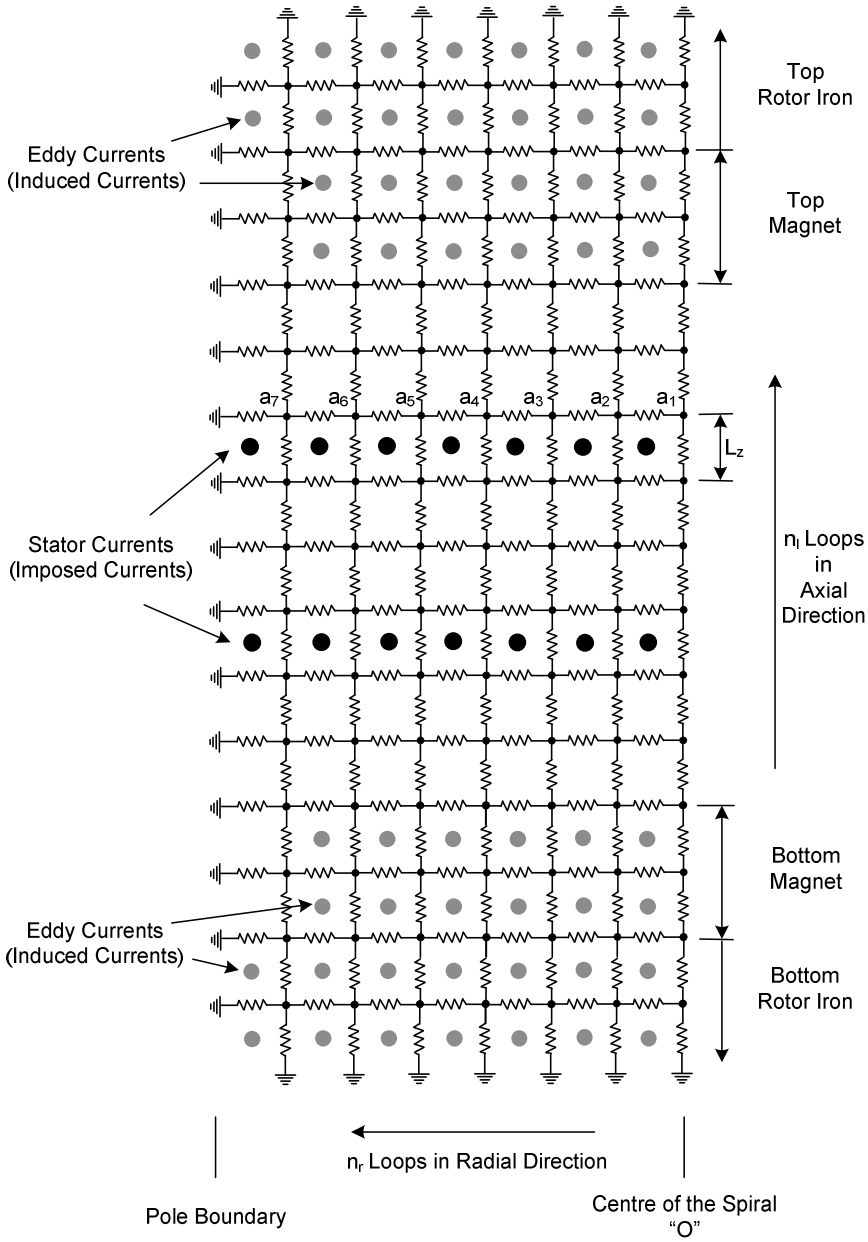

Figure 7.5(a) : Planar Reluctive Network

Similarly all nodes shown between 0Z and 0Y in figure 7.4 have been joined to form the planar network in figure 7.5(b).

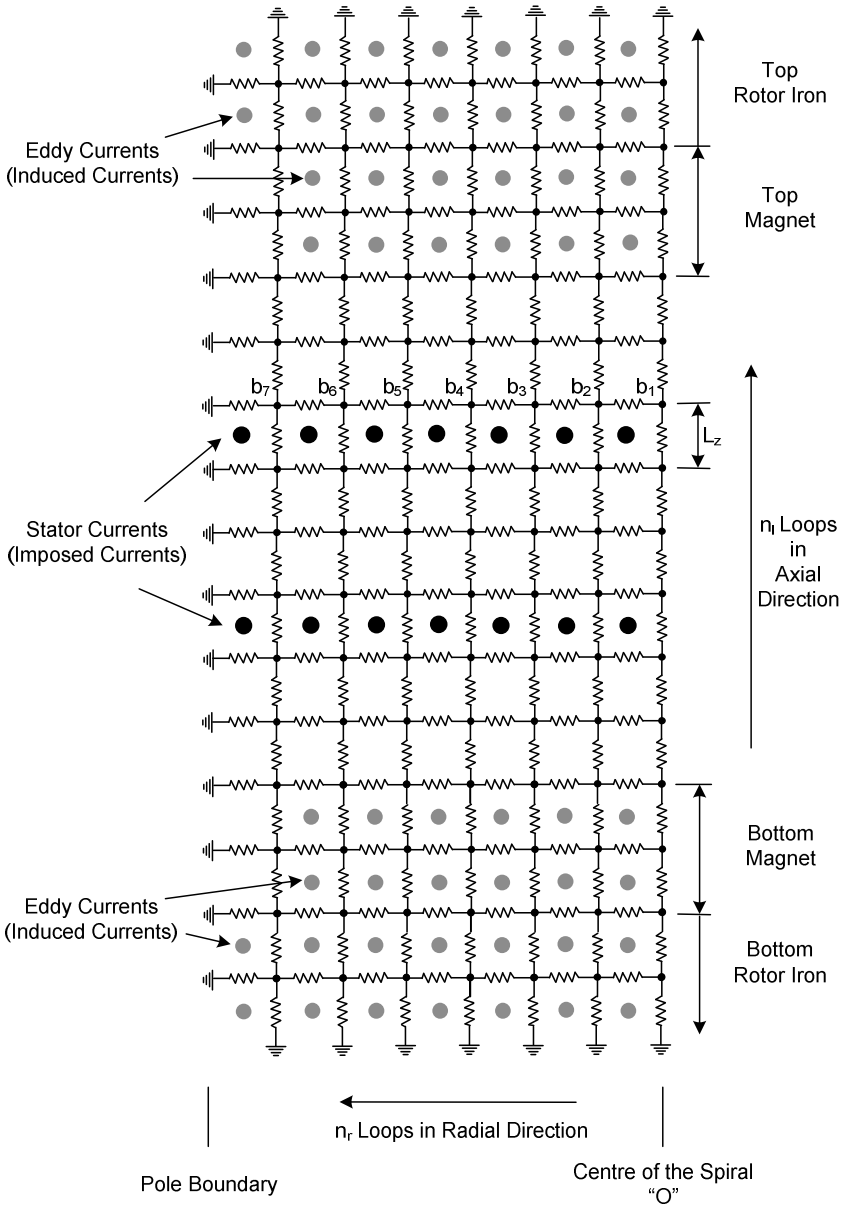

Figure 7.5(b) : Planar Reluctive Network

For example all nodes between those lines have been joined to form nodes b1, b2, b3, b4, b5, b6 and b7 in the planar network of figure 7.5(b).

All nodes between 0Y and 0X in figure 7.4 have been joined appropriately to form the planar network in figure 7.5(c).

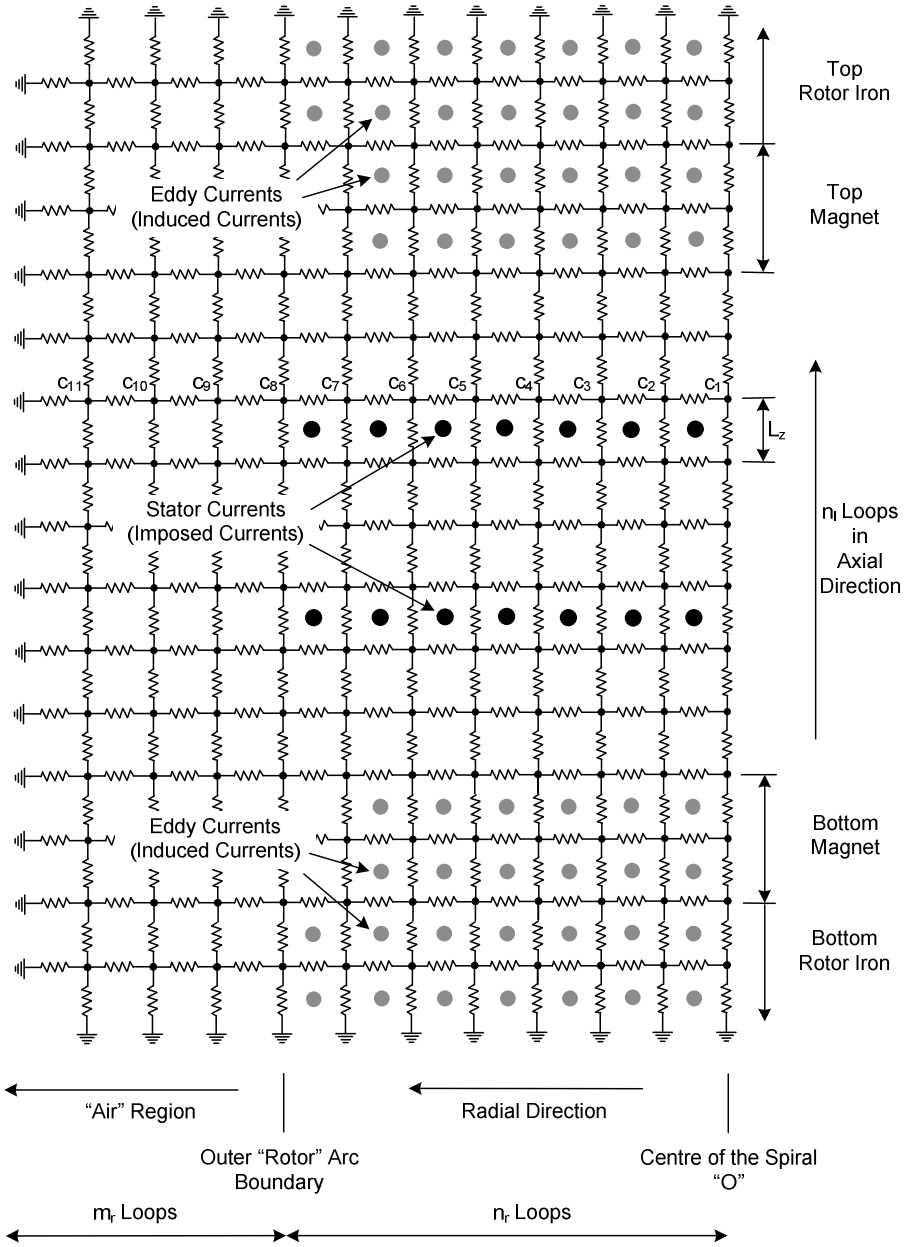

Figure 7.5(c) : Planar Reluctive Network

It has been assumed that electric currents, whether imposed or induced, flow only in planes parallel to the stator coil plane. Electric circuits link the magnetic network as shown in figures 7.3 and 7.5. Both imposed and induced currents are represented in figure 7.5. The imposed current is the current flowing through one phase of the stator, the other two phase windings being open circuited. Currents are induced in the magnets and in the rotor iron.

7.3.2 Branch Reluctance and Loop Resistances

The reluctance in the axial direction R_z up to the outer edge of the rotor iron, is given by:

$$R_z = \frac{L_z}{\mu A_z} \tag{7.1}$$

where:

L_z = axial separation (defined in figure 7.5)

A_z = area between conductor loops (as defined for each network in figure 7.4)

μ = permeability of material

The reluctance in the radial direction R_r , is given by

$$R_r = \frac{L_r}{\mu A_r} \tag{7.2}$$

where:

L_r = mean separation between inter-conductors mid-lines as shown in figure 7.6

A_r = (conductor perimeter) x (axial separation)

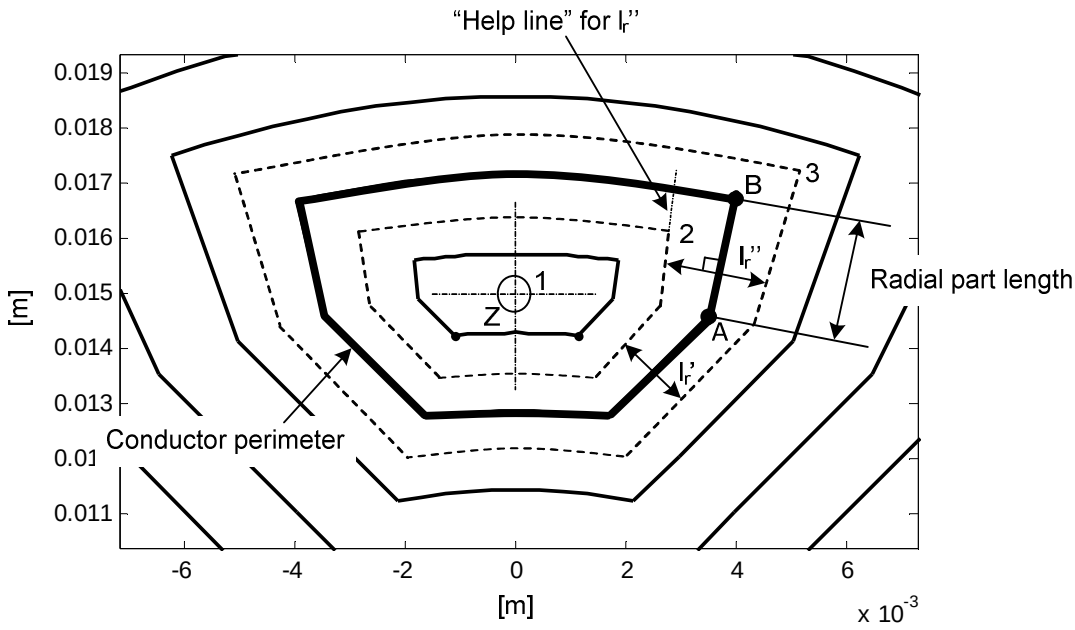

Figure 7.6 : Definition of 'radial' Length Lr

Note:

a) The same formulae are used for calculation of reluctances in the stator region, air-gap region, magnet region or iron region. For the first three regions a relative permeability of one was used. For the iron region the value of permeability was based on flux density distribution in the iron due to the magnets. The flux density distribution was obtained from a 3-D non-linear magnetostatic solution generated by FEA.

b) Equations similar to (7.1) and (7.3) were used for branch reluctances of network 7.5(c) which fall in the region beyond the outer radius of the machine.

The resistance of the stator current loops are not required because stator currents are imposed currents. Resistance values are required for the loops representing eddy current paths in the

magnet and in the rotor iron. As shown in figure 7.5, the magnet and the rotor iron are sliced in layers parallel to the stator coil. Each layer has its own set of current loops. Figure 7.7 shows the magnet profile superimposed on the stator conductor loops. For all the magnet and rotor iron conducting loops except for the outermost ones in the magnet,

$$R = \frac{perimeter_{conductor}}{\sigma L_r L_z} \tag{7.3}$$

where:

σ = conductivity of the magnet.

The outermost eddy current loop has a perimeter that is equal to the average of the perimeter of the stator conductor that falls fully within the magnet profile and the perimeter of the magnet. Equation (7.3) is still used to calculate the resistance of the loop but with cross-sectional area equal to L_z times the average of L_x. As shown in figure 7.7, L_x is the weighted average of all discrete distances between the last stator conductor that falls fully within the magnet profile and the edge of the magnet.

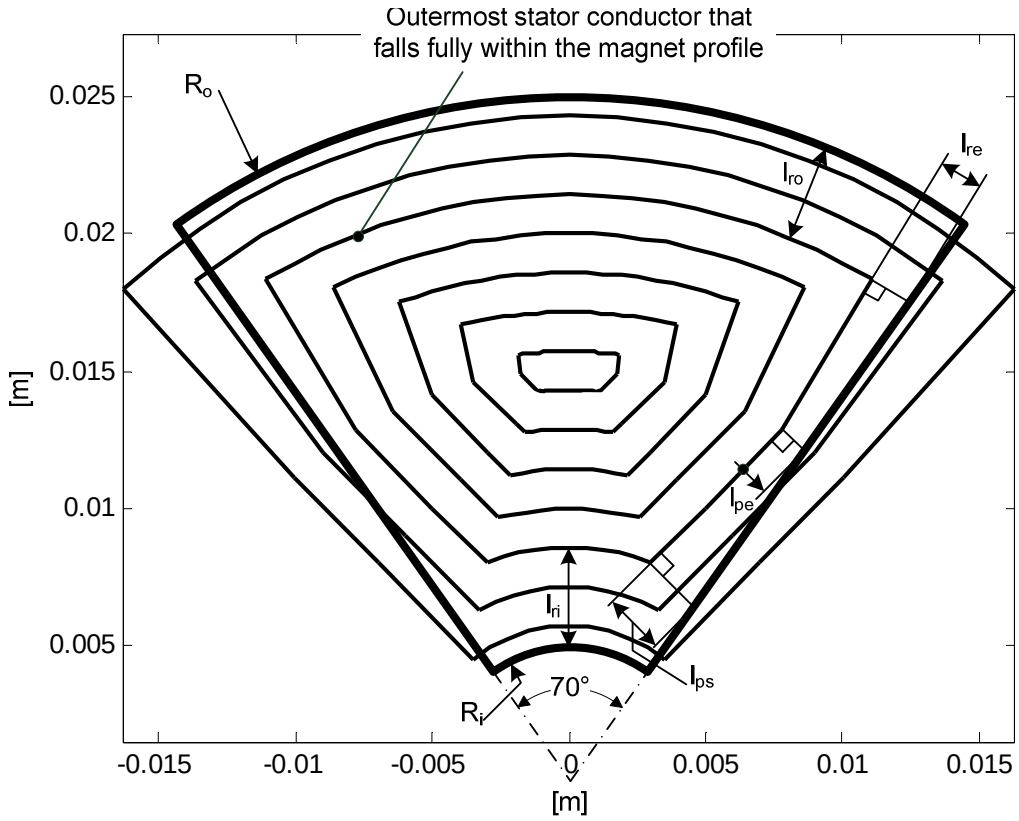

Figure 7.7 : Calculation of Eddy Current Loop Resistances

7.3.3 Boundary Conditions

At the centre of the spiral it is assumed that the flux density is purely axial. Hence, as shown the right hand side in figure 7.5, a zero flux or magnetic insulation condition is assumed. The left hand side of figure 5(a) and 5(b) corresponds to the outer periphery of the stator coil. The reluctive branches on that side represents magnetic paths back to the magnetic zero potential plane which is the plane separating neighbouring stator coils or neighbouring rotor magnets.

That plane also contains the quadrature axis. In calculating the reluctance of those branches equation 7.2 has been used. The radial lengths were arrived at as follows:

a) For network b), a weighted average 'radial' distance has been used as shown in figure 7.8
b) For network c), the radial length was assumed to be made up of two sections as shown in figure 7.8

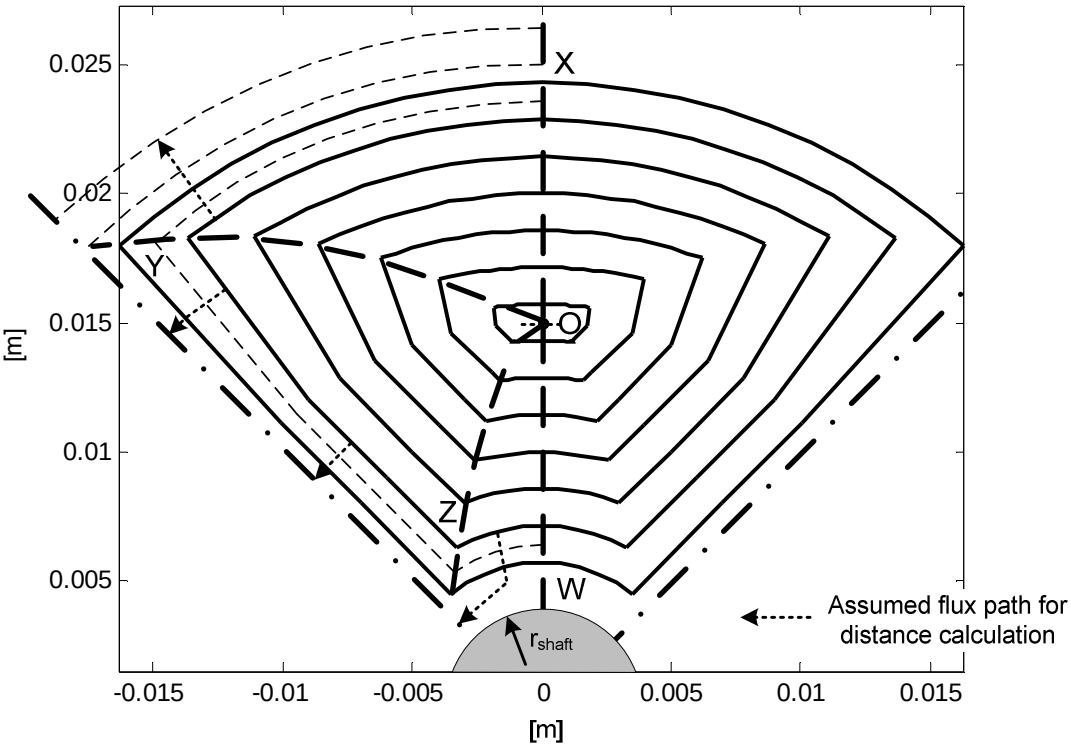

Figure 7.8 : Calculation of radial Distance at Boundary

The left hand side of figure 7.5(c) represents the boundary conditions at the outer arc shown in figure 7.3.

The network in figure 7.5(c) was extended sufficiently enough in the radial direction so that it did not matter whether the adopted boundary condition at the radial boundary was a magnetic short-circuit or a magnetic open-circuit.

7.3.4 Magnetic Circuit Loop Analysis

Ampère's Law states that:

$$\oint Hdl = enclosed\ current \tag{7.4}$$

The above equation is analogous to Kirchhoff's voltage law for electric circuits. It states that the summation of magnetic potential drops around a loop in a magnetic network is equal to the current enclosed by that loop.

Magnetic potential drop = Reluctance x Branch Flux (7.5)

Branch flux is related to loop flux in exactly the same way that branch currents and loop currents in an electrical circuit are related to each other. Examples of flux loops are given in figure 7.9. Magnetic loop analysis results in the following matrix equation:

$$\begin{bmatrix} M_{aa} & M_{ab} & M_{ac} & M_{ad} \\ M_{ba} & M_{bb} & M_{bc} & M_{bd} \\ M_{ca} & M_{cb} & M_{cc} & M_{cd} \\ M_{da} & M_{db} & M_{dc} & M_{dd} \end{bmatrix} \begin{bmatrix} \phi_a \\ \phi_b \\ \phi_c \\ \phi_d \end{bmatrix} = \begin{bmatrix} I_a \\ I_b \\ I_c \\ I_d \end{bmatrix} \tag{7.6}$$

or $M\phi = I$

where:

M_{aa}, M_{bb}, M_{ac}, …, M_{cb} and M_{cc} are n x n submatrices

M_{ad}, M_{bd}, M_{cd} are n x m submatrices

M_{da}, M_{db}, M_{dc} are m x n submatrices

M_{dd} is m x m matrix

ϕ_a, ϕ_b, ϕ_c are n x 1 loop flux vectors

ϕ_d is an m x 1 loop flux vectors

I_a, I_b, I_c are n x 1 imposed current vectors

I_d is an m x 1 imposed current vector

M is an (n+m) x (n+m) matrix

n, equal to n_r x n_l is the number of loops in network 5(a) or 5(b), made up of n_r loops in the radial direction and n_l loops in the axial direction.

(n+m), equal to (n_r + m_r) x n_l, is the number of loops in network 5(c).

$$\phi = \begin{bmatrix} \phi_a^T & \phi_b^T & \phi_c^T & \phi_d^T \end{bmatrix}^T$$

$$I = \begin{bmatrix} I_a^T & I_b^T & I_c^T & I_d^T \end{bmatrix}^T$$

The loop flux vectors are unknowns that need to be determined. The imposed currents are assumed to be known. The real part of the diagonal elements of M_{aa}, M_{bb}, M_{cc} and M_{dd} is equal to the sum of reluctances around the loop corresponding to that element. The imaginary part of the diagonal elements of M_{aa}, M_{bb} and M_{cc} is equal to $\frac{j\omega}{R}$ where R is the loop resistance calculated using equation 7.3. If a magnetic loop is not linked by an induced current loop, the corresponding diagonal entry for this loop will have an imaginary part equal to zero. For

example the diagonal matrix entry for loop x in figure 7.9 is (R_{m1} + R_{m2} + R_{m3} + R_{m4} + $\frac{j\omega}{R_x}$) whereas the diagonal entry for loop y is (R_{m5} + R_{m6} + R_{m7} + R_{m4}). The imaginary part of the diagonals elements of M_{dd} is equal to zero.

Each off-diagonal element of M_{aa}, M_{bb}, M_{cc} and M_{dd} is a function of the spatial relation between the two corresponding loops. If the two loops are neighbours then the corresponding matrix entry is equal to $-R_m$ where R_m is the branch reluctance common to the two loops. If the two loops are not neighbours then the corresponding matrix entry is equal to zero.

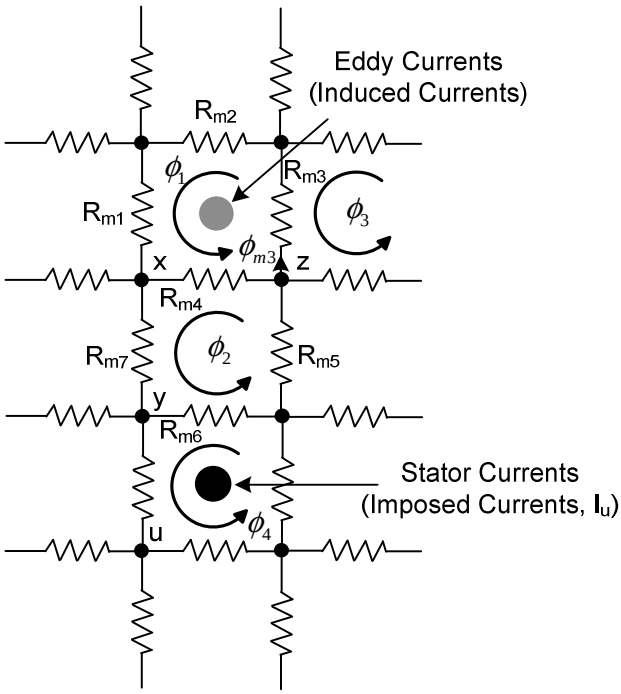

Figure 7.9 : Example of Loop Equations

For example for loop x and loop y the corresponding matrix entry is $-R_{m4}$. For loop y and loop z the corresponding matrix is zero.

The loops have been numbered so that the imaginary part of $M_{aa}(i,i)$ is equal to the imaginary part of $M_{bb}(i,i)$ and $M_{cc}(i,i)$. The real parts of all entries of M_{ab}, M_{ac}, M_{ba}, M_{bc}, M_{ca} and M_{cb} are equal to zero. The imaginary part of $M_{ab}(i,i)$, $M_{ac}(i,i)$, $M_{ba}(i,i)$, $M_{bc}(i,i)$, $M_{ca}(i,i)$, $M_{cb}(i,i)$ are all equal to the imaginary part of $M_{aa}(i,i)$. All entries of M_{ad}, M_{bd}, M_{cd}, M_{da}, M_{db}, M_{dc} are equal to zero.

For a magnetic loop that is not linked by an imposed current, the corresponding entry in the imposed current vector will be zero. For example for loop x in figure 7.9, the entry in the imposed current vector will be zero, whereas for loop u it will be equal to I_u. In equation 7.6:

$I_a(i)=I_b(i)=I_c(i)$.

All the entries of I_d are equal to zero.

From equation 7.6 we have:

$$\begin{bmatrix} \phi_a \\ \phi_b \\ \phi_c \\ \phi_d \end{bmatrix} = \phi = M^{-1} I \tag{7.7}$$

Once loop fluxes have been obtained from equation 7.7, branch flux, if needed can be easily deduced. From example branch flux ϕ_{m3} in figure 7.9 is equal to $(\phi_1 - \phi_3)$.

By definition inductance is equal to the flux linkage per ampere. All imposed currents in the model of figure 7.5 are equal to 1 A. Therefore:

$$\text{Coil inductance} = \phi^T I \tag{7.8}$$

Phase inductance = Number of coils x coil inductance x coupling factor (7.9)

The value of the coupling factor is 0.96. This value was found empirically. It represents the magnetic coupling between co-axial spirals on different layers of the printed circuit. This coupling factor may be considered constant for a wide range of stator design.

7.4 Prediction of Quadrature Inductances

Figure 7.10 gives a set of self-inductance measurements made on a prototype machine. All measurements were carried out at 20 kHz with the rotor at standstill.

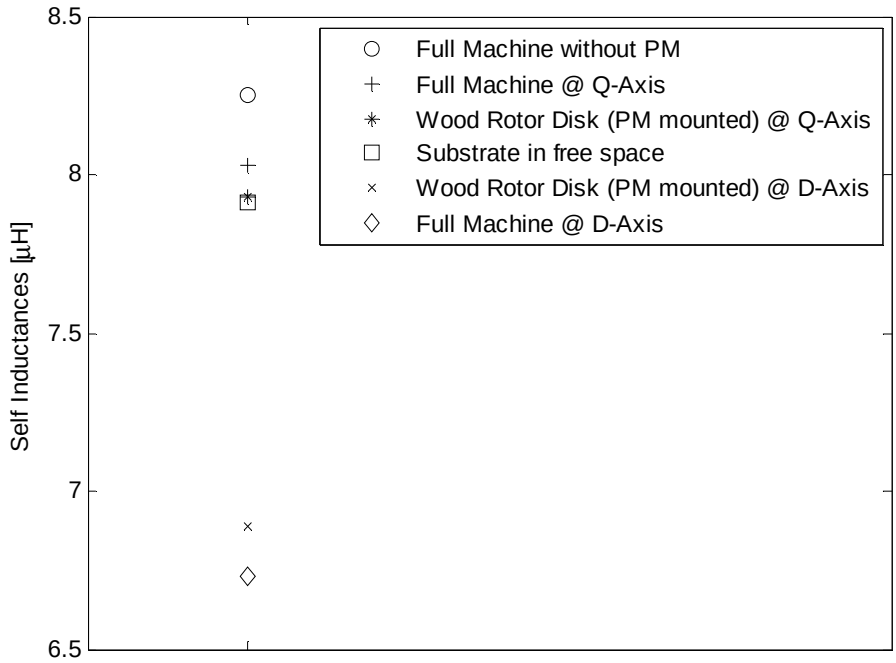

Figure 7.10 : Self Inductance Measurements carried out at 20 kHz with Different Machine Configurations

Two of those measurements were carried out with the iron rotor replaced by a wooden rotor. The normal q-axis inductance (with iron rotors) and the machine inductance without permanent magnets (but with iron rotors) are respectively 8.03 µH and 8.25 µH. These values illustrate that the presence of the permanent magnet has relatively less effect on the q-axis phase inductance. The reason for this is the air-gap between neighbouring magnets. While the magnets still form part of eddy current loops, there are no current loops that are totally within magnets as in the case when stator coils are directly aligned with the rotor direct axis. As shown in figure 7.11 an eddy current loop section that is through a magnet is connected to the rest of the loop, which is within a neighbouring magnet, by loop sections within the rotor iron. The current flowing in loops such as the one shown in figure 7.11 tends to be small compared with the current that would flow in a loop that is totally within a permanent magnet. The reason for this is the high resistance of the loop sections within the iron. Resistance in the iron is higher because of the skin effect. Figure 7.12 illustrates the coupled network model that has been used to evaluate q-axis inductances. The model is technically the same as the one used for the d-axis model as shown in figure 7.5. The same solution procedure was followed. The conductive effect of the magnet was transferred to the current paths representing eddy currents in the rotor.

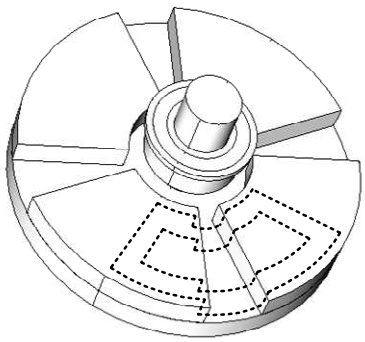

Figure 7.11 : Q-Axis Eddy Current Paths (for graphical clarity only two loops show)

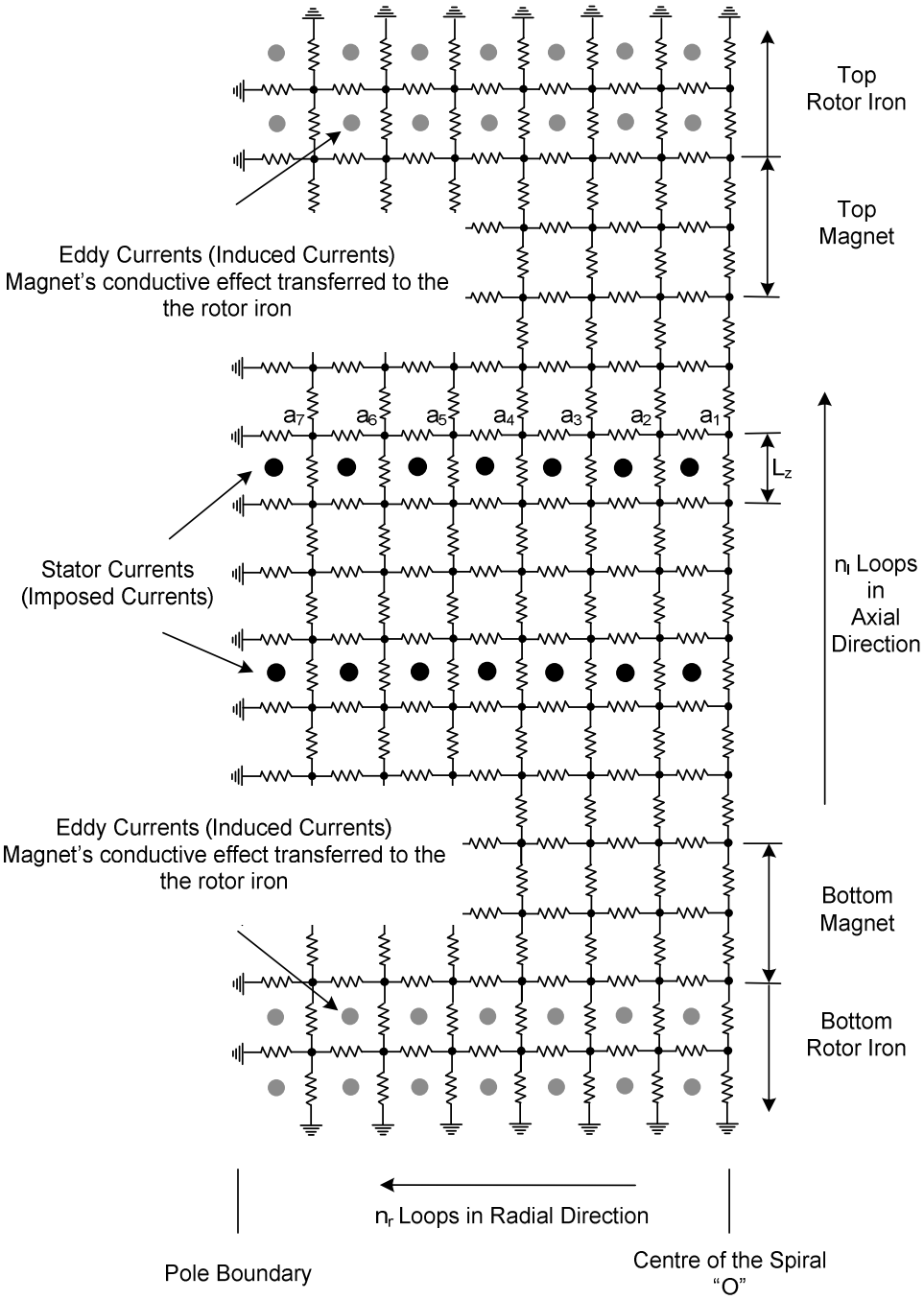

Figure 7.12(a) : Planar Reluctive Network (Q-Axis) between 0W and 0Z

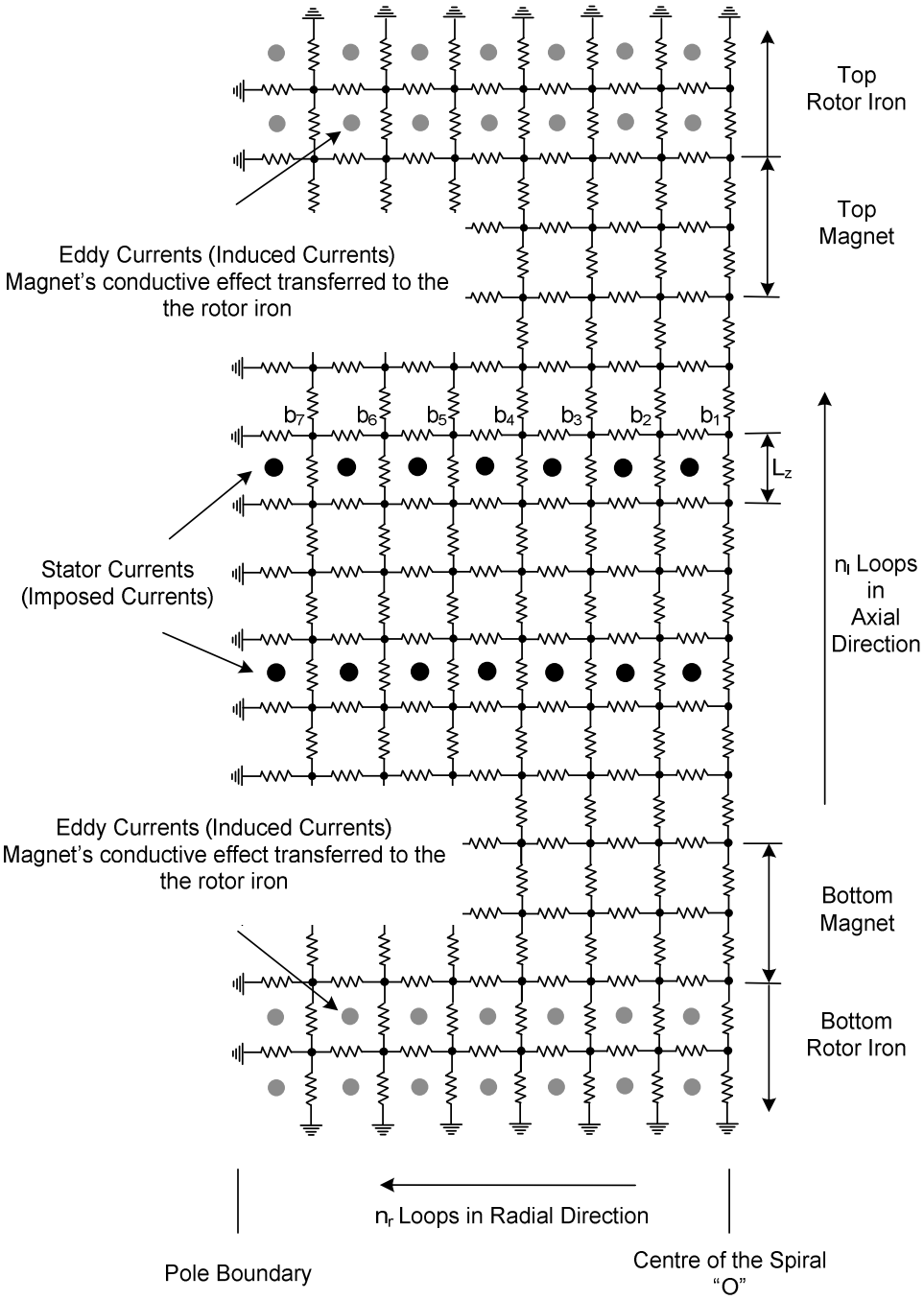

Figure 7.12(b) : Planar Reluctive Network (Q-Axis) between 0Z and 0Y

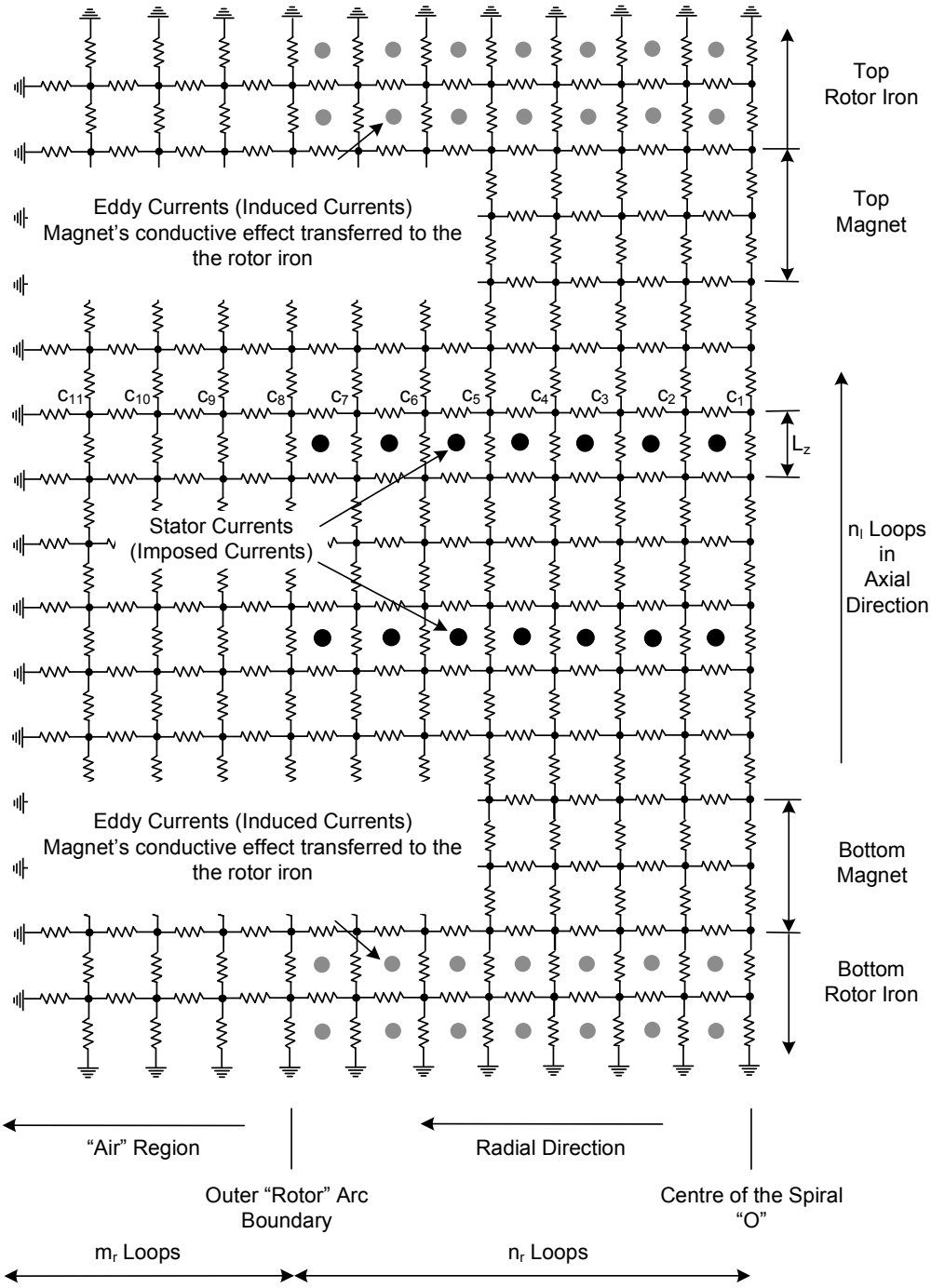

Figure 7.12(c): Planar Reluctive Network (Q-Axis) between 0Y and 0X

This was done by distributing the conductance of the current path through the magnet equally to the assumed rotor eddy current paths. Clearly, this constitutes an approximation. But the error due to this approximation is not greater than about 1.5%.

7.5 Calculation of Mutual Inductances

The procedure to determine mutual inductance consists of two steps. Assuming the mutual inductance between phase ‘a’ and phase ‘b’ is to determined, flux density distribution due to a current of 1 A flowing through the ‘a’ phase winding is first determined. The next step consists of evaluating the flux linking the ‘b’ phase winding.

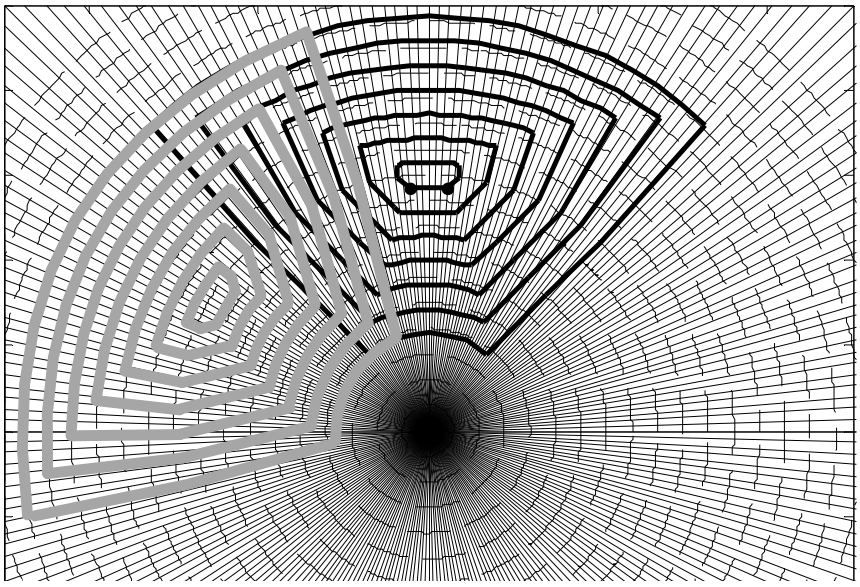

Figure 7.13 : Determination of Mutual Inductance

Refer to figure 7.13. The dotted lines, radial and circumferential, define cells. A value of axial flux density is assigned to each cell. This value is calculated by using the loop flux results from sections 7.3 or 7.4. Flux for each axial branch is obtained in the normal manner. For example in figure 7.9, branch flux ϕ_{m3} in figure 7.9 is equal to $(\phi_1 - \phi_3)$.

Corresponding branch fluxes, one from each of the three networks (figure 7.5 or figure 7.12) are summed to obtain the total flux for the area between neighbouring closed conducting loops. These areas have been termed 'sectors' in figure 7.14. Axial flux density for each cell is defined according to the following rules:

If, as shown in figure 7.14, the cell is not 'cut' by a sector boundary:

$$\text{Axial flux density through cell} = \frac{Flux_{Sector}}{Area_{Sector}} = \frac{\phi_{Sector}}{A_{Sector}} \tag{7.10}$$

If, as shown in figure 7.14, the cell is 'cut' by a sector boundary:

$$\text{Axial flux density through cell} = \frac{A_{CellFractionSector2}\left(\frac{\phi_{Sector2}}{A_{Sector2}}\right) + A_{CellFractionSector3}\left(\frac{\phi_{Sector3}}{A_{Sector3}}\right)}{A_{Cell}} \tag{7.11}$$

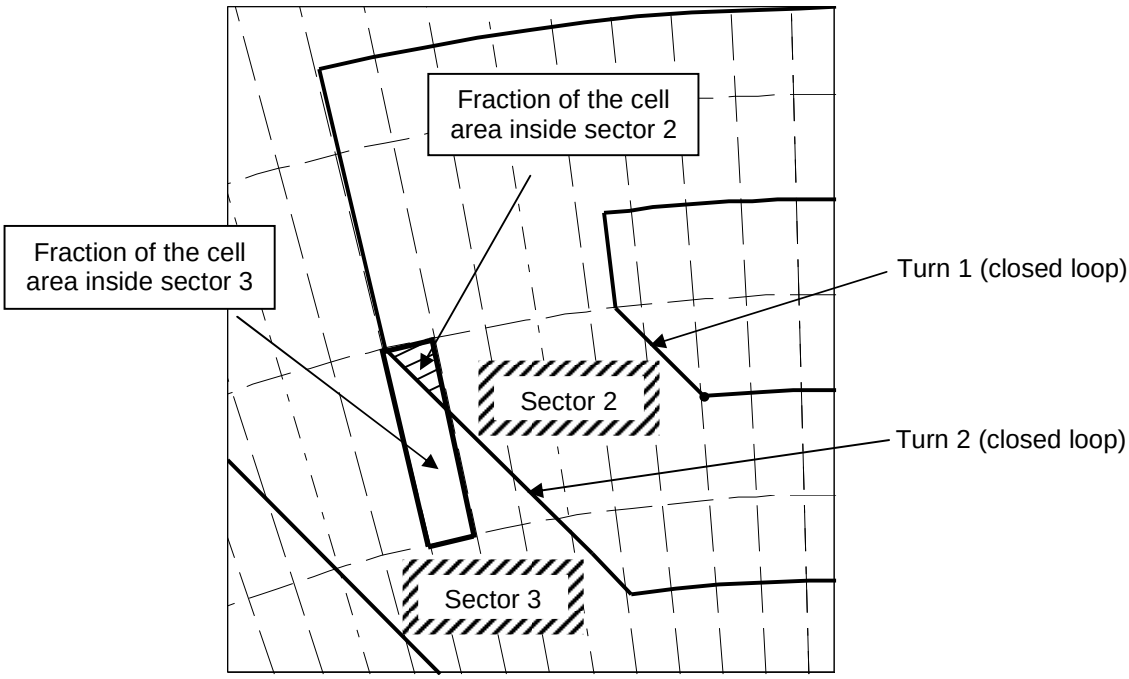

Figure 7.14 : Flux Density Distribution

Once cell flux density due to current in the ‘a’ phase winding has been determined, mutual inductance can be computed. This is done by first calculating the flux linking each turn of the phase winding. Summation of the flux linkage for all turns making up the ‘b’ phase winding gives the mutual inductance between phase ‘a’ and phase ‘b’. The flux linkage for a turn is the total axial flux enclosed by that turn. The total axial flux is computed using the flux density values of each cell that fall within the turn. A cell that is ‘cut’ by the turn contributes an amount of flux that is proportional to its area that falls within the turn.

Examples of calculated flux density distributions due to a stator coil of 1 A are given in figures 7.15 and 7.16.

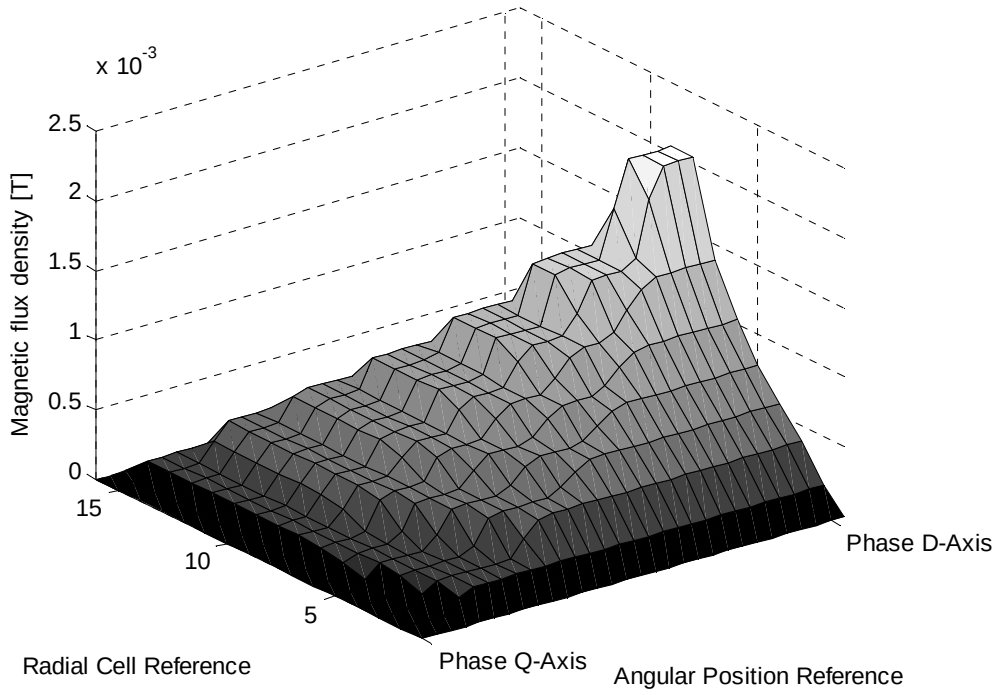

Figure 7.15 : Calculated Flux Density Distribution due to Stator Current (a-phase only energised and a-phase aligned with d-axis)

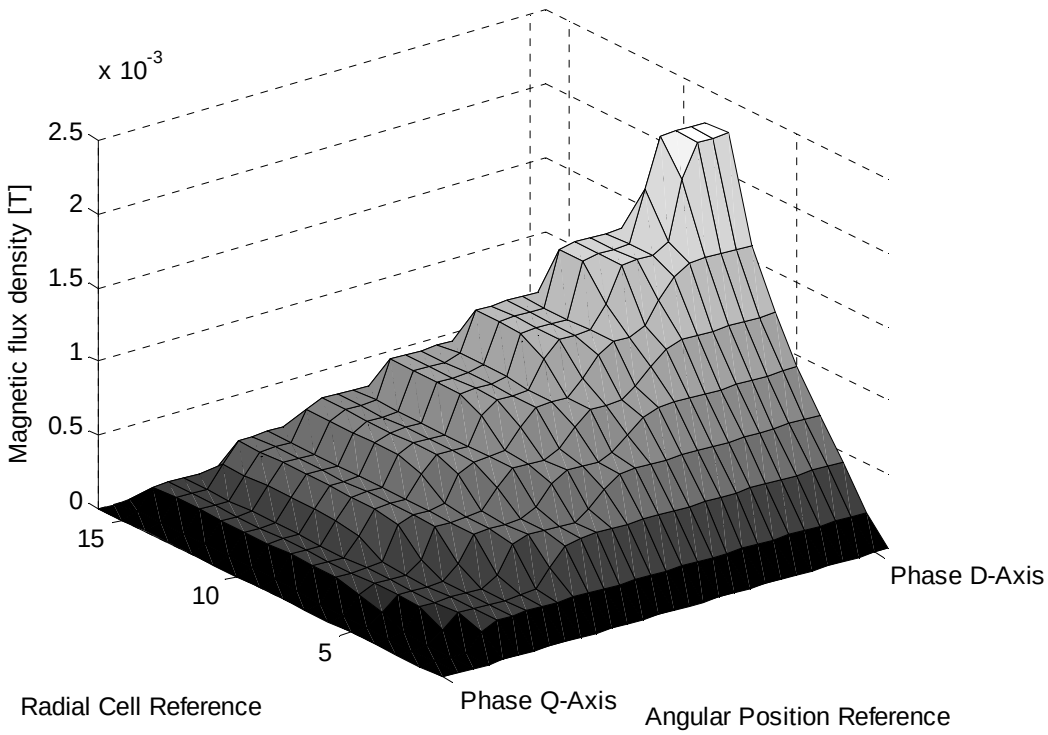

Figure 7.16 : Calculated Flux Density Distribution due to Stator Current (a-phase only energised and a-phase aligned with q-axis)

7.6 Experimental Validation

As stated in chapter 5, the assumption is that self and mutual inductances satisfy the following equation:

$$L_{aa} = L_{s0} + L_{s2}\cos(2\theta) \tag{7.12}$$

$$L_{bb} = (L_{s0} + \Delta L_{s0}) + (L_{s2} - \Delta L_{s2})\cos\left(2\theta + \frac{2\pi}{3}\right) \tag{7.13}$$

$$L_{cc} = L_{s0} + L_{s2}\cos\left(2\theta - \frac{2\pi}{3}\right) \tag{7.14}$$

$$L_{ab} = L_{ba} = -L_{m0} + L_{m2}\cos\left(2\theta - \frac{2\pi}{3}\right) \tag{7.15}$$

$$L_{bc} = L_{cb} = -L_{m0} + L_{m2}\cos(2\theta) \tag{7.16}$$

$$L_{ca} = L_{ac} = -(L_{m0} - \Delta L_{m0}) + (L_{m2} - \Delta L_{m2})\cos\left(2\theta + \frac{2\pi}{3}\right) \tag{7.17}$$

It can be deduced, based on the above assumption, that four self-inductance and four mutual inductance values are needed to fully describe the stator's inductance behaviour as rotor position changes. The chosen four self-inductances are L_{da}, L_{db}, L_{qa} and L_{qb} which are respectively the direct and quadrature axis self-inductances of phase 'a' and 'b'. The chosen mutual inductances M_{bd}, M_{cd}, M_{bq} and M_{cq} which are respectively mutual inductances when phase 'a' is aligned with the rotor direct axis and quadrature axis. Table 7.1 and 7.2 give measured and predicted values for L_{da}, L_{db}, L_{qa}, L_{qb}, M_{bd}, M_{cd}, M_{bq} and M_{cq}. The measured and predicted values correlate within less than 3%.

Measurements were carried out at 20 kHz which is the switching frequency of the PWM voltage applied to the test motor during normal operation. A commercial instrument was used to measure self inductances. Based on the rated accuracy of the instrument the estimated maximum error in the measured self-inductance is ±0.05 μH.

The mutual inductances were measured were determined by energising one phase with a known (measured) current and measuring the voltages induced in the other windings. The estimated maximum error due to instrument inaccuracies is ±0.1 μH.

Table 7.1: Measured and Predicted Self Inductances

		Magnet Pitch [°]	
		70	60
L_{da} [μH]	Measured	6.58	6.89
	Predicted	6.64	6.99
L_{db} [μH]	Measured	6.78	7.09
	Predicted	6.82	7.17
L_{qa} [μH]	Measured	8.06	8.19
	Predicted	7.99	8.08
L_{qb} [μH]	Measured	7.97	8.13
	Predicted	7.92	8.04

Table 7.2: Measured and Predicted Mutual Inductances

		Magnet Pitch 70 [°]
M_{bd} [μH]	Measured	-1.52
	Predicted	-1.56
M_{cd} [μH]	Measured	-2.26
	Predicted	-2.30
M_{bq} [μH]	Measured	-2.75
	Predicted	-2.72
M_{cq} [μH]	Measured	-3.68
	Predicted	-3.64

Machine constants k_1, k_2, k_3, k_4 and k_5 which were defined in chapter 5, need to be pre-loaded into memory of the BLDC motor controller. As per equations (5.22) to (5.26), constants are expressed in terms of L_{s0}, L_{s2}, L_{m0}, L_{m2}, ΔL_{s0}, ΔL_{s2}, ΔL_{m0} and ΔL_{m2} which are deduced by using:

$$L_{s0} = \frac{\left(L_{da} + L_{qa}\right)}{2} \tag{7.18}$$

$$L_{s2} = \frac{\left(L_{qa} - L_{da}\right)}{2} \tag{7.19}$$

$$\Delta L_{s0} = \frac{\left(L_{db} + L_{qb}\right)}{2} - \frac{\left(L_{da} + L_{qa}\right)}{2} \tag{7.20}$$

$$\Delta L_{s2} = \frac{\left(L_{qa} - L_{da}\right)}{2} - \frac{\left(L_{qb} - L_{db}\right)}{2} \tag{7.21}$$

$$L_{m0} = -\frac{\left(M_{bd} + M_{bq}\right)}{2} \tag{7.22}$$

$$L_{m2} = -\frac{\left(M_{bq} - M_{bd}\right)}{2} \tag{7.23}$$

$$\Delta L_{m0} = \frac{\left(M_{cd} + M_{cq}\right)}{2} - \frac{\left(M_{bd} + M_{bq}\right)}{2} \tag{7.24}$$

$$\Delta L_{m2} = \frac{\left(M_{cq} - M_{cd}\right)}{2} - \frac{\left(M_{bq} - M_{bd}\right)}{2} \tag{7.25}$$

Table 7.3 presents a comparison between values of machine constants k_1 to k_5 based on theoretical prediction and those based on measurements.

Table 7.3: Comparison between Values of k_1 to k_5

k_1	Measured	0.1978
	Predicted	0.1846
k_2	Measured	0.1813
	Predicted	0.1692
k_3	Measured	0.0162
	Predicted	0.0148
k_4	Measured	0.0836
	Predicted	0.0832
k_5	Measured	0.2856
	Predicted	0.3035

There is reasonable agreement between measured and predicted values. It should be noted that expected values of k_3 and k_4 are relatively small. This means that the percentage discrepancy between predictions and measured values could be large. The error values in table 7.3 are useful in that they provide designers with some idea of the expected range within which the actual values of k_1 to k_5 are likely to be. Sensitivity analysis can be carried out to ensure that operation in the sensorless mode will be satisfactory over the expected range of k_1 to k_5.

7.7 Concluding Remarks

As expected, this chapter is based on well-known equations that define the inductances of electrical machines. However the techniques that have been developed to evaluate those inductances are new. The techniques are based on representation of the machine by a coupled network model. The main advantages of the proposed network are computational efficiency and its flexibility. Difficulties arise with traditional finite element methods because of geometric complexities and large aspect ratios of components such as air-gaps and tracks. With the proposed method computation mesh resolution did not have to be greater than 0.04 mm and computation times were less than 75 seconds.

Chapter 8

Conclusions

8.1 Thesis Project Achievements

The aim of this thesis project was to develop low cost systematic methods that will allow design optimisation of sensorless axial field printed circuit brushless DC motors. In achieving this aim a number of design tools have been developed and experimentally validated. Also a new sensorless technique, based on inductive saliency, has been developed and tested. A summary of the innovative features of the design tools and the sensorless technique are given below.

(d) Design equations have been derived based on geometric analyses which allow the number of turns per printed stator coil to be maximised for commonly used coil shapes. The coil shapes considered were the rhomboidal coil, the parallel coil and the radial coil.

A mixed track shape, partly radial and partly parallel was developed and was found to be the most effective shape from the point of view of torque production. The design equations require stator inner radius, stator outer radius, clearance between tracks and track width need to be specified. The raw calculated value for maximum number of turns is generally a non-integer which needs to be rounded down to the nearest integer. This provides an opportunity to increase the track width to a value higher than the original specification.

(e) The design equations mentioned in (a) above were used to develop an algorithm and a computer program which automatically plots the spiral shaped stator coil tracks. The electronic version of the track plots can and have been used as input to the PCB manufacturing process.

(f) The track plots were also used as input to another computer program which predicts instantaneous winding EMFs and compares torque capability of alternative coil stator designs. The program imports flux density distribution data from a 3-D non-linear magnetostatic finite element (FEM) model of the motor. FEMLAB® was used for the FEM model. The non-linearity results from the magnetic behaviour of the rotor being represented by its measured magnetic saturation curve. The program uses the flux density information to evaluate instantaneous phase EMFs at a given rotational speed. Using the track plot it also evaluates the per phase resistance. For a given maximum allowable resistive power loss, the torque capability of a motor is proportional to its phase back EMF and inversely proportional to the square root of the phase resistance.

The program can therefore be used for objective comparison of motor designs using different track shapes. It was deduced, by using the program that the mixed track shape results in highest torque capability for given stator dimensions. The program can also be used to select rotor, magnet and stator axial dimensions that would result in the highest torque rating for a given motor space envelope.

(g) The track width determined by the program described in (c) above needs to be constrained to avoid excessive eddy current losses induced in the stator copper. A numerical model for prediction of stator eddy current distribution has been developed. The model, which has been validated by test results, is based on the assumption that the eddy currents are resistively limited. In other words the inductive effects of the eddy currents are neglected. This greatly simplifies the algorithm for determination of the eddy current distribution. The computer program that determines the stator eddy current loss distribution imports flux density distribution data from the 3-D non-linear magnetostatic finite element (FEM) model described in (c) above. The copper tracks are represented by two dimensional resistive grids. The voltage induced in each loop of the grids at a given rotor speed is determined by using Faraday's Law. The currents in each branch of the grid are then determined by using loop analysis. Once the branch currents are known, eddy current loss distribution and parasitic torque due to the eddy currents are calculated. It was found that for the prototype machines, whose tracks were 1 mm wide, stator eddy current loss was negligible compared to the full load stator I^2R loss.

(h) The adopted sensorless commutation technique is based on the previously reported equal inductance method which is based on the existence of stator inductive saliency. The advantage of the equal inductance method over the very widely used back EMF zero crossing method is that it is effective down to zero speed. The back EMF zero crossing method does not work below a certain level of back EMF, which means that it is useless at low speeds. The equal inductance method is very suitable as a complement the back EMF method. As part of this thesis project the originally proposed commutation algorithm, based on the equal inductance method, was enhanced to achieve motor start-up with practically zero back rotation. The enhancement consists of detection of the motor's initial position and energising of correct phase pair so that rotation takes place in the desired direction.

The previously proposed equal inductance method was based on the assumption of stator three phase symmetry. The printed circuit motors considered in this thesis project, because of the axial position of their stators phases, exhibit significant phase asymmetry. As a result, the equal inductance method had to be generalised to make it applicable to those motors. Test results confirmed the effectiveness of the generalised equal inductance method.

(i) In the case of symmetrical motors, except for a check that there is sufficient saliency, no quantitative information on motor inductances are needed in order to implement the equal inductance method. In the case of asymmetrical motors, stator inductance values are needed. Those values can be obtained by measurement. However, there may be a

need to check suitability of the equal inductance method at the design stage when physical prototypes are not available. In that case inductance values have to be theoretically determined. Predicted values of stator inductance are also useful for the theoretical determination of peak stator current which can be relatively high during the initial rotor position detection since the algorithm relies on application of bipolar PWM with duty cycle near 50 per cent.

The rotor position estimated by the equal inductance method is proportional to the difference between quadrature and direct axis inductances. This difference is typically of the order of 10 to 20 percent of the average of the quadrature and direct axis inductances. Therefore theoretical assessment of suitability of the equal inductance method for a particular motor should be based on values of inductances that have been determined with an accuracy of better than two or three per-cent.

An electromagnetic model, based on a hybrid of the coupled network method and the assumed flux path method, has been developed to evaluate d-axis and q-axis phase self-inductances and mutual inductances for printed circuit motors. Tests performed on prototype motors gave results that were within three per-cent of values predicted from the model. Predictions of the proposed model can be used to pre-determine the machine constants necessary for practical implementation of sensorless commutation control based on the equal inductance method.

8.2 Future Work

This thesis project has focussed on the electromagnetic design and performance analysis of the printed circuit axial flux brushless DC motor. There is a need for further investigations into the mechanical and thermal aspects of the motor.

Accelerated aging tests need to be carried out to ensure that the stators of motors used in practical environments remain in good condition over the design life of the motor. In particular there is a need to find out whether mechanical and thermal stress lead to early failure resulting from buckling of the FR4 substrate.

Only stator power losses have been investigated in this thesis project. Rotor power losses are likely to be low, but this needs confirmation. Electromagnetic analysis is required to determine permanent magnet and rotor iron eddy current loss. This could be based on models similar to the ones described in (f) above. Some measure of rotor bearing and aerodynamic loss may also be of interest to those interested in prediction of overall motor efficiency.

Prediction of thermal performance of the motor requires knowledge of heat transfer coefficients. These are functions of rotor design, outer case design, rotor speed and the operating environment. Modelling of air-flow inside the motor needs to be carried out to help determine the necessary heat transfer coefficients.

The equal inductance method requires sensing of the voltage at the terminal of the un-energised phase of the BLDC motor. The resolution achieved by the method would theoretically allow sensorless control of brushless motors operating in synchronous mode.

However, further research work is necessary to adapt the equal inductance method to this class of motors because they have all three phases energised simultaneously .

It was found that the prototype motors had back emfs that were very close to sinusoidal (less than 2% distortion). This implies that the motors are suitable for operation in synchronous mode. If the inverter injects sinusoidal currents into phase windings, torque ripple will be minimal. The fact that the back emf waveforms are closer to sinusoidal than trapezoidal means that torque ripple will be present during operation of the motor in brushless DC mode. It is expected that the motors will operate satisfactorily in the BLDC mode for most applications. Detailed investigation aiming at minimising torque ripple in brushless DC mode remains to be done.

References

[1] Miller T.J.E., '*Brushless Permanent-Magnet and Reluctance Motor Drives'*, Oxford University Press, Oxford, 1989

[2] Ahfock A. and Gambetta D., '*Technique for Sensorless Commutation of Brushless DC Motors* ', Swiss Institute of Intellectual Property, Bern, Patent Application Number 00342/05, 2005.

[3] Gambetta D., '*Sensorless Technique for BLDC Motors*', MPhil Dissertation, University of Southern Queensland, Australia, 2006

[4] Baudot J.H., '*Rotating Electric Machines with Printed Circuit Windings*', United States Patent Office, patent number 3144574, Aug 11, 1964.

[5] Swiggett R.L., '*Printed Circuit Armature'*, United States Patent Office, patent number 2970238, patented Jan 31, 1961.

[6] Jang G.H. and Chang J.H., *'Development of Dual Air Gap Printed Coil BLDC Motor'*, IEEE Transaction On Magnetics, Vol. 35, No. 3, May 1999, pp. 1789-1792

[7] Tsai M. and Hsu L., '*Design of a Miniature Axial-Flux Spindle Motor with Rhomboidal PCB Winding*', IEEE Transactions On Magnetics, Vol 42, No. 10, October 2006, pp. 3488-3490.

[8] Jang G.H. and Chang J.H., '*Development of an Axial-Gap Spindle Motor for Computer Hard Disk Drives Using PCB Winding and Dual Air Gaps*', IEEE Transactions On Magnetics, vol 38, No. 5, September 2002, pp. 3297-3299.

[9] Low T.S., Jabbar M.A. and Tan T.S., '*Design Aspects and Performance of Slotless PM Motor for Hard Disk Drives*', Magnetic Technology Centre, National University of Singapore, Singapore

[10] Takano H., Ito T., Mori K. and Sakuta A., '*Optimum Values for Magnet and Armature Winding Thickness for Axial Field Permanent Magnet Brushless DC Motors*', Department of Electrical Engineering, University of Osaka Prefecture, Sakai, Osaka 591, Japan

[11] Walker A.M and Pullen K.R., '*An axial flux machine design with an airgap winding using flat conductors*', 3rd IET International Conference on Power Electronics, Machines and Drives (PEMD 2006), Dublin, Ireland, 4-6 April 2006, pp 221-225

[12] Wang R and Kamper M. J., '*Evaluation of Eddy Current Losses in Axial Flux Permanent Magnet (AFPM) Machine with an Ironless Stator*, Proceedings of IAS Annual Meeting, 37th IEEE Industry Applications Conference IAS '02, pp. 1289 1294

[13] Prokop L., '*3-phase BLDC motor control with sensorless back-EMF ADC zero crossing detection using the 56F805, Designer reference manual'*, Motorola Czech System Laboratories, Roznov pod Radhostem, Czech Republic, 2003

[14] Bolognani S., Oboe R. and Zigliotto M., *'Sensorless full-digital PMSM drive with EKF estimation of speed and rotor position'*, IEEE Transaction On Industrial Electronics, Volume 46, Issue 1, 1999, pp. 184-191

[15] Kim S. and Sul S, *'New approach for high-performance PMSM drives without rotational position sensors'*, IEEE Transaction On Power Electronics,Volume 12, Issue 5, 1997, pp. 904-911

[16] Petrovic V., Stankovic A. and Blasko V., *'Position estimation in salient PM synchronous motors based on PWM excitation transients'*, IEEE Transaction On Industry Applications, Volume 39, Issue 3, 2003, pp. 835-843

[17] Robeischl E. and Schroedl M., *'Optimized INFORM measurement sequence for sensorless PM synchronous motor drives with respect to minimum current distortion'*, IEEE Transaction On Industry Applications, Volume 40, Issue 2, 2004, pp. 591-598

[18] Schmidt P., Gasperi M., Ray, G. and Wijenayake A., *'Initial rotor angle detection of a non-salient pole permanent magnet synchronous machine'*, IEEE Industry Applications Society Annual Meeting, New Orleans, 1997

[19] Shouse K. and Taylor D., *'Sensorless velocity control of permanent-magnet synchronous motors'*, IEEE Transaction Control System Technology, Volume 6, Issue 3, 1998, pp. 313-324

[20] Wang L. and Lorenz R., *'Rotor Position Estimation for Permanent Magnet Synchronous Motor Using Saliency-Tracking Self-Sensing Method'*, Proceedings of IEEE IAS Annual Meeting, Rome, Italy, 2000, pp. 445-450

[21] Ueki Y., *'Detection of relative position between magnetic pole and drive coil in brushless dc motor'*, United State Patent, Patent Number 5,159,246,1992

[22] Weiss W., *'Artificial heart with sensorless motor'*, United State Patent, Patent Number 5,751,125, 1998

[23] Lawrenson P.J. and Agu I.A., '*Theory and performance of polyphase reluctance machine*', ibid, 111, (8) , 1964, pp. 1435-1445

[24] *'IEEE test procedures for synchronous machines*', IEEE publication 115, 1965, p. 52

[25] Jones C.V., '*The unified theory of electrical machines*', Butterworths, 1967

[26] Prescott J.C. and El-Kharashi A.K., *'A method of measuring self inductance applicable to large electrical machines*', Proc. IEE, 106A, 1959, pp. 169-173

[27] Kaminosono H. and Uyeda K., *'New measurement of synchronous machine quantities*', IEEE Trans., PAS-87, 1968, pp. 1908-1918

[28] Carter G.W., Leach W.I. and Sudworth J., '*The inductance coefficients of a salient pole alternator in relation to two-axis theory*', Proc. IEE, 108A, 1961, pp. 263-269

[29] Ahfock A. and Hart B., '*New method for measuring Xd and Xq based on the P-Q diagram of the lossy salient-pole machine*', IEEE Proceedings, Vol. 131, Pt. B, No. 6, November 1984

[30] Salon S., '*Finite Element analysis of Electrical Machines, Kluwer Academic Publishers'*, 101 Philip Drive, Assinippi Park, Norwell, Massachusetts 02061, 1995

[31] Abdel-Razek A., Coulomb J., Feliachi, M. and Sabbonnadierre, J., '*Conception of an air-gap element for the dynamic analysis of the electromagnetical field in electric machines*', IEEE Transactions On Magnetics MAG-18(2) , 1982, pp. 655-659

[32] DeBortoli M., Lee M., Salon S. and Lee K., '*Coupling finite elements and analytical solution in the airgap of electric machines*', IEEE Transactions On Magnetics 27(5) , 1991, pp. 3955-3957

[33] Hewitt A. J. and Ahfock A., '*Sub-domain scaling for finite element analysis of electrical machines*', IEE Proceedings – Electrical Power Applications 152(2) , 2005, pp. 149-156

[34] Feliachi M., Coulomb J. and Mansir H., '*Second order air-gap element for the dynamic finite-element analysis of the electromagnetic field in electric machines*', IEEE Transactions On Magnetics MAG-19(6) , 1983, pp. 2300-2303

[35] Guerin C., Tanneau G., Meunier G., Brunotte X. and Albertini J., '*Three dimensional magnetostatic finite elements for gaps and iron shells using magnetic scalar potentionals*', IEEE Transactions On Magnetics 30(5) , 1994, pp. 2885-2888

[36] Bödrich, Th. Roschke, A, '*Magnetic Library for Modelica', Proceedings of the 4th International Modelica Conference*, Hamburg, March 7-8, 2005, Gerhard Schmitz (editor)

[37] Petrinchenko D., Hecquet M, Brochet P., Kuznetsov V. and Laloy D., ‚*Design and Simulation of Turbo-Alternators Using a Coupled Permeance Network Model*', IEEE Transactions On Magnetics, Vol. 42, No. 4, 2006, pp. 1259-1262

[38] Wang X., Li Q., Wang S. and Li Q:,'*Analytical Calculation of Air-Gap Magnetic Field Distribution and Instantaneous Characteristics of Brushless DC Motors*', IEEE Transactions On Energy Conversion, Vol. 18, No. 3, 2002, pp. 424-432

[39] Demenko A., '*Three dimensional eddy current calculation using reluctance-conductance network formed by means of FEM method*', IEEE Transaction On Magnetics 36(4) , 2000, pp. 741-745

[40] Balchin M.J. and Davidson J. A. M., '*3-dimensional eddy-current calculation by the network method*', Proceedings of the IEE 130(2), 1983, pp. 88-92, Part A

[41] Davidson J. and Balchin, M., '*Three dimensional eddy current calculation using a network method*', IEEE Transaction On Magnetics MAG-19(6), 1983, pp. 2325-2328

[42] Davidson J. A. M. and Balchin, M. J., '*Experimental verification of network methods for calculating flux and eddy-current distributions in three dimensions*', IEE Proceedings 128(7), 1981, pp. 492-496, Part A

[43] Balchin M.J. and Davidson, J. A. M., '*Numerical method for calculating magnetic-flux and eddy-current distributions in three dimensions*', IEE Proceedings 127(1), 1980, pp. 46-53, Part A

[44] Carpenter C.J., '*Theory of flux penetration into laminated iron and associated losses*', Proceedings of the IEE 124(7), 1977, pp. 659-664

[45] Carpenter C.J., '*Finite-element network models and their application to eddy-current problems*', Proceedings of the IEE 122(4), 1975a, pp. 455-462

[46] Carpenter C.J., '*A network approach to the numerical solution of eddy-current problems*', Transactions On Magnetics Mag-11(5), 1975b, pp.1517-1522

[47] Carpenter C.J., '*Three-dimensional numerical solution of eddy-current in thin plates*', Proceedings of the IEE 122(6), 1975c, pp. 681-688

[48] King E. I., '*Equivalent circuits for the two-dimensional magnetic fields: I – the static filed*', IEEE Transactions On Power Apparatus and System PAS-85(9), 1966a, pp. 927-935

[49] King E. I., '*Equivalent circuits for the two-dimensional magnetic fields: II – the sinusoidally time-varying field*', IEEE Transaction on Power Apparatus and System PAS-85(9), 1966b, pp. 936-945

[50] Ahfock T. L. and Hewitt A., '*Curvature-related eddy-current losses in laminated axial flux machine cores*', IEE Proceedings on Electrical Power Applications, 152(5), 2005, pp. 1350-1358. ISSN 1350-2352

[51] Hewitt, A., '*The effects of curvature on axial flux machine cores*', PhD Dissertation, 2005, University of Southern Queensland, Australia

[52] Guo, Y. and Zhu, J., '*Magnetic field calculation of claw pole permanent magent machines using magnetic network method*', Journal of Electrical and Electronics Engineering 22(1), 2002, pp. 69-75

[53] Stöcker H., '*Taschenbuch der Physik*', Harri Deutsch, 1998

[54] Gieras J.; Wang R-J.; Kamper M., '*Axial Flux Permanent Magnet Brushless Machines*', Kluwer Academic Publishers, 2004

[55] Grover F.W., '*Inductance Calculations – Working Formulas and Tables*", 1946, D. Van Nostrand Co., Inc.

[56] Wheeler H. A., '*Inductance formulas for circular and square coils*' Proc. IEEE, vol. 70, pp. 1449-1450, 1982.

[57] Miller H. C., '*Inductance formulas for a single layer circular coil*' Proc. IEEE, vol. 75, Issue 2, 1982.

[58] Cheng K.W.E., Chan H.L. and Sutanto D., '*Power Electronics and Variable Speed Drives'*, 18-19 September 2000, Conference Publication No. 475, IEE 2000

Appendix A

First Order Magnetic Model

A.1 The model

The airgap flux density in equation (3.11) has been computed using the model geometry presented in figure A.1.

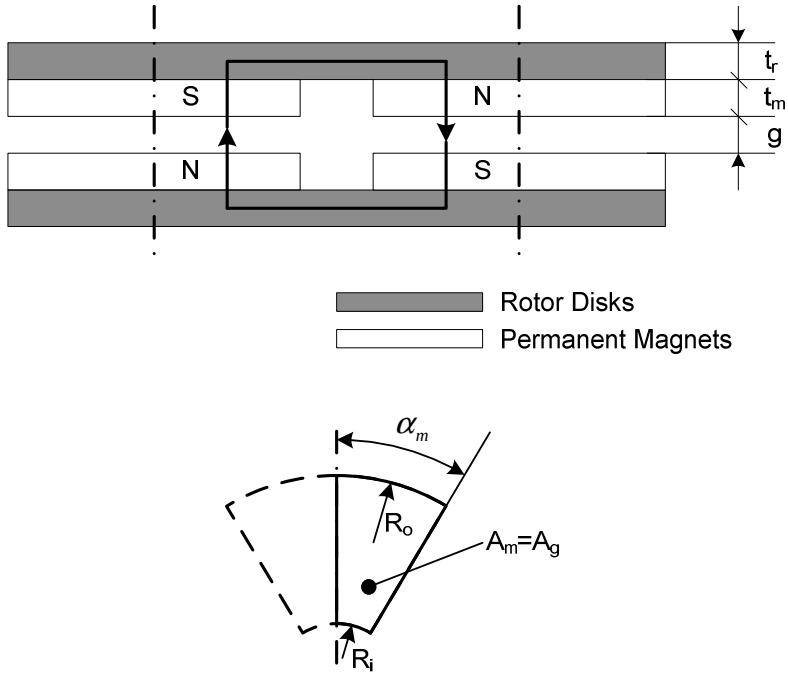

Figure A.1 : Model Geometry

Figure A.2 introduces the electromagnetic model relative to the geometry presented in figure A.1

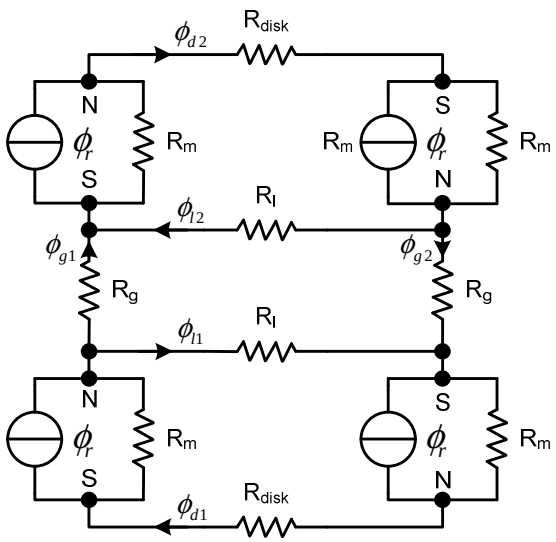

Figure A.2 : Model Geometry

By neglecting the leakage flux between neighbouring permanent magnets, figure A.2 can be simplified as shown in figure A.3:

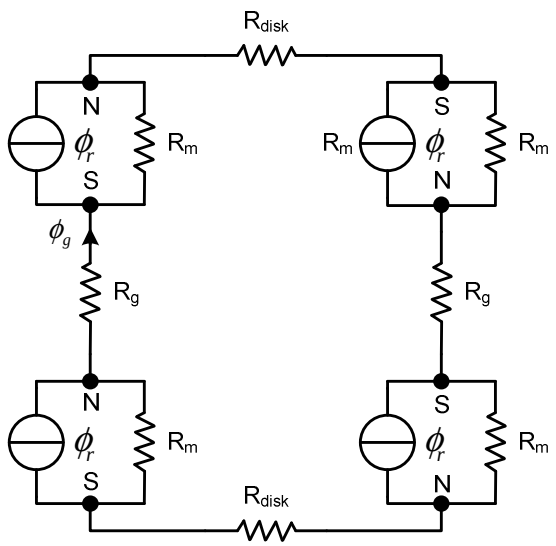

Figure A.3 : Simplified Model Geometry

By re-arranging and grouping the various reluctances and flux sources, the model can be further simplified as presented in figure A.4:

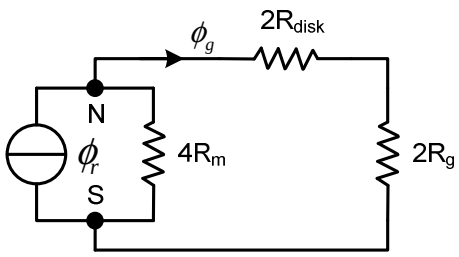

Figure A.4 : Further Simplified Model Geometry

A.2 Reluctance Computation

$$R_m = \frac{t_m}{\mu_0 \mu_{r\_pm} A_m} \tag{A.1}$$

where:

$$A_m = \frac{\left(R_o^{\,2}\pi - R_i^{\,2}\pi\right)}{2\pi}\alpha_m \tag{A.2}$$

$$\alpha_m = \frac{\left(\frac{2\pi}{P}\right)}{2}0.7 \qquad \text{(0.7 is the clearance factor between two magnets)} \tag{A.3}$$

Inserting (A.2) and (A.3) in (A.1):

$$R_m = \frac{t_m P}{1.4\mu_0 \mu_{r\_pm}\left(R_o^{\,2}\pi - R_i^{\,2}\pi\right)} \tag{A.4}$$

$$R_g = \frac{g}{\mu_0 A_g} \tag{A.5}$$

where:

$$A_g = A_m \tag{A.6}$$

Inserting (A.6) in (A.5):

$$R_g = \frac{gP}{1.4\mu_0 \left(R_o^{\,2}\pi - R_i^{\,2}\pi \right)} \tag{A.7}$$

$$R_{disk} = \frac{l_{disk}}{\mu_0 \mu_{r\_disk} A_{disk}} \tag{A.8}$$

where:

$$l_{disk} = 2\left(\frac{t_r}{2}\right) + \frac{\left(\frac{\left(R_o + R_i\right)}{2}\right)2\pi}{P} \tag{A.9}$$

$$A_{disk} = \left(R_o - R_i\right) t_r \tag{A.10}$$

$$R_{disk} = \frac{2\left(\frac{t_r}{2}\right) + \frac{\left(\frac{\left(R_o + R_i\right)}{2}\right)2\pi}{P}}{\mu_0 \mu_{r\_disk} \left(R_o - R_i\right) t_r} \tag{A.11}$$

A.3 Flux Density Computation

Based on figure A.4:

$$\phi_g = \frac{4R_m}{\left(4R_m + 2R_{disk} + 2R_g\right)}\phi_r \tag{A.12}$$

where:

$$\phi_r = B_r A_m \qquad \text{(B}_\text{r} \text{ from permanent magnet datasheet)} \tag{A.13}$$

$$B_g = \frac{\phi_g}{A_g} = \left(\frac{4R_m}{\left(4R_m + 2R_{disk} + 2R_g\right)}\phi_r\right)\frac{1}{A_g} \tag{A.14}$$

Assuming $u_{r\_disk} = \infty$ and $u_{r\_pm} = 1$:

$$B_g = \frac{B_r t_m}{\left(t_m + \frac{g}{2}\right)} \tag{A.15}$$

Appendix B

First Order Stator Eddy Current Model

B.1 The model

At first the total volume of copper winding in each track width case has been computed. Results are presented in table B.1.

Table B.1: Total Volume of Copper Windings (per layer)

Track Width [mm]	Base Cu Thickness [µm]	Radial+Parallel Parts Length [m]	Total Spiral Length [m]	Radial+Parallel Parts Volume [mm^3]	Total Spiral Volume [mm^3]
1.0	35	0.1124	0.3088	3.93	10.81
2.4	35	0.0565	0.1461	4.75	12.27
3.7	35	0.0385	0.0943	4.99	12.21

In [54] a first order model is presented, which doesn't consider end-windings. The author knows that at certain rotor positions eddy current are also induced in the end-winding, but for a first estimation of the eddy current losses, this approximation is applicable and as shown, the results are acceptable.

$$\Delta P_e = \frac{\pi^2}{3}\frac{\sigma}{\rho} f^2 a^2 m_{con} B_{mz}{}^2 = \frac{\pi^2}{3}\sigma f^2 a^2 V_{con} B_{mz}{}^2 \tag{B.1}$$

where:

σ = Electric conductivity = 47e6 S/m

f = Frequency (electrical) at 1000 rpm = 33.33 Hz

a = Track width = 1e-3 / 2.4e-3 / 3.7e-3 m

V_{con} = Conductor volume without end-winding = 3.93e-9 / 4.75e-9 / 4.99e-9 m^3

B_{mz} = Peak Axial flux density = 0.7 T

The formula assumes a sinusoidal flux density distribution (no distortion)

Table B.2: Predicted Loss per Phase

Track Width [mm]	Total Eddy Current Loss [mW]
1.0	3.8
2.4	26.4
3.7	65.6

Agreement with results presented in chapter 6 is within 20%.

Appendix C

First Order Self Inductance Model

C.1 The model

Different publications are available on inductance computation of single layer and spiral coils. A very interesting handbook on inductance calculations has been published by [55]. This book represents a nice short cut for engineers or designers. An analytical formula for the self-inductance of a single layer circular coil of any $\frac{lenght}{diameter}$ ratio has been given by Wheeler [56]:

$$L = \frac{\mu N^2 \pi r^2}{c} K \tag{C.1}$$

where:

$$K = \frac{1}{3\pi}\left[\left(\frac{dc}{r^2}\right)\left[F(k) - E(k)\right] - \frac{4d}{c}E(k) - \frac{8r}{c}\right]$$

r	=	radius of the coil
c	=	axial length of the coil
d	=	$\sqrt{4r^2 - c^2}$
N	=	number of turns
K	=	$\frac{2r}{d}$
F(k), E(k)	=	Elliptic integrals of first and second order

A closed solution of the elliptic integrals is not immediate. Miller [57] introduced an iterative method to determine F(k) and E(k). The primary objective of the intended first order model is a fast estimation of the motor phase self inductance. This is useful for first evaluation of control possibilities of the planned machines. Therefore the formula should not contain iterative loops, which would require significant computational effort.

Chan, Cheng and Sutanto [58] introduced a simplification of the Neumann's Formula. In this case the elliptic integrals are approximated by a logarithmic function.

To overcome difficulties with elliptic integrals, Wheeler [56] published different approximate formulae, which are nowadays well diffused. In one particular case he derived an approximation for a spirally shaped coplanar coil, by collapsing the coplanar turns in one "mean" turn under assumption that the conductor width is much larger than the clearance between each conductor.

This is a reasonable assumption also in the case of printed circuit spiral. The flat spiral air-core coil inductance by Wheeler [56] can be easily computed by:

$$L = \frac{N^2 r^2}{(2r + 2.8d)10^5} k_g \tag{C.2}$$

where:

r = mean radius of the coil

c= axial length of the coil

d= outer coil radius (r_o) - outer coil radius (r_i)

and,

$k_g = P^2 \cdot \frac{l_{ps} - l_{ops}}{l_{cs}}$, where:

P= number of stator poles

l_{cs}= length of the circular spiral (used by equation (2)) $\cong 2r\pi N$

l_{ps}= length of the phase spiral (real track shape from algorithm).

l_{ps}= length of the outer arcs of the spiral (real track shape from algorithm).

The inductance computed by (C.2) is in free space. This condition is not reflected in the motor. By measurements presented in figure 7.10, the coil q-axis inductance is near to the coil inductance in free space.

The first order model delivers a value which is closer to the q-axis inductance, within 25%.

Appendix D

Photo Gallery

D.1 Photos of Hardware

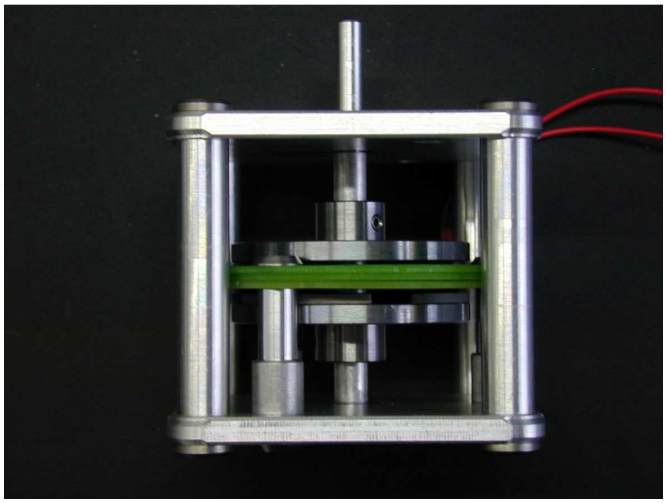

Figure D.1 : The Motor Prototype

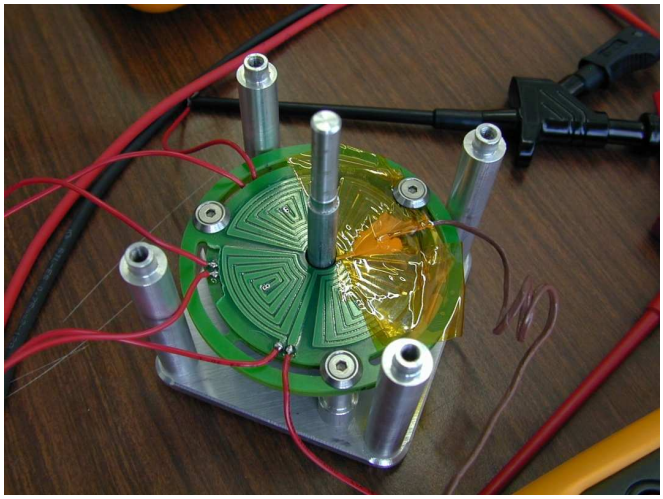

Figure D.2 : Thermal Measurements on first Prototype

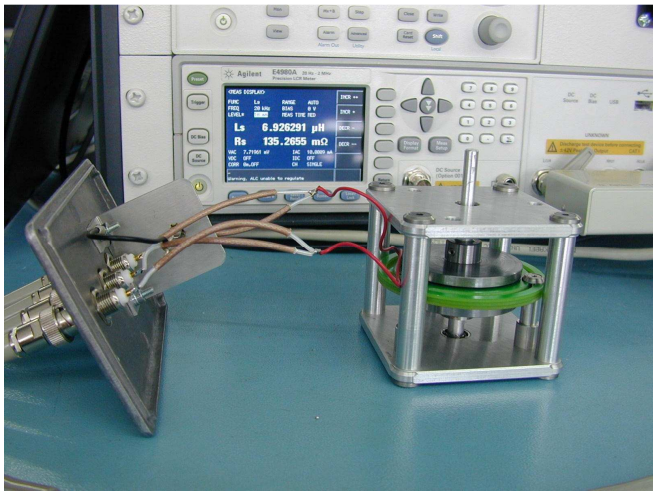

Figure D.3 : Self-Inductance Measurements